ANL/EES-TM-271

Numerical Techniques for Steady Two-Dimensional Transcritical Stratified Flow Problems, with an Application to the Intermediate Field Dynamics of Ocean Thermal Energy Conversion Plants

J. M. Jones, G. H. Jirka, and D. A. Caughey

RETURN TO REFERENCE FILE
TECHNICAL PUBLICATIONS
DEPARTMENT

ANL
EES

ARGONNE NATIONAL LABORATORY
Energy and Environmental Systems Division

Operated by
THE UNIVERSITY OF CHICAGO for U. S. DEPARTMENT OF ENERGY
under Contract W-31-109-Eng-38

Argonne National Laboratory, with facilities in the states of Illinois and Idaho, is owned by the United States government, and operated by The University of Chicago under the provisions of a contract with the Department of Energy.

DISCLAIMER

This report was prepared as an account of work sponsored by an agency of the United States Government. Neither the United States Government nor any agency thereof, nor any of their employees, makes any warranty, expressed or implied, or assumes any legal liability or responsibility for the accuracy, completeness, or usefulness of any information, apparatus, product, or process disclosed, or represents that its use would not infringe privately owned rights. Reference herein to any specific commercial product, process, or service by trade name, trademark, manufacturer, or otherwise, does not necessarily constitute or imply its endorsement, recommendation, or favoring by the United States Government or any agency thereof. The views and opinions of authors expressed herein do not necessarily state or reflect those of the United States Government or any agency thereof.

This informal report presents preliminary results of ongoing work or work that is more limited in scope and depth than that described in formal reports issued by the Energy and Environmental Systems Division.

Printed in the United States of America. Available from National Technical Information Service, U. S. Department of Commerce, 5285 Port Royal Road, Springfield, Virginia 22161.

ARGONNE NATIONAL LABORATORY
9700 South Cass Avenue
Argonne, Illinois 60439

ANL/EES-TM-271

NUMERICAL TECHNIQUES FOR STEADY TWO-DIMENSIONAL TRANSCRITICAL STRATIFIED FLOW PROBLEMS, WITH AN APPLICATION TO THE INTERMEDIATE FIELD DYNAMICS OF OCEAN THERMAL ENERGY CONVERSION PLANTS

by

Janet M. Jones, Gerhard H. Jirka, and David A. Caughey

Cornell University
School of Civil and Environmental Engineering

work performed under the direction of

Argonne National Laboratory
Energy and Environmental Systems Division

March 1983

Published January 1985

work sponsored by

U.S. DEPARTMENT OF ENERGY
and
NATIONAL SCIENCE FOUNDATION

NOTICE

This report has been published by Argonne National Laboratory in the form received from Cornell University, with no enhancement of the camera-ready copy.

FOREWORD

Argonne National Laboratory has been involved in several technical aspects of ocean thermal energy conversion (OTEC) since 1976, including research in the areas of power systems, biofouling and corrosion, and environmental studies. With support from the U.S. Department of Energy, Argonne was responsible for an activity known as *OTEC Project Management Support: Physical and Climatic Environmental Impact*. Research focused on problems related to the physical effects of OTEC plant operation on the ocean and, conversely, of the ocean on OTEC plant operation.

The heat engines of OTEC plants are driven by the temperature difference between the cold, deep water and the warm, surface water of tropical and semitropical oceans. Thermodynamic limitations dictate that large amounts of ocean water be withdrawn from and discharged to the ocean. As the flow rates are an order of magnitude greater than those associated with conventional steam-electric coastal power plants of equivalent power capacity, no precedents had been established for the external flow fields generated by operating such plants.

Under Argonne's supervision, research was undertaken to address the external flow field problems at scales ranging from those of plumes generated near the effluent discharge from the plant to oceanographic scales as large as the Gulf of Mexico. Analyses and numerical codes were developed and laboratory hydraulic modeling was applied to predict external flow fields. The studies were carried out by private firms, universities, and Argonne.

The study reported here -- numerical techniques for steady two-dimensional transcritical stratified flow problems -- was carried out at Cornell University under this program. It attempts to deal with what has been known as intermediate-field plume behavior, or the gravity collapse of a

buoyant jet in a current. This aspect of the external fluid mechanics of OTEC plant operation is important in terms of the potential environmental effects of individual plants and the spacing of multiple plants in the same region.

ACKNOWLEDGMENTS

The authors acknowledge support from the Ocean Systems Branch, Division of Central Solar Technology, of the U.S. Department of Energy under Contract No. ET-78-S-02-4683. The work was administered by Cornell University, Office of Sponsored Programs, under Account No. E87-8553, as a subcontract from the Massachusetts Institute of Technology. Technical support and program management from Argonne National Laboratory under John D. Ditmars and Robert A. Paddock are gratefully acknowledged.

Additional support was provided by a grant from the Fluid Mechanics Program, National Science Foundation, Grant No. CME-8012682 (Cornell Office of Sponsored Programs, No. E87-8401). George K. Lea was program manager.

The assistance of Frank Sargent, Pablo Huq, and Phillip Mineart, graduate research assistants, in carrying out concurrent experimental investigations is also gratefully acknowledged. Computer work was performed using the IBM 370-168 of Cornell Computer Services.

The study was carried out by Janet M. Jones, Graduate Research Assistant, and was submitted in essentially similar form as a thesis in partial fulfillment of the requirements for the Doctor of Philosophy degree at Cornell University. The study was supervised by Gerhard H. Jirka, Associate Professor of Civil and Environmental Engineering. Additional supervision, notably on aspects of the numerical model formulation, was provided by David A. Caughey, Associate Professor of Mechanical and Aerospace Engineering.

TABLE OF CONTENTS

		Page
LIST OF SYMBOLS		xxxiii
ABSTRACT		xxxix
Chapter		
1	INTRODUCTION	1
1.1	Environmental Occurrences of Two-Dimensional Density Currents	5
	Cooling water	5
	Effluents from sewage treatment plants	5
	River or estuarine inflow	5
	Spillages of liquefied gases	7
	Buoyant plumes from smokestacks and cooling towers	7
1.2	Overview of Fluid Mechanical Aspects of Ocean Thermal Energy Conversion (O.T.E.C.)	9
1.3	Problem Statement and Summary	10
2	REVIEW OF PREVIOUS WORK ON TWO- AND ONE-DIMENSIONAL DENSITY CURRENT DYNAMICS INCLUDING ANALOGOUS SHALLOW WATER AND GAS FLOW THEORIES	13
2.1	Dynamics of One-Dimensional Density Intrusions and Applications to Two-Dimensional Problems	14
2.1.1	The bulk shape: Density currents versus density wedges	14
	Density currents	14
	Density wedges	14

Chapter Page

2.1.2 Force balance of density currents. 17

2.1.3 One-dimensional density current dynamics applied to two-dimensional problems . . . 22

a) Purely convective-buoyant spreading regimes 22

Case A: Surface source on homogeneous ambient 27

Case B: Interface source with step-wise ambient stratification. 27

Case C: Linearly stratified ambient . . 27

b) The additional effect of interfacial friction. 28

2.2 The Transcritical Nature of Two-Dimensional Density Currents 31

2.2.1 General properties 31

2.2.2 The internal hydraulic jump. 38

2.3 Comparison of Density Current Theory with that for Free Surface Shallow Water Flows and Compressible Gas Flows 44

2.3.1 Free surface shallow water theory. 47

2.3.2 Compressible gas flow theory 48

2.4 Stability and Entrainment of a Density Current. 53

Chapter Page

2.4.1 Interfacial stability. 53

2.4.2 Turbulent entrainment. 54

2.4.2.1 Non-buoyant jet entrainment 54

2.4.2.2 Buoyant density current entrainment . . . 56

Applications 59

2.5 Previous Two-Dimensional Density Current Solutions. 60

2.6 Numerical Techniques. 66

2.6.1 The characteristic nature of super- and sub-critical flows. 66

2.6.2 Numerical techniques for supercritical flow. 69

2.6.3 Numerical techniques for transcritical flow. 75

2.6.3.1 The hodograph method 75

2.6.3.2 Numerical finite difference and finite element techniques 77

Shock-patching 77

Shock-smearing or shock-capturing. . . 78

Explicit artificial viscosities. . . . 78

Implicit artificial viscosities. . . . 78

Finite difference techniques 79

Finite element techniques. 81

3 PHYSICAL CONCEPTS. 84

3.1 General OTEC-Ambient Ocean Schematization: Definition of Scales 84

Chapter		Page
	a) Velocity and Density Profiles.	84
	Case A: Surface Source with Homogeneous Ambient	87
	Case B: Interface Source with Stepwise Stratification.	87
	Case C: Equilibrium Source with Linear Stratification.	89
	b) Unsteadiness	90
	c) Shallow density current.	90
3.1.1	Definition of scales	92
	1) Near Field Region (Section 3.4).	94
	2) Intermediate Field Region (Section 3.5).	96
	a) The transcritical flow region	96
	b) The supercritical flow region	96
	3) Far Field Region	96
3.2	Governing Equations.	97
	Case A: Surface Source on Homogeneous Ambient.	103
	Case B: Interface Source with Stepwise Stratification	103
	Case C: Interface Source with Linear Stratification	103
	1. Near-Field Region (Entraining Regime)	105

Chapter Page

2. Intermediate Field Region. 105

a) Transcritical flow region (convective regime) 105

b) Supercritical region (convective and frictional regimes) 106

3.3 General Boundary Conditions 106

3.3.1 Ambient fluid. 106

3.3.2 Density current interactions with ambient flow. 107

i. Front conditions. 107

ii. Source conditions 108

3.4 Near-Field Region 110

3.4.1 Governing equations. 110

3.4.2 Boundary conditions and possible downstream controls. 111

3.4.3 Non-dimensionalization for the near field equations 112

3.5 Intermediate Field Region 115

3.5.1 Transcritical flow region. 115

3.5.1.1 Nondimensionalization of the transcritical flow region 117

3.5.2 Supercritical flow region 120

3.5.2.1 Nondimensionalization of supercritical flow region. 121

Chapter | Page

3.6 Transition Conditions for the Boundary Between the Near and Intermediate Fields. . . 121

4 THE NEAR FIELD SOLUTION 127

4.1 Numerical Computations - MacCormack's Method . . 127

4.1.1 Finite volume formulation 131

4.1.2 Solution details. 133

4.1.3 Initial and boundary conditions 134

4.2 Results for Stagnant Ambient ($\hat{u}_a = 0.0$). 137

4.3 Results for Moving Ambient ($\hat{u}_a > 0$). 141

4.3.1 Computational grid. 141

4.3.2 Solution properties 143

4.4 A Simplified Model for Moving Ambient ($\hat{u}_a > 0$) . 147

4.4.1 Rotationality of the flow 152

5 THE INTERMEDIATE FIELD (TRANSCRITICAL FLOW REGION) SOLUTION 156

5.1 Problem Definition 156

5.2 Choice of Solution Technique 158

Finite element methods. 160

Choice of solution method 160

5.3 Numerical Scheme 161

5.3.1 Upwinding considerations. 161

5.3.2 Finite volume scheme and associated lumping error. 162

Chapter Page

5.3.3 Addition of artificial viscosity. 165

5.3.4 Solution of the difference equations. 167

5.4 Numerical Experiment: Flow in a Radially Expanding Channel 175

5.4.1 Shock determination - switching function. . . 178

5.4.2 Values of the coefficients ω and ω_s 180

5.5 Application of the Transcritical Model to a Radial Discharge Into a Moving Ambient: General Procedures. 180

5.5.1 Near-intermediate field transition conditions. 181

5.5.2 Generation of an orthogonal grid (using a Boundary Integral Equation Method) 183

5.5.3 Obtaining a transcritical flow solution for a given grid 192

a) grid points 192

b) boundary conditions. 192

c) initial conditions 192

Convergence Estimation 193

5.5.4 Successive grid modification until full matching at frontal boundary 194

5.6 Fully-matched Solutions. 203

5.7 Summary of (Fully Matched) intermediate field solutions 218

Chapter Page

6 THE INTERMEDIATE FIELD (SUPERCRITICAL FLOW REGION) SOLUTION. 223

6.1 Numerical Computations - MacCormack's Method. . 223

6.1.1 Solution details 225

6.1.2 Initial and boundary conditions. 225

6.1.3 Automatic grid generation and matching of the frontal boundary. 226

6.2 Numerical Experiment: Application of the MacCormack Supercritical Scheme to an Initially Uniform Grid 228

6.3 Application to the Intermediate Field Supercritical Domain. 232

6.3.1 Typical values of the frictional parameter, $\lambda_i V'$. 232

6.3.2 Results. 232

6.3.3 Additional comments 241

High velocities 241

Non-orthogonality of grid 249

7 SUMMARY OF PREDICTIONS, COMPARISONS WITH EXPERIMENTAL DATA AND ENVIRONMENTAL APPLICATIONS. . . 250

7.1 Complete Predictions. 250

7.1.1 Summary of intermediate field results. . . . 250

7.1.2 Additional comments: Near field and downstream extensions 258

Chapter Page

a) Near field. 258

b) Downstream extension. 263

7.2 Comparison with Experimental and Field Data. . . 263

7.2.1 Experimental data 263

7.2.2 Field data. 272

7.3 Predictions. 275

7.3.1 Application to a river discharge. 276

7.3.2 Application to an OTEC discharge. 283

7.3.2.1 Ocean baseline conditions. 283

7.3.2.2 Plant design 285

7.3.2.3 Applicability of the present model to OTEC discharges. 286

7.3.2.4 Density current sensitivity. 289

8 SUMMARY, CONCLUSIONS AND SUGGESTIONS FOR FUTURE WORK 293

8.1 The Near-Field 294

8.2 Intermediate Field 295

8.3 Suggestions for Future Work. 297

8.4 Comparison with Observations 299

8.5 Environmental Applications 300

REFERENCES. 301

APPENDIX I. OCEAN THERMAL ENERGY CONVERSION (OTEC): PAST, PRESENT AND FUTURE 312

Chapter		Page
I-1	Historical Development.	312
I-2	Present Day OTEC Technology	314
I-3	Potential Future OTEC Uses and Applications . .	318
APPENDIX II	HISTORICAL OVERVIEW OF THE HYDRAULIC ANALOGY TO COMPRESSIBLE GAS FLOW	320

LIST OF TABLES

Page

Table 2-1

Classification of the type of different regions of the potential Equation (2.35). 35

Table 2-2

Deviation with upstream Froude number of height ratios across a jump for the conservation of energy, (E curve), relative to the conservation of momentum (M curve) 44

Table 2-3a

Analogy between compressible gas flow and stratified fluid (shallow water) flow in the absence of flow discontinuities. 45

Table 2-3b

Classification of flow discontinuities for compressible gas flow and stratified fluid (shallow water) flow 46

Table 3-1

Length scale values (in km) for typical OTEC and oceanic conditions 95

Table 3-2

Near field scale definitions 114

Table 3-3

Near field nondimensionalized initial conditions 116

Table 3-4

Intermediate field parameter and length scales 119

Page

Table 5-1

Summary table of the results presented for the intermediate field transcritical region. 204

Table 6-1

A summary of the results presented for the intermediate field supercritical region. 233

Table 7-1

Summary table of the results presented for the full intermediate field 251

Table 7-2

Range of flow parameters used in various experimental data sources 268

Table 7-3

Summary of some of Garvine's (1974) Connecticut River discharge data. 279

Table 7-4

Riverine discharge predictions. 280

Table 7-5

OTEC-100 intermediate field predictions 288

LIST OF FIGURES

Page

Figure 1-1

Top and lateral views of a hot water density current produced in the laboratory (after Jirka *et al.*, 1980). 2

Figure 1-2

Schematic representation of a density current similar to that in Figure 1-1, showing streamlines and surface velocity vectors (after Jirka *et al.*, 1980) 4

Figure 1-3

The Connecticut River plume discharging into Long Island Sound. The salinity field shown is at a depth of 0.5 m, the readings being taken after flood tide. The ship track is marked by arrows (after Garvine, 1974) 6

Figure 1-4

Vertical density section across the Connecticut River plume, during ebb tide (after Garvine, 1977). Sampling points are shown by solid dots. σ_T units are used. 8

Figure 2-1

Typical one-dimensional surface density intrusions 15

Figure 2-2

Variation of drag coefficient, C_D, with density current to ambient depth ratio, h/H 20

Page

Figure 2-3

A comparison of theoretical and experimental relations between the drag coefficient, C_D, and the relative current to ambient water depth, h/H, (after Sargent, 1983). 21

Figure 2-4

Larsen and Sorensen's (1968) density current schematization . 23

Figure 2-5

Schematic view of momentum block spreading applied to density currents (after Bache, 1976). 26

Figure 2-6

Convective and frictional regimes for density current spreading, (after Jirka et al., 1980)

a) Homogeneous or stepwise ambient stratification, (Cases A and B, respectively), s = 0 32

b) Linear ambient stratification, (Case C), s = 1. . 33

Figure 2-7

Variations of mass flux/unit width with velocity

a) Homogeneous or stepwise ambient stratification, s = 0. 37

b) Linear ambient stratification, s = 1 37

Figure 2-8

The percentage energy loss across a jump relative to the upstream energy, as a function of upstream Froude number.

Page

a) Homogeneous or stepwise ambient stratification, s = 0 40

b) Linear ambient stratification, s = 1. 40

Figure 2-9

The variation of the ratio of downstream to upstream jump (shock) heights with upstream Froude (Mach) number

a) Homogeneous or stepwise ambient stratification s = 0 41

b) Linear ambient stratification, s = 1. 42

Figure 2-10

Various buoyant entrainment functions in comparison with the data of Ellison and Turner (1959) 57

Figure 2-11

Geometry of combined density current upstream intrusion, convective and frictional regimes, (after Jirka et al., 1980)

a) Homogeneous or stepwise ambient stratification, s = 0 62

b) Linear ambient stratification, s = 1. 63

Figure 2-12

The resulting flow field (after Garvine, 1982), for a discharge at an angle of 39° and velocity of 1.0 units, into an ambient velocity of 0.68 units. The dashed lines show streamlines. No entrainment is assumed 65

Page

Figure 2-13

Regions of influence and dependence in supercritical flow. . . 67

Figure 2-14

The appropriate explicit finite difference step size for a given characteristic slope 71

Figure 3-1

Typical σ_T profiles and values of Brunt-Vaisala frequency, N, for tropical and sub-tropical oceans. 85

Figure 3-2

Example of a detailed vertical record of temperature (density) and velocity distributions from the Gulf of Mexico (after Thomas et al., 1979) 86

Figure 3-3

Local schematizations of the ocean density structure in regions of the intermediate field layer. 88

Figure 3-4

Example of a longterm record of temperature and density within the thermocline of the Gulf of Mexico (after Thomas et al., 1979). 91

Figure 3-5

Intermediate field flow and density structure. 101

Figure 3-6

Schematized two-dimensional density current (OTEC) in an ambient crossflow. 109

Page

Figure 4-1

Relationship between the Cartesian and Contravariant planes. . 130

Figure 4-2

Radial entraining discharge into a stagnant ambient using the entrainment function of Jirka (1982), Equation (2.79). Near field nondimensionalization used. 139

Figure 4-3

Radial entraining discharge into a stagnant ambient using the entrainment function of Stolzenbach and Harleman (1971), Equation (2.78). Near-field nondimensionalization used . . . 140

Figure 4-4

The orthogonal grid used for the numerical computations of a source in an ambient flow ($\hat{u}_a > 0$). 144

Figure 4-5

Equi-Froude number and equi-buoyancy contours for a radial source discharging into an ambient flow. Near-field nondimensionalization is used.

a) $\hat{u}_a = 0.157$. 146

b) $\hat{u}_a = 0.250$. 146

c) $\hat{u}_a = 0.500$. 146

Figure 4-6

Centerline properties for a radial discharge into a moving ambient, $\hat{u}_a = 0.157$, using the entrainment function of Jirka (1982). Near-field nondimensionalization is used . . . 148

Page

Figure 4-7

Equi-velocity and equi-height contours for a radial source discharging into an ambient flow. Near-field nondimensionalization is used.

a) $\hat{u}_a = 0.157$. 149

b) $\hat{u}_a = 0.250$. 149

c) $\hat{u}_a = 0.500$. 149

Figure 4-8

Centerline properties from the simplified model of a radial discharge into a moving ambient, $\hat{u}_a = 0.157$. 151

Figure 4-9

A comparison of the buoyancy and Froude numbers from the simplified and accurate models for a radial discharge into a moving ambient, $\hat{u}_a = 0.157$.. 153

Figure 4-10

Variation of circulation around a contour, Γ, (as a percentage of the local normal mass flux) with $\hat{x}_\Gamma$, the downstream point of intersection of Γ with the $\hat{x}$ axis. Circulation values for $\hat{u}_a$ values of 0.157, 0.250 and 0.500 are considered. 154

Figure 5-1

The rotated difference stencil. Showing the points contributing to the upwinded (ϕ_{ss}) and central differenced (ϕ_{nn}) parts of the potential Equation (5.2) when applied to a

Page

supercritical region, (after Jameson, 1978) 163

Figure 5-2

Velocity and artificial mass flux as a function of distance for a radial channel, using the transcritical program .

a) Velocity as a function of radial distance. . . . 176

b) Ratio of artificial mass flux, P, to contravariant mass flux, hDU 176

Figure 5-3

The variation of the transition radius, $\hat{r}_T$, with the relative intermediate to near-field strengths, ℓ_I/ℓ_N 182

Figure 5-4

An early grid, G1, developed using the BIEM method, and used for the transcritical program 184

Figure 5-5

Definition sketches of the BIEM applications required for the grid generation. 186

Figure 5-6

Definition diagram for the boundary integration used in the BIEM method. The arrows indicate the direction of integration around the boundary curve, Γ, of the domain D. P is a singularity separated from D by the circle σ, radius r_o, (after Liggett and Liu, 1983). 188

Page

Figure 5-7

A typical grid, G5, developed using the BIEM method, and used for the transcritical program 191

Figure 5-8

Height contours for the non-matched solution for ℓ_I/ℓ_n = 41.2. Calculated using grid G1, Figure 5-4 195

Figure 5-9

The stages involved in obtaining a fully matched frontal boundary shape.

a) Grid G1, (1) boundary
(2) height variation. 197

b) Grid G2, (1) boundary
(2) height variation. 198

c) Grid G3, (1) boundary
(2) height variation. 199

d) Grid G4, (1) boundary
(2) height variation. 200

e) Grid G5, (1) boundary
(2) height variation. 201

Figure 5-10

Internal and boundary heights and the boundary profile for matched grids corresponding to various ℓ_I/ℓ_N values.

a) Grid G6, ℓ_I/ℓ_N = 14.1 (1) boundary shape
(2) height variation. . . 205

Page

b) Grid G11, $\ell_I/\ell_N = 7.0$ (1) boundary shape
(2) height variation. . . 206

c) Grid G8, $\ell_I/\ell_N = 3.0$ (1) boundary shape
(2) height variation. . . 207

d) Grid G12, $\ell_I/\ell_N = 1.5$ (1) boundary shape
(2) height variation. . . 208

(e) Grid G10, $\ell_I/\ell_N = 0.88$ (1) boundary shape
(2) height variation. . . 209

Figure 5-11

Results for the transcritical region of the intermediate field, for $\ell_I/\ell_N = 41.2$ (Grid G5).

a) Height contours. 210

b) Velocity vectors, every 10th point plotted . . . 211

c) Velocity vectors, every 2nd point plotted. . . . 212

Figure 5-12

Results for the transcritical region of the intermediate field, for $\ell_I/\ell_N = 14.1$ (Grid G6).

a) Height contours 213

b) Velocity vectors, every 10th point 214

Figure 5-13

Results for the transcritical region of the intermediate field, for $\ell_I/\ell_N = 3.0$ (Grid G8).

a) Height contours 215

b) Velocity vectors, every 10th point 216

Page

Figure 5-14

The stagnation length as a function of the relative intermediate to near-field length scales. 219

Figure 5-15

Variation of transcritical region boundary shape with ℓ_I/ℓ_N. 222

Figure 6-1

A typical grid used for the supercritical region of the intermediate field (every other point in the 'i' direction shown). 229

Figure 6-2

Boundary variation with downstream distance for the one-dimensional model of Jirka et al., 1980, and the numerical simulation for 'uniform' initial conditions 230

Figure 6-3

Results for the supercritical region of the intermediate field, for $\ell_I/\ell_N = 41.2$.

a) $\lambda_i V' = 0.0$ (1) velocity vectors

(2) height contours. 235

b) $\lambda_i V' = 0.01$ (1) velocity vectors

(2) height contours. 236

c) $\lambda_i V' = 0.05$ (1) velocity vectors

(2) height contours. 237

d) $\lambda_i V' = 0.10$ (1) velocity vectors

(2) height contours. 238

Page

Figure 6-4

Boundary variation with downstream distance for one-dimensional model of Jirka et al., 1980, together with numerical simulation for the supercritical region of the intermediate field corresponding to $\ell_I/\ell_N = 41.2$ 240

Figure 6-5

Results for the supercritical region of the intermediate field for $\ell_I/\ell_N = 41.2$ - downstream extension.

a) $\lambda_i V' = 0.0$ (1) velocity vectors

(2) height contours. 242

Figure 6-6

Variation of matched boundary curves with friction coefficient for the case of $\ell_I/\ell_N = 41.2$. 243

Figure 6-7

Results for the supercritical region of the intermediate field for $\ell_I/\ell_N = 14.1$.

a) $\lambda_i V' = 0.0$ (1) velocity vectors

(2) height contours. 244

b) $\lambda_i V' = 0.1$ (1) velocity vectors

(2) height contours. 245

Figure 6-8

Results for the supercritical region of the intermediate field for $\ell_I/\ell_N = 7.0$.

a) $\lambda_i V' = 0.0$ (1) velocity vectors

(2) height contours. 246

Page

Figure 6-9

Results for the supercritical region of the intermediate field for $\ell_I/\ell_N = 3.0$.

a) $\lambda_i V' = 0.0$ (1) velocity vectors

(2) height contours. 247

b) $\lambda_i V' = 0.1$ (1) velocity vectors

(2) height contours. 248

Figure 7-1

Results for the full intermediate field for $\ell_I/\ell_N = 41.2$.

a) $\lambda_i V' = 0.0$ (1) velocity vectors

(2) height contours. 252

b) $\lambda_i V' = 0.1$ (1) velocity vectors

(2) height contours. 253

Figure 7-2

Results for the full intermediate field for $\ell_I/\ell_N = 14.1$.

a) $\lambda_i V' = 0.0$ (1) velocity vectors

(2) height contours. 254

b) $\lambda_i V' = 0.1$ (1) velocity vectors

(2) height contours. 255

Figure 7-3

Results for the full intermediate field for $\ell_I/\ell_N = 3.0$.

a) $\lambda_i V' = 0.0$ (1) velocity vectors

(2) height contours. 256

b) $\lambda_i V' = 0.1$ (1) velocity vectors

(2) height contours. 257

Page

Figure 7-4

Variation of matched boundary curves, for the full intermediate field, with friction coefficient for the case of $\ell_I/\ell_N = 41.2$. 259

Figure 7-5

Variation of matched boundary curves, for the full intermediate field, with friction coefficient for $\ell_I/\ell_N = 14.1$. . 260

Figure 7-6

Variation of matched boundary curves, for the full intermediate field, with friction coefficient, for $\ell_I/\ell_N = 3.0$. . 261

Figure 7-7

Comparison of intermediate field boundary shapes for various ℓ_I/ℓ_N values, (for zero interfacial friction, $\lambda_i V' = 0.0$). 262

Figure 7-8

Variation of total near-field dilution, $\hat{Q}$, with relative intermediate to near-field strengths, ℓ_I/ℓ_N. 264

Figure 7-9

Comparison of experimental and field data with the numerical estimation of the normalized stagnation length, $|x_s|/\ell_I$. . . 266

Figure 7-10

Comparison of experimental and field data with the numerical estimation of the normalized current width at the source, $\frac{b(x = 0)}{\ell_I}$, as a function of the ratio of intermediate to near-field strengths, ℓ_I/ℓ_N. 267

Page

Figure 7-11

Schematic diagram of Riverine plume. 277

Figure 7-12

Comparison of predicted with actual boundary shapes for the Connecticut River plume, April 21, 1972, (field data from Garvine, 1974). 281

Figure 7-13

Comparison of predicted with actual boundary shapes for the Connecticut River plume, May 1, 1972, (field data from Garvine, 1974) 282

Figure 7-14

Sensitivity runs for Riverine discharges 284

Figure 7-15

OTEC-100 sensitivity runs: plan view 290

Figure 7-16

OTEC-100 sensitivity runs: side view 291

Figure I-1

A closed-cycle OTEC heat engine (after Cohen, 1979/80) . . . 313

Figure I-2

The annual average monthly temperature differences between the ocean surface and 1,000 m depth, shown in degrees Celsius, (after Cohen, 1979/80).

a) for the Western hemisphere

b) for the Eastern hemisphere 315

LIST OF SYMBOLS

a = speed of sound in a gas

$b(x)$ = density current half width

c = speed of a small amplitude long wave or local internal wave speed

C_D = drag coefficient

C_p = specific heat capacity of a gas at constant pressure

C_v = specific heat capacity of a gas at constant volume

D = determinant of the Jacobian of the transformation from Cartesian to Contravariant coordinates

E = specific energy

F = $\frac{q}{c}$ Froude number

F_{art} = artificial Froude number value used to aid convergence in transcritical program

F_b = $\frac{s+1}{s+2} \rho_o \sigma h^{s+2}$ buoyant spreading force

F_D = $C_D \rho_a \frac{(u_a \sin \theta)^2}{2} h_B$ ambient drag force

F_ℓ = local Froude number

F_s = discharge Froude number

g = gravitational acceleration

g' = $g \frac{\Delta \rho}{\rho_o}$ effective gravity or buoyancy

g'_o = $g \frac{\Delta \rho_o}{\rho_o}$ effective gravity at discharge

$h(x,y)$ = density current half height

h_b = density current "inner" boundary half height

h_B = density current "external" boundary half height

$\tilde{h}_B(\theta)$ = $(\sin\theta)^{\frac{1}{s+1}}$ density current "external" half height normalized by the intermediate field height scale, h_s

h_e = enthalpy of a gas

h_o = discharge height

h_s = $\left\{\frac{s+2}{s+1}\ \frac{C_D}{2\sigma}\ u_a{}^2\right\}^{\frac{1}{s+1}}$ height scale or density current half height at the stagnation point

$h_1, h_2(x,y)$ = location of density current interfaces

J = Jacobian of the transformation from Cartesian to Contravariant co-ordinates

k = coefficient in the isentropic gas law

ℓ_F = far field length scale

ℓ_I = $\frac{Q}{2\pi u_a h_s}$ intermediate field length scale

ℓ_{IF} = frictional length scale

ℓ_N = near field length scale

ℓ_o = discharge length scale

ℓ_R = Coroilis length scale

ℓ_I/ℓ_N = relative intermediate to near field strengths

M = q/c Mach number

M_m = momentum

M_o = discharge momentum flux

N = Brunt Vaisala frequency

p = pressure

Q = $S\,Q_o$ intermediate field mass flux after mixing

Q_o = discharge mass flux

$\bar{q}=(u,v)$ = two dimensional (x,y) velocity field

q_c = critical speed

q_{max} = maximum speed

r = radial coordinate

r_o = discharge radius

R = gas constant

R_e = Reynolds number

R_i = Richardson number

s = stratification parameter

= 0 for homogeneous or stepwise ambient stratification

= 1 for linear ambient stratification

S = mixing factor

T = temperature

$u_{j,j=1,2,3}$ = three-dimensional velocity field in a three-dimensional coordinate system, $x_{j,j=1,2,3}$

u_a = ambient velocity

u_c = centerline velocity in a density current

U_o = discharge velocity

$\left.\begin{matrix} U \\ V \end{matrix}\right\}$ = Contravariant velocities

V' = $\dfrac{Q}{2\pi\, u_a h_s^2}$ volume flux parameter

w_e = entrainment velocity

$x_{j,j=1,2,3}$ = three-dimensional Cartesian coordinate system with x_3 pointing upwards, in the opposite direction to gravity

x_s = stagnation length, or distance from the source to the stagnation point

x, y, z — three-dimensional Cartesian coordinate system with z in the opposite direction to gravity

X, Y — two-dimensional Contravariant coordinate system

α = entrainment coefficient for a nonbuoyant case

α^* = entrainment coefficient for a buoyant case

ϵ = $-\frac{1}{\rho_a}\frac{d\rho}{dz}$ density stratification

θ = boundary angle

ρ = density

ρ_o = intrusion density

$\rho_a(z)$ = ambient density stratification

ϕ = velocity potential

ψ = stream function

σ stratification parameter

$= g'$ if $s = 0$

$= \frac{1}{2}N^2$ if $s = 1$

τ^i = interfacial shear

λ_i = interfacial friction coefficient

γ = ratio of gas specific heats

λ = wavelength

Σ_o = discharge buoyancy conservation parameter

μ = switching function in transcritical numerical scheme

ω = over-relaxation parameter in transcritical numerical scheme

ω_s = damping parameter in transcritical numerical scheme

Superscripts

$\bar{}$ = vector

$\hat{}$ = near field nondimensionalization

$\tilde{}$ = intermediate field nondimensionalization

ABSTRACT

This study is concerned with the development of predictive techniques for the predominantly horizontal, layered fluid motions that result when a continuous buoyant source is discharged into an ambient fluid at a bounding surface, interface or equilibrium level. In general, the ambient fluid will have a cross-current which then leads to horizontal front formations which delineate the density current.

A detailed knowledge of the properties of the resulting density current is of great importance in a variety of environmental problems. Typical applications are fresh river water discharges into coastal water, cooling water discharges into rivers or oceans, and, in particular, the discharged effluents from ocean thermal energy conversion (OTEC) plants.

Although the numerical techniques developed herein are applicable to general discharge configurations, the model development is focused on the particular case of a radial source of buoyancy and momentum discharged into a uniform ambient crossflow, this case being of particular concern for the OTEC geometry. The resulting density current is analyzed by application of the depth-integrated hydrodynamic equations. The flow domain is divided into two regions for individual study -- an entraining supercritical near field and a nonentraining intermediate field region. The latter is further subdivided into a transcritical region and a supercritical region, the latter allowing for frictional effects. The two supercritical regions are modeled using a MacCormack method (MacCormack, 1971), while the transcritical region, which includes internal hydraulic jumps, is modeled using an extension of the numerical techniques developed for inviscid transonic gas flows by Caughey and Jameson (1979).

The density current dynamics are shown to vary with the relative intermediate- to near-field strengths, as characterized by the ratio of their respective length scales. The complete range of this interaction, from small near-field effects to large near-field effects, is investigated. Results are presented as the depth integrated velocity and current thickness distributions for different field strength values.

The model predictions are compared to two sets of laboratory data and to limited field information, involving a river discharge and a submerged outfall into the ocean. Good agreement is obtained in all cases.

Finally, the model results are applied to the prediction of a river plume into a coastal ocean current and to the continuous discharge from an OTEC plant operating in the stratified ocean. In both cases, the results indicate the significant horizontal extent (order of several kilometers) of the resulting current, together with their limited vertical extent (order of several meters). Their strong sensitivity to ambient current magnitude and stratification strength is demonstrated.

CHAPTER 1

INTRODUCTION

Density currents (or gravity currents) are formed when a mass of one fluid is introduced into another fluid of different density. The intruding fluid may spread horizontally along an ambient boundary, an internal density interface, or at the equilibrium level if the ambient fluid is continuously stratified. This vertical collapse (horizontal spreading) tends to minimize the gravitational potential energy of the system. The nature of the flow in the horizontal plane can be one- or two-dimensional, depending on the physical boundary conditions of the ambient domain. For example, if the intruding fluid is discharged from a finite source into an ambient fluid which is unrestricted horizontally, such as a lake, ocean, or a wide experimental basin, the density current will be horizontally two-dimensional. However, if the discharge is into a horizontally bounded ambient fluid, such as a narrow river or laboratory flume, the density current will be restricted to horizontally one-dimensional flow.

Figure 1-1 shows a density current produced experimentally by introducing dyed heated water through a "point" source into ambient water which is moving with a constant velocity. The top view shows the two-dimensional spreading of the density current, and in particular, a region of upstream penetration, whereas the lateral view shows

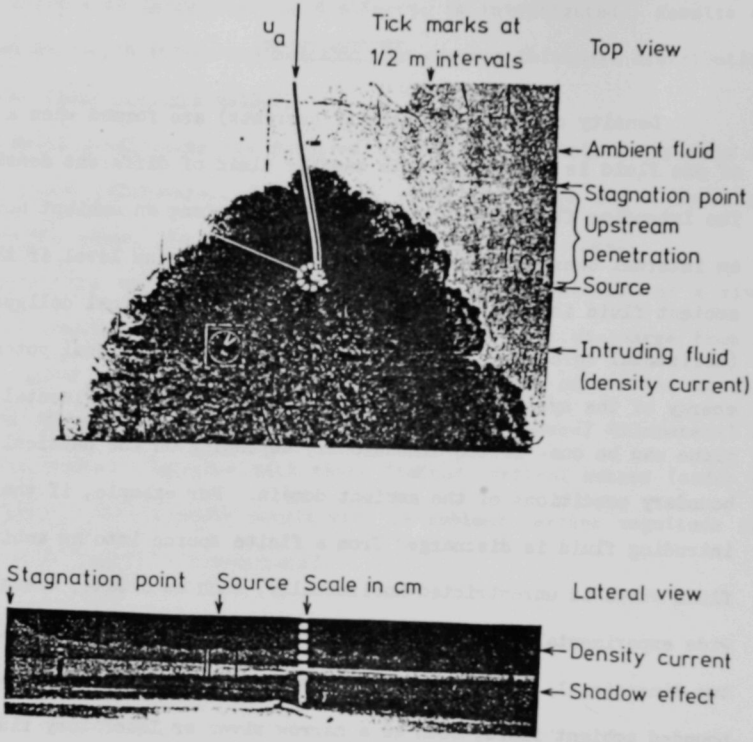

Figure 1-1 Top and lateral views of a hot water density current produced in the laboratory (after Jirka *et al.*, 1980)

relatively small height variations. Figure 1-2, obtained from a similar experiment, shows the approximate pathlines for floats released near the source.

Both Figures 1-1 and 1-2 serve to emphasize the two-dimensional nature of the flow produced by discharging a fluid into a horizontally infinite environment. This can be understood as being due to the intrusion's freedom to spread out in both horizontal directions, subject to the boundary conditions imposed on it by the ambient flow. This two-dimensional density current exhibits a transcritical flow field, comprising subcritical flow near the stagnation point (at which the velocity must equal zero, Figure 1-1), supercritical flow downstream (where the height tends to zero), and critical or supercritical flow around the source. In this case, criticality statements are based on an internal densimetric Froude number definition. No previous investigations of such two-dimensional, transcritical, stratified flow problems have been made.

In principle, one-dimensional flows also exhibit transcriticality, but the transitions would only occur at channel transitions, making them easy to predict, in contrast to the two-dimensional case. The dynamics of one-dimensional flow, comprising density currents and wedges, has been investigated by many authors, a recent study being that of Sargent (1983), while Simpson (1982) gives a detailed review of previous work.

Various environmental occurrences of two-dimensional density currents are discussed in Section 1.2. The major impetus for the

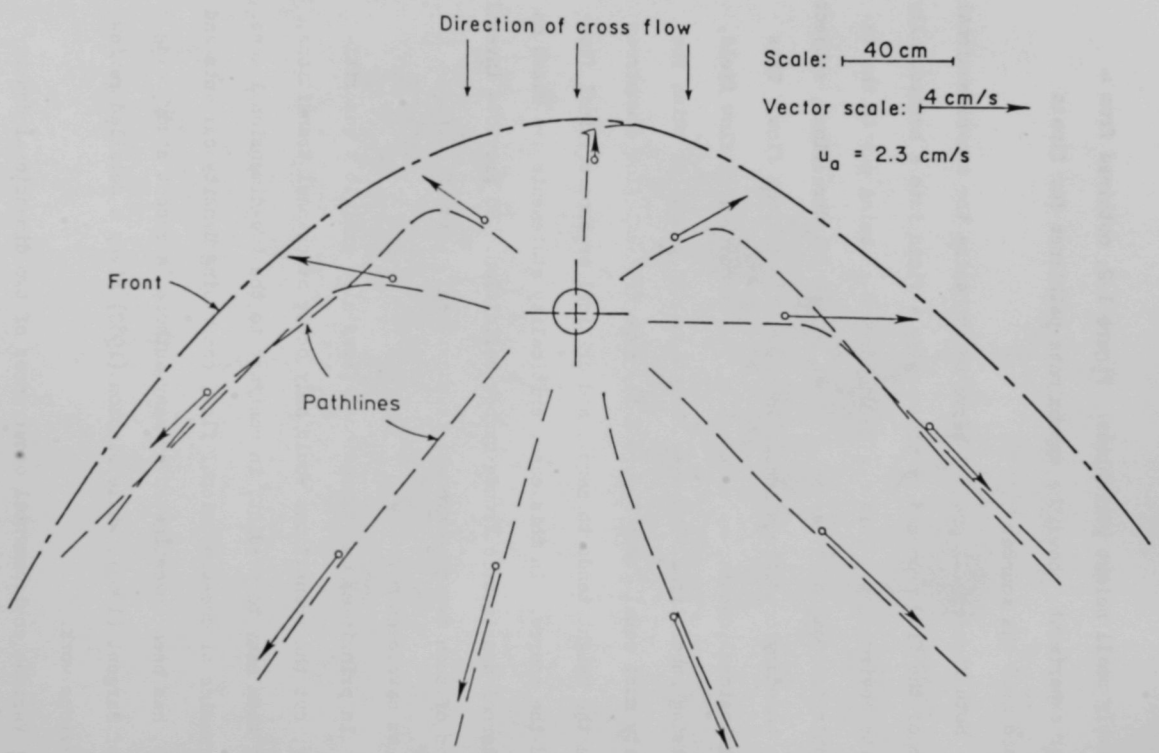

Figure 1-2 Schematic representation of a density current similar to that in Figure 1-1, showing streamlines and surface velocity vectors (after Jirka et al., 1980) .

present study, however, is given by the need for a complete understanding of the large scale fluid motions produced by Ocean Thermal Energy Conversion (OTEC) plants in the surrounding stratified ocean. This is discussed in Section 1.3.

1.1 Environmental Occurrences of Two-Dimensional Density Currents

Examples of two-dimensional density currents that are at, or near, steady-state conditions are discussed in the following:

Hydrospheric Occurrences:

- Cooling water carrying waste heat from fossil fueled and nuclear power plants, discharged into lakes, rivers and oceans. The analysis of the buoyant spreading motion of these discharges is crucial for determining the recirculation potential (i.e., possible return into the plant intake), and for a reliable thermal impact evaluation, (Williams, 1973).

- Effluents from sewage treatment plants. These are discharged into lakes and oceans through a single port discharge or through multiport diffuser located on the bottom. The effluent forms a buoyant plume which rises until the water surface, or its equilibrium level, is reached. They will then behave as density currents, spreading out horizontally, as previously described.

- River or estuarine inflow (fresh or brackish water), into the ocean (salt). The lighter inflow forms a naturally occurring surface density current, with convergence regions along its front, frequently denoted by floating debris. Figure 1-3 shows the plan view

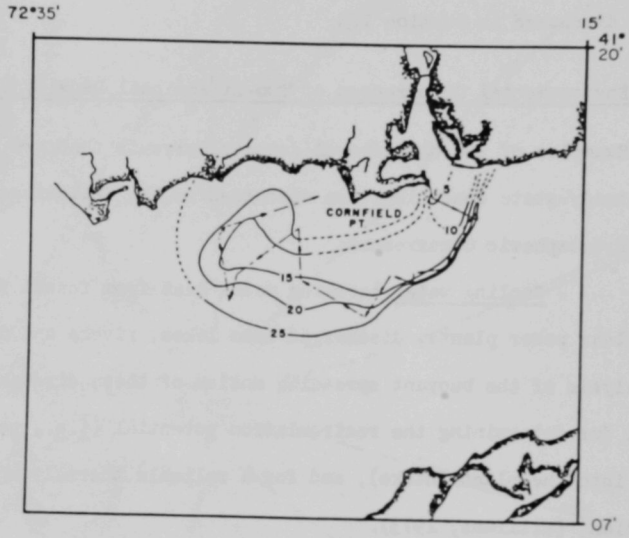

Figure 1-3 The Connecticut River plume discharging into Long Island Sound. The salinity field shown is at a depth of 0.5 m, the readings being taken after flood tide. The ship track is marked by arrows (after Garvine, 1974)

of the inflow of the Connecticut River into Long Island Sound, with Figure 1-4 showing a corresponding vertical profile. Both figures show a clearly defined frontal region along the leading edge of the plume. An approximate depth to width ratio is 10^{-4}. Similar conditions are suggested by the photograph of a two-river discharge plume in Fischer et al. (1979, Figure 9-29).

Atmospheric Occurrences:

- Spillages of liquefied gases (e.g., liquefied natural gas, propane, butane and chlorine). These chemicals are being stored and transported in ever increasing quantities. If released into air, by the accidental rupture of storage tanks, for example, they form negatively buoyant density currents. These chemicals, when mixed with air, may be explosive, corrosive or poisonous. A detailed knowledge of the likely spreading under the given wind conditions is very important for determination of appropriate storage or plant siting and evacuation procedures. (Fay, 1980).

- Buoyant plumes from smoke stacks and cooling towers, or, simply, the urban heat island effect, if trapped below an atmospheric inversion. The inversion stops the buoyant ascent of these flows and causes them to spread horizontally as density currents.

In summary, in all of these situations, thin and horizontally spread out layers are found. These layers, in turn, can become carriers of significant amounts of physical, chemical or biological wastes, or "pollutants" in general.

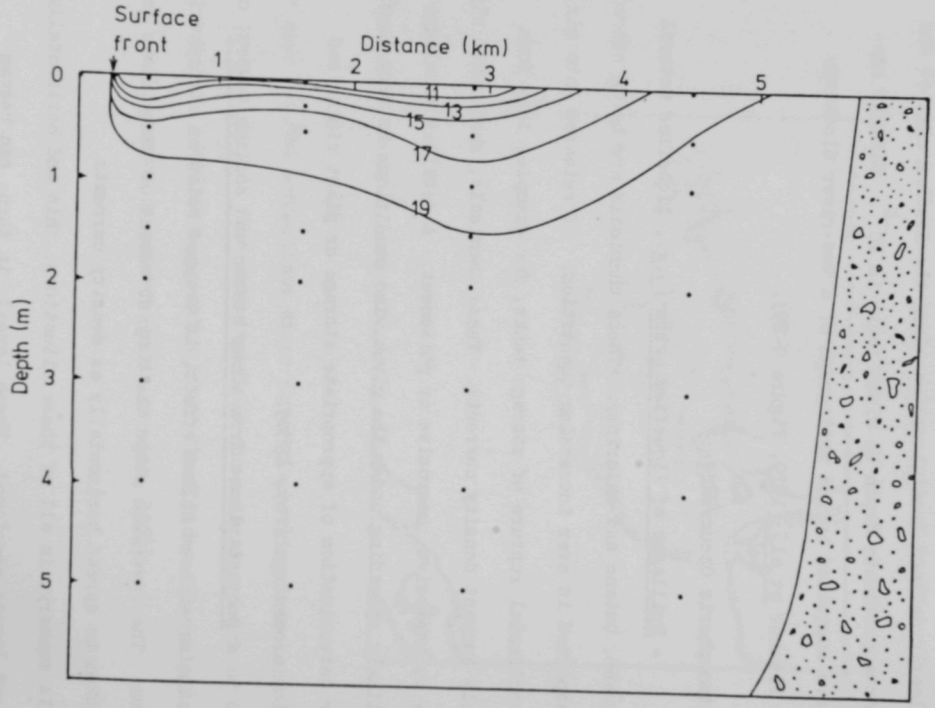

Figure 1-4 Vertical density section across the Connecticut River plume, during ebb tide (after Garvine, 1977). Sampling points are shown by solid dots. σ_T units are used.

1.2 Overview of Fluid Mechanical Aspects of Ocean Thermal Energy Conversion (O.T.E.C.)

The tropical ocean exhibits a temperature difference, ΔT, of the order of 20°C between its surface and depths due to the upper layers acting as large solar energy collectors, while the lower depths are fed by cold water currents from the poles as part of the global oceanic circulation. Ocean thermal energy conversion (OTEC) plants utilize this temperature difference, taking in surface water and pumping up water from a depth of between 500 and 1000 m, to drive conventional heat engines. In a closed cycle engine these alternately vaporize and liquefy a working fluid such as ammonia in order to drive turbines which generate electricity. Thus OTEC utilizes one of the renewable geophysical energy resources of the sea, i.e., the thermal gradient, to generate useful energy.

It has been proposed by Richards (1979), that by the year 1995, a total of several gigawatts of electricity could be generated for use in the U.S. islands alone by OTEC, in particular as small OTEC plants are ideal for the island market. He also estimated that worldwide, more than 100 GW might be installed by the year 2010.

The warm and cold ocean waters, after use, have to be discharged into the ocean, with care being taken that no recirculation occurs into the plant intake, which would deplete the thermal resource. Various methods of discharge have been investigated, including:

- Discharge of the effluents separately. However, the warm water discharge might then be liable to recirculate with the warm

water intake.

- Mixed discharge of warm and cold water effluents. This will reduce the buoyancy of the warm water discharge so that the most likely position for the resulting flow will be near the oceanic thermocline (for details see Jirka et al., 1981).

In either of these schemes, the angle at which the water is discharged has a further effect on both the recirculation potential and on the location of the horizontal spreading layer.

For economic reasons, OTEC plants are likely to be grouped together in "parks". This requires a detailed knowledge of the shape of the density current formed from the individual effluents, in order to position the plants so as not to deplete the thermal resource. A provisional Environmental Impact Assessment for these OTEC plants is given in Friedman and Reitzel (1979). This lists some key environmental issues as organism entrainment and impingement, chlorine (used in biofouling control) releases and ammonia leakage to the sea. For these processes to be evaluated adequately, an understanding of the details of the two-dimensional density current formed by OTEC effluents is required. A detailed summary of the historical and future uses of OTEC is given in Appendix I.

1.3 Problem Statement and Summary

The objective of this study is the development of a comprehensive technique for the prediction of the horizontal, two-dimensional transcritical density current flow field produced by the steady

discharge of a finite fluid source into an ambient cross-flow of infinite horizontal extent. The ambient stratification conditions may be:

- one homogeneous layer with a surface source discharging a positively buoyant fluid;
- two homogeneous layers separated by a density discontinuity at which a source discharges a fluid of intermediate density;
- a linearly stratified region in which a source discharges a fluid at its equilibrium density level.

This method is only applicable after the fluid has reached a level at which it will expand horizontally; any prior vertical motion after discharge from the source must be accounted for by other means.

Chapter 2 summarizes the basic hydrodynamic concepts, including frontal boundary conditions, interfacial stability, and jet-like entrainment concepts. Present two-dimensional theories, none of which takes account of the transcritical nature of the flow, are discussed. The analogy existing between two-dimensional density currents, shallow-water free surface flow, and two-dimensional compressible gas flow, is mentioned, as this suggests various applicable analytical and numerical techniques.

The derivation of an appropriate set of governing equations is presented in Chapter 3, together with scaling arguments suggesting the division of the flow field into near and intermediate field regions. Simplified equations for each flow region are then developed.

The solution of the near field flow by the application of the MacCormack method - an explicit, stepping, numerical finite difference technique - is described in Chapter 4, together with results obtained for both a stagnant and moving ambient region.

The transcritical region of the intermediate field is predicted using a finite difference technique developed by Caughey and Jameson (1979), which takes automatic account of its transcritical nature. The scheme and results are described in Chapter 5.

The supercritical region of the intermediate field is solved by a second application of the MacCormack method. This application, and the results obtained, are discussed in Chapter 6.

Chapter 7 collects the results of the separate regions for a solution of the entire density current. This is compared with data obtained using the Stratified Flow Facility at Cornell, (Jirka et al., 1980; Huq, 1983).

CHAPTER 2

REVIEW OF PREVIOUS WORK ON TWO- AND ONE-DIMENSIONAL DENSITY CURRENT DYNAMICS, INCLUDING ANALOGOUS SHALLOW WATER AND GAS FLOW THEORIES

Section 2.1 addresses the problem of whether density currents or wedges are to be expected for the two-dimensional intrusion under consideration. Elements of one-dimensional theory applicable to two-dimensional cases, such as force balances and drag coefficients are also discussed. It concludes with a discussion of simple generalizations of one-dimensional dynamics to "pseudo" two-dimensional solutions.

More general stratified flow theory is discussed in Section 2.2, including internal hydraulic jump formation and energy losses. These concepts are considered from the viewpoint of the analogous free surface shallow water flow and compressible gas flow cases in Section 2.3. The former serves to illustrate the hydraulic jump concepts, whereas the latter is useful for suggesting possible numerical schemes applicable to the problem solution.

Section 2.4 discusses the stability and entrainment relations occurring in density current theory.

Section 2.5 reviews the previous two-dimensional density current solutions.

Sections 2.6 and 2.7 consider the various numerical schemes

available for supercritical and transcritical flows.

2.1 Dynamics of One-Dimensional Density Intrusions and Applications to Two-Dimensional Problems.

2.1.1 The bulk shape: density currents versus density wedges

Many studies (mostly one-dimensional) of density intrusions exist in the literature, with recent comprehensive reviews given by Simpson (1982), and Chen (1980). Two major types of intrusions have been investigated: density wedges and density currents. Both of these exist for the various stratified flow conditions discussed in Section 1.3. Little information is available to enable prediction of the intrusion type likely to occur under given flow conditions, although a recent comparative study by Sargent (1983), attempts to address the problem.

Density currents exhibit a marked "head" region as shown in Figure 2-1. A localized drag force exerted by the ambient fluid at this head is the main mechanism controlling their advance due to internal buoyant forces.

Density wedges are characterized by a long, gradually sloping profile (Figure 2-1). Their buoyant spreading is mainly counteracted by interfacial shear effects.

Various experimental investigations of one-dimensional intrusions indicate that boundary conditions exert a strong influence over the choice between currents and wedges. Keulegan (1966), Riddell (1970) and Grubert (1980) obtained density wedges when steady

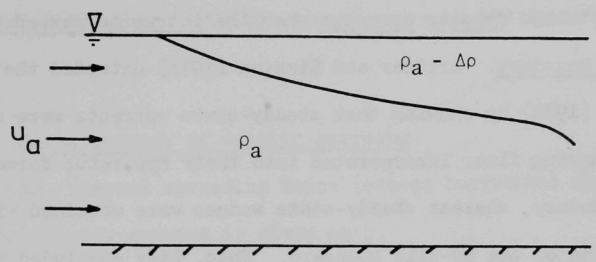

(a) Density wedge

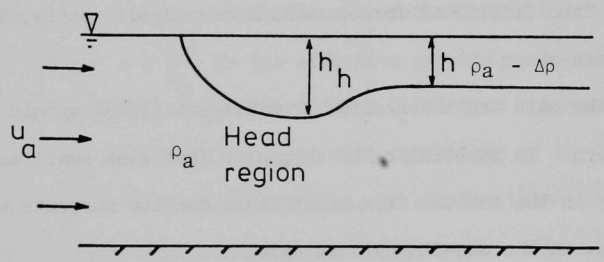

(b) Density current

Figure 2-1 Typical one-dimensional surface density intrusions

intrusions were opposed by ambient currents passing over no-slip boundaries. Ippen and Harleman (1952), Keulegan (1957, 1958), Middleton (1966), Wilkinson and Wood (1972) and Simpson (1969, 1972) obtained density currents when the intrusion passed over a no-slip boundary. Britter and Simpson (1978) extended the work of Simpson (1972) by showing that steady-state currents were obtained when a moving floor incorporated into their apparatus formed a slip boundary, whereas steady-state wedges were obtained with the resumption of the no-slip boundary. Thus, they concluded that the reduced ambient flow in the close vicinity of a no-slip boundary provided insufficient drag to, alone, counteract the buoyant driving force. Thus frictional forces contributed significantly, leading to a wedge-shape.

The data and conclusions from Sargent (1983) uphold this assumption. In particular, he suggested that even small localized deficits in the ambient flow might cause density currents to convert to wedges in the one-dimensional case.

It should be emphasized, however that the preceding experiments have involved only one-dimensional flows. Two-dimensional investigations were carried out by Jirka et al. (1980), and Huq (1983). These involved surface (and some interface) intrusions, so that the possibility of no-slip boundary conditions was minimized. (Surface-skimmers were used to reduce possible surface pollution.) In all these experiments, density currents, rather than wedges, were most often seen to occur. Sargent (1983)

suggested that density current formation would be encouraged by the extra degree of freedom available in the two-dimensional case.

Hence, in this study of two-dimensional density intrusions, the frontal dynamics will be assumed to be of the density current type.

2.1.2 Force balance of density currents

The buoyant spreading force (excess horizontal force), F_b, for the density current is given as

$$F_b = \frac{\rho_o}{2} g' h^2, \tag{2.1}$$

computed by evaluating the hydrostatic forces within and upstream of the density current, over the density current half height, h (see Figure 2-1). $g' = g \frac{\Delta\rho}{\rho_o}$ is the effective gravity or buoyancy, ρ_o is the intrusion density and $\Delta\rho$ the density difference between the intrusion and ambient. It should be noted that the height of the density current, h_h, as shown in Figure 2-1, is greater than that of the density current behind it. Sargent (1983) quotes values of h_h of two or three times h. The added head height is attributable to the more complicated flow dynamics within this region (Britter and Simpson, 1978), which includes vertical accelerations and also a moderate amount of entrainment, occuring in the lee of the head.

For density currents, as previously discussed, the buoyant force is opposed by an ambient drag force,

$$F_D = C_D \rho_o \frac{u_a^2}{2} h \tag{2.2}$$

where u_a is the ambient velocity and C_D a drag coefficient. This drag force (pressure drag) is due to local vertical accelerations which develop in the region around the head, causing perturbations of the ambient hydrostatic pressure field in this region. Equating the buoyant and drag forces, Equations (2.1) and (2.2), yields

$$\frac{u_a}{\sqrt{g'h}} = \frac{1}{\sqrt{C_D}} \tag{2.3}$$

as an expression relating the drag coefficient to the front velocity. A more general analysis by Benjamin (1968) with limited ambient fluid depth, H, showed that this drag coefficient should vary with the relative depths of the intruding fluid, as a greater intrusion would result in greater perturbations of the ambient, and hence greater drag effects. He investigated flow past a one-dimensional surface density current, using the classical flow force (momentum flux plus pressure force) conservation across a control volume around the current head. This yielded,

$$\frac{u_a}{\sqrt{g'h}} = \left[\frac{(1 - \frac{h}{H})\ (2 - \frac{h}{H})}{(1 + \frac{h}{H})}\right]^{1/2} \tag{2.4}$$

Comparison with Equation (2.3) gives a general drag coefficient expression.

$$C_D = \frac{(1 + \frac{h}{H})}{(1 - \frac{h}{H})\ (2 - \frac{h}{H})} \tag{2.5}$$

This relation between the drag coefficient and the relative density current to ambient depth is shown in Figure 2-2. It predicts the drag coefficient as varying from 1/2 to 2 as the relative depth increases from zero (infinite ambient depth) to 0.5.

Britter and Simpson (1978) extended Benjamin's (1968) study by introducing an extra "internal flux" parameter, or entrainment rate,

$$Q_e = \frac{g' u h}{u_a^3} \tag{2.6}$$

where u is the velocity of the density current behind the head. Q_e takes account of any entrainment of ambient fluid into the density current, which may occur in the region directly behind the head. $Q_e = 0$ corresponds to Benjamin's (1968) non-entraining theory. Increasing the entrainment rate, had the effect of increasing the front velocity, i.e., decreasing C_D (Equation 2.3), as they showed both experimentally and theoretically, Figure 2-3. Britter and Simpson's (1978) results regarding the role of entrainment, were confirmed by Sargent (1983).

Jirka et al. (1980) also considered both homogeneous and linear ambient stratification cases for an infinite ambient depth, H. They obtained, using the previous force balance together with use of a Beruoulli equation, a general value of

$$C_D = \frac{s+1}{s+2} \tag{2.7}$$

where s = 0 for a homogeneous ambient and s = 1 for a linearly

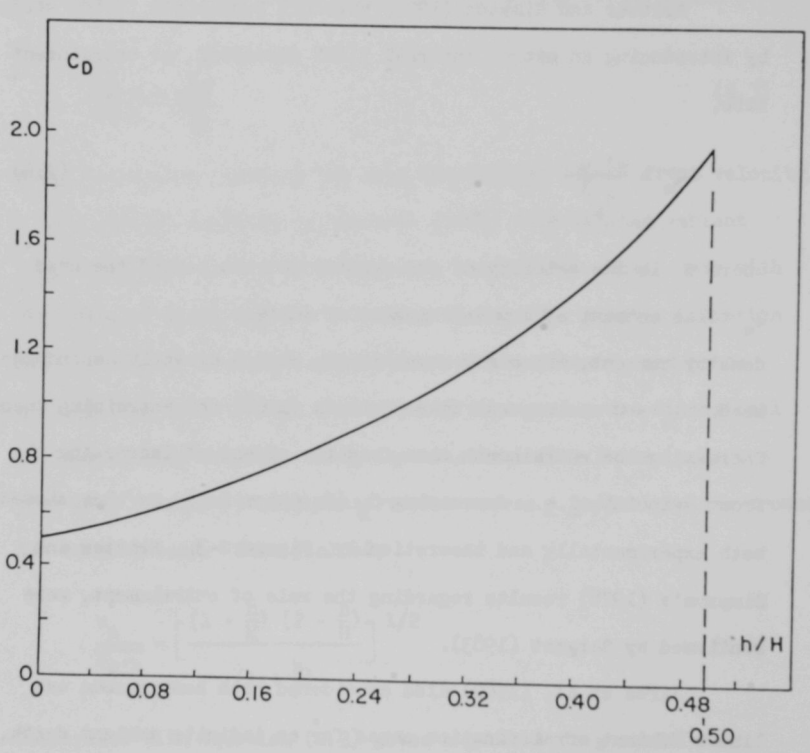

Figure 2-2 Variation of drag coefficient, C_D, with density current to ambient depth ratio, h/H

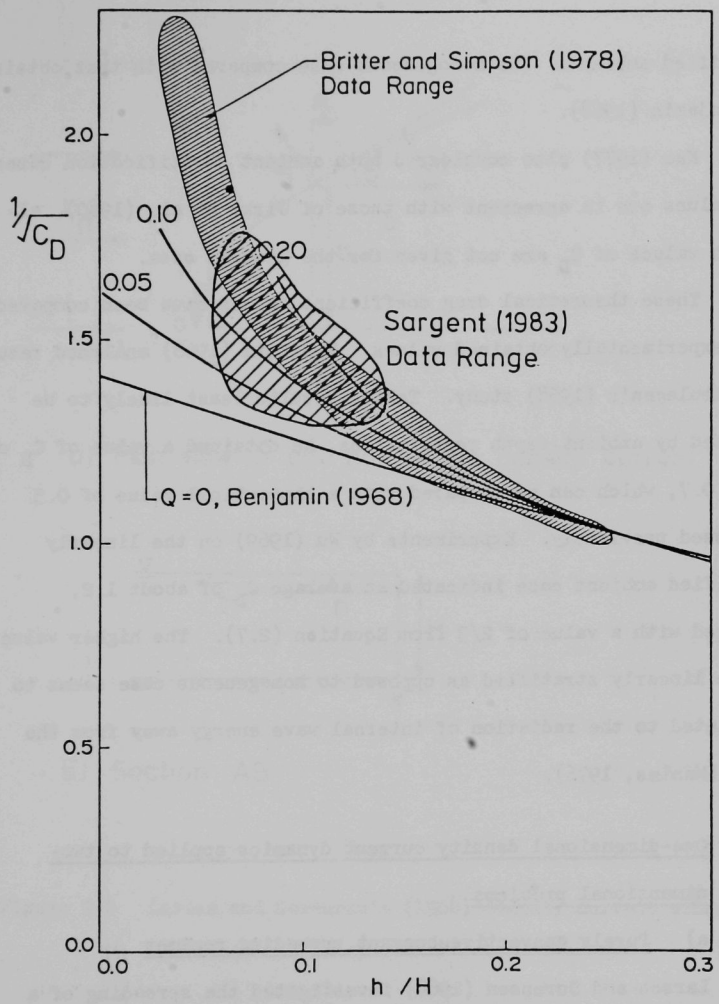

Figure 2-3 A comparison of theoretical and experimental relations between the drag coefficient, C_D, and the relative current to ambient water depth, h/H, (after Sargent, 1983)

stratified ambient. The homogeneous case compares with that obtained by Benjamin (1968).

Kao (1977) also considered both ambient stratification cases. His values are in agreement with those of Jirka et al. (1980), although values of C_D are not given for the general case.

These theoretical drag coefficient values have been compared with experimentally obtained values. Benjamin (1968) analyzed results from Keulegan's (1958) study. Taking results least likely to be affected by ambient depth restrictions, he obtained a value of C_D of about 0.7, which can be compared with a theoretical value of 0.5 discussed previously. Experiments by Wu (1969) on the linearly stratified ambient case indicated an average C_D of about 1.2, compared with a value of 2/3 from Equation (2.7). The higher value in the linearly stratified as opposed to homogeneous case seems to be related to the radiation of internal wave energy away from the front (Manins, 1976).

2.1.3 One-dimensional density current dynamics applied to two-dimensional problems

a) Purely convective-buoyant spreading regimes

Larsen and Sorensen (1968) investigated the spreading of a buoyant discharge at the surface of a homogeneous ambient crossflow. Rather than a point source, they assumed that the discharge had an initial finite width, b_o (Figure 2-4). This approach is basically one-dimensional, in that the density current was assumed to have a constant velocity in the x-direction, equal to the ambient, u_a, and

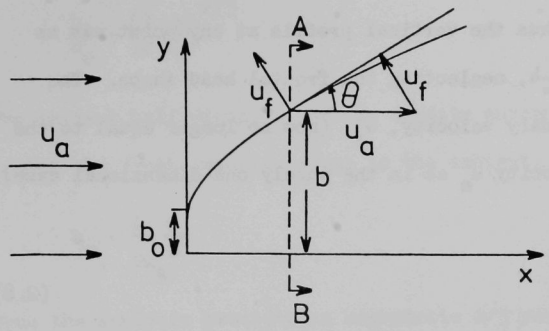

a) Plan view of one half of the density current

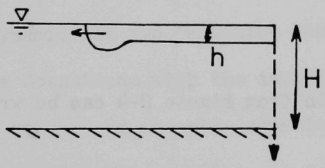

b) Section AB

Figure 2-4 Larsen and Sorensen's (1968) density current schematization

also a constant height, h, along its width (perpendicular to the ambient flow). Thus the vertical profile at any point was as shown in Figure 2-4, neglecting the frontal head shape. The spreading or boundary velocity, u_f, (now no longer equal to the local ambient velocity u_a as in the purely one-dimensional case) was given by

$$u_f = \sqrt{g'h} \tag{2.8}$$

which can be compared with Equation (2.3) with the drag coefficient set equal to one. Figure 2-4 shows that u_f can be written in terms of u_a and the boundary angle, θ, as

$$u_f = u_a \sin\theta \tag{2.9}$$

The spreading rate, $\frac{db}{dx}$, again from Figure 2-4 can be written as

$$\frac{db}{dx} = \tan\theta \ . \tag{2.10}$$

Larsen and Sorensen (1968) approximated tan θ by sin θ - without explicitly stating so - (this being true only for small angles, i.e., far downstream). With the simple continuity equation,

$$Q = 2b\ h\ u_a, \tag{2.11}$$

together with Equations (2.8) and (2.9) one can integrate Equation (2.10) to give

$$\frac{b}{b_o} = \left(\frac{3}{2}\frac{x}{b_o} + 1\right)^{2/3} \tag{2.12}$$

which they approximate (for no clear reason) by

$$\frac{b}{b_o} = \left(\frac{3}{2}\frac{x}{b_o}\right)^{2/3} + 1$$

The initial half width, b_o of the density current, is evaluated by taking the front velocity equal to the ambient, u_a, as

$$b_o = \frac{g' Q}{2u_a^3} \tag{2.13}$$

Thus the analysis predicts an asymptotic 2/3 power law relationship for the width as a function of x.

Bache (1976) suggested an alternative approach for two-dimensional density current spreading in a cross-flow. He represented the current dynamics as two "momentum blocks", shown in Figure 2-5, which move downstream with the ambient velocity. Applying conservation of volume and momentum equations, he calculated a spreading rate for the current. However, as pointed out by Roberts (1977), the blocks having subdivided once from the initial volume, have no reason to stop doing so, and should thus continue to divide. However, this analysis could be applied to shallow water flows if the initial current depth is equal to the ambient depth. This would then enable the initial division to be accounted for with continuity arguments within the restricted flow region.

Roberts (1977) applied Larsen and Sorensen's (1968) results to the spreading of a diffuser plume, extending it to include some entrainment, which, however, only alters the proportionality constant, leaving their 2/3 power law intact.

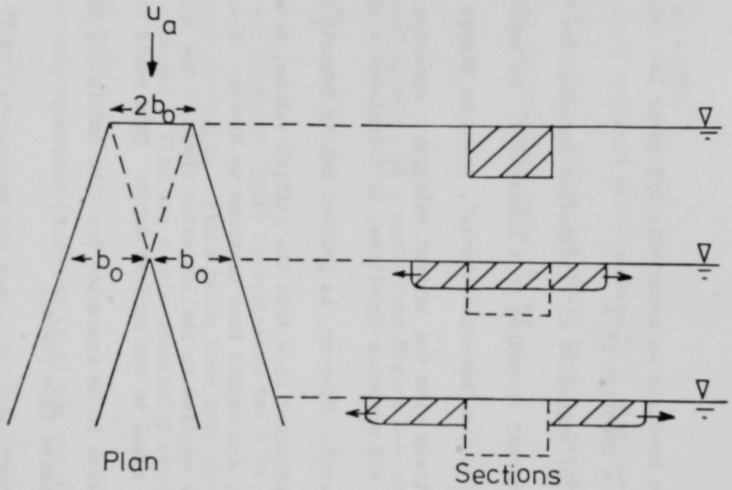

Figure 2-5 Schematic view of momentum block spreading applied to density currents (after Bache, 1976)

Jirka et al. (1980) investigated both homogeneous and linearly stratified ambient flows. They equated expressions for the drag force, F_D, given in Equation (2.2), and buoyant force, F_b, given in Equation (2.1), the latter being generalized to include linear stratification as

$$F_b = \frac{s+1}{s+2} \rho_o \sigma h^{s+2} \tag{2.14}$$

where s and σ are the stratification parameters such that:

<u>Case A: Surface source on homogeneous ambient</u>, and

<u>Case B: Interface source with step-wise ambient stratification</u>

$$\sigma = \frac{\Delta\rho}{\rho_a} g \ , \ s = 0 \tag{2.15}$$

where $\Delta\rho$ is the density difference between the density current and ambient. (In Case B the density current is assumed at an intermediate density between the two layers.)

<u>Case C: Linearly stratified ambient</u>

$$\rho = \frac{1}{2} \epsilon g = \frac{1}{2} N^2 \ , \ s = 1 \tag{2.16}$$

where $\epsilon = -\frac{1}{\rho_a} \frac{d\rho}{dz}$ and N is the Brunt-Vaisala frequency of the system.

This yielded, with the additional approximation $u_a \sin\theta \approx u_f$ the expression.

$$\frac{u_f^2}{(s+1)\sigma h^{s+1}} = \frac{2}{C_D (s+2)} \tag{2.17}$$

This could be combined with the mass continuity equation over the

half width of the density current, as

$$u_a \, h \, b = \frac{Q}{2} \, , \tag{2.18}$$

including the approximation $\sin\theta \approx \tan\theta$, as used in Larsen and Sorensen (1977) which allows the relation $u_f \approx u_a \frac{db}{dx}$, giving

$$b^{\frac{s+1}{2}} \frac{db}{dx} = \left\{ \frac{s+1}{s+2} \frac{2\sigma}{C_D} \left(\frac{Q}{2}\right)^{s+1} \frac{1}{u_a^{\,s+3}} \right\}^{1/2} \tag{2.19}$$

On integration this yields

$$\frac{b}{\ell_I} = \left\{ \left(\frac{b_o}{\ell_I} \right)^{\frac{s+3}{2}} + \frac{s+3}{2} \pi^{\frac{s+1}{2}} \left(\frac{x}{\ell_I} - \frac{x_o}{\ell_I} \right) \right\}^{\frac{2}{s+3}} \tag{2.20}$$

where b_o and x_o are the initial conditions for the spreading, and ℓ_I is a length scale defined as

$$\ell_I = \frac{Q}{2\pi \, u_a h_s} \tag{2.21}$$

where

$$h_s = \left\{ \frac{s+2}{s+1} \frac{C_D}{2\sigma} u_a^{\,2} \right\}^{\frac{1}{s+1}} \tag{2.22}$$

The scales ℓ_I and h_s will assume greater significance in Chapter 3.

For the homogeneous ambient case, the spreading relation is the same 2/3 power law as arrived at by Larsen and Sorensen (1968).

b) <u>The additional effect of interfacial friction</u>

Both Roberts (1977) and Jirka et al. (1980) considered regimes in which interfacial friction becomes more important than the inertial forces as a balance for the buoyancy. These would occur downstream of the convective - buoyant regimes previously discussed.

Roberts (1977) took an expression for the interfacial shear, τ^i, which varied linearly with the boundary velocity as

$$\tau^i = \frac{\alpha \epsilon}{2h} v \tag{2.23}$$

with α a constant, ϵ a constant "effective viscosity coefficient", and v the lateral velocity such that $v \approx u_f = u_a \frac{db}{dx}$. Thus, equating the buoyant and frictional forces, yielded

$$\frac{1}{2} g' h^2 = \frac{\alpha \epsilon b}{4h \rho_a} u_f \tag{2.24}$$

Using the previous assumptions allows Equation (2.24) to be evaluated, giving

$$b \propto x^{\frac{1}{5}} \tag{2.25}$$

i.e., a $\frac{1}{5}$ power law relation.

Jirka et al. (1980), however, adopted an interfacial shear stress relation, quadratic in the velocity term, such that

$$\tau^i = \frac{1}{\rho_a} \lambda_i v^2 \tag{2.26}$$

where λ_i is an interfacial friction coefficient ($\approx 10^{-3}$, Adams et al., 1981). This allows the momentum equation to be written as

$$\sigma h \frac{\delta}{\delta y} h^{s+1} - \lambda_i v^2 = 0$$

where s and σ are the stratification parameters defined previously. Again, using $u_f \approx u_a \frac{db}{dx}$, together with a linear variation for the

lateral velocity, $v = u_f \frac{y}{b}$ a uniform depth h, and a continuity equation as Equation (2.18), gives

$$b^{\frac{s+3}{2}} \frac{db}{dx} = \left(\frac{3\,\sigma}{u_a^2\,\lambda_i} \quad \frac{s+1}{s+2} \left(\frac{Q}{2u_a} \right)^{s+2} \right)^{1/2} \tag{2.27}$$

On integrating and nondimensionalizing as previously, one obtains

$$\frac{b}{\ell_I} = \left(\left(\frac{b_{oc}}{\ell_I} \right)^{\frac{s+5}{2}} + \frac{s+5}{2} \left(\frac{3}{2} \pi^{s+2} \right)^{1/2} \left(\frac{C_D}{\lambda_i V'} \right)^{1/2} \left(\frac{x}{\ell_I} - \frac{x_{oc}}{\ell_I} \right) \right)^{\frac{2}{s+5}} \tag{2.28}$$

where $\frac{\lambda_i V'}{C_D}$ enters as a measure of the importance of the frictional effect, ($V' = \ell_I/h_s$, Equations (2.21) and (2.22), also Chapter 3), and b_{oc} and x_{oc} denote the initial conditions for the frictional regime. Thus the power law is given as $\frac{2}{s+5}$, which gives a value of $\frac{2}{5}$ for a homogeneous ambient.

Thus, comparing Roberts (1977) and Jirka et al. (1980), shows that the former, using a linear frictional relation gets a power law of $\frac{1}{5}$, whereas the latter, with a quadratic friction law gets $\frac{2}{5}$, for the homogeneous ambient case. The former linear relation is generally true for laminar density currents, having a low Reynolds number value. This value would be more applicable under experimental conditions. However, the quadratic friction law appears more applicable to the turbulent, high Reynolds number flows encountered under field conditions. Equations (2.20) and (2.28) give the exponent relations for convective and frictional regimes as $\frac{2}{s+3}$ and $\frac{2}{s+5}$, respectively, thus showing a reduced spreading tendency in the latter. It can also be seen that in both regimes the linearly

stratified case (s=1) spreads less than the corresponding homogeneous ambient case (s=0). Both convective and frictional regimes from this study are shown for s=0 and s=1 in Figures 2-6a and b, respectively, for various values of $\frac{\lambda_i V'}{C_D}$.

2.2 The Transcritical Nature of Two-Dimensional Density Currents

In Section 1.3, mention was made of the transcritical nature of the two-dimensional density current. This will be discussed further in this section.

2.2.1 General Properties

The discussion is presented in a general form, covering all three stratification cases (A to C) given in Section 2.1. The general two-dimensional convective-buoyancy equations (derived in Section 3.1) will be used, i.e.,

$$\frac{\partial}{\partial x}(uh) + \frac{\partial}{\partial y}(vh) = 0 \tag{2.29}$$

$$\frac{\partial}{\partial x}(u^2h) + \frac{\partial}{\partial y}(uvh) = -\sigma h \frac{\partial h^{s+1}}{\partial x} \tag{2.30a}$$

$$\frac{\partial}{\partial x}(uvh) + \frac{\partial}{\partial y}(v^2h) = -\sigma h \frac{\partial h^{s+1}}{\partial y} \tag{2.30b}$$

where u and v are the velocities in the x and y direction, respectively, and s and σ are stratification parameters defined in Equations (2.15) and (2.16).

In addition, a Bernoulli or energy equation can be defined,

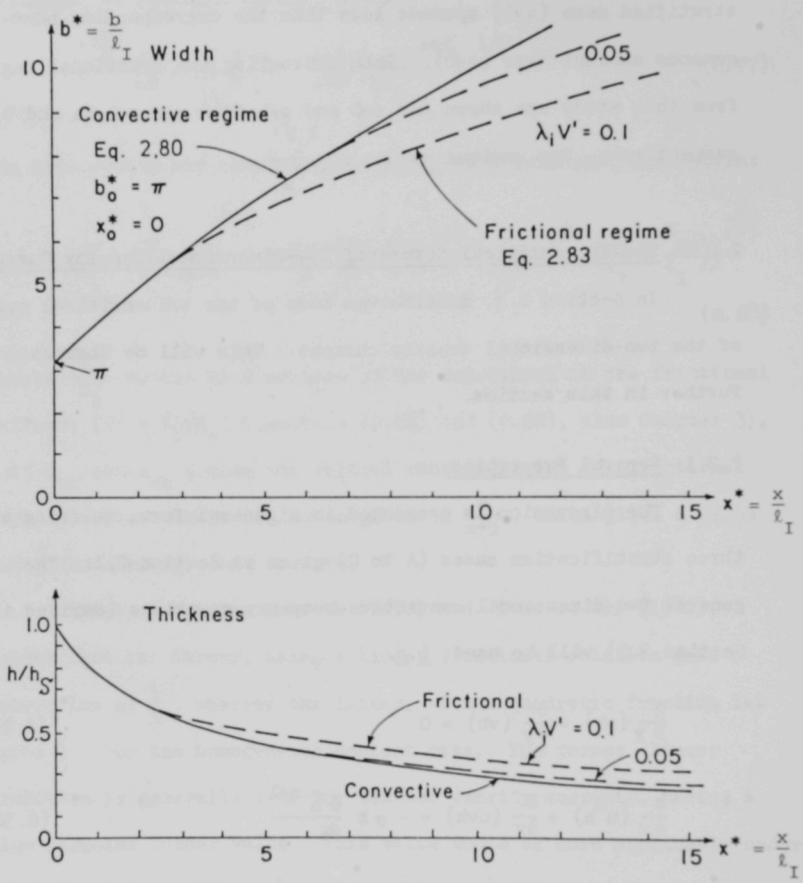

Figure 2-6 Convective and frictional regimes for density current spreading, (after Jirka et al., 1980)

a) Homogeneous or stepwise ambient stratification, (Cases A and B, respectively), s = 0 .

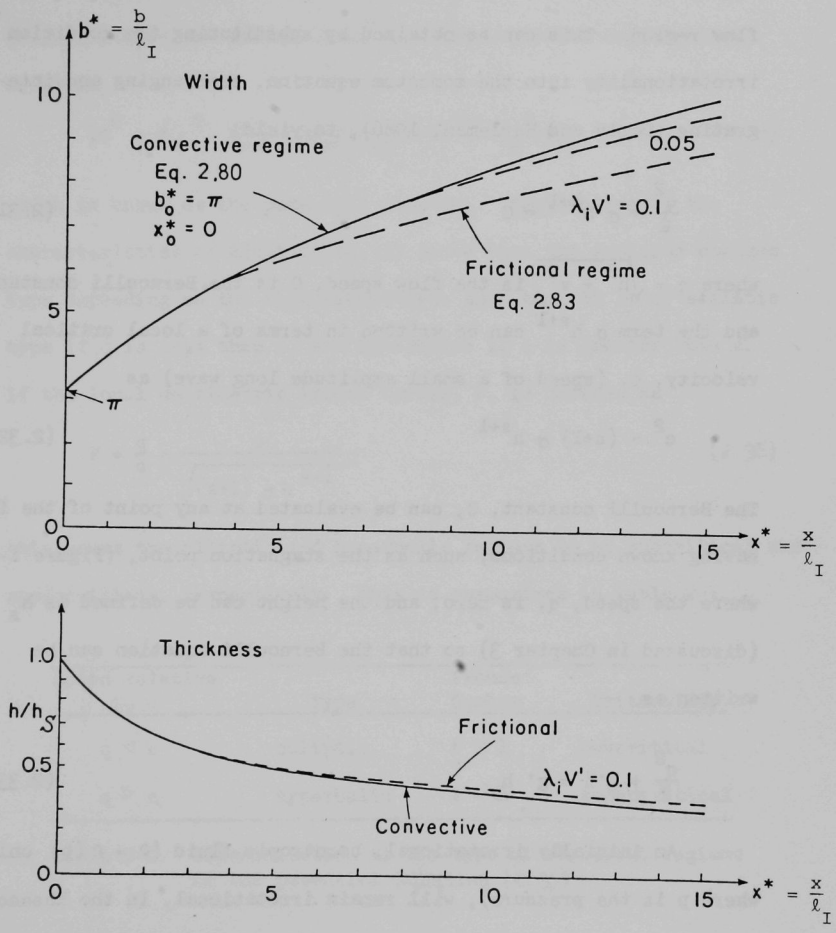

b) Linear ambient stratification, (Case C), s = 1.

which, in the absence of rotational effects is valid for the whole flow region. This can be obtained by substituting the condition for irrotationality into the momentum equation, rearranging and integrating (Daily and Harleman, 1966), to yield

$$\frac{q^2}{2} + \sigma h^{s+1} = C \tag{2.31}$$

where $q = \sqrt{u^2 + v^2}$ is the flow speed, C is the Bernoulli constant, and the term σh^{s+1} can be written in terms of a local critical velocity, c, (speed of a small amplitude long wave) as

$$c^2 = (s+1)\, \sigma h^{s+1} \tag{2.32}$$

The Bernoulli constant, C, can be evaluated at any point of the flow having known conditions, such as the stagnation point, (Figure 1-1), where the speed, q, is zero, and the height can be defined as h_s (discussed in Chapter 3) so that the Bernoulli equation can be written as

$$\frac{q^2}{2} + g'h = g'\, h_s. \tag{2.33}$$

An initially irrotational, barotropic fluid ($\rho = \rho(p)$ only, where p is the pressure), will remain irrotational, in the absence of rotational effects (Bjerknes' theorem, Turner, 1973). This allows the definition of a velocity potential, ϕ, such that

$$\bar{q} = \nabla \phi \tag{2.34}$$

Substituting this definition into Equations (2.29) and (2.30), yields the second order non-linear partial differential equation

$$(c^2 - \phi_x{}^2)\,\phi_{xx} - 2\phi_x\phi_y\phi_{xy} + (c^2 - \phi_y{}^2)\phi_{yy} = 0 \qquad (2.35)$$

which is known as the potential equation. Examination of the characteristics of Equation (2.35) shows that the equation changes type depending on the flow properties, such that it is of elliptic type if q is less than c, and hyperbolic if q is greater than c. If the local densimetric Froude number, F, is defined as

$$F = \frac{q}{c} = \frac{q}{\sqrt{(s+1)\,\sigma\, h^{s+1}}} \qquad (2.36)$$

this shows the elliptic and hyperbolic regions to be subcritical and supercritical, respectively. This is summarized in Table 2-1.

Speed Relative to c	Type	Froude Number	Criticality
$q < c$	elliptic	$F < 1$	subcritical
$q > c$	hyperbolic	$F > 1$	supercritical

Table 2-1. Classification of the type of different regions of the potential Equation (2.35).

An additional appreciation of the flow differences in the supercritical and subcritical regions can be obtained by considering the variation of mass flow per unit width with the velocity, using the Bernoulli equation, Equation (2.33). This allows the mass flux per unit width, hq, to be defined as

$$hq = q\left(h_s^{s+1} - \frac{q^2}{2\sigma}\right)^{\frac{1}{s+1}} \tag{2.37}$$

which can be rearranged to

$$\frac{h}{h_s}\frac{q}{\sqrt{\sigma h_s^{s+1}}} = \frac{q}{\sqrt{\sigma h_s^{s+1}}}\left(1 - \frac{q^2}{2\sigma h_s^{s+1}}\right)^{\frac{1}{s+1}} \tag{2.38}$$

which is a function of q having a maximum value when

$$\frac{q}{\sqrt{\sigma h_s^{s+1}}} = q_c = \sqrt{\frac{2(s+1)}{(s+3)}} \tag{2.39}$$

(Note that $q_c = \sqrt{\frac{2}{3}}$ for s = 0 and $q_c = 1$ for s = 1). A minimum value of zero is obtained at $\frac{q}{\sqrt{g'h_s}} = 0$ and $= \sqrt{2}\,(= q_{max})$ for both s values. The latter two values define the range of the problem. The variation of $\frac{h}{h_s}\frac{q}{\sqrt{g'h_s}}$ with q from Equation (2.38) is shown in Figure 2-7 for both stratification cases. This shows that in the subcritical region a decrease in mass flux per unit width is accompanied by a decrease in velocity, whereas in the supercritical region, a similar mass flux decrease must be accompanied by an increase in q. Thus, if a subcritical flow is allowed to expand, its velocity will decrease, whereas the velocity of a supercritical flow will increase.

Transitions from one flow type to another occur in two ways: (1) The flow passes smoothly from sub- to supercritical conditions forming critical lines in the flow domain. (2) The reverse transition from super- to subcritical flow may also occur smoothly (in very special cases) but is more likely to occur across a discontinuity

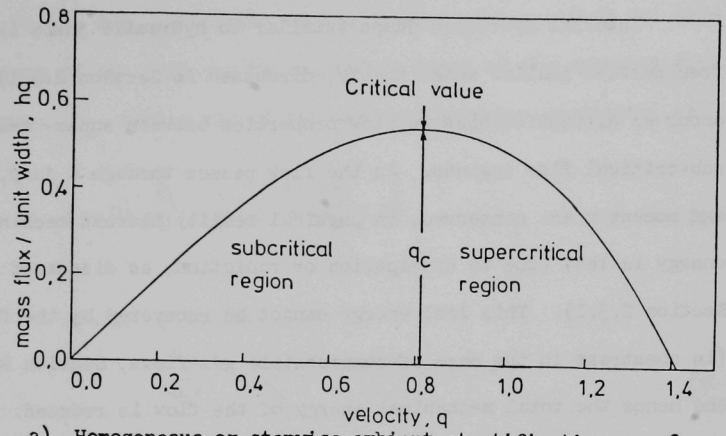

a) Homogeneous or stepwise ambient stratification, s = 0.

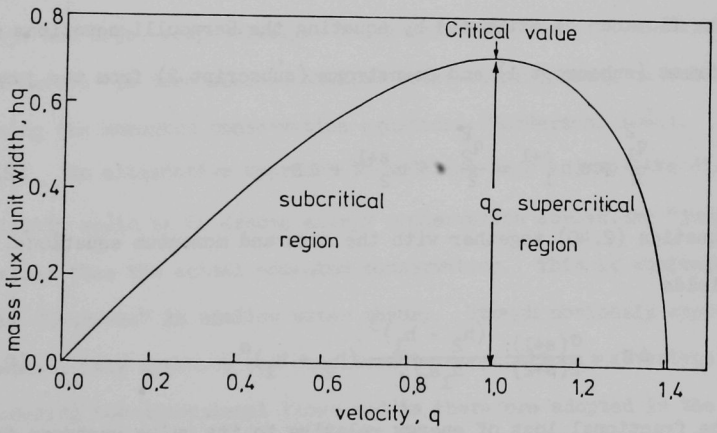

b) Linear ambient stratification, s = 1 .

Figure 2-7 Variations of mass flux/unit width with velocity

in the form of an internal hydraulic jump.

2.2.2 The internal hydraulic jump

Internal hydraulic jumps (similar to hydraulic jumps in free-surface shallow water theory, discussed in Section 2.3.1) occur as discontinuities in flow properties between super- and sub-critical flow regions. As the flow passes through a jump, mass and momentum are conserved, in physical reality whereas mechanical energy is lost (due to dissipation or radiation, as discussed in Section 2.3.1). This lost energy cannot be recovered by the fluid (in constrast to the case of compressible gas flows, Section 2.3.2), and hence the total mechanical energy of the flow is reduced.

The amount of specific energy lost, ΔE, in a jump normal to the flow can be estimated by equating the Bernoulli equations upstream (subscript 1) and downstream (subscript 2) from the jump, as

$$\frac{q_1^2}{2} + \sigma h_1^{s+1} = \frac{q_2^2}{2} + \sigma h_2^{s+1} + \Delta E \tag{2.40}$$

Equation (2.40) together with the mass and momentum equations, yields

$$\Delta E = \frac{\sigma(s+1)}{2(s+2)} \frac{(h_2 - h_1)^3}{h_1 h_2} (h_2 + h_1)^s \tag{2.41}$$

The fractional loss of energy relative to its value upstream from the jump, E_1, is given by

$$\frac{\Delta E}{E_1} = 1 - \frac{F_1^2 (s+1) \frac{h_1^2}{h_2^2} + 2\left(\frac{h_2}{h_1}\right)^{s+1}}{F_1^2(s+1) + 2} \tag{2.42}$$

These losses for various upstream Froude number values are shown in Figure 2-8. The ratio of the fluid depths upstream and downstream of the jump can be related in terms of the upstream Froude number, F_1, making use of the mass and momentum equations, as:

$$s = 0: \quad \frac{h_2}{h_1} = \frac{1}{2}\left(\sqrt{1 + 8F_1^2} - 1\right) \tag{2.43}$$

$s = 1$: Solution of:

$$\left(\frac{h_2}{h_1}\right)^3 + \left(\frac{h_2}{h_1}\right)^2 + \left(\frac{h_2}{h_1}\right) - 3F_1^2 = 0 \tag{2.44}$$

Equations (2.43) and (2.44) are represented graphically in Figures 2-9a and 2.9b, respectively. These equations are equivalent to the "M-curves" in free surface shallow water theory, being calculated using the Momentum conservation equations (Henderson, 1966).

An alternative approach to modeling such a jump-like discontinuity would be to assume energy conservation across the "jump", rather than the actual momentum conservation. This is equivalent to the "E-curves" in shallow water theory. Though obviously approximative, this approach has considerable computational advantage when modeling two-dimensional flows and is therefore adopted in the remainder of this study. The amount of momentum, ΔM_m, gained in a "jump" normal to the flow can be estimated by applying the momentum equation across the "jump" as

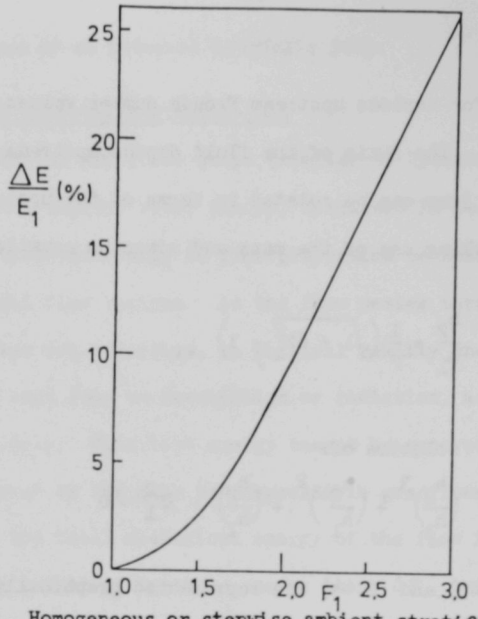

a) Homogeneous or stepwise ambient stratification, s = 0 .

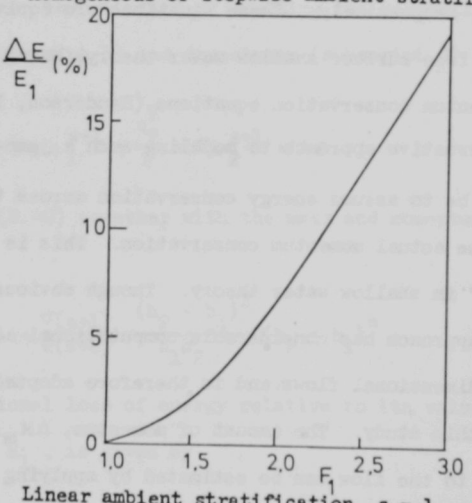

b) Linear ambient stratification, s = 1.

Figure 2-8 The percentage energy loss across a jump relative to the upstream energy, as a function of upstream Froude number.

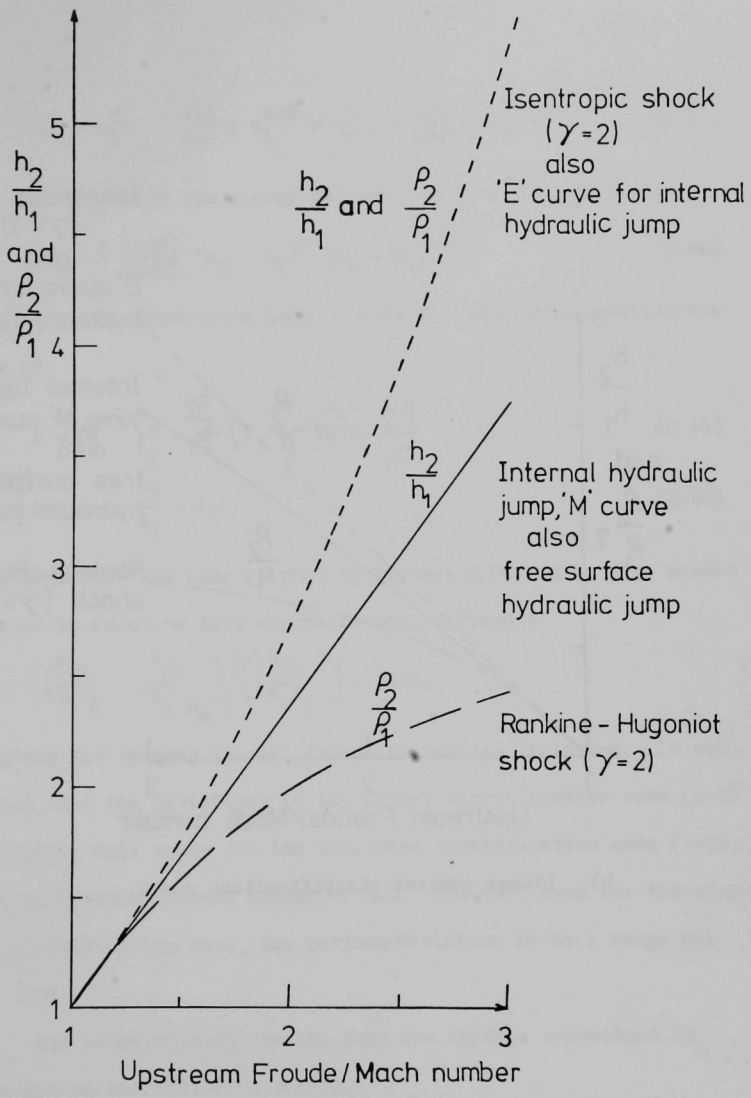

Figure 2-9 The variation of the ratio of downstream to upstream jump (shock) heights with upstream Froude (Mach) number

a) Homogeneous or stepwise ambient stratification s = 0

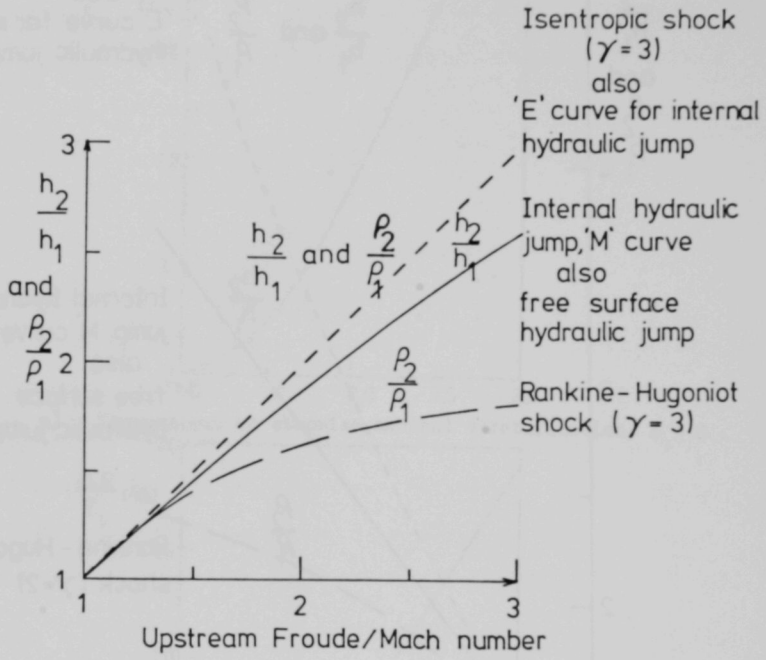

b) Linear ambient stratification, s = 1.

$$\Delta M_m + q_1^2 h_1 + \frac{s+1}{s+2}\sigma h_1^{s+2} = q_2^2 h_2 + \frac{s+1}{s+2}\sigma h_2^{s+2} \tag{2.45}$$

This, together with the energy and continuity equations gives

$$\Delta M_m = \sigma \frac{(s+1)}{(s+2)} (h_2 - h_1)^3 (h_2 + h_1)^{s-1}. \tag{2.46}$$

The upstream to downstream depth ratios for this approximation are given by:

$$s = 0: \quad \frac{h_2}{h_1} = \frac{F_1}{4}\left(F_1 + \sqrt{F_1^2 + 8}\right) \tag{2.47}$$

$$s = 1: \quad \frac{h_2}{h_1} = F_1 \tag{2.48}$$

These equations are also graphed in Figures 2.9a and b. The errors involved in adopting this approximation, defined as

$$\left[\left(\frac{h_2}{h_1}\right)_E - \left(\frac{h_2}{h_1}\right)_{M_m}\right] \Big/ \left[\left(\frac{h_2}{h_1}\right)_E\right] \cdot 100\%,$$

are given for various initial Froude numbers in Table 2-2. It can be seen that the deviations in the linear stratification case (s=1) are roughly half those for the step-wise stratification case (s=0), up to an upstream Froude number of 3.0. However, even for the step-wise stratification case, the maximum deviation in this range was only +30%.

The properties across the jump are further summarized in Table 2-3 of the following section.

Froude Number, F_1	Relative Deviation in Height Ratios for 'E' and 'M' Curves	
	Stepwise Stratification (s=0)	Linear Stratification (s=1)
1.0	0%	0%
2.0	+13%	+6%
3.0	+29%	+13%

Table 2-2. Deviation with upstream Froude number of height ratios across a jump for the conservation of energy, (E curve), relative to the conservation of momentum (M curve).

2.3 Comparison of Density Current Theory with that for Free Surface Shallow Water Flows and Compressible Gas Flows

The analogy between free surface shallow water flow and compressible gas flow has been known for many years. Use has been made of it, mainly by conducting experiments on free surface flows, in order to predict compressible gas flows. A brief historical sketch of the usage of the analogy is given in Appendix II.

This section discusses free surface shallow water theory (Section 2.3.1) and compressible gas flow theory (Section 2.3.2). Both exhibit a mathematical analogy with each other and with the density current dynamics. The basis of these analogies will be discussed and summarized in Table 2-3.

Table 2-3a: Analogy between compressible gas flow and stratified fluid (shallow water) flow in the absence of flow discontinuities.

	Stratified Fluid Flow		Compressible Gas Flow	
flow type	layered system of 2-D, inviscid irrotational homogeneous fluids, the upper layer being shallow, and having negligible vertical accelerations.		2-D flow of an irrotational inviscid, homogeneous, gas having a constant ratio of specific heat capacities, γ subject to the isentropic law $p = k\rho^{\gamma}$	
mass continuity	$\frac{\partial}{\partial x}(uh) + \frac{\partial}{\partial y}(vh) = 0$	(2.29)	$\frac{\partial}{\partial x}(u\rho) + \frac{\partial}{\partial y}(v\rho) = 0$	(2.51)
momentum conservation	$\frac{\partial}{\partial x}(u^2h) + \frac{\partial}{\partial y}(uvh) = -\sigma h \frac{\partial h^{s+1}}{\partial x}$	(2.30a)	$\frac{\partial}{\partial x}(u^2\rho) + \frac{\partial}{\partial y}(uv\rho) = -k\frac{\gamma}{\gamma-1}\rho\frac{\partial}{\partial x}\rho^{\gamma-1}$	(2.52a)
	$\frac{\partial}{\partial x}(uvh) + \frac{\partial}{\partial y}(v^2h) = -\sigma h \frac{\partial h^{s+1}}{\partial y}$	(2.30b)	$\frac{\partial}{\partial x}(uv\rho) + \frac{\partial}{\partial y}(v^2\rho) = -k\frac{\gamma}{\gamma-1}\rho\frac{\partial}{\partial y}\rho^{\gamma-1}$	(2.52b)
energy equation	mechanical energy:		total energy:	
	$d(\frac{q^2}{2}) + d(\sigma h^{s+1}) = 0$	(2.55)	$d(\frac{q^2}{2}) + d(h_e) = 0$	(2.56)
requirements for analogy	height, h analogous to density, ρ $s + 2 = \gamma$ $(s+1)\sigma = k\gamma$			
wave speed	internal wave velocity		sound velocity	
	$c = \sqrt{(s+1)\sigma h^{s+1}}$	(2.32)	$a = \sqrt{k\gamma\rho^{\gamma-1}}$	(2.63)
			$= \left(\frac{dp}{d\rho}\right)^{1/2}$	(2.61)
potential equation	$(c^2 - \phi_x^2)\phi_{xx} - 2\phi_x\phi_y\phi_{xy} + (c^2 - \phi_y^2)\phi_{yy} = 0$	(2.35)	$(a^2 - \phi_x^2)\phi_{xx} - 2\phi_x\phi_y\phi_{xy} + (a^2 - \phi_y^2)\phi_{yy} = 0$	(2.62)
definition of criticality	Froude number $F = \frac{q}{c} = 1$	(2.36)	Mach number, $M = \frac{q}{a} = 1$	(2.64)
flow regions	Supercritical flow, $F > 1$		supersonic flow, $M > 1$	
	Subcritical flow, $F < 1$		subsonic flow, $M < 1$	
discontinuous transition (see Table 2-3b)	Wave of elevation (hydraulic jump)		compression wave (shock wave)	
continuous transition	Wave of depression (hydraulic drop)		expansion wave	

Table 2-3b: Classification of flow discontinuities for compressible gas flow and stratified fluid (shallow water) flow.

	Stratified (or Shallow Water) Fluid Flow*			Compressible Gas Flow	
	Real Fluid Behavior	Computational Idealization to Behavior**		Real Fluid Behavior	Computational Approximation**
name of discontinuity	hydraulic jump			shock	
applicable equations	"jump with momentum conservation"	"jump with energy conservation"		Rankine-Hugoniot relations	isentropic shock approximation
conservation principle	mass, momentum	mass, mechanical energy		mass, momentum, total energy	mass, entropy, total energy
non-conserved quantities	mechanical energy	momentum		entropy	momentum
change in non-conserved quantities (normal shock or jump)	loss of energy:	gain of momentum:		gain of entropy:	gain of momentum:
	$\Delta E = \frac{2(s+1)}{3(s+2)} \frac{(h_2-h_1)^3}{h_2\, h_1} (h_2+h_1)^s$ (2.41)	$\Delta M_m = \frac{2(s+1)}{(s+2)} (h_2-h_1)\,(h_2+h_1)^{s-1}$ (2.46)		$\frac{\Delta S}{R} = \frac{(\gamma+1)}{12\,\gamma^2} \frac{(p_2-p_1)^3}{p_1^{\,3}}$ (2.65)	$\Delta M_m = k(\rho_2-\rho_1)^3\,(\rho_1+\rho_2)^{\gamma-3}$ (2.68)
ratios of analogous quantities, after/before shock or jump (normal shock or jump)	$s=0$: $\frac{h_2}{h_1} = \frac{1}{2}\left(\sqrt{1+8F_1^{\,2}} - 1\right)$ (2.43)	$s=0$: $\frac{h_2}{h_1} = \frac{F_1}{4}\left(F_1 + \sqrt{F_1^{\,2}+8}\right)$ (2.47)		$\frac{p_2}{p_1} = \frac{(\gamma+1)M_1^{\,2}}{(\gamma-1)M_1^{\,2}+2}$ (2.67)	$\gamma=2$: $\frac{\rho_2}{\rho_1} = \frac{M_1}{4}\left(M_1 + \sqrt{M_1^{\,2}+8}\right)$ (2.69)
	$s=1$: solution of $\left(\frac{h_2}{h_1}\right)^3 + \left(\frac{h_2}{h_1}\right)^2 + \left(\frac{h_2}{h_1}\right) - 3F_1^{\,2} = 0$ (2.44)	$s=1$: $\frac{h_2}{h_1} = F_1$ (2.48)			$\gamma=3$: $\frac{\rho_2}{\rho_1} = M_1$ (2.70)

* $s=0$ applies to simple free surface flow if $g' = g$.

** as used in Jameson and Caughey (1977).

*** as used in this study.

2.3.1 Free Surface Shallow Water Theory

The governing equations for two-dimensional free surface, shallow water theory are, in conservation form (Daily and Harleman, 1973).

$$\frac{\partial}{\partial x}(hu) + \frac{\partial}{\partial y}(hv) = 0 \tag{2.49}$$

$$\frac{\partial}{\partial x}(u^2h) + \frac{\partial}{\partial y}(uvh) = -gh\frac{\partial h}{\partial x} \tag{2.50a}$$

$$\frac{\partial}{\partial x}(uvh) + \frac{\partial}{\partial y}(v^2h) = -gh\frac{\partial h}{\partial y} \tag{2.50b}$$

for flow along a frictionless channel. A comparison of Equations (2.49) and (2.50) with those governing density current dynamics, Equations (2.29) and (2.30) for the case of s=0 (corresponding to stratification cases A and B, Section 2.1) shows that they are identical if g is replaced by g'. This indicates the physical analogy that exists between these two situations, which enables the use of the well-known theory of open channel flow to aid the understanding of density current dynamics.

Hydraulic jumps are included in this analogy such that the up- and downstream depth ratios for the M-curves and E-curves are as given in Equations (2.43) and (2.47), respectively.

Much research has been undertaken, for shallow water flows, on the nature of the energy losses occurring in the jump. Henderson (1966), Chow (1959) and earlier Benjamin and Lighthill (1954), examined the types of energy loss for jumps of various strengths.

Henderson and Chow classified jumps according to the value of the upstream Froude number, F_1, this being in accordance with the U.S. Bureau of Reclamation Studies (1955) and those of Bradley and Peterka (1957). Jumps having F_1 values less than 1.7 are called "undular jumps". These differ from stronger jumps in that instead of the breaking wave, they consist of a sequence of unbroken standing waves. The energy loss, ΔE, in the latter case will be partially radiated downstream by these waves (also partly dissipated by bottom friction), whereas for breaking waves, the energy will be dissipated by the turbulence generation. Benjamin and Lighthill (1954) showed that theoretically, energy radiation alone could account for energy losses only up to $F_1 = 1.25$. However, the effects of bed roughness were found to account for unbroken jumps up to $F_1 = 1.7$.

For jumps having Froude numbers greater than 1.7, the energy losses are due to dissipative effects. The classification continues from a "weak jump" for $1.7 < F_1 < 2.5$, through to a "strong jump" for $F_1 > 9.0$.

2.3.2 Compressible Gas Flow Theory

The two-dimensional flow of an inviscid, homogeneous, isentropic gas of constant density having a constant ratio of specific heats, γ, may be described by the following equations (Shapiro, 1953):

$$\frac{\partial}{\partial x}(\rho u) + \frac{\partial}{\partial y}(\rho v) = 0 \qquad (2.51)$$

$$\frac{\partial}{\partial x}(u^2\rho) + \frac{\partial}{\partial y}(uv\rho) = -k\,\frac{\gamma}{\gamma-1}\,\rho\,\frac{\partial}{\partial x}\,\rho^{\gamma-1} \tag{2.52a}$$

$$\frac{\partial}{\partial x}(uv\rho) + \frac{\partial}{\partial y}(v^2\rho) = -k\,\frac{\gamma}{\gamma-1}\,\rho\,\frac{\partial}{\partial y}\,\rho^{\gamma-1} \tag{2.52b}$$

where ρ is the gas density, and k the coefficient in the isentropic gas law

$$p = k\,\rho^{\gamma}\,. \tag{2.53}$$

A comparison of Equations (2.51) and (2.52) with Equations (2.29) and (2.30) shows them to be similar, that is, that a <u>mathematical</u> analogy exists between the two equation sets, <u>provided</u> h^s is analogous to $\rho^{\gamma-2}$, or

$$\gamma = s + 2 \tag{2.54}$$

together with

ρ analogous tc h.

This analogy could also have been arrived at by considering the respective energy equations. For the hydraulic case, the energy equation is given by Equation (2.31), which can also be written in the form

$$d\left(\frac{q^2}{2}\right) + d(\sigma\,h^{s+1}) = 0 \tag{2.55}$$

while for the case of the compressible gas (Shapiro, 1953) it is

$$dh_e + d\left(\frac{q^2}{2}\right) = 0 \tag{2.56}$$

where h_e is the enthalpy of the gas, such that

$$dh_e = C_p dT \tag{2.57}$$

where C_p is the specific heat capacity of the gas at constant pressure, and T is its temperature. The enthalpy h_e or total energy per unit mass of a gas is defined as

$$h_e = u + \frac{p}{\rho} \tag{2.58}$$

where u is the internal energy of the gas. The perfect gas law is

$$p = R\rho T \tag{2.59}$$

where R is the gas constant. The ratio of specific heats is defined as

$$\gamma = C_p/C_v \tag{2.60}$$

with C_v the specific heat capacity of the gas at constant volume. The speed of sound, a, is given by

$$a^2 = \left(\frac{\delta p}{\delta \rho}\right)_s \tag{2.61}$$

where $)_s$ denotes at constant entropy. Equations (2.53), (2.55), (2.59), (2.60) and (2.61) combine to give the potential equation

$$(a^2 - \phi_x{}^2)\phi_{xx} - 2\phi_x\phi_y\phi_{xy} + (a^2 - \phi_y{}^2)\phi_{yy} = 0 \tag{2.62}$$

Since the flow is irrotational with the usual definition of a velocity potential ϕ. Equation (2.62) can be seen to be identical to that for the hydraulic situation, Equation (2.35), provided the velocity of sound, a, is analogous to the velocity of propagation of an

infinitessimal disturbance, or the local internal wave speed, c. Thus

$$a^2 = k\gamma\rho^{\gamma-1} \tag{2.63}$$

must be analogous to Equation (2.32), yielding a similar requirement to Equation (2.54) and in addition, $k\gamma$ is analogous to $(s+1)\sigma$.

A consideration of the characteristics of the potential equation, (2.62), as for the density current case in Section 2.2, shows again elliptic (subsonic) and hyperbolic (supersonic) regions, denoted by $M < 1$ and $M > 1$, respectively. M in this case is denoted by

$$M = \frac{q}{c} \tag{2.64}$$

and is known as the Mach number of the flow, (analogous to the hydraulic Froude number with sub- and supersonic regions analogous to sub- and supercritical regions, respectively).

However, the transition from super to subsonic flows, the shock wave, differs in nature from the hydraulic jump. In real gases (as opposed to isentropic flow theory, which does not allow these discontinuities), discontinuities of pressure, density, temperature and velocity occur at shock waves. These discontinuities are governed by the Rankine-Hugoniot relations, which admit conservation of mass, momentum, and total energy (mechanical and internal), whereas hydraulic jumps while conserving mass and momentum, experience a loss of mechanical energy. This difference is due to the mechanical energy

in both cases (shock and jump) being converted into internal energy. However, while for the hydraulic case this energy is irretrievably lost to the system, for the gas flow, mechanical and internal energy are interchangeable if the flow is adiabatic (zero heat transfer with its surroundings), but the entropy, s, of the system will be increased. Thus, for the Rankine-Hugoniot shock, mass, momentum and total energy are conserved, whereas entropy is not.

An expression for the entropy loss is given (Shapiro, 1953) to lowest order as

$$\frac{\Delta s}{R} \cong \frac{\gamma + 1}{12\,\gamma^2}\left(\frac{\Delta p}{p_1}\right)^3 \tag{2.65}$$

where $\Delta p = p_2 - p_1$, p being the pressure, and the subscripts 1 and 2 denoting upstream and downstream values, respectively. The ratio $\frac{\Delta p}{p}$ is known as the "shock strength", and can be written in terms of the upstream Mach number, M_1, (Shapiro, 1953) as:

$$\frac{\Delta p}{p_1} = \frac{2\gamma}{\gamma+1}\left(M_1^{\,2} - 1\right) \tag{2.66}$$

The ratio of densities, ρ_2/ρ_1 , for the Rankine-Hugoniot shock is

$$\frac{\rho_2}{\rho_1} = \frac{(\gamma+1)M_1^{\,2}}{(\gamma-1)M_1^{\,2} + 2} \tag{2.67}$$

On the other hand, if, for computational purposes the gas flow is idealized as satisfying conservation of mass, total adiabatic energy and entropy, the momentum loss across this "computational jump"

can be calculated as

$$\Delta M_m = k(\rho_2 - \rho_1)^3 (\rho_1 + \rho_2)^{\gamma-3} \tag{2.68}$$

The corresponding density ratios are given by

$$\gamma=2: \quad \frac{\rho_2}{\rho_1} = \frac{M_1}{4}\left(M_1 + \sqrt{M_1^2 + 8}\right) \tag{2.69}$$

$$\gamma=3: \quad \frac{\rho_2}{\rho_1} = M_1 \tag{2.70}$$

These are also represented in Figure 2.9.

2.4 Stability and Entrainment of a Density Current

2.4.1 Interfacial Stability

The interface between the density current and ambient flow region forms an interior shear layer, which may be stable or unstable. Turner (1973) discusses the various types of instabilities which are likely to occur along such an interface. He quotes experimental results suggesting that the instabilities most likely to be observed in a stably stratified environment are of Kelvin-Helmholtz (K-H) type. These are inviscid in character and result in a "violent breakdown at the interface and in a region on each side of it." The K-H criterion means that for the case of an infinitely deep ambient, short wavelength, λ, disturbances will become unstable if

$$\frac{(\Delta U)^2}{g'\lambda} > \frac{1}{\pi} \tag{2.71}$$

where ΔU is the velocity difference across the interface. The left-

hand side of Equation (2.71) has the form of an inverse bulk Richardson number, based on the wavelength of the disturbance. (The bulk Richardson number" is more generally defined as

$$R_i = \frac{g'h}{(\Delta U)^2} \tag{2.72}$$

where ΔU is the velocity change across an interface of finite depth, h).

Thus, the interfacial stability can be commonly expressed by a Richardson number criterion. High Richardson number flows tend to be stable with respect to long wave disturbances (i.e., of the order of the depth), while some short wave instabilities may still exist. However, over reasonably short distances, the interface can, for high Richardson numbers ($R_i > 1$), for any practical purposes, be assumed as stable and without mixing.

2.4.2 Turbulent Entrainment

In flows (whether buoyant or nonbuoyant) which are injected into an ambient at high Reynolds number, the resulting turbulent zone tends to entrain the non-turbulent ambient fluid, in a process that is called "turbulent entrainment." The nature of turbulent entrainment in buoyant and non-buoyant flows will be discussed in the following.

2.4.2.1 Non-buoyant jet entrainment

Jirka (1982), on the basis of experimental evidence, deduced that the turbulent energy required for entrainment to occur, was

produced by internal shearing processes within the density current, accounting for about 10% of the mean flow energy. This is in agreement with independent measurements by Heskestad (1965), and others (see Rodi, 1975).

An expression for the entrainment velocity, w_e, is conventionally obtained by setting it proportional to a characteristic local jet velocity, such as its centerline velocity, u_c, as

$$w_e = \alpha\, u_c \tag{2.73}$$

where the constant of proportionality, α , is known as the entrainment coefficient. This basic proportionality concept was first introduced by Taylor (1954), and further expounded by Morton, Taylor and Turner (1956).

This entrainment coefficient for a two-dimensional non-buoyant jet, can be related analytically to the observed spreading rate of a jet, using an integral approach. The integral properties of the jet are the mass flow, $Q = I_1\, u_c h$ and the momentum, $M_m = I_2\, u_c^2 h$ where I_1 and I_2 are integral coefficients obtained from integrating the jet velocity and the jet momentum, respectively, over the current depth - the velocity of any point being given as $u = u_c\, f(\eta)$ where f is a given shape function and η a nondimensional variable. Then the mass flux conservation, $\frac{dQ}{dx} = w_e = \alpha\, u_c$, (Equation (2.73)) together with the conservation of momentum, $\frac{dM_m}{dx} = 0$, combine to give

$$\alpha = \frac{I_1}{2}\frac{\partial h}{\partial x} = \frac{I_1}{2} k \tag{2.74}$$

where k is the spreading rate of the jet.

The actual values for the spreading rate have to be taken from experimental data, which show that k is a constant, (a linear spreading rate) in conformance with the jet similarity properties. Particular values of k have also been estimated. Using experimental data (see Albertson et al., 1950, and Rodi, 1975), jet spreading values for the assumption of top-hat profiles, $I_1 = I_2 = 1$, can be deduced as $k = 0.165$, and the associated entrainment coefficient is

$$\alpha = 0.083 \tag{2.75}$$

2.4.2.2 Buoyant density current entrainment

Horizontal turbulent density currents having a low buoyancy ($R_i \rightarrow 0$), behave similarly to non-buoyant jets. However, at high Richardson numbers ($R_i > 0$), the effect of buoyancy will be to dampen the turbulent kinetic energy which leads to entrainment. Estimates of the amount and nature of this damping are obtained from experimental evidence. Ellison and Turner (1959) conducted laboratory experiments and found that the entrainment coefficient for a buoyant case, α^*, was a monotonic decreasing function of the local Richardson number, R_i, (Figure 2-10) defined as

$$R_i = \frac{g'h}{u_c^2} \tag{2.76}$$

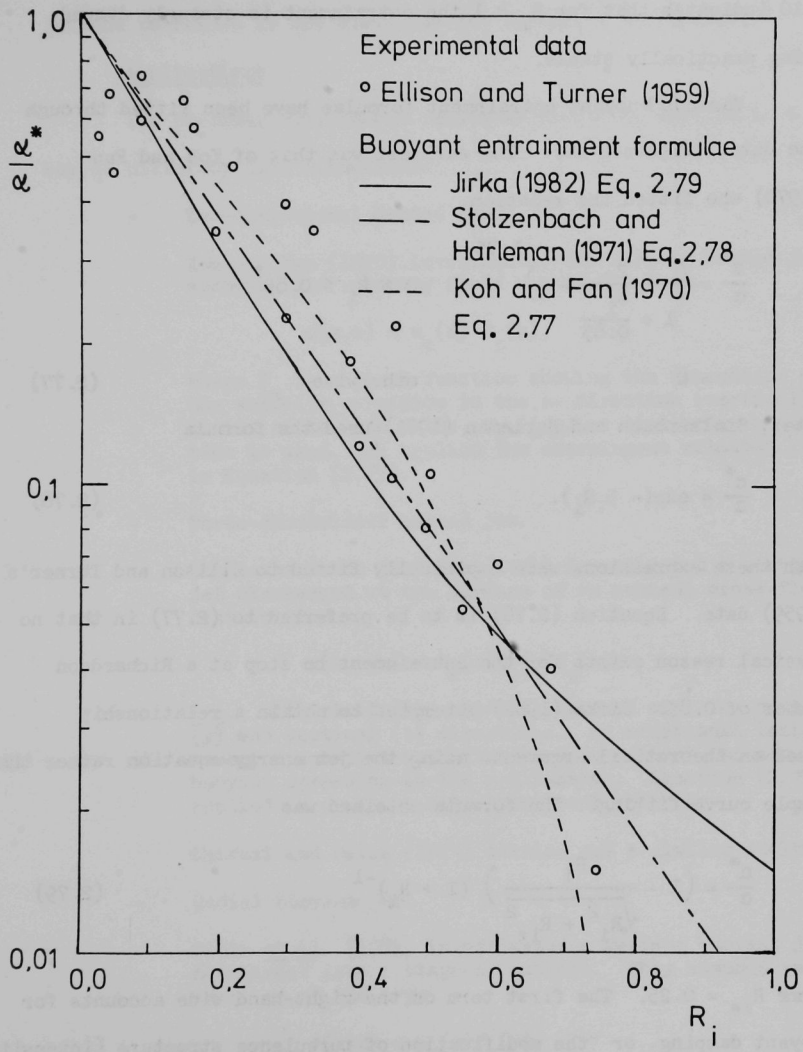

Figure 2-10 Various buoyant entrainment functions in comparison with the data of Ellison and Turner (1959)

where u_c is the centerline velocity of the density current. Figure 2-10 indicates that for $R_i > 1$ the entrainment is strongly damped, being practically stable.

Various buoyant entrainment formulae have been fitted through the data, (Figure 2-10). The earliest was that of Koh and Fan (1970) who fitted the relation

$$\frac{\alpha^*}{\alpha} = \left(\frac{2}{1 + \frac{R_i}{0.85}} - 1\right)^{1.75} \qquad 0 \le R_i \le 0.85$$

$$= 0 \qquad \text{otherwise} \qquad (2.77)$$

Later, Stolzenbach and Harleman (1971) used the formula

$$\frac{\alpha^*}{\alpha} = \exp(-\,5\,R_i). \qquad (2.78)$$

Both these expressions were empirically fitted to Ellison and Turner's (1959) data. Equation (2.78) is to be preferred to (2.77) in that no physical reason exists for the entrainment to stop at a Richardson number of 0.85. Jirka (1982) attempted to obtain a relationship based on theoretical arguments using the jet energy equation rather than simple curve fitting. The formula obtained was

$$\frac{\alpha^*}{\alpha} = \left(1 - \frac{R_i}{\sqrt{R_i^{\,2} + R_{i*}^{\,2}}}\right)(1 + R_i)^{-1} \qquad (2.79)$$

where $R_{i*} = 0.25$. The first term on the right-hand side accounts for buoyant damping, or "the modification of turbulence structure (intensity reduction and profile distortion) by buoyancy," and the second term

for," the additional pressure work that must be done by the buoyant jet and therefore is not available for turbulent entrainment."

Applications

The previous entrainment relations have been applied in a number of different flow situations:

- Two-dimensional heated jet.

  Koh and Fan (1970) investigated the surface heated jet by assuming its velocity field was of the form

  $$u(x,z) = u_c(x)\ f_z(z),$$

  where f_z is a given function showing the dependence of the velocity variation in the z- direction (vertical) on its centerline value, u_c, i.e., a similarity assumption is used. He applied the entrainment relation given in Equation (2.77).

- Three-dimensional heated jet.

  Stolzenbach and Harleman (1971) investigated a heated jet discharged at the surface of an ambient cross-flow distribution as

  $$u(x,y,z) = u_c(x) f_y(y) f_z(z)$$

  i.e., with similarity profiles assumed over the horizontal (y) and vertical (z) directions. An additional lateral momentum equation was introduced to predict the non-linear, buoyant spreading in the y-direction. Equation (2.78) was applied to evaluate the entrainment velocity.

  Shirazi and Davis (1974) carried out a similar analysis.

- Radial buoyant jet.

  Jirka et al. (1981) investigated a surface buoyant jet discharged into a stagnant ambient. They assumed velocity profiles of the type

  $$u(r,z) = u_c(r) f_z(z),$$

  where r is the radial displacement, and applied Equation (2.78) to evaluate the entrainment velocity.

Both the expressions of Stolzenbach and Harleman (1971), Equation (2.78) and Jirka (1982), Equation (2.79), will be used later as described in Chapter 4 of this study.

2.5 Previous Two-Dimensional Density Current Solutions

Section 2.1.3 dealt with the "pseudo" two-dimensional density current approximations obtained by the extension of one-dimensional theory. This section discusses fully two-dimensional density current theory.

In addition to the "pseudo" two-dimensional solution applicable downstream from the source, Jirka et al. (1980), attempted to account for the upstream intrusions likely to occur. They approximated the full problem as a sequence of constant height solutions, which thus reduces the potential Equation (2.35) (representing the convective-buoyancy regime) to a Laplace equation at each step. (It should be noted that this is equivalent, using the gas flow analogy, to approximating a compressible gas flow by an incompressible one.) Shen (1977) concluded that "the streamline pattern usually does not greatly alter because of compressibility effects," which indicates that the constant height approximation is a reasonable first step toward a full solution. The Laplace equation was then solved for a given intrusion shape. The height required along this boundary was obtained by equating drag and buoyant forces, as described in Section 2.1, yielding an expression for the boundary height, which can be written for general stratification conditions as

$$h_B = \left\{ \frac{s+2}{s+1} \frac{C_D}{2\sigma} u_B^{\,2} \right\}^{\frac{1}{s+1}} \tag{2.80}$$

where the B subscript denotes boundary values. The velocity variation along the boundary obtained from the Laplace solution, was used in the Bernoulli equation, Equation (2.33), to obtain a height variation which could be compared with Equation (2.80). Various boundary shapes were examined until a height matching was obtained. They then matched together this solution with the downstream convective and frictional regimes, to obtain the complete solutions shown in Figures 2-11 a and b for s=0 and s=1, respectively.

Although the approach of Jirka et al. (1980), considered upstream intrusions, it contained significant approximations. The assumption of a constant height Laplace solution requires subcritical velocities in this region, which although it may be applicable locally does not necessarily hold overall. Also, the Schwarz-Christoffel transformation (Kantorovich and Krylov, 1958) employed to solve the Laplace equation requires the boundary to be approximated by a series of straight lines. Due to complexities associated with many lines, the boundary approximation was kept at three lines, which would lead to inaccuracies.

Garvine (1982) examined the inflow of the Connecticut River into Long Island Sound, as discussed in Section 1.2. He assumed that the inflow was supercritical as was the whole of the subsequent flow. This allowed him to use the method of characteristics in order to

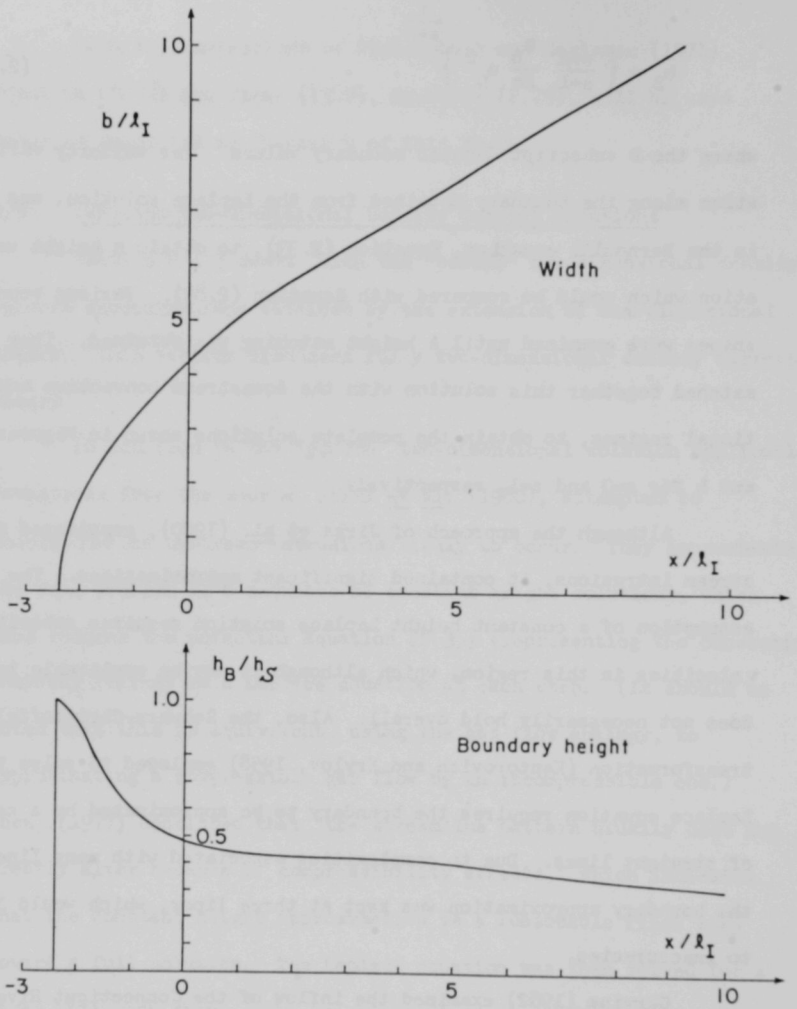

Figure 2-11 Geometry of combined density current upstream intrusion, convective and frictional regimes, (after Jirka et al., 1980)

a) Homogeneous or stepwise ambient stratification, s = 0 .

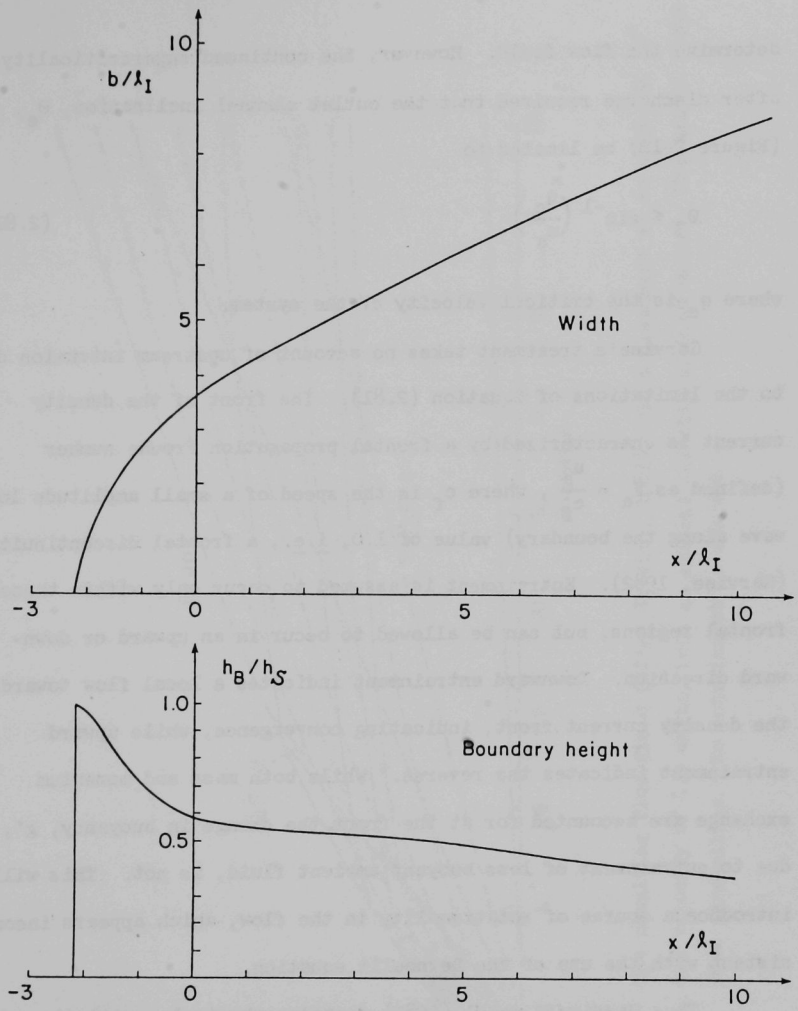

b) Linear ambient stratification, s = 1.

determine the flow field. However, the continued supercriticality after discharge required that the outlet channel inclination, θ_e, (Figure 2-12) be limited to

$$\theta_3 \leq \sin^{-1}\left(\frac{q_c}{u_a}\right) \tag{2.81}$$

where q_c is the critical velocity of the system.

Garvine's treatment takes no account of upstream intrusion due to the limitations of Equation (2.81). The front of the density current is characterized by a frontal propagation Froude number (defined as $F_a = \frac{u_a}{c_f}$, where c_f is the speed of a small amplitude long wave along the boundary) value of 1.0, i.e., a frontal discontinuity, (Garvine, 1982). Entrainment is assumed to occur only within these frontal regions, but can be allowed to occur in an upward or downward direction. Downward entrainment indicates a local flow towards the density current front, indicating convergence, while upward entrainment indicates the reverse. While both mass and momentum exchange are accounted for at the front, the change in buoyancy, g', due to entrainment of less buoyant ambient fluid, is not. This will introduce a source of rotationality in the flow, which appears inconsistent with the use of the Bernoulli equation.

Thus Garvine's model (1982) contains physical restrictions on the discharge (as discussed above) and only considers a convective buoyant regime. However, a complete solution (comprising the internal flow field) is obtained (see typical solution, Figure 2.12), as opposed to the previous solutions discussed.

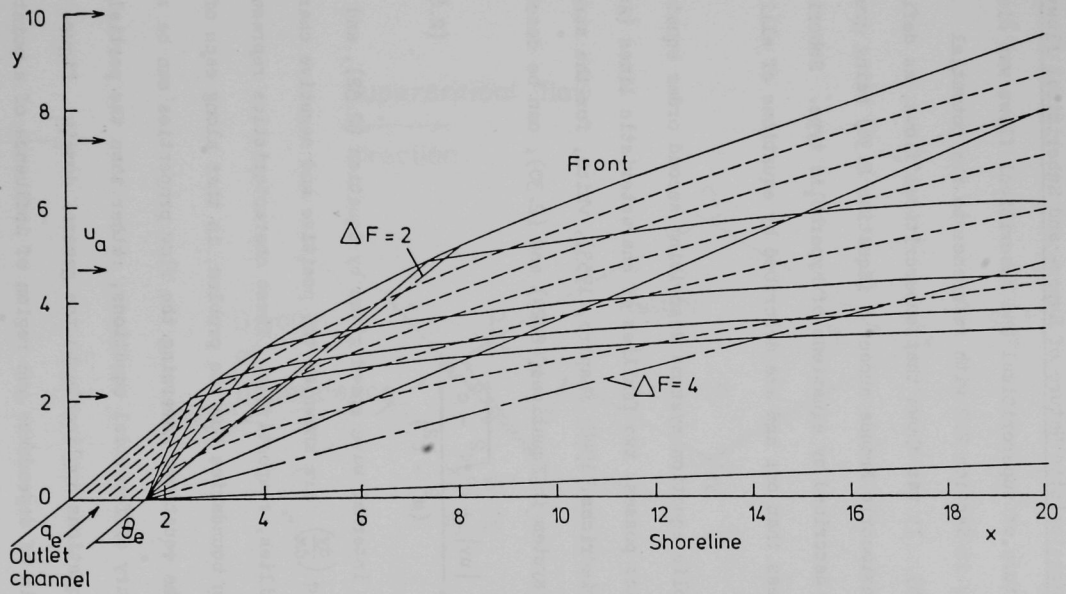

Figure 2-12 The resulting flow field (after Garvine, 1982), for a discharge at an angle of 39° and velocity of 1.0 units, into an ambient velocity of 0.68 units. The dashed lines show streamlines. No entrainment is assumed .

2.6 Numerical Techniques

2.6.1 The Characteristic Nature of Super- and Subcritical Flows

The nature of supercritical and subcritical flows was discussed briefly in Section 2.2 with reference to the potential Equation (2.35). It was shown that supercritical flows, as defined by a local densimetric Froude number F (Equation 2.36) being greater than one, are described by equations of hyperbolic type. Subcritical flows have F less than one and are described by equations of elliptic type.

Hyperbolic equation systems describing second order equations in two variables possess two families of characteristic lines (Ames, 1965; Courant and Friedrichs, 1948; Shapiro, 1953), which, for the stratified flow equation system in Equations (2.29) and (2.30), can be described by

$$\left(\frac{dy}{dx}\right)_{\pm} = \frac{|uv| \pm c\sqrt{q^2 - c^2}}{(u^2 - c^2)} \tag{2.82}$$

where c is the internal wave speed given by Equation (2.32), and where $\left(\frac{dy}{dx}\right)_+$ and $\left(\frac{dy}{dx}\right)_-$ are known as the positive and negative characteristic families, respectively. These characteristics represent the information boundaries for the problem, in that along each of these lines, the equations governing the flow properties can be reduced to ordinary differential equations, rather than the partial differential equations applicable in the general domain. Figure 2.13 shows the domain of dependence and region of influence of a point P situated in a supercritical flow field. The former is the region

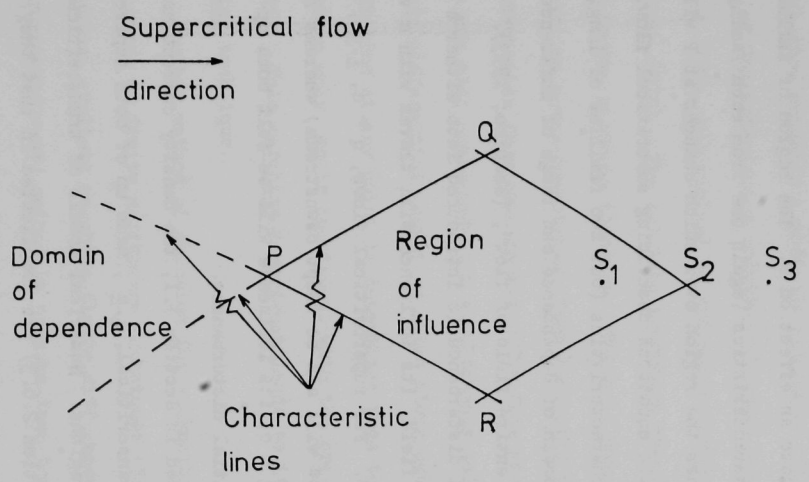

Figure 2-13 Regions of influence and dependence in supercritical flow

lying between the members of each family of characteristics, which intersect at P. It denotes the region within which a change in flow properties will have an effect on P. The region of influence of P is bounded by two characteristics (again one from each family) originating at P. This defines the region over which changes at P will be felt.

The elliptic equations describing subcritical flow, however, possess no real characteristics (but two families of imaginary ones) such that "the domain of dependence and range of influence for each point covers the entire field of flow", (Shapiro, 1953).

If a small disturbance is introduced into either a super- or subcritical flow field, its influence will travel with a velocity c (Equation 2.32). For supercritical flows, $q > c$, i.e., information of the disturbance will all be swept downstream, whereas for subcritical flows, $q < c$, its influence will be felt both up- and downstream of the initial disturbances.

As discussed in Section 1.1, the density current under consideration is transcritical, i.e., made up of both supercritical and subcritical regions. Numerical models of transcritical flows (discussed in Section 2.6.3) are complicated in that they must describe the flow properties in each region. Purely supercritical flows are much more simply and inexpensively modeled, thus whenever possible a purely supercritical scheme will be used. Available supercritical schemes are discussed in Section 2.6.2.

2.6.2 Numerical Techniques for Supercritical Flow

The existence of the two characteristic families in supercritical flow suggests a possible method of solution known as the Method of Characteristics solution (Courant and Friedrichs, 1948; Owczarek, 1964, and applied to hydraulic problems, Mahmood and Yevjevich, 1975). The solution procedure starts with the known values on the upstream boundary. The grid points are determined as the solution moves downstream, from the point of intersection of characteristics from each family. The flow properties at these points are also evaluated by a simultaneous solution of the ordinary differential equations valid along each streamline. Thus the solution at any point is determined from the upstream flow conditions only, as is consistent with the previous physical analysis. This marching downstream leads to its description as a marching technique.

Another method of solution for a hyperbolic equation system is by means of finite difference techniques (Roache, 1976). In particular, explicit marching finite difference techniques are a more straightforward method to program than the Method of Characteristics, the grid being definable in advance, and the flow properties at downstream points being simply evaluated from those preceeding them. However, care must be taken in the choice of a step size, such that the new point, S does not lie outside the zone of influence of its predecessors, as would S_3 in Figure 2.13, as opposed to S_1 and S_2. In the case of S_3, one is attempting to determine conditions

without knowing certain data essential for those conditions and an instability would result. This requirement is stated in the C-F-L (Courant, Friedrichs and Lewy) condition for stability, and is discussed in some detail in various texts such as Ames (1965), and applied to hydraulic cases in Mahmood and Yevjevich (1975). Thus the downstream step size must be small enough to satisfy the stability bound but large enough to finish the computations without excessive computation time. An estimate of this bound is obtained from consideration of the Method of Characteristics, an approach followed by Kutler and Lomax (1971) and Kutler, Warming and Lomax (1973). The point S is chosen such that its upstream positive characteristic passes between Q and R, and its negative characteristic between P and Q, thus ensuring that the domain of dependence of S contains no unknown information. A typical condition for Figure 2-14 would be

$$\frac{\Delta y}{\Delta x} \geq \left| \left(\frac{dy}{dx}\right)_{\pm} \right| \tag{2.83}$$

where Δy and Δx are the grid sizes as shown in Figure 2-14 and $\left(\frac{dy}{dx}\right)_{\pm}$ are the slopes of the families of characteristics as given in Equation (2.82).

Explicit stepping techniques are easier to program than characteristic methods (Mahmood and Yevjevich, 1975). Many explicit finite difference stepping techniques are available, with two-step Lax-Wendroff methods being "currently the most popular

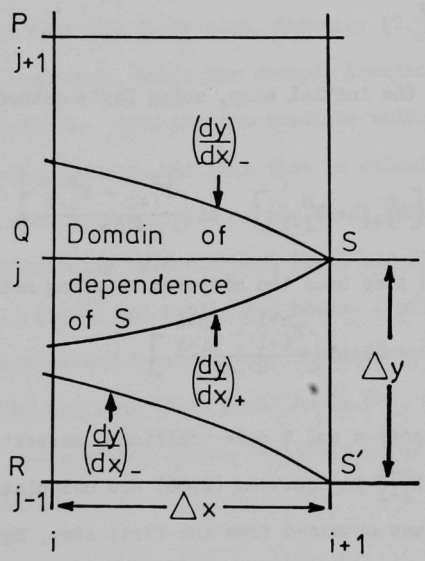

Figure 2-14 The appropriate explicit finite difference step size for a given characteristic slope

methods for solving compressible flow problems" (Roache, 1976). Section 2.3 has shown that certain types of compressible flow problems are analogous to the density current flows under consideration, thus these methods will be discussed more fully.

The basic two-step Lax-Wendroff method was suggested by Richtmyer (1963). Applied to the equation

$$\frac{\partial U}{\partial t} = - \frac{\partial F}{\partial x} \tag{2.84}$$

for simplicity, the initial step, using Lax's method, can be shown to be

$$U_i^{n+1} = \frac{1}{2}\left[U_{i+1}^n + U_{i-1}^n \right] - \Delta t \left[\frac{F_{i+1}^n - F_{i-1}^n}{2 \Delta x} \right] \tag{2.85}$$

while the second step uses the midpoint leapfrog method, as

$$U_i^{n+2} = U_i^n - (2\Delta t) \left[\frac{F_{i+1}^{n+1} - F_{i-1}^{n+1}}{2 \Delta x} \right] \tag{2.86}$$

where i and n denote x and t node positions, respectively. The values F_{i+1}^{n+1} and F_{i-1}^{n+1} in Equation (2.86) are calculated from the intermediate values obtained from the first step, Equation (2.85). These intermediate values have no physical significance, this only being attached to results of the second step. Thus the two steps may be thought of as a predictor-corrector couplet, with physical significance only attached to the corrected values.

Another type of two-step Lax-Wendroff method, was suggested by MacCormack (1969, 1971). Applied to Equation (2.84) for a

comparison with the basic method, Equations (2.85) and (2.86), this scheme can be written as

$$UB_i^{n+1} = U_i^n - \Delta t \left[\frac{F_{i+1}^n - F_i^n}{\Delta x} \right] \tag{2.87}$$

$$U_i^{n+1} = \frac{1}{2} \left\{ U_i^n + UB_i^{n+1} - \Delta t \left[\frac{FB_i^{n+1} - FB_{i-1}^{n+1}}{\Delta x} \right] \right\} \tag{2.88}$$

It can be seen that the first step, Equation (2.87) uses a forward differencing technique, while the second, Equation (2.88) uses a backward difference. Here the intermediate value, UB_i^{n+1} again has no physical significance, but this time is calculated as a provisional value at the same grid position as the final step. This method has been used successfully by MacCormack (1969 and 1971); Kutler, (1969), Lomax, et al., (1970) and Kutler and Lomax, (1971).

The dissipation introduced by the MacCormack scheme can be investigated by applying it to Equation (2.84), with F = U = u for simplicity. The combined steps, Equations (2.87) and (2.88) then give the relation

$$\frac{u_i^{n+1} - u_i^n}{\Delta t} = - \frac{1}{2\Delta x} (u_{i+1}^n - u_{i-1}^n) + \frac{1}{2} \frac{\Delta t}{(\Delta x)^2} (u_{i+1}^n - 2u_i^n + u_{i-1}^n) \tag{2.89}$$

This can be rewritten as

$$\frac{\partial u}{\partial t} + \frac{\partial u}{\partial x} = \underbrace{\frac{\Delta t^2}{6}\left(1 - \frac{\Delta x^2}{\Delta t^2}\right)\frac{\partial^3 u}{\partial x^3}}_{\text{dissipation term}} \tag{2.90}$$

It can be seen that the dissipation term introduced by the scheme is of second order.

The method of characteristics, being an exact technique, however, introduces no dissipative terms.

An additional finite difference technique is available for hyperbolic equations-using implicit methods. These have the advantage over explicit techniques of not being limited by the CFL condition. As opposed to explicit techniques which solve for <u>one</u> downstream point at a time, in terms of known upstream points, implicit schemes solve for a <u>group</u> of downstream points using simultaneous equations including the unknowns at all points in the group.

Roache (1976) mentions that some implicit methods have been applied to compressible fluid flows, such as Gourlay and Mitchell (1966a and b) who developed a two-dimensional unconditionally stable scheme. However, it had not been applied to nonlinear problems or been proven for an actual fluid dynamics problem. Roache (1976) felt that until the adaptation of these techniques to compressible flow problems were more advanced, the proven explicit methods were preferable.

A more recent investigation of explicit and implicit methods for compressible flow problems is given in Caughey (1980). He

points out that implicit schemes are to be preferred, where as large a step size as possible is required for the solution, i.e., if the step size limitation (CFL condition) associated with explicit schemes is unacceptable. Briley and McDonald (1975) and Beam and Warming (1976), have developed implicit schemes (known as block alternating direction implicit - ADI - schemes) useful under these conditions. However, Caughey (1980) again concludes that for cases where a large step size is not a major requirement, explicit schemes, such as those discussed previously, are to be preferred, being much easier to program.

2.6.3 Numerical Techniques for Transcritical Flow

Any numerical scheme employed to model transcritical flows should be able to model each equation type, elliptic and hyperbolic, appropriately, i.e., be type-dependent. In addition, the continuous transition from subcritical to supercritical flow, and discontinuous transition from supercritical to subcritical flows, both of which have been discussed in Section 2.2 must be accounted for.

The main solution techniques for transcritical problems are the hodograph method and numerical techniques (finite difference and finite element).

2.6.3.1 The Hodograph Method

This involves a linearization of the full potential Equation (2.35), by transforming it into the velocity or hodograph plane

Ames (1965). The latter has (q,θ), the speed, q, and velocity angle, θ, as independent variables, whereas the independent variables in the physical (x,y) plane, now become the dependent variables.

If a streamfunction, ψ, is defined in terms of the physical mass fluxes, hu, and hv, as

$$hu = \frac{\partial\psi}{\partial y} \qquad hv = -\frac{\partial\psi}{\partial x} \tag{2.91}$$

then the linear hodograph equation, obtained from the nonlinear potential Equation (2.35), can be written as

$$\frac{\partial^2\psi}{\partial q^2} + \frac{1}{q}\left(1 + \frac{q^2}{c^2}\right)\frac{\partial\psi}{\partial q} + \frac{1}{q^2}\left(1 - \frac{q^2}{c^2}\right)\frac{\partial^2\psi}{\partial\theta^2} = 0 \tag{2.92}$$

as derived in Jirka and Jones (1978), following that of von Mises (1958) and von Karman (1940). Solutions of this equation can then be obtained by means of hypergeometric functions. However, singularities due to the hodograph transformation exist, known as limit lines and branch lines, occurring when the Jacobian of the transformation,

$$J = \frac{\partial(x,y)}{\partial(q,\theta)} \tag{2.93}$$

takes on zero and infinite values, respectively. The former occur near shocks, causing singularities in the physical plane, where none exist in the hodograph plane. The latter are associated with singularities in the hodograph plane, which in the physical plane are

characteristics, at all points of which, a line of constant speed, a line of constant direction, and a characteristic of the other family touch each other. Their properties are discussed in detail in Howarth (1953). The nature of the treatment of shocks (discontinuous solutions) discourages their use for the physical problem under consideration. In addition, difficulties in representing curved boundaries exist, as will be discussed in Section 5.2.

2.6.3.2 Numerical Finite Difference and Finite Element Techniques

A major problem for numerical finite differencing techniques when applied to the transcritical flow problem is the treatment of the flow discontinuities associated with shocks, for gas flows, and via the analogy discussed in Section 2.2, jumps in stratified fluid flows. The methods employed for this feature may be separated into two categories (Roache, 1976):

- shock patching methods
- shock-smearing or shock-capturing methods

Shock patching methods maintain the shock wave (jump) as a discontinuity, the values of the variables on either side being calculated using relations resulting from non-isentropic flow theory, such as the Rankine-Hugoniot relations in compressible gas flows, or the jump conditions in stratified fluid flows. The rest of the flow can be modeled using methods applicable to shock-free flows, of either super- or subsonic type.

Shock-smearing or shock-capturing methods allow the calculation to proceed without any special treatment of shocks/jumps which may develop. An artificial viscosity $\approx \Delta x$, the grid spacing, is required to smear the shock over several grid spacings.

Explicit artificial viscosities are generally introduced in the case of a strong shock. A term of the form $-\alpha_B \frac{\partial u}{\partial x}$ is added onto the pressure term in the momentum equation, where

$$\alpha_B \propto \alpha \left|\frac{\partial u}{\partial x}\right| \Delta x$$

in the region of a compression wave (shock/hydraulic jump) (Roache, 1976), but zero near a rarefaction wave (hydraulic drop). Thus the diffusion process is now driven by

$$\frac{\partial}{\partial x}\left(\frac{\partial u}{\partial x}\right)^2$$

instead of

$$\frac{\partial}{\partial x}\left|\frac{\partial u}{\partial x}\right|$$

causing dissipation over a shorter distance, and an artificially smeared out shock such that $\delta_s = 3$ to $5\ (\Delta x)$. Thus details in the region of the shock are lost while a correct jump in properties across it are maintained.

Implicit artificial viscosities are sufficient if only a weak shock is present, but problems involving strong shocks may require the addition of explicit viscosities if more damping is

required. Implicit damping can be introduced simply from the form of the difference equations, i.e., a nonzero coefficient of the second space derivative, or, as in the method of Courant, Isaacson and Reis (1952), by using an upwind differencing scheme in the supercritical region, where the effective "viscosity" is introduced through the truncation error in the one-sided scheme.

The shock capturing methods are preferred to the patching methods, since the latter require the position of the shock to be known beforehand, or the use of an iterative approach.

Finite difference techniques

A recent review article, Caughey (1982), summarizes previous and present work on transonic gas dynamics (which is analogous to stratified flow problems as shown in Section 2.2). It considers the problems of applying boundary conditions along curved boundaries, such as found in curved wings in aerodynamic applications, (or, analogously, curved frontal regions in stratified flow theory). This can be dealt with by adopting boundary-conforming co-ordinate systems. These can be obtained by applying conformal transformations to simple domains as in Jameson (1971 and 1974), or, if a suitably exact transformation cannot be found easily, by taking a good approximation and subsequently applying weak shearing transformations as applied to aerofoils in wind tunnels by Caughey and Jameson (1977a). Caughey (1982) points out that the tedious nature of analytical transformations of the full potential equation and also the lack of

analytical transformation derivates for numerically generated grids make the finite volume technique preferable, (Caughey and Jameson, 1977b and Caughey and Jameson, 1979). The finite volume technique comprises a local transformation within each mesh cell, evaluated numerically using the Cartesian coordinates of the corner points.

A method of accounting for the appropriate type of the potential equation in super- and subsonic flows past thin aerofoils was introduced by Murman and Cole (1971). They considered a simplified form of the potential equation, known as the small-disturbance equation, and given as

$$(K - (\gamma + 1)\phi_x)\phi_{xx} + \phi_{yy} = 0$$

where K is a similarity constant, dependent on M_∞, and the tendency of the disturbance to spread laterally. This simplified equation has the advantage of having characteristics locally symmetric around the x-direction, such that the hyperbolic region can be appropriately modeled by simply upwinding the differencing in the x-direction. They applied centered difference approximations in the subsonic region, to account for information flow both up- and downstream. However, in the supersonic region they added an artificial viscosity implicitly (proportional to the grid spacing Δx) by using an upwinded difference approximation for ϕ_{xx} in supersonic zones. A central difference approximation was used in subsonic regions, which allows a sharp representation of the shock. Thus a

type-dependent approximation to the small disturbance equation was obtained.

However, in the full potential equation, the upwind direction is not known in advance, being independent of the co-ordinate system. Jameson (1974) introduced a method of rotating the upwinding to lie in the streamwise direction, i.e., a 'rotational difference scheme'. This again involves adding artificial viscosities in a form to mimic an upwinded difference approximation, only now this was aligned with the local velocity direction.

A later refinement, introduced by Jameson and Caughey (1977b) and Caughey and Jameson (1979) was to add the finite volume representation to the scheme, and apply it to various wing and wing-fuselage geometries.

Thus, the scheme can now capture the shock, automatically difference the equations appropriately for their type, and account for curved boundary geometry.

Finite element techniques

A recent review article by Shen (1977) summarizes the application of finite element techniques to general fluid flows, while Chung (1978a) presented a state-of-the-art review of finite element applications to transonic flow or mixed-type equations. The former emphasizes the flexibility of the finite element method, in that the domain under consideration can be subdivided into irregularly shaped elements, thus accounting for curved boundaries

as long as they can be approximated by a number of linear segments.

When applied to supersonic flows, however, finite element techniques encounter difficulties, there being no "counterpart of the 5-point backward-difference formula in finite-difference schemes, which is unconditionally stable for computation in the supersonic zone" (Shen, 1977). When applied to regimes of mixed type, patched solutions are frequently used (Chen, 1976), with supersonic solutions patched onto subsonic finite element solutions.

Transonic flow techniques similar to those applied to finite difference schemes by Murman and Cole (1971), discussed previously, were applied by Chan et al. (1975). For supersonic elements they ignored the contribution from downstream nodes in order to represent the true physical situation and thence stabilize the scheme in supersonic regions.

Chung and Hooks (1976, 1977) and Chung (1978b) showed that the method of discontinuous functions enables the global finite element equations to find the location and intensity of shocks. Friedrichs (1958) showed how a symmetric positive definite system, as obtained by using the least squares approximation, gave a computational algorithm which was the same for both the elliptic and hyperbolic regions, being type-insensitive, while Chung (1978b) discussed this in connection with the full potential equation. In particular, Chung, in this article, shows how, in the full potential equation, the discontinuous functions can be used in the formation of the finite element matrices combining the shock boundaries. The

shock's position and intensity was found using an iterative numerical technique in which convergence was obtained by means of a scheme similar to artificial viscosity. This scheme was applied to a symmetric aerofoil.

More recent applications of finite element methods to transonic flow calculations have been made by Tatum (1982) and Bredif (1983). These again incorporated artificial viscosity terms in order to introduce the required upwind bias into the finite element formulation in the supersonic regions. The technique they used was the artificial compressibility method developed by Hafez et al. (1978). Thus, finite element methods were again used in both super- and subsonic regions, with an artificial viscosity concept automatically modeling the shock position and correct equation type.

CHAPTER 3

PHYSICAL CONCEPTS

This chapter considers the physical concepts involved in the investigation of the steady-state two-dimensional horizontal motion of a shallow density current emanating from a radial source in a moving stratified ocean. Although the mathematical framework developed herein, is for the general case of horizontally two-dimensional intrusions (see Chapter 1 for examples), it is applied, in this particular study, to discharges from ocean thermal energy conversion (OTEC) plants.

3.1 General OTEC-Ambient Ocean Schematization: Definition of Scales

The following basic schematization of the ambient ocean structure and its interaction with OTEC is adopted:

a) Velocity and Density Profiles

The general tropical or subtropical ocean exhibits nonuniform velocity and density (mainly temperature influenced) profiles. Density profiles for various locations are shown in Figure 3-1. Velocity and temperature profiles for a Gulf of Mexico example are shown in Figure 3-2. It can be seen that the density profile usually exhibits a pycnocline zone, i.e., a region of strongest density variation, which often lies between 50 and 150 m depth as shown in Figure 3-1. It is in this zone that the intermediate field density

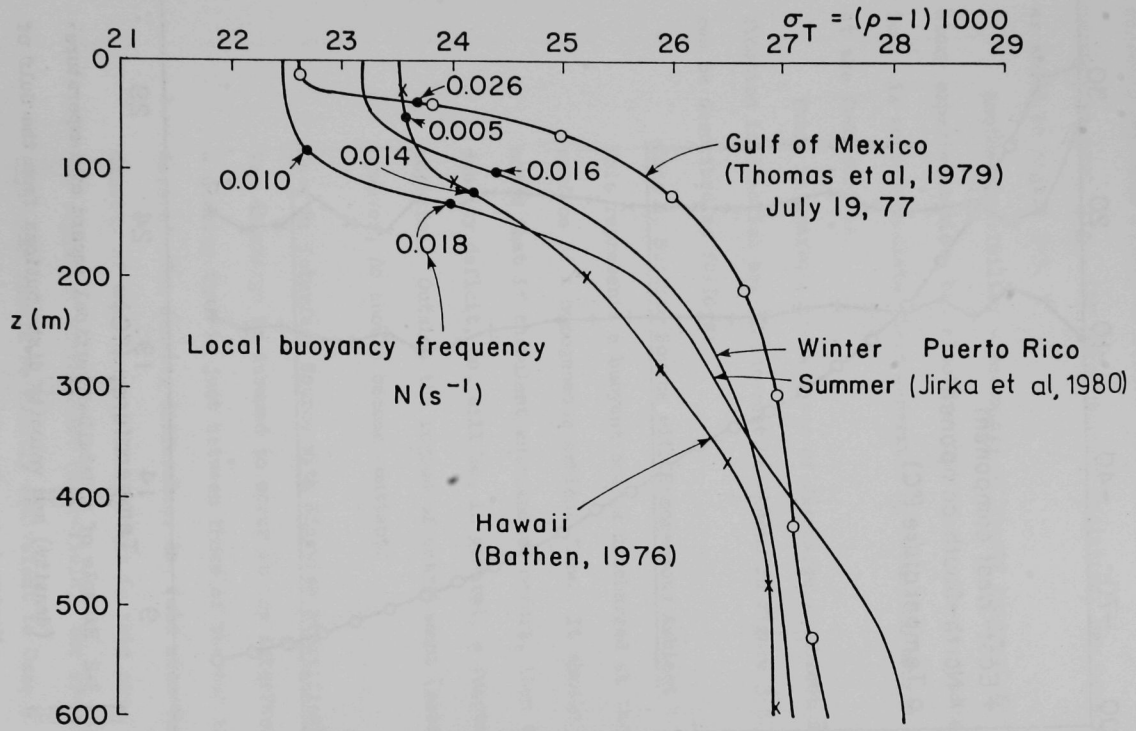

Figure 3-1 Typical σ_T profiles and values of Brunt-Vaisala frequency, N, for tropical and sub-tropical oceans

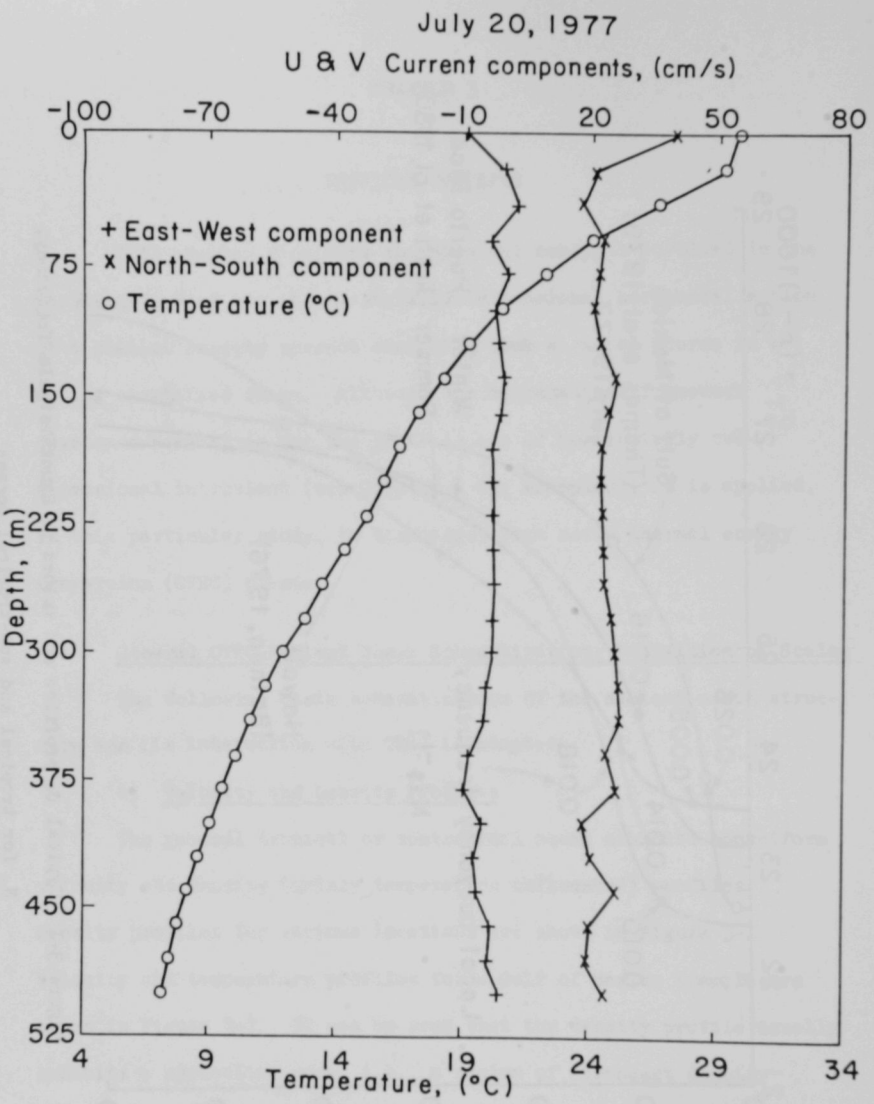

Figure 3-2 Example of a detailed vertical record of temperature (density) and velocity distributions from the Gulf of Mexico (after Thomas et al., 1979)

currents are most likely to occur. The essential feature of the pycnocline zone, i.e., its sharp density variation, may be schematized as shown in Figure 3-3.

Another possibility - certainly of strong interest for laboratory experimentation, but also for OTEC discharges as discussed below - is an intermediate field generated by a buoyant source directly at the free surface.

Thus, in general, three cases of discharge - ambient stratification interaction are of interest, as shown in Figure 3-3. These can be described as follows:

Case A: Surface Source with Homogeneous Ambient

This represents a buoyant source discharged at the free surface of a homogeneous ambient flow. It should be noted that if turbulent entrainment occurs, then the density deficit, $\Delta\rho$, will be, in general, a function of position. Outside the region of entrainment (near-field), however, $\Delta\rho$ should become constant.

Case B: Interface Source with Stepwise Stratification

The discharge is assumed to occur at the interface, with a density that is just between those of the two individual layers. The density difference, $\Delta\rho$, (and also the actual density of the current) is constant in this case. Outside the region of entrainment (near-field), the dynamics for this case should be exactly equivalent to Case A.

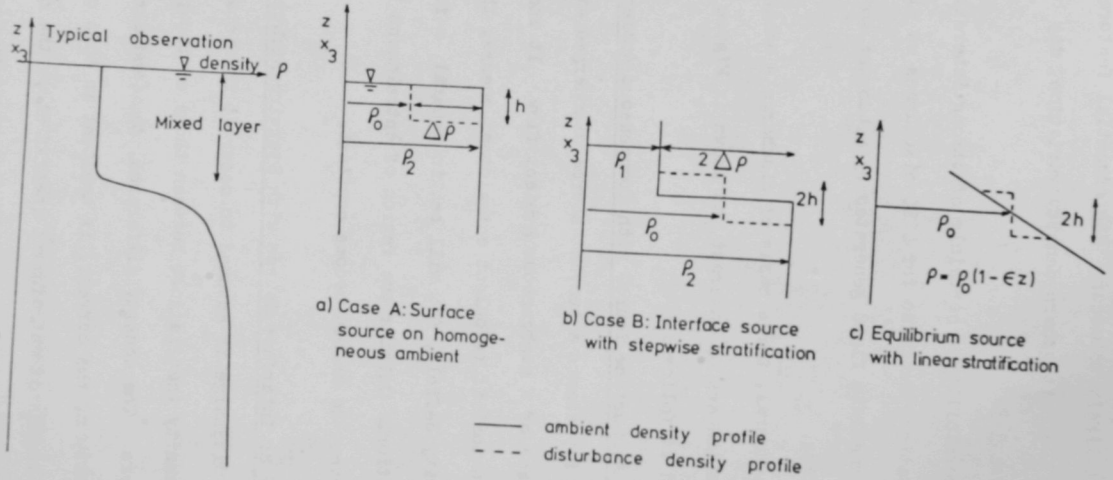

Figure 3-3 Local schematizations of the ocean density structure in regions of the intermediate field layer.

Case C: Equilibrium Source with Linear Stratification

The discharge is assumed to occur at its equilibrium level, (equal density level, i.e., $\rho_o = \rho_a(z)$) within the linear stratification profile. In this case, as in Case B, the actual current density, ρ_o, will remain constant both within and without the region of entrainment (near-field).

It should be noted that Case A may also be an acceptable approximation for an interface discharge. If the discharge density, ρ_o, is much closer to that of one layer, say ρ_2, so that $(\rho_2 - \rho_o) << (\rho_2 - \rho_1)$, then the discharge will behave as if the interface were a rigid lid, similar to the surface in Case A. This can be understood by examining the local Richardson number, R_i of the current (Equation 2.76), with respect to either of the two adjacent layers. A small density difference, say $(\rho_2 - \rho_o)$ in this case leads to small Richardson numbers and hence likely instabilities, as discussed in Section 2.4. However, large density differences, say $(\rho_1 - \rho_o)$, lead to large R_i values and stable conditions without entrainment from that layer. (An application of this type has been discussed by Jirka et al., 1981). Thus, under such conditions Case A is qualitatively similar to an interface situation, and is also more easily obtained experimentally - enabling verification of theoretical predictions. Therefore, although the equation set is derived for all cases, the actual solutions in later chapters will be confined to Cases A and B.

b) Unsteadiness

Long term temperature and velocity variations in the thermocline do occur as illustrated in Figure 3-4. A (volumetric) time scale representing the OTEC discharge adjustment time for unsteady conditions is

$$T_i = \left(\frac{Q}{u_a^3}\right)^{1/2} .$$

Using the values given in Section 3.1.1 gives $T_i \approx 15$ mns. Thermocline variations of shorter time scale than this will not affect the final density current position, while those of longer time scale will blend into the ambient background. Figure 3-4 shows that the major variations are over about 12 hours, although much shorter and longer time variations also occur. Thus the reasonable assumption of steady ambient current conditions are considered in general, although the stagnant case is analyzed for the near field.

Sudden stepwise current changes (equivalent to discharge changes) were considered experimentally in Jirka et al. (1980)

c) Shallow density current

This assumes that the ambient ocean motion is very little affected by the presence of a shallow intermediate field current and is, to a first order, unperturbed. This will be discussed further in Section 3.3. Thus, referring to Figure 3-3, the discharge current layer depths, h, are smaller than the ambient vertical domain (e.g., mixed layer depth).

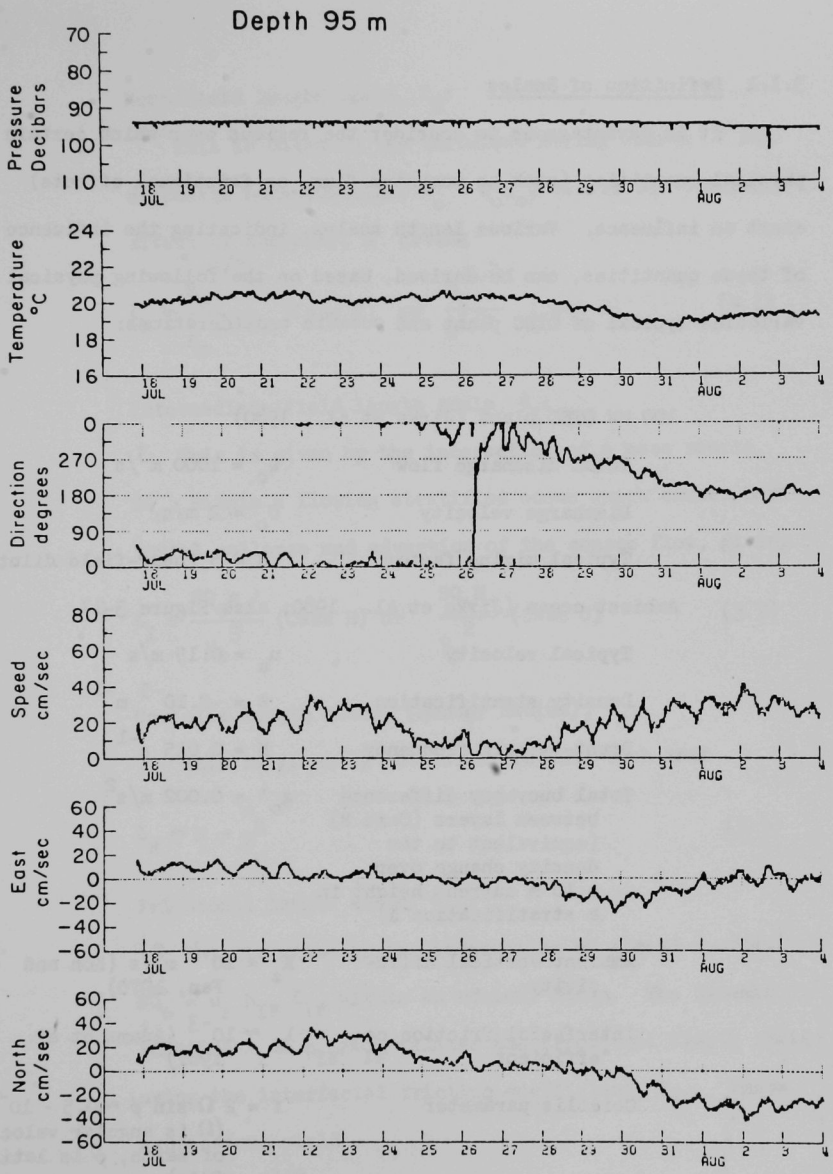

Figure 3-4 Example of a longterm record of temperature and density within the thermocline of the Gulf of Mexico (after Thomas et al.,1979)

3.1.1 Definition of Scales

It is advantageous to consider the regions over which certain physical quantities (such as momentum flux or frictional effects) exert an influence. Various length scales, indicating the influence of these quantities, can be derived, based on the following physical variables typical of OTEC plant and oceanic considerations:

100 MW OTEC plant (Jirka et al., 1980)

Total discharge flow	$Q_o = 1000\ m^3/s$
Discharge velocity	$U_o = 2\ m/s$
Typical mixing factor	$S = 5$ (near-field dilution)

Ambient ocean (Jirka et al., 1980; also Figure 3-1)

Typical velocity	$u_a = 0.15\ m/s$
Density stratification	$\epsilon = -2.10^{-5}\ m^{-1}$
Brunt-Vaisala frequency	$N = 0.015\ s^{-1}$
Total buoyancy difference between layers (Case B) (equivalent to the density change over a 10 m current height in a stratification N)	$g_o' = 0.002\ m/s^2$
Ambient vertical diffusivity	$K_z = 10^{-4}\ m^2/s$ (Koh and Fan, 1970)
Interfacial friction coefficient	$\lambda_i \approx 10^{-3}$ (Adams et al., 1981)
Coriolis parameter	$f = 2\,\Omega \sin\phi \approx 0.5 \cdot 10^{-4}/s$ (Ω is angular velocity of earth, ϕ is latitude).

Length scales, based on dimensional analysis and simple physical reasoning, can now be defined as:

Near-field length scale, ℓ_N:

This is based on the turbulent mixing action of the discharge momentum flux, $M_o = Q_o U_o$, versus the stability effect of buoyancy, N giving

$$\ell_N \approx \frac{M_o^{1/3}}{g_o'^{1/3}} \text{ (Case B) or } \frac{M_o^{1/4}}{N^{1/2}} \text{ (Case C)} \qquad (3.1)$$

Intermediate-field length scale, ℓ_I:

This is given by the interaction of a mass source, SQ_o, within a flowing stratified ocean which causes horizontal collapse and advection of the source flow, giving

$$\ell_I \approx \frac{SQ_o g_o'}{u_a^3} \text{ (Case B) or } \frac{SQ_o N}{u_a^2} \text{ (Case C)} \qquad (3.2)$$

Coriolis length scale, (Rossby Radius), ℓ_R:

This is given by the Rossby radius, such that

$$\ell_R \approx R = \frac{u_a}{f_o} \qquad (3.3)$$

Frictional length scale, ℓ_{IF}:

This is given by the interaction of a mass source, $SQ_o = u_a h_{IF} \ell_{IF}$ within an ambient ocean. The dynamic relation $\lambda_i = h_{IF}/\ell_{IF}$ relates the frictional length scales using the interfacial friction coefficient, λ_i. These expressions yield

$$\ell_{IF} = \left(\frac{SQ_o}{\lambda_i u_a}\right)^{1/2} \qquad (3.4a)$$

as a frictional length scale. It should be noted that Equation (3.4a) can be rearranged to

$$\ell_{IF} = \frac{\ell_I}{(\lambda_i V')^{1/2}} \tag{3.4b}$$

where $(\lambda_i V')^{1/2}$ is a parameter discussed in Section 2.1 as a measure of the importance of the frictional effect, V' being a parameter discussed more fully in Section 3.5.

Far-field length scale, ℓ_F:

This is given by the action of ambient diffusion over a vertical disturbance height H^* (caused by the near and intermediate field processes and $\approx$ 10 m (Jirka et al., 1980) versus the simultaneous ambient advection

$$\ell_F \approx u_a \frac{H^{*2}}{K_z} \tag{3.5}$$

Using the values of the physical quantities given previously, typical length scale magnitudes are as shown in Table 3-1. Although these are only typical values (for example, Section 3.6 discusses cases when the near- and intermediate-field length scales are of the same order), they still serve as an indication that the density current may be modeled as subsequent flow regimes of increasing length scale:

(1) <u>Near Field Region (Section 3.4):</u>

This has a horizontal extent of order ℓ_N (100 m). Supercritical velocities are expected, due to plant discharge criteria, as discussed

Table 3-1: Length scale values (in km) for typical OTEC and oceanic conditions

	Stratification Case B	Stratification Case C
ℓ_N	O(0.1)	O(0.1)
ℓ_I	O(1)	O(1)
ℓ_R	O(10)	O(10)
ℓ_{IF}	O(10)	O(10)
ℓ_F	O(100)	O(100)

further in Section 3.3. The importance of the destabilizing momentum flux in this region compared with the stabilizing buoyancy leads to low Richardson numbers, and entraining flow, as discussed in Section 2.4.

(2) Intermediate Field Region (Section 3.5)

The intermediate field region is modeled as stable non-entraining flow.

a) The transcritical flow region is made up of super- and subcritical flow regions, separated by internal hydraulic jumps and critical lines, (Section 2.2). These phenomena occur in the region of the intermediate field closest to the source, where frictional effects are unlikely to be important. Thus it can be assumed a region where the flow is convectively controlled.

b) The supercritical flow region occurs after the transcritical flow region and extends downstream until the diffusive effects of the far field become dominant. Frictional effects become increasingly important in this region.

(3) Far Field Region

The ambient stratified ocean is characterized by weak (and often patchy) turbulence. This ambient diffusion (as indicated by the ℓ_F values in Table 3-1) assumes importance at large distances from the source, leading to a gradual diffusion of the mass and heat contained in the density current.

It should be noted that the Coriolis length scale, ℓ_R, is shown in Table 3-1 to be about an order of magnitude greater than

the intermediate field length scale, ℓ_I, i.e., the Coriolis influence may be felt several intermediate field length scales downstream. However, even then its effect would be global, i.e., it would affect the entire ocean current structure rather than only the internal hydrodynamics of the density current.

3.2 Governing Equations

The basic equations linking the spatial variations of velocity u_j, $j = 1, 2, 3$, density, ρ, pressure, p and temperature T, within a fluid in steady-state, may be represented using tensor notation, as

Mass Continuity $$\frac{\partial u_j}{\partial x_j} = 0 \tag{3.6}$$

Momentum $$\underbrace{\frac{\partial}{\partial x_j}(u_i u_j)}_{\text{convective acceleration}} = \underbrace{-\frac{1}{\rho}\frac{\partial p}{\partial x_i}}_{\text{pressure force}} \underbrace{- g\delta_{3i}}_{\text{gravitational force}} \underbrace{+ \frac{1}{\rho}\frac{\partial \tau_{ij}}{\partial x_j}}_{\text{turbulent shear stress}}$$

$$\underbrace{- \epsilon_{jki}\,\Omega_j\, u_K}_{\text{Coriolis acceleration}} \tag{3.7}$$

Scalar Conservation $$\underbrace{\frac{\partial}{\partial x_j}(u_j T)}_{\text{convective transport}} = \underbrace{-\frac{\partial}{\partial x_j}(q_{hj})}_{\text{turbulent scalar transport}} \tag{3.8}$$

Linearized equation of State $$\frac{\partial \rho}{\partial T} + a = 0 \tag{3.9}$$

for i, j, k = 1, 2, 3, with a Cartesian coordinate system, x_3 pointing upwards against the action of gravity. Ω_j is the angular velocity vector of the earth, $\tau_{ij}(= \overline{u_i'u_j'})$ and $q_{hj}(= \overline{u_j'T'})$ are the turbulent shear stress and turbulent transport tensors, respectively, where u_i' and T' represent velocity and temperature fluctuations, the overbar denoting averaging over a time scale greater than the fluctuating time scale, δ_{ij} is the Kronecker delta, ϵ_{ijk} is the alternating tensor, (the Einstein summation convention being used) and a is the thermal expansion coefficient.

Incorporated into these equations are the assumptions of incompressibility and neglect of both diffusion and shear molecular transport terms. The Boussinesq assumption is adopted, requiring that the actual density variations are small relative to the reference state apart from the pressure term.

Further assumptions include:

The density can be written as $\rho(x_3) = \rho_a(x_3) + \rho^*(x_3)$, where $\rho_a(x_3)$ is the ambient value and $\rho^*(x_3)$ is a small dynamic perturbation, which can be written as $\rho^*(x_3) = aT^*(x_3)$ using the linearized equation of state, thus incorporating this into the other equations.

The adoption of a hydrostatic vertical momentum equation, requiring that vertical accelerations, gradients of dynamic pressure, rate of change of turbulence and the vertical Coriolis force, are second order terms.

The equation set, incorporating the above assumptions is:

$$\frac{\partial u_j}{\partial x_j} = 0. \tag{3.10}$$

$$\frac{\partial}{\partial x_j}(u_i u_j) = -\frac{g}{\rho_o x_3}\frac{\partial}{\partial x_i}\int_{x_3=-\infty}^{x_3} \rho^*(x_3)dx_3$$

$$-\frac{1}{\rho}\frac{\partial}{\partial x_j}\tau_{ij} - \epsilon_{jki}\,\Omega_j u_K \tag{3.11}$$

$$\frac{\partial p^*}{\partial x_3} = -\rho^* g \tag{3.12}$$

$$\frac{\partial}{\partial x_j}(u_j T) = -\frac{\partial}{\partial x_j}(q_{hj}) \tag{3.13}$$

$$i,j = 1,2; \quad k = 1,2,3$$

where the pressure term in the horizontal momentum equation has been obtained from the vertical momentum Equation (3.12). p^* now indicates the hydrostatic pressure deviation.

It should be noted at this point that the horizontal exchange terms (both horizontal shear stress and diffusivity, these being related via the Reynolds analogy) are negligible compared with other terms in the equations, and will be neglected hereafter. In addition, based on the scaling arguments in Section 3.1, the Coriolis term will also be neglected from this point.

The equations can now be integrated vertically over the region

of the density current, i.e., $h_1(x_1,x_2) < x_3 < h_2(x_1,x_2)$, where h_1 and h_2 define the "interfaces" of the current as shown in Figure 3-5. The assumption of constant vertical velocity (top-hat) profiles is made for this integration. (Note, if non-constant values were assumed, profile dependent constants would appear in the integrated equations, these constants having values somewhat different from unity.)

Also incorporated into the equations at this point are turbulence closure approximations and boundary conditions along the interfaces $x_3 = h_k$, $(k = 1,2)$. These are given as:

1) Kinematic Condition:

$$u_1 \frac{\partial h_k}{\partial x_1} + u_2 \frac{\partial h_k}{\partial x_2} - u_3 = - w_{ek} \text{ at } x_3 = h_k \tag{3.14}$$

where w_{ek} is the net velocity across the interface, i.e., a turbulent entrainment velocity. For Case A stratification, $w_{ek} = 0$ at $x_3 = 0$, its upper boundary.

2) Dynamic Conditions:

a) $p^* = 0$ at $x_3 = h_k$ (3.15)

b) $$\tau_{i3} = \tau^i = \pm \rho\lambda_i(u_{ai} - u_i)\left[(u_{ai} - u_i)(u_{ai} - u_i)\right]^{1/2}$$

$$\text{at } x_3 = h_k \tag{3.16}$$

where u_{ai} is the ambient velocity so that $(u_{ai} - u_i)$ is the velocity difference across the interface. This is a generalization of the interfacial shear equation and has been suggested in this form by Dronkers (1969) in order

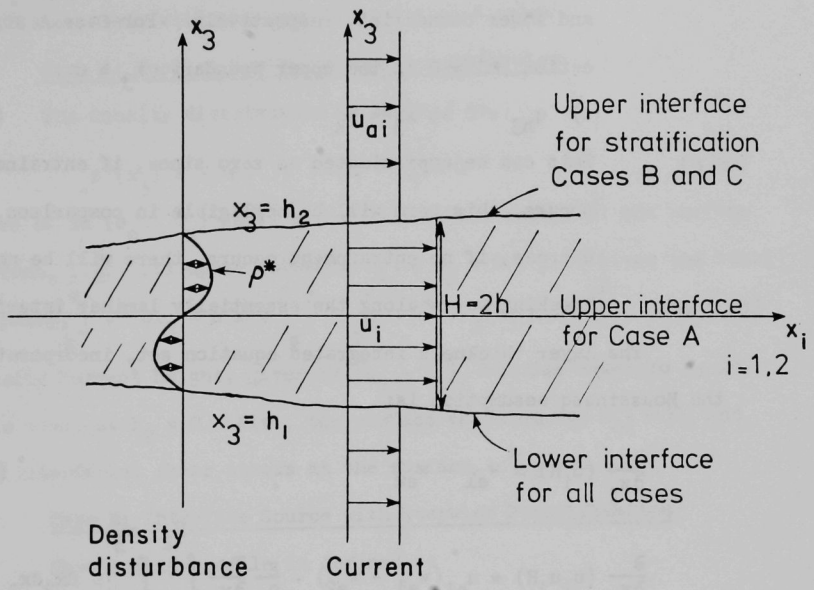

Figure 3-5 Intermediate field flow and density structure

to provide the correct total energy dissipation in the flow: the positive and negative signs refer to the upper and lower boundaries, respectively. For Case A stratification, $\tau^i = 0$ at the upper boundary, $x_3 = 0$.

c) $q_{h3} = 0$ at $x_3 = h_k$ (3.12)

This can be approximated as zero since, if entrainment occurs, this term will be negligible in comparison, whereas, if no entrainment occurs, there will be no breaking waves along the essentially laminar interface.

The layer thickness integrated equation set, incorporating the Boussinesq assumption is:

$$\frac{\partial}{\partial x_j}(u_i H) = w_{e1} - w_{e2} \tag{3.17}$$

$$\frac{\partial}{\partial x_j}(u_i u_j H) = u_{ai}(w_{e1} - w_{e2}) - \frac{g}{\rho_o}\frac{\partial}{\partial x_i}\int_{h_1}^{h_2}\int_{h_1}^{x_3} \rho^* dx_3 dx_3 + \frac{g}{\rho_o}\int_{h_1}^{h_2} \rho^* dx_3 \frac{\partial h_2}{\partial x_i} + \frac{1}{\rho_o}\left(\tau^i\big|_2 - \tau^i\big|_1\right) \tag{3.18}$$

$$\frac{1}{a}\frac{\partial}{\partial x_j}\left(u_j \int_{h_1}^{h_2} \rho^* dx_3\right) = 0 \tag{3.19}$$

where the terms $(w_{e1} - w_{e2})$ and $u_{ai}(w_{e1} - w_{e2})$ represent the entrainment of outside fluid mass and momentum, respectively into the internal flow. The pressure integrals in these equations have to be evaluated for the various stratification cases (A, B and C).

In the following, the definition sketch in Figure 3-5 is referred to and symmetry of the current around the $x_3 = 0$ axis, i.e., $h = h_2 = h_1$, is assumed (with the exception of Case A below).

Case A: Surface Source on Homogeneous Ambient

The density distribution is defined as

$$\rho^*(x_3) = -\Delta\rho \qquad -h < x_3 < 0 \tag{3.20}$$

where $\Delta\rho$ is $(\rho_o - \rho_a)$ and $-h < x_3 < 0$ is the extent of the surface current, i.e., its upper boundary is at $x_3 = 0$. This gives the total buoyancy, $\int_{-h}^{o} \rho^* \, dx_3 = h$ and $\int_{-h}^{o} \int_{-h}^{x_3} \rho^* \, dx_3 dx_3 = \Delta\rho \frac{h^2}{2}$. The total density current height, given by $(h_2 - h_1)$, becomes equal to h, in this case, as $h_2 = 0$. Also, the surface entrainment, $w_{e2} = 0$, and the interfacial shear stress at the surface, $\tau^i|_2 = 0$.

Case B: Interface Source with Stepwise Stratification

The density profile is defined as

$$\rho^*(x_3) = \begin{cases} +\Delta\rho & 0 < x_3 < h \\ -\Delta\rho & -h < x_3 < 0 \end{cases} \tag{3.21}$$

where $\Delta\rho = (\rho_2 - \rho_1)/2$, i.e., half the total density difference between the layers. The total buoyancy, $\int_{-h}^{h} \rho^*(x_3) dx_3$ is zero, as expected for a neutrally buoyant jet. The integral from the pressure term $\int_{-h}^{h} \int_{-h}^{x_3} \rho^* dx_3 dx_3$ becomes $\Delta\rho h^2$. In this case, symmetry assumptions are made for the interfacial friction and entrainment terms, such that $\tau^i|_2 = \tau^i|_1 = \tau^i$ and $w_{e2} = -w_{e1} = -w_e$, respectively.

Case C: Interface Source with Linear Stratification

The density profile is defined as:

$$\rho^*(x_3) = \rho_o \, \epsilon \, x_3 \tag{3.22}$$

where $\epsilon = -\frac{1}{\rho_o}\frac{d\rho}{dx_3} = \frac{N^2}{g}$ is the density gradient and N is the Brunt Vaisala frequency of the system. Again the total buoyancy is zero, but the pressure integral becomes $\frac{2}{3}\rho_o \, \epsilon \, h^3$. Symmetry assumptions for the interfacial friction and entrainment terms are made as for Case B.

The equation set can now be written as:

$$\frac{\partial}{\partial x_j}(u_j h) = w_e \tag{3.23}$$

$$\frac{\partial}{\partial x_i}(u_i u_j h) = w_e \, u_{ai} - \sigma h \frac{\partial h^{s+1}}{\partial x_i} + \frac{\tau^i}{\rho_o} \tag{3.24}$$

$$\frac{\partial}{\partial x_j}(u_j \, g' \, h) = 0 \qquad \text{(Case A only)} \tag{3.25}$$

$$\sigma = \text{constant} \qquad \text{(Cases B and C)} \tag{3.26}$$

where the stratification parameters, s and σ are defined as:

Case A, B. $\sigma = g'$; $s = 0$ (3.27)

Case C. $\sigma = \frac{1}{2}\epsilon g = \frac{1}{2}N^2$; $s = 1$ (3.28)

It should be noted that Equation (3.26) results from an intermediate step of $\frac{d}{dx_j}\left[u_j(\sigma x_3^{s+1}|_h + (-1)^s \sigma x_3^{s+1}|_{-h})\right] = 0$. As u_j and h are both arbitrary, this necessitates the relation σ = constant. The equation set will now be divided into the separate regions discussed in Section 3.1.

1. Near-Field Region (Entraining Regime)

The equations for entraining stratified flow are: (i,j=1,2)

$$\frac{\partial}{\partial x_j}(u_j h) = w_e \tag{3.29}$$

$$\frac{\partial}{\partial x_i}(u_i u_j h) = w_e\, u_{ai} - \sigma h \frac{\partial h^{s+1}}{\partial x_i} \tag{3.30}$$

$$\frac{\partial}{\partial x_j}(u_j g' h) = 0 \text{ (Case A)} \tag{3.31}$$

$$\sigma = \text{const} \quad \text{(Cases B and C)} \tag{3.32}$$

These equations are applicable in the vicinity of the source where interfacial friction is less important. In general, entrainment will occur in the near field as discussed in Sections 2.4, 3.1, and 3.3.

2. Intermediate Field Region

a) Transcritical Flow Region (Convective Regime)

The equations for non-entraining stratified flow are: (i,j=1,2)

$$\frac{\partial}{\partial x_i}(u_j h) = 0 \tag{3.33}$$

$$\frac{\partial}{\partial x_i}(u_i u_j h) = -\sigma h \frac{\partial h^{s+1}}{\partial x_i} \tag{3.34}$$

$$\frac{\partial}{\partial x_j}(u_j g' h) = 0 \text{ (Case A)} \tag{3.35}$$

$$\sigma = \text{const.} \quad \text{(Cases B and C)} \tag{3.36}$$

b) Supercritical Region (Convective and Frictional Regimes)

The equation set becomes: (i,j=1,2)

$$\frac{\partial}{\partial x_j}(u_j h) = 0 \tag{3.37}$$

$$\frac{\partial}{\partial x_i}(u_i u_j h) = -\sigma h \frac{\partial h^{s+1}}{\partial x_j} + \frac{\tau_o^i}{\rho_o} \tag{3.38}$$

$$\frac{\partial}{\partial x_j}(u_j g' h) = 0 \qquad \text{(Case A)} \tag{3.39}$$

$$\sigma = \text{constant (Cases B and C)} \tag{3.40}$$

3.3 General Boundary Conditions

3.3.1 Ambient Fluid

The outside fluid is assumed unperturbed apart from a narrow region bounding the density current. The ambient velocity field is thus given by

$$u_{ai} = \text{const}, \qquad i = 1,2 \tag{3.41}$$

This assumption requires that the thickness of the density current, h, be much smaller than the typical vertical dimension of the ambient fluid layer, H. In oceanic conditions, typical values are $h \approx 10$ m and $H \approx 100$ m. However, this condition is occasionally difficult to achieve experimentally, h sometimes approaching a significant fraction ($\frac{1}{2}$) of H. Drag effects likely to occur under these conditions can be dealt with as described in Section 2.1.

In a narrow region of the ambient flow along the front of the

density current, significant local vertical accelerations are assumed to occur, thus violating the hydrostatic pressure conditions applicable throughout the remaining ambient flow. Generalizing to two-dimensions Benjamin's (1968) one-dimensional analysis of this pressure deviation (discussed in Section 2.1), by taking the component of the ambient velocity normal to the boundary ($u_a \sin \theta$) rather than u_a, results in a form drag F_D, normal to the front. The expression for F_D is given as

$$F_D = C_D \rho_a \frac{(u_a \sin \theta)^2}{2} h_B \tag{3.42}$$

where h_B = half thickness along the front, ρ_a = ambient density, θ = local front angle and C_D = drag coefficient. This drag force acts as an arresting mechanism for the density current.

3.3.2 Density Current Interactions with Ambient Flow

i. Front Conditions:

The front between the density current and the outside fluid is a streamline, giving

$$v_B = u_B \frac{db}{dx} \text{ at } y = b(x) \tag{3.43}$$

where u_B and v_B are velocities along the front. A buoyant force, F_b, acts along the front of the density current, as discussed in a one-dimensional context in Sections 2.1. Its magnitude is obtained from the pressure term in the momentum Equation (3.24), which rearranged, yields $\frac{\partial F_b}{\partial x_i}$ where F_b is given by

$$F_b = \frac{s+1}{s+2} \rho_o \sigma h_B^{s+2} \tag{3.44}$$

Along the front, a pressure equilibrium must exist between the accelerating buoyant force, F_b, and arresting drag force, F_D, in steady-state. Thus the two expressions, Equations (3.44) and (3.42) may be equated, thereby relating the boundary thickness,

$$h_B = \left(\frac{s+2}{s+1} \frac{C_D}{2\sigma} u_a^2 \sin^2 \theta \right)^{\frac{1}{s+1}} \tag{3.45}$$

to the boundary angle θ (see Figure 3-6). Equation (3.45) is a two-dimensional generalization of Equation (2.80). For the special case of the stagnation point, S, (Figure 3-6) $\theta = 90^o$, giving the "stagnation height",

$$h_s = \left(\frac{s+2}{s+1} \frac{C_D}{2\sigma} u_a^2 \right)^{\frac{1}{s+1}} \tag{3.46}$$

ii) Source Conditions:

The conditions at the source must be specified in order to give an inner boundary for the near field region. Thus an inner velocity and height

$$\bar{q} = \bar{q}_i, \; h = h_i \quad \text{at } y = b_i(x) \; ,$$

where $b_i(x)$ defines the inner boundary, are defined such that the total flow, Q, is appropriate, and the overbar denotes the vector representation.

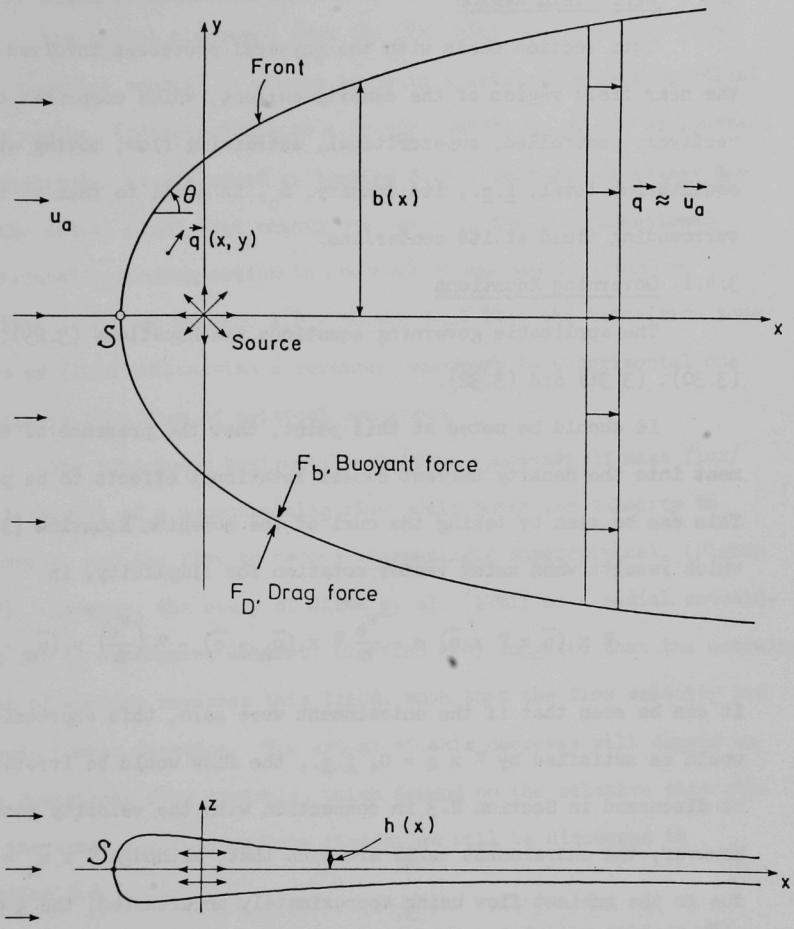

Figure 3-6 Schematized two-dimensional density current (OTEC) in an ambient crossflow.

3.4 Near-Field Region

This section deals with the physical processes involved in the near field region of the density current, which comprises convectively controlled, supercritical, entraining flow, moving at its equilibrium level, i.e., its density, ρ_o, is equal to that of the surrounding fluid at its centerline.

3.4.1 Governing Equations

The applicable governing equations are Equations (3.29), (3.30), (3.31) and (3.32).

It should be noted at this point, that the presence of entrainment into the density current causes rotational effects to be present. This can be seen by taking the curl of the momentum Equation (3.30), which results, when using vector notation for simplicity, in

$$\nabla \times (\bar{q} \times \nabla \times \bar{q}) = -\frac{w_e}{h} \nabla \times (\bar{u}_a - \bar{q}) - \nabla \left(\frac{w_e}{h}\right) \times (\bar{u}_a - \bar{q})$$

It can be seen that if the entrainment were zero, this expression would be satisfied by $\nabla \times \bar{q} = 0$, i.e., the flow would be irrotational, as discussed in Section 2.3 in connection with the velocity potential. However, the entrainment terms are such that, although $\nabla \times \bar{u}_a = 0$, due to the ambient flow being approximately unperturbed, the gradient $\nabla\left(\frac{w_e}{h}\right)$ is not zero. Thus $\nabla \times \bar{q} = 0$ does not satisfy the equation, i.e., the flow is rotational. The presence of rotational effects will be further discussed in Section 3.5.

3.4.2 Boundary Conditions and Possible Downstream Controls

The radial discharge from the OTEC plant (or from any other environmental source) is likely to be in a critical or supercritical flow regime, (corresponding to a Froude number, F, of one or greater, respectively, as discussed in Section 2.2). This may be either due to the actual plant exit conditions, or - if the two-dimensional horizontal spreading motion is preceded by vertically rising or falling jets, see Section 1.2 - to the fact that the transition zone from an fluid motion with a vertical component to a horizontal one is always some form of critical condition.

The subsequent horizontal expansion (decrease of mass flux/ unit length) of a nonentraining flow would cause the velocity to increase, and the flow to become increasingly supercritical, (Figure 2-7). However, the study of Jirka et al. (1981) on a radial entraining jet in a stagnant ambient, (Section 2.4) suggests that the entrainment of ambient reverses this trend, such that the flow velocity and Froude number decrease. The extent of this decrease will depend on the downstream flow controls, which depend on the relative strengths of the near- and intermediate fields, as will be discussed in Section 3.6.

The flow will be symmetric with respect to the ambient flow direction (x - axis), so that modeling efforts (Chapter 4) could confine themselves to the positive (x, +y) half plane.

3.4.3 Non-dimensionalization for the Near Field Equations

The Boussinesq-type flow under consideration takes place into an infinite receiving fluid with an ambient velocity. This physical situation can be described by means of the ambient velocity, u_a, together with the source variables, velocity, U_o, buoyancy parameter, g_o', for Case A or B and N for Case C, length parameter, ℓ_o, where ℓ_o is obtained in terms of the initial radius, r_o, and discharge depth, h_o, as

$$\ell_o^2 = 2\pi r_o h_o \tag{3.48}$$

The source variables can be grouped into the integral quantities of momentum flux, M_o, volume flux, Q_o and a buoyancy conservation parameter Σ_o, where, if top-hat profiles are taken,

$$M_o = U_o^2 \ell_o^2 \tag{3.49}$$

$$Q_o = U_o \ell_o^2 \tag{3.50}$$

$$\Sigma_o = \begin{cases} J_o = U_o g_o' \ell_o^2 & \text{Case A} \\ g_o' & \text{Case B} \\ N & \text{Case C} \end{cases} \tag{3.51}$$

Thus the initial conditions can now be characterized by the more fundamental integral quantities, M_o, Q_o and Σ_o, together with a characteristic length, r_o. Thus any flow property, ϕ, such as velocity, can be written in terms of position, x and y, and the above variables, as

$$\phi = f(x, y, M_o, \Sigma_o, Q_o, r_o, u_a). \tag{3.52}$$

The momentum flux, M_o, and the buoyancy related parameter Σ_o represent the two fundamental opposing mechanisms for the jet flow, M_o causing instability, which is counteracted by the stabilizing effects of buoyancy, Σ_o. Thus it appears appropriate to use these as the two normalizing variables. Length, volume flux, velocity and buoyancy scales are developed by dimensional arguments as shown in Table 3-2, together with their relationships to the non-integral conditions, U_o, g_o' (N), ℓ_o and the discharge Froude number F_s.

Thus the nondimensionalized form of Equation (3.52) can be written as

$$\hat{\phi} = f\left(\hat{x} = \frac{x}{\ell_N}, \hat{y} = \frac{y}{\ell_N}, \frac{1}{F_s}, \hat{r}_o = \frac{r_o}{\ell_N}, \hat{u}_a = u_a \frac{F_s}{U_o}\right) \tag{3.53}$$

where ^ denotes nondimensionalization using the quantities M_o and Σ_o and $\frac{1}{F_s}$ denotes for all straification cases, the initial discharge, Q_o, or initial slot height

$$\hat{h}_o = \begin{cases} \dfrac{1}{2\pi\, \hat{r}_o\, F_s^{\,2}} & \text{Case A} \\[2ex] \dfrac{1}{2\pi\, \hat{r}_o\, F_s^{\,4/3}} & \text{Case B} \\[2ex] \dfrac{1}{2\pi\, \hat{r}_o\, F_s} & \text{Case C} \end{cases} \tag{3.54}$$

Table 3-2: Near field scale definitions.

	Conserved Quantities	Length Scale ℓ_N	Volume Flux Scale Q_N	Buoyancy Scale g'_N	Velocity Scale u_N	Frequency Scale $\frac{1}{t_N}$	Discharge Froude Number F_s
Case A: Surface Source with Homogeneous Ambient	M_o $\Gamma_o = J_o = g_o' Q_o$	$\frac{M_o^{\frac{3}{4}}}{J_o^{\frac{1}{2}}} = \ell_o F_s$	$\frac{M_o^{\frac{5}{4}}}{J_o^{\frac{1}{2}}} = Q_o F_s$	$\frac{J_o^{\frac{3}{2}}}{M_o^{\frac{5}{4}}} = \frac{g_o'}{F_s}$	$\frac{J_o^{\frac{1}{2}}}{M_o^{\frac{1}{4}}} = \frac{U_o}{F_s}$	$\frac{J_o}{M_o}$	$\frac{U_o}{\sqrt{g_o' \ell_o}}$
Case B: Interface Source with Stepwise Stratification	M_o $\Gamma_o = g_o'$	$\frac{M_o^{\frac{1}{3}}}{g_o'^{\frac{1}{3}}} = \ell_o F_s^{\frac{2}{3}}$	$\frac{M_o^{\frac{5}{6}}}{g_o'^{\frac{1}{3}}} = Q_o F_s^{\frac{2}{3}}$	g_o'	$M_o^{\frac{1}{6}} g_o'^{\frac{1}{3}} = \frac{U_o}{F_s^{\frac{2}{3}}}$	$\left(\frac{g_o'}{M_o}\right)^{\frac{1}{6}}$	$\frac{U_o}{\sqrt{g_o' \ell_o}}$
Case C: Equilibrium Source with Linear Stratification	M_o $\Gamma_o = N$	$\frac{M_o^{\frac{1}{4}}}{N^{\frac{1}{2}}} = \ell_o F_s^{\frac{1}{2}}$	$\frac{M_o^{\frac{3}{4}}}{N^{\frac{1}{2}}} = Q_o F_s^{\frac{1}{2}}$	$M_o^{\frac{1}{4}} N^{\frac{3}{2}} = \ell_o N^2 F_s^{\frac{1}{2}}$	$M_o^{\frac{1}{4}} N^{\frac{1}{2}} = \frac{U_o}{F_s^{\frac{1}{2}}}$	N	$\frac{U_o}{N \ell_o}$

Thus the problem is defined by three parameters, F_s, $\hat{r}_o$ and $\hat{u}_a$, for all stratification cases.

The governing equation set, Equations (3.29) to (3.32) can be written in nondimensional form as:

$$\frac{\partial}{\partial \hat{x}} (\hat{h}\ \hat{u}) + \frac{\partial}{\partial \hat{y}} (\hat{h}\ \hat{v}) = \hat{w}_e \tag{3.55}$$

$$\frac{\partial}{\partial \hat{x}} (\hat{u}^2\ \hat{h}) + \frac{\partial}{\partial \hat{y}} (\hat{u}\ \hat{v}\ \hat{h}) = \hat{w}_e\ \hat{u}_a - \frac{(s+1)^s}{(s+2)} \frac{\partial}{\partial \hat{x}} (\hat{g}'^{1-s}\ \hat{h}^{s+2}) \tag{3.56}$$

$$\frac{\partial}{\partial \hat{x}} (\hat{u}\ \hat{v}\ \hat{h}) + \frac{\partial}{\partial \hat{y}} (\hat{v}^2\ \hat{h}) = - \frac{(s+1)^s}{(s+2)} \frac{\partial}{\partial \hat{y}} (\hat{g}'^{1-s}\ \hat{h}^{s+2}) \tag{3.57}$$

$$\frac{\partial}{\partial \hat{x}} (\hat{g}'\ \hat{h}\ \hat{u}) + \frac{\partial}{\partial \hat{y}} (\hat{g}'\ \hat{h}\ \hat{v}) = 0 \qquad \text{(Case A)} \tag{3.58}$$

$$\hat{g}' = \text{const (Case B)} \tag{3.59}$$

$$\hat{N} = \text{const (Case C)} \tag{3.60}$$

The nondimensionalized initial conditions are given in Table 3-3.

The ^ notation will be retained hereafter only in the figures, and in the text, where confusion would otherwise result.

3.5 Intermediate Field Region

3.5.1 Transcritical Flow Region

This comprises the inviscid, convectively controlled region into which the fluid passes after the near field. The inner

Table 3-3: Near field nondimensionalized initial conditions.

	$\hat{u}_o$	$\hat{g}_o'$	$\hat{\ell}_o$	$\hat{h}_o$	$\hat{u}_a$
Case A	F_s	F_s	$\frac{1}{\sqrt{2\pi \hat{r}_o \hat{h}_o}}$	$\frac{1}{2\pi \hat{r}_o F_s^2}$	$u_a \frac{F_s}{U_o}$
Case B	$F_s^{\frac{2}{3}}$	1	$\frac{1}{\sqrt{2\pi \hat{r}_o \hat{h}_o}}$	$\frac{1}{2\pi \hat{r}_o F_s^{\frac{4}{3}}}$	$u_a \frac{F_s}{U_o}^{\frac{2}{3}}$
Case C	$F_s^{\frac{1}{2}}$	not applicable	$\frac{1}{\sqrt{2\pi \hat{r}_o \hat{h}_o}}$	$\frac{1}{2\pi \hat{r}_o F_s}$	$u_a \frac{F_s}{U_o}^{\frac{1}{2}}$

boundary of the transcritical region is determined by conditions at the end of the near field, and the exact transition conditions, which will be discussed in Section 3.6.

The transcritical region, as indicated in Figure 3-6, comprises the density current within and somewhat downstream of the head region. It is characterized by a highly variable, two-dimensional velocity field, $\bar{q}(x,y)$, with an internal jump occurring between its inner boundary and the downstream stagnation point, S (Figure 3-6). The outer boundary is as shown in Figure 3-6, which is controlled by the balancing of drag and buoyant forces, as discussed in Section 3.3.

The transcritical flow region does not have a downstream boundary as such, in that it becomes supercritical, and may then be said to pass into the purely supercritical region, which will be discussed in Section 3.5.2. No downstream boundary conditions need to be defined as the flow conditions will be self-determined by the flow, it being described by a hyperbolic equation system (Section 2.2).

The governing equations are those given in Equations (3.33), (3.34), (3.35) and (3.36), although the buoyancy conservation Equations (3.35) and (3.36) are not required in this discussion (no entrainment) and will not be addressed hereafter.

3.5.1.1 Nondimensionalization of the Transcritical Flow Region

The flow parameters involved in this description are: stratification parameters, s and σ, ambient velocity, u_a, drag coefficient, C_D, and total flow, Q. These can be combined into two length scales

and a parameter, as: A vertical length scale, the "stagnation height", h_s, given by (Section 3.3)

$$h_s = \left\{ \frac{s+2}{s+1} \frac{C_D}{2\sigma} u_a^{\,2} \right\}^{\frac{1}{s+1}} \tag{3.61}$$

A "volume flux parameter", which has the form

$$V' = \frac{Q}{2\pi u_a h_s^{\,2}} , \tag{3.62}$$

and a horizontal length scale, the "intermediate field length scale", ℓ_I, given by

$$\ell_I = h_s V'. \tag{3.63}$$

h_s, V' and ℓ_I are summarized in general and for the particular stratification configurations, in Table 3-4. Thus, the variables can be nondimensionalized as

$$\tilde{x}, \tilde{y} = \frac{x,y}{\ell_I} ; \quad \tilde{h} = \frac{h}{h_s} ; \quad \tilde{u},\tilde{v},\tilde{q} = \frac{u,v,q}{\sqrt{\sigma h_s^{\,s+1}}} \tag{3.64}$$

yielding:

$$\frac{\partial}{\partial \tilde{x}} (\tilde{h}\, \tilde{u}) + \frac{\partial}{\partial \tilde{y}} (\tilde{h}\, \tilde{v}) = 0 \tag{3.65}$$

$$\frac{\partial}{\partial \tilde{x}} (\tilde{u}^2 h) + \frac{\partial}{\partial \tilde{y}} (\tilde{u}\, \tilde{v}\, \tilde{h}) = - \tilde{h} \frac{\partial}{\partial \tilde{x}} (\tilde{h}^{s+1}) \tag{3.66a}$$

$$\frac{\partial}{\partial \tilde{x}} (\tilde{u}\, \tilde{v}\, \tilde{h}) + \frac{\partial}{\partial \tilde{y}} (\tilde{v}^2 h) = - \tilde{h} \frac{\partial}{\partial \tilde{y}} (\tilde{h}^{s+1}) \tag{3.66b}$$

$$\frac{\tilde{q}^2}{2} + \tilde{h}^{s+1} = 1 \tag{3.67}$$

$$\tilde{h}_s = 1 \tag{3.68}$$

Table 3.4: Intermediate field parameter and length scales.

	General s, σ	Step-wise Stratification $s = 0$ $\sigma = g'$	Linear Stratification $s = 1$ $\sigma = \frac{1}{2} N^2$
Vertical Length Scale h_s	$\left\{\frac{s+2}{s+1} \frac{C_D}{2\sigma} u_a^2\right\}^{\frac{1}{s+1}}$	$C_D \frac{u_a^2}{g'}$	$\left(\frac{3}{2} C_D\right)^{1/2} \frac{u_a}{N}$
Volume Flux Parameter V'	$\frac{Q}{2\pi u_a h_s^2}$	$\frac{Q g'^2}{2\pi C_D^2 u_a^5}$	$\frac{Q N^2}{2\pi \frac{3}{2} C_D u_a^3}$
Horizontal Length Scale $\ell_I = V' h_s$	$\frac{Q}{2\pi u_a h_s}$	$\frac{Q g'}{2\pi C_D u_a^3}$	$\frac{Q N}{2\pi (\frac{3}{2} C_D)^{1/2} u_a^2}$

$$\tilde{c} = \sqrt{(s+1)\tilde{h}} \tag{3.69}$$

$$\tilde{h}_c \left(\tilde{h}_c{}^s + \frac{(s+1)}{2}\right) = 1 \tag{3.70}$$

$$\tilde{q}_c = \sqrt{(s+1)\tilde{h}_c} \tag{3.71}$$

Again, the ~ will be dropped apart from in the figures, and where both near and intermediate field nondimensionalized variables occur together.

Thus the transcritical flow region can be seen to be governed by two parameters only, i.e., the volume flux parameter, V', and the drag coefficient, C_D.

3.5.2 Supercritical Flow Region

The upstream boundary of this region comprises nonentraining, supercritical flow, entering from the transcritical flow region. The outer boundary is identical with that for the latter. Within this region, frictional effects become increasingly important as the flow passes downstream. Again, no downstream boundary is required, as for the transcritical flow region.

The governing equations are Equations (3.37), (3.38), (3.39) and (3.40), although again the buoyancy conservation Equations (3.39) and (3.40) are not required.

3.5.2.1 Nondimensionalization of Supercritical Flow Region

The equations governing the supercritical flow region are nondimensionalized using the same scales as for the transcritical flow region. Thus, Equations (3.37) and (3.38) become

$$\frac{\partial}{\partial \tilde{x}} (\tilde{h}\,\tilde{u}) + \frac{\partial}{\partial \tilde{y}} (\tilde{h}\,\tilde{v}) = 0 \tag{3.72}$$

$$\frac{\partial}{\partial \tilde{x}} (\tilde{u}^2\,\tilde{h}) + \frac{\partial}{\partial \tilde{y}} (\tilde{u}\,\tilde{v}\,\tilde{h}) = -\tilde{h}\,\frac{\partial}{\partial \tilde{x}}\,\tilde{h}^{s+1} + \lambda_i V' \,(\tilde{u}_a - \tilde{u})|\tilde{u}_a - \tilde{u}| \tag{3.73a}$$

$$\frac{\partial}{\partial \tilde{x}} (\tilde{u}\,\tilde{v}\,\tilde{h}) + \frac{\partial}{\partial \tilde{y}} (\tilde{v}^2\,\tilde{h}) = \tilde{h}\,\frac{\partial}{\partial \tilde{y}}\,\tilde{h}^{s+1} + \lambda_i V' \,(-\tilde{v})|-\tilde{v}| \tag{3.73b}$$

where $\tilde{u}_a$ is taken as $(\tilde{u}_a, 0)$, where $\tilde{u}_a$ is given by

$$\tilde{u}_a = \frac{2}{C_D}\,\frac{(s+1)}{(s+2)} \tag{3.74}$$

Thus the frictional regime requires the "additional" parameter $\lambda_i V'$ as a measure of the importance of the frictional effect.

3.6 Transition Conditions for the Boundary Between the Near and Intermediate Fields

This section considers the boundary conditions existing between the near and intermediate fields of the density current, as a function of their relative field strengths. The field strength is estimated by its respective length scale, which, for the near field (Section 3.3) is given from Table 3-2, as

$$\ell_N = \begin{cases} \ell_o F_s & \text{Case A} \\ \ell_o F_s^{2/3} & \text{Case B} \\ \ell_o F_s^{1/2} & \text{Case C} \end{cases} \tag{3.75}$$

For the intermediate field (Section 3.5), Table 3-4 gives the length

scale as

$$\ell_I = \frac{Q}{2\pi u_a h_s}, \tag{3.76}$$

which can also be written as:

$$\ell_I = \begin{cases} \dfrac{1}{2\pi C_D} \dfrac{J_o}{u_a^3} & \text{Case A} \\[2ex] \dfrac{1}{2\pi C_D} \dfrac{Qg_o'}{u_a^3} & \text{Case B} \\[2ex] \dfrac{1}{\pi} \dfrac{1}{(6C_D)^{1/2}} \dfrac{QN}{u_a^2} & \text{Case C} \end{cases} \tag{3.77}$$

This boundary is particularily important as it defines the inflow into, and hence characteristics of, the intermediate field. An analysis is required, that relates the transition flow properties to the relative field strength, ℓ_I/ℓ_N .

As shown in Equation (3.56), the flow is clearly rotational due to the entrainment of ambient flow momentum. A precise discussion of the transition conditions to the intermediate field, including an evaluation of the degree of rotationality, must necessarily rely on the complete results of the near field numerical model that will be given in Chapter 4.

At this point, however, it is possible to present an approximate and simplified treatment of the near-field and its transition condition. This treatment is based on the notion that - at least for weak cross-flows - the near field flow field is still predominately

radial, as it would be exactly for the stagnant case. (Note that in fact, one might expect the cross-flow to perturb the exactly radial flow pattern by shifting successive circles of constant flow properties in the downstream direction; this analogy to the true cross-flow discharge condition is discussed in Chapter 4).

Assuming then, in the first place, that the transition between the near-field and intermediate field (modeled as irrotational) occurs in the form of a circular geometry, the following additional assumptions are made:

i) Assume the boundary shape is circular, although the circle center will be downstream of the source.

ii) Assume that uniform conditions exist along this circle, i.e., that they form equi-Froude number, equi-height, equi-velocity, equi-buoyancy, etc. curves. Also the flow must be normal to the curve, for consistency with these underlying assumptions.

iii) The flow is assumed irrotational, i.e., any residual rotationality still present in the near field solution will be neglected. This assures that no entrainment will be present along the interface. The assumptions contained in (i), (ii) and (iii) will be justified in Chapter 4.

iv) Along their interface, both the near and intermediate field flows will be assumed to have equal energies. This "Equi-Energy Transition" can be represented by equating

the Bernoulli equation in dimensional units for the near and intermediate field flow, as

$$\underbrace{\frac{q_T^{\,2}}{2\sigma_T} + h_T^{s+1}}_{\text{Near Field}} = \underbrace{\frac{(s+2)}{(s+1)}\frac{C_D}{2\sigma_T}\,u_a^{\,2}}_{\text{Intermediate Field}} \text{ at transition.} \tag{3.78}$$

where the subscripted 'T' emphasizes the values of these quantities at the transition line, and the Bernoulli constant for the intermediate field, $\frac{(s+2)}{(s+1)}\frac{C_D}{2\sigma_T}\,u_a^{\,2}$ is evaluated at the stagnation point, S ($q = 0$, $h = h_s$, Equation 3.46). It should be emphasized that this equation is valid only along the irrotational, radial boundary separating the two flows. The term $\frac{q_T^{\,2}}{2\sigma_T}$ may be written, using the radial continuity equation $Q = 2\pi rhq$, as $\frac{Q_T^{\,2}}{(2\sigma_T)\,(2\pi r_T)^2 h_T^{\,2}}$. A local Froude number, F_ℓ, is defined as

$$F_\ell = \frac{Q}{(2\pi rh)\sqrt{(s+1)\sigma h^{s+1}}} \tag{3.79}$$

which allows Equation (3.78) to be written as

$$\frac{1}{2}F_{\ell\,T}^{\;2} + \frac{1}{(s+1)} = \frac{(s+2)}{(s+1)^2}\,\frac{C_D}{2\sigma}\,\frac{u_a^{\,2}}{h_T^{\,s+1}} = \frac{(s+2)}{(s+1)^2}\,\frac{C_D}{2\hat{\sigma}_T}\,\frac{\hat{u}_a^{\,2}}{\hat{h}_T^{\,s+1}} \tag{3.80}$$

where, as previously, ^ denotes near field, non-dimensionalization. The non-dimensionalized ambient velocity is given in Table 3-2. Using Equations (3.75) and (3.77) gives

$$\hat{u}_a = \begin{cases} \left(\frac{1}{2\pi C_D} \frac{\ell_N}{\ell_I}\right)^{1/3} & \text{Case A} \\ \left(\frac{1}{2\pi C_D} \frac{S}{F_s^{2/3}} \frac{\ell_N}{\ell_I}\right)^{1/3} & \text{Case B} \\ \left(\left(\frac{1}{6C_D}\right)^{1/2} \frac{1}{\pi} \frac{S}{F_s^{1/2}} \frac{\ell_N}{\ell_I}\right)^{1/2} & \text{Case C} \end{cases} \tag{3.81}$$

where S denotes the mixing due to the entrainment, such that $Q = S\,Q_o$.

Substitution of Equation (3.81) into Equation (3.80) and rearranging yields the relations

$$\frac{\ell_I}{\ell_N} = \begin{cases} \frac{C_D^{1/2}}{2\pi} \frac{1}{(\hat{g}_T'\,\hat{h}_T)^{3/2}} \frac{1}{\left(\frac{1}{2} F_{\ell T}^{\;2} + 1\right)^{3/2}} & \text{Case A} \\ \frac{C_D^{1/2}}{2\pi} \frac{1}{(\hat{g}'\,\hat{h}_T)^{3/2}} \frac{S}{F_s^{2/3}} \frac{1}{\left(\frac{1}{2} F_{\ell_T}^{\;2} + 1\right)^{3/2}} & \text{Case B} \\ \frac{3}{2\pi}\left(\frac{C_D}{6}\right)^{1/2} \frac{1}{\hat{h}_T^{\;2}} \frac{S}{F_S^{1/2}} \frac{1}{(F_{\ell T}^{\;2} + 1)} & \text{Case C} \end{cases} \tag{3.82}$$

This equation describes the conditions along the transition. The quantities $\hat{\sigma}_T$, $\hat{h}_T$, S and $F_{\ell T}$ are by virtue of the near-field solution all unique functions of $\hat{r}_T$, the radius of the transition circle, and thus Equation (3.82) effectively relates the relative

field strength, ℓ_I/ℓ_N to the transition radius. The functions, $\hat{\sigma}(\hat{r})$, $\hat{h}(\hat{r})$, $S(\hat{r})$ and $F_{\ell_T}(\hat{r})$ require numerical evaluation, (the results being presented in Section 4), which allows evaluation of $\ell_I/\ell_N = f(\hat{r}_T)$. Thus, for field strength ratios appropriate to a particular problem, the inverse relation $\hat{r}_T = F\left(\frac{\ell_I}{\ell_N}\right)$, again given in Chapter 4 can be used to estimate $\hat{r}_T$, which in turn allows definition of the flow conditions between the near and far fields.

The exact location of the transition "circle" and, in fact, the relationship of this approximate treatment to the more general near-field in a cross-flow requires the results of the near field model that is given in the following chapter.

CHAPTER 4

THE NEAR FIELD SOLUTION

This chapter deals with the numerical solution of the near field region for both a stagnant and moving ambient. Section 4.1 considers the adaptation of the finite difference scheme chosen (the MacCormack scheme as discussed in Section 2.6) to the problem under consideration. Section 4.2 deals with the case of a stagnant ambient ($\hat{u}_a = 0.0$), while the results for a moving ambient are presented in Section 4.3.

Section 4.4 discusses a simplified model for the moving ambient, which is of use in approximating the near-intermediate field boundary.

4.1 Numerical Computations - MacCormack's Method

The near field consists of supercritical, entraining, convective flow, the nondimensionalized equations having been given by Equations (3.29) to (3.32). However, throughout this chapter, only the Case A stratification type will be considered, so that Equation (3.32) will not be required.

The flow is supercritical, indicating that the equation system is of hyperbolic type; i.e., the flow properties at any point are only affected by changes upstream and can only affect points downstream. Hyperbolic equation systems, their properties and general solution methods have been discussed in Section 2.6. The solution method

decided on is an explicit stepping technique rather than the Method of Characteristics, due to ease of programming. As discussed in Section 2.6, care must be taken in establishing an appropriate step size for an explicit technique, so as not to introduce instabilities. These instabilities are due to attempting to evaluate the solution at a point for which all the information is not available. That this is not the case here is checked by the approach discussed in Section 2.6, summarized by Equation (2.83).

The finite difference method chosen was the second order method of MacCormack, which is a two-step Lax-Wendroff-type method (Roache, 1976, Section 2.6). If the nondimensional controlling Equations (3.29) to (3.32) are written in vector form as

$$\frac{\partial \bar{F}}{\partial x} + \frac{\partial \bar{G}}{\partial y} = \bar{H} \tag{4.1}$$

where $\bar{F} = \begin{Bmatrix} hu \\ u^2h + \frac{1}{2} g'h^2 \\ uvh \\ g'hu \end{Bmatrix}$, $\bar{G} = \begin{Bmatrix} hv \\ uvh \\ v^2h + \frac{1}{2} g'h^2 \\ g'hv \end{Bmatrix}$; $\bar{H} = \begin{Bmatrix} w_e \\ w_e u_a \\ 0 \\ 0 \end{Bmatrix}$

then the basic MacCormack scheme can be defined by

$$FB_j^{i+1} = F_j^i - \frac{\Delta x}{\Delta y}\left(G_{j+1}^i - G_j^i\right) + \Delta x\, H_j^i \tag{4.2a}$$

$$F_j^{i+1} = \frac{1}{2}\left(F_j^i + FB_j^{i+1} - \frac{\Delta x}{\Delta y}\left(GB_j^{i+1} - GB_{j-1}^{i+1}\right) + \Delta x \quad HB_j^{i+1}\right) \tag{4.2b}$$

where the superscripts and subscripts refer to a spatial mesh of points (x_i, y_j) with spacing Δx and Δy and the vector notation for F, G and H being dropped hereafter for convenience. Equations (4.2a) and (4.2b) form a predictor-corrector set, with FB, GB and HB denoting provisional values of F, G and H, respectively, with significance only attached to the results from the corrector step. The difference scheme, Equation (4.2) consists of a forward differencing of G in the predictor and backward differencing in the corrector, but MacCormack (1971) pointed out that the forward and backward sequence could easily be reversed, or even used alternately for each predictor-corrector couplet, in an attempt to produce unbiased results. The effect of the various permutations was investigated by Kutler, Warming and Lomax (1973), who summarized the various alternatives as

$$FB_j^{i+1} = F_j^i - \frac{\Delta x}{\Delta y}\left((1 - \epsilon)G_{j+1}^i - (1 - 2\epsilon)G_j^i + \epsilon G_{j-1}^i\right) + \Delta x\, H_j^i \tag{4.3a}$$

$$F_j^{i+1} = \frac{1}{2}\left((F_j^i + FB_j^{i+1}) - \frac{\Delta x}{\Delta y}\left(\epsilon GB_{j+1}^{i+1} + (1 - 2\epsilon)GB_j^{i+1} + (\epsilon - 1)GB_{j-1}^{i+1}\right) + \Delta x\, HB_j^{i+1}\right) \tag{4.3b}$$

where $\epsilon = 0$ reproduces Equations (4.2), and $\epsilon = 1$, its alternative.

This system introduces second order dissipative effects as shown in Equation (2.90).

$$\begin{pmatrix} U \\ V \end{pmatrix} = J^{-1} \begin{pmatrix} u \\ v \end{pmatrix} , \tag{4.5}$$

where these velocities are estimated at the cell centers. Thus the scheme involves a flux balance across the faces of "auxiliary cells", which, as shown in Figure 4-1, are formed by joining cell centers in the contravariant plane. The local relation within each cell is

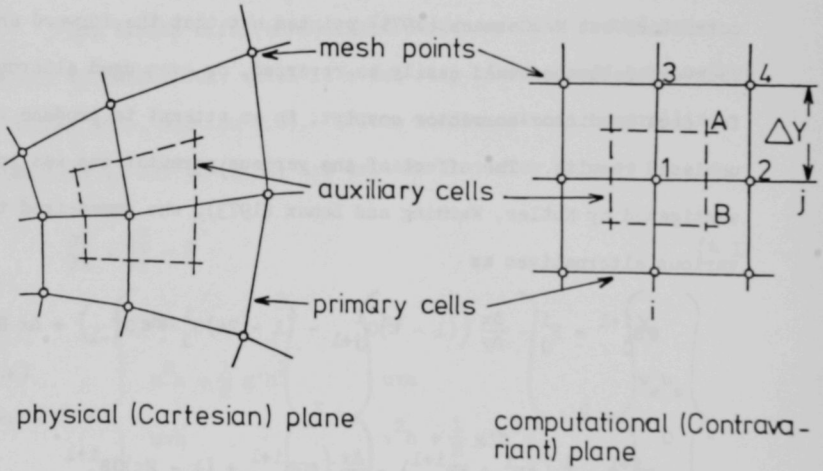

Figure 4-1. Relation between Cartesian and Contravariant planes.

assumed given by a bilinear mapping

4.1.1 Finite Volume Formulation

This formulation (mentioned in Section 2.6) is generally used when complicated boundary shapes would normally require use of a boundary-conforming coordinate system or special interpolation formulae to be adopted in their vicinity. It has the additional advantage of allowing efficient clustering of mesh points. These advantages proved particularly useful for the transonic region of the intermediate field, as will be discussed in Chapter 5. The finite volume formulation is used in the near field for consistency with the intermediate field scheme. This transformation is based upon a purely local transformation of a mesh cell in a Cartesian (x,y) grid into a cell in a transformed or contravariant (X,Y) grid *i.e.*, no information is required regarding the global nature of the transformation. If the Jacobian matrix, J, for an arbitrary, non-singular, and not necessarily orthogonal, transformation from Cartesian to contravariant coordinates, is defined as

$$J = \begin{pmatrix} x_X & x_Y \\ y_X & y_Y \end{pmatrix} \text{ and } J^{-1} = \frac{1}{D}\begin{pmatrix} y_Y & -x_Y \\ -y_X & x_X \end{pmatrix} \tag{4.4}$$

where D is the determinant of J and x_X, x_Y, y_X, y_Y are known as the metric terms of the transformation. If the contravariant velocity components are defined as U, V, then they can be related to their Cartesian counterparts u,v as

$$x = 4\sum_{i=1}^{4} x_i \left(\frac{1}{4} + X_i X\right)\left(\frac{1}{4} + Y_i Y\right)$$

$$y = 4\sum_{i=1}^{4} y_i \left(\frac{1}{4} + X_i X\right)\left(\frac{1}{4} + Y_i Y\right) \tag{4.6}$$

where x_i, y_i are the coordinates of the cell corners in Cartesian space, and X_i, Y_i those in contravariant space, which can be taken, with no loss of generality as (- 1/2, - 1/2), (1/2, - 1/2), (- 1/2, 1/2), and (1/2, 1/2) respectively, giving $\Delta X = \Delta Y = 1$. Equation (4.6) can be differentiated to give formulae such as

$$x_X = \mu_Y \delta_X x$$
$$x_Y = \mu_x \delta_Y x \tag{4.7}$$

on evaluation at the cell center (0,0), with similar expressions for y_X and y_Y , where the averaging and differencing expressions μ_X and δ_X, respectively, are defined as

$$\mu_X f_{i,j} = \frac{1}{2}\left(f_{i+1/2,\,j} + f_{i-1/2,\,j}\right)$$

$$\delta_X f_{i,j} = \left(f_{i+1/2,\,j} - f_{i-1/2,\,j}\right) \tag{4.8}$$

where i, j are mesh indices in the X, Y direction.

Thus, the relations between Cartesian and contravariant coordinates can be summarized by Equation (4.5) together with the relation

$$\begin{pmatrix} \partial/\partial x \\ \partial/\partial y \end{pmatrix} = \frac{1}{D} \begin{pmatrix} y_Y & -y_X \\ -x_Y & x_Y \end{pmatrix} \begin{pmatrix} \partial/\partial X \\ \partial/\partial Y \end{pmatrix}$$

$$= (J^{-1})^T \begin{pmatrix} \partial/\partial X \\ \partial/\partial Y \end{pmatrix} \tag{4.9}$$

The nondimensionalized near field Equations (4.1) can then be expressed in contravariant form as

$$\frac{\partial}{\partial X} F + \frac{\partial}{\partial Y} G = H \tag{4.10}$$

where

$$F = \begin{Bmatrix} hDU \\ hDUu + \frac{1}{2} y_Y g' h^2 \\ hDUv + \frac{1}{2} x_Y g' h^2 \\ g' hDU \end{Bmatrix} ; G = \begin{Bmatrix} hDV \\ hDVu - \frac{1}{2} y_X g' h^2 \\ hDVv - \frac{1}{2} x_X g' h^2 \\ g' hDV \end{Bmatrix} ; H = \begin{Bmatrix} w_e D \\ w_e u_a D \\ 0 \\ 0 \end{Bmatrix}$$

4.1.2 <u>Solution Details</u>

The solution procedure, using the MacCormack method (Equation 4.3), for the present physical problem, defined by Equation (4.10), can be summarized in the following points.

1) FB is calculated, using the 'predictor' Equation (4.3a), from values of F, G and H, at points already solved for, or known from boundary conditions.

2) 'Predicted' values of the dependent variables, u, v, h, w_e and g', are calculated from FB, using the relations (obtained from Equation 4.10).

$$v = \frac{x_Y}{y_Y} \quad \frac{FB(2)}{FB(1)} + \frac{FB(3)}{FB(1)} - u \quad \frac{x_Y}{y_Y} \tag{4.11}$$

$$u = \left(y_Y \quad \frac{FB(1)}{h} + x_y^{\,2} \frac{FB(2)}{FB(1)} + y_Y \, x_Y \frac{FB(3)}{FB(1)}\right) \Big/ \left(y_Y^{\,2} + x_Y^{\,2}\right) \tag{4.12}$$

$$g' = \frac{FB(4)}{FB(1)} \tag{4.13}$$

$$0.5 \; g \quad h^3 + \left(\frac{x_Y \; FB(3) - y_Y \cdot FB(2)}{x_Y^{\,2} + y_Y^{\,2}}\right) h + \frac{FB(1)^2}{(x_Y^{\,2} + y_Y^{\,2})} = 0, \tag{4.14}$$

where the appropriate root of Equation (4.14) determines the height. The entrainment relation,

$$w_e = w_e \; (u, \; v, \; h, \; g', \; u_a) \tag{4.15}$$

must be defined, together with an appropriate ambient velocity, u_a.

GB and HB are calculated from the 'predicted' dependent variable values.

3) Steps 1 and 2 are repeated using the 'corrector' Equation (4.3b), yielding the final values at the node in question.

4.1.3 Initial and Boundary Conditions

The initial conditions of the problem (required at the inner

boundary only, as a marching scheme is being used) can be obtained from the parameters F_s, $\hat{r}_o$ and $\hat{u}_a$. Values of F_s and $\hat{r}_o$ were selected as $F_s = 100$ and $\hat{r}_o = 0.5$, i.e., a high Froude number value and small radius to simulate a radial point source (as defined by Jirka et al., 1981) and make the downstream results independent of the upstream boundary. Parameter values of $\hat{u}_a$ were chosen as either zero (stagnant ambient) or, as finite ($\hat{u}_a > 0$) using Equation (3.81), to relate them to the ratio of relative intermediate to near field length scales, ℓ_I/ℓ_N.

In principle, the problem should be solved in the entire x-y plane (i.e., within a 360° sector around the source). Because the solutions must be symmetric about the x-axis, however, the solution only in the (x, +y) half-plane need be determined in general. In the case of a stagnant ambient, the solution is radially symmetric, and only a sector of the half-plane is used. In both cases the symmetry boundaries introduced by computational subdivision are no-flux boundaries.

Inspection of Equation (4.3), which defines the MacCormack solution method, shows that only values of the G fluxes are required in order to define the boundary conditions on these radial lines. These G fluxes may be thought of as a combination of actual flux terms, hDV, hDVg', hDVu and hDVv together with pressure terms $\frac{1}{2} y_X g'h^2$ and $\frac{1}{2} x_X g'h^2$ which can in turn be split into an actual pressure force, $p = \frac{1}{2} g'h^2$, together with the metric terms y_X and x_X. All

of these must be evaluated separately outside the boundary and then recombined giving the required G fluxes.

Consider first the flux terms hDV, hDVg', hDVu and hDVv. These comprise the actual contravariant V flux, and the buoyancy and u and v physical velocities advected by this flux. If j = 2 is used to denote a boundary line, then hDV at j = 1 and 2 must have opposite signs and identical magnitudes, so that they exactly cancel at the actual boundary. Thus the boundary conditions become

$$hDV|_1 = - hDV|_2$$

$$hDVg'|_1 = - hDVg'|_2$$

$$hDVu|_1 = - hDVu|_2$$

$$hDVv|_1 = - hDVv|_2 \tag{4.16}$$

Consider estimation of the actual pressure term p outside the boundary. Rearrangement of the horizontal and vertical momentum equations in contravariant form, as given in Equation (4.10) yield respectively,

$$- \frac{\partial}{\partial X}\left(y_Y p\right) + \frac{\partial}{\partial Y}\left(y_X p\right) = \frac{\partial}{\partial X}\left(hDUu\right) + \frac{\partial}{\partial Y}\left(hDVu\right) - w_e\, u_a D$$
$$= R1 \tag{4.17}$$

$$\frac{\partial}{\partial X}\left(x_y p\right) - \frac{\partial}{\partial Y}\left(x_X p\right) = \frac{\partial}{\partial X}\left(hDUv\right) + \frac{\partial}{\partial Y}\left(hDVv\right)$$
$$= R2 \tag{4.18}$$

which on expanding and rearranging yield

$$p_Y = -\frac{1}{D}(x_Y \quad R1 + y_Y \quad R2) \tag{4.19}$$

where D is the determinant of the Jacobian as defined earlier, which can be evaluated using differencing techniques and a knowledge that hDV at the boundary, is zero. The gradient of p in the Y direction, yields the required p_1 value by extrapolation.

The metric terms y_X and x_X are evaluated, also by extrapolation, as

$$y_{X,1} = 2y_{X,b} - y_{X,2}$$

$$x_{X,1} = 2x_{X,b} - x_{X,2} \tag{4.20}$$

where $y_{X,b}$, the boundary value, is evaluated simply as $= y_{i+1,2} - y_{i,2}$ as opposed to $y_{X,2} = y_{i+1,2} - y_{i,2} + y_{i+1,3} - y_{i,3}$, and similarly for $x_{X,b}$.

Thus generation of all the G fluxes required for the boundary conditions have been discussed. No downstream boundary condition is required as this will be self-determined by the marching technique.

4.2 Results for Stagnant Ambient ($\hat{u}_a = 0.0$)

The stagnant ambient solution was investigated using a radial grid, with $\hat{r}_o = 0.5$, and $F_s = 100.0$. Because of the radial symmetry, only a radial sector of 5° was used, subdivided into 10 subsectors of $1/2^o$ each. Solutions were obtained for two types of buoyant

entrainment functions, the model of Jirka (1982), Equation (2.79), and the exponential function of Stolzenbach and Harleman (1971), Equation (2.78).

The results obtained for both entrainment functions (Figures 4.2 and 4.3, respectively) show practically identical behavior. In both cases, a rapid decrease in velocity, buoyancy and Froude number, together with increase in height, occurs in the initially highly entraining region in which the behavior is largely that of a non-buoyant jet. Thereafter the entrainment is heavily damped, but still has a significant effect due to the increasing surface area. After a Froude number of about 1.25 is obtained, the rate of change becomes smaller and smaller as the Froude number decreases slowly to 1.0. In this region, a jump could occur very easily, depending on the downstream conditions. (These are comparable with "undular jumps" in open channel flow, as discussed in Section 2.3).

This solution can be compared with a somewhat similar stagnant discharge investigation by Jirka et al. (1981). The latter treatment assumed polynomial velocity and buoyancy profiles, compared with the 'top hat' or constant value profile assumed herein; also one dimensional integral ordinary differential equations and the exponential entrainment function Equation (2.78) was used. The comparison with the results of Jirka et al. (1981) is best made via the bulk property, $\hat{Q}$, which represents the overall flow rate, as this should be relatively insensitive to the particular profiles adopted. It

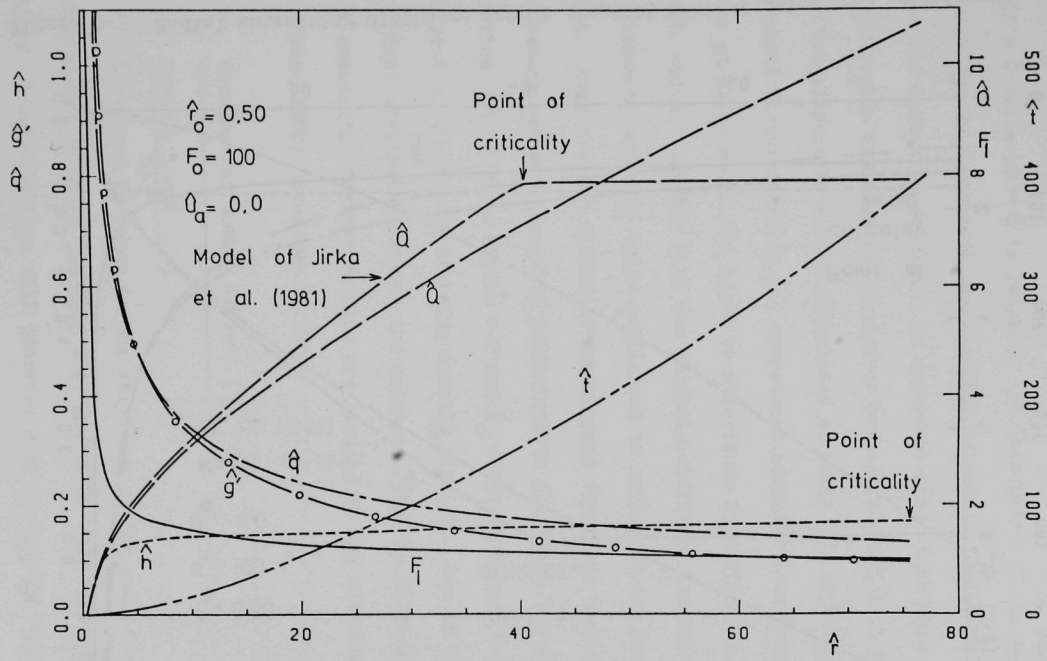

Figure 4-2 Radial entraining discharge into a stagnant ambient using the entrainment function of Jirka (1982), Equation (2.79). Near field nondimensionalization used.

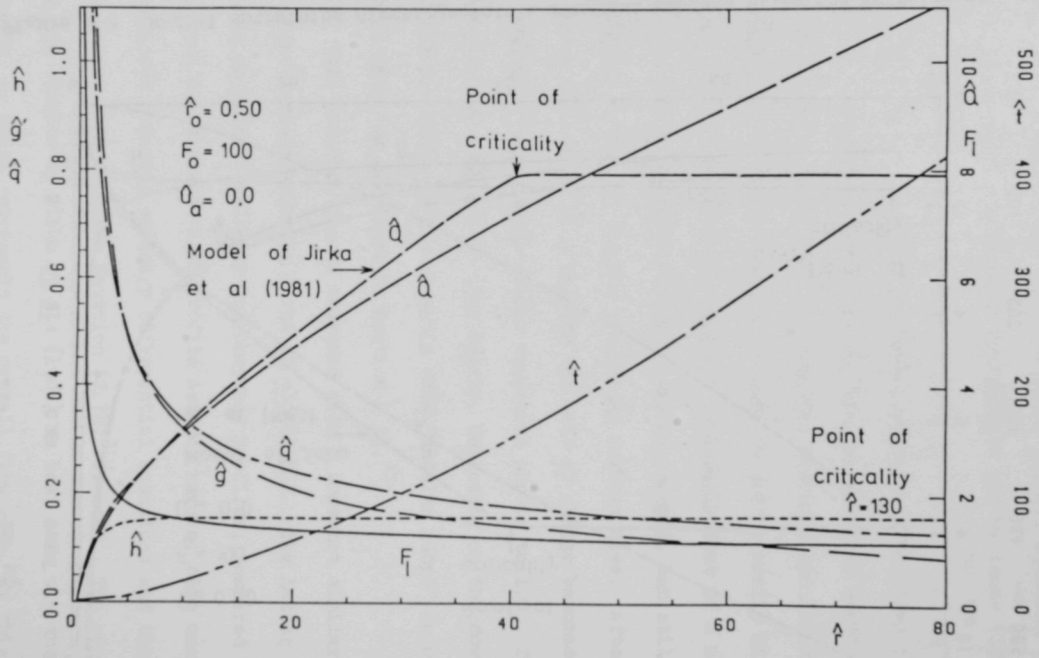

Figure 4-3 Radial entraining discharge into a stagnant ambient using the entrainment function of Stolzenbach and Harleman (1971), Equation (2.78). Near-field nondimensionalization used .

can be seen in Figures 4-2 and 4-3 that good agreement is obtained until a $\hat{Q}$ value of ~ 8 is reached. At this point, Jirka et al's solution becomes constant, as the flow becomes critical at this point and ceases to entrain. It should be noted that this occurs in the region having a Froude number between 1.0 and 1.25 in which such transitions have been postulated as being easily triggered by any small disturbances (e.g., downstream effects) (see Section 2.3). Jirka et al.'s model did begin to experience instabilities at this point, which, together with the slightly different treatment of the entrainment, would be quite sufficient to influence the transition point. Even the two different entrainment functions used in the MacCormack scheme were quite sufficient to alter the transition position, ($\hat{r}_c = 76$ in Figure 4-2 and $\hat{r}_c = 130$ in Figure 4-3) with the rest of the treatment being exactly similar. Due to the essential similarity between the solutions for the different entrainment relations, further results are limited to the entrainment model of Jirka (1982), Equation (2.79).

4.3 Results for Moving Ambient ($\hat{u}_a > 0$)

4.3.1 Computational Grid

Care must be taken in the selection of the grid for this case. The stagnant solution (Section 4.2) has shown that the supercriticality of the discharge will decrease with increasing distance from the source until the critical point is reached, (Figures 4-2 and 4-3)

or a jump occurs. The presence of an ambient flow introduces an asymmetry around the source, such that the critical point is reached closer to the source on the upstream and further away on the downstream side (this being verified by the results presented in this section). The MacCormack scheme is only applicable to the supercritical region (governed by hyperbolic equations), the solution evolving as the scheme marches away from the source. Once a velocity is encountered which is critical or less (in the direction of marching), the solution can no longer continue. Thus it is advantageous to arrange the step-size such that the critical point is reached at approximately the same time at all points of the grid, in order to obtain the maximum information possible regarding the supercritical regime. In addition, it would be advantageous to have the grid aligned with the (initially unknown) streamline direction in order to have the velocity and the stepping direction aligned. Ideally, such calculations should, therefore, be carried out iteratively, that is, adjusting the computational grid after a model run.

The grid chosen was orthogonal (in order to decrease the possibility of instabilities occurring). The flow pattern produced by a source and sink of equal strength, μ (=1), and separated by a distance, a (=1), was calculated, with the grid taken as the intersection of potential lines, ϕ, and streamlines, ψ. The potential lines are given by the circles

$$(x - \text{cotanh}\ \phi)^2 + y^2 = (\text{cosech}\ \phi)^2 \qquad (4.21)$$

and the streamlines by circles

$$x^2 + (y + \text{cotan}\ \psi)^2 = (\text{cosech}\ \psi)^2 \qquad (4.22)$$

The maximum value of ϕ was chosen to satisfy the previously described requirements of the criticality positions.

The grid used for all calculations is shown in Figure 4-4.

4.3.2 Solution Properties

The results from three runs, having $\hat{u}_a$ values of 0.157, 0.25 and 0.50 (together with initial conditions of $\hat{r}_o = 0.5$ and $F_s = 100.0$ as in the stagnant case) will be discussed in the following.

The entrainment relation used was that of Jirka (1982), Equation (2.79), this being Richardson number dependent. Section 2.4, Equation (2.76) gives the Richardson number as being dependent on the velocity of the current. This involves the assumption that the velocity of the density current, being much larger than the ambient, is responsible for the entrainment. It could be argued that a Richardson number dependent on the velocity difference between the density current and ambient is more representative, notably if the density current velocity is much closer to that of the ambient. Some runs made using this alternative relation were compared with those made using a Richardson number dependent on the density current velocity alone. The solution was found to exhibit no great sensitivity to the choice of Richardson number definition, so that hereafter one dependent on density current velocity alone will be adopted.

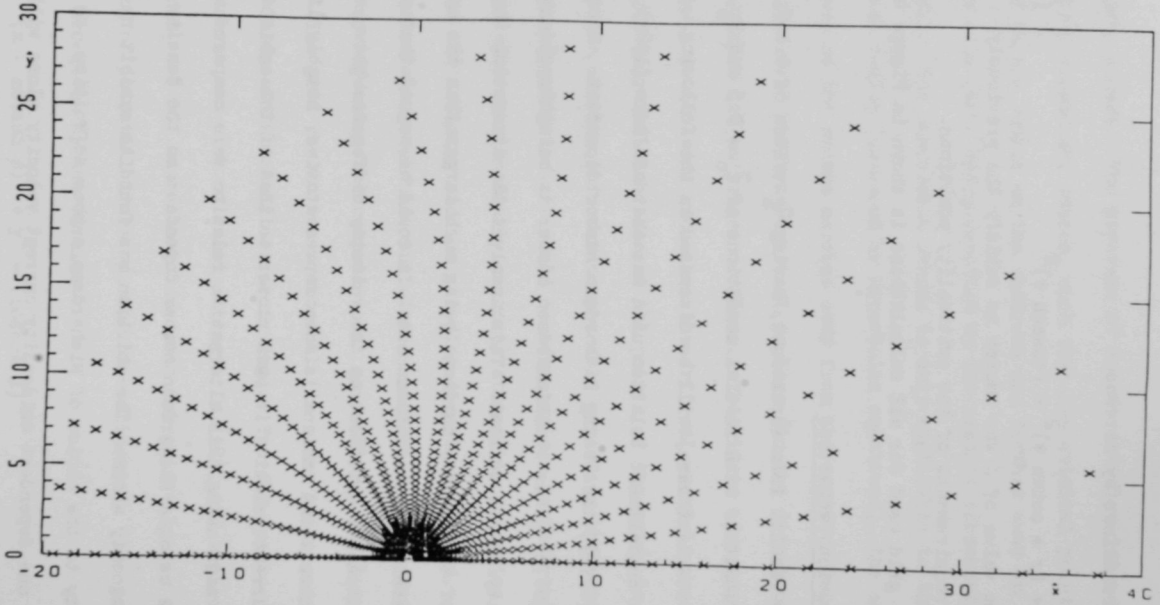

Figure 4-4 The orthogonal grid used for the numerical computations of a source in an ambient flow ($\hat{u}_a > 0$).

It should be noted at this point that, as discussed previously, the marching solution stops when a local Froude number, based on a velocity, q_m, in the marching direction becomes close to one. This frequently occurs in the (-x, y) quadrant some distance from the x-axis, due to the velocity there pointing in the +x direction, while the grid is algined more upstream in this region. Thus, although the actual Froude number, q/c is greater than one, the component along the marching direction, q_m/c, has a value of one.

Figure 4-5 (a to c) shows equi-Froude number contours for values 1.5, 2.0 and 2.5, and equi-buoyancy contours for values 0.3, 0.5 and 1.0. It can be seen that both Froude numbers and buoyancy contours assume almost circular shapes, the former being displaced downstream and the latter upstream. The Froude numbers decrease much more quickly upstream of the source than downstream. This could be expected as the upstream flow moves against the ambient, entraining negative momentum flux, which would slow it down more quickly than the positive momentum flux entrained by the downstream flow.

Also, the buoyancy decreases more quickly downstream than upstream. The buoyancy is dependent on the amount of entrainment of ambient fluid of greater density. The entrainment, however, is inversely proportional to the Richardson number (Equation 2.79), which is itself inversely proportional to the density current velocity upstream has just been discussed, this supports the

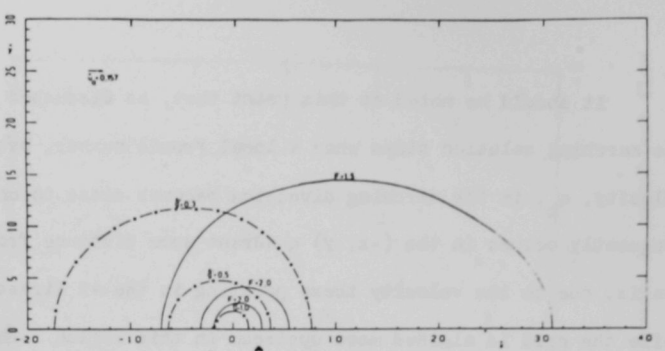

a) $\hat{u}_a = 0.157.$

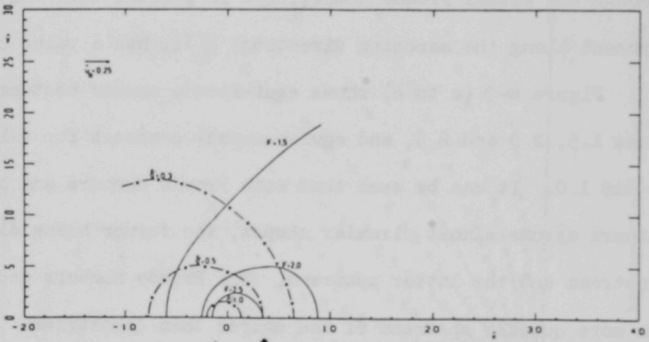

b) $\hat{u}_a = 0.250.$

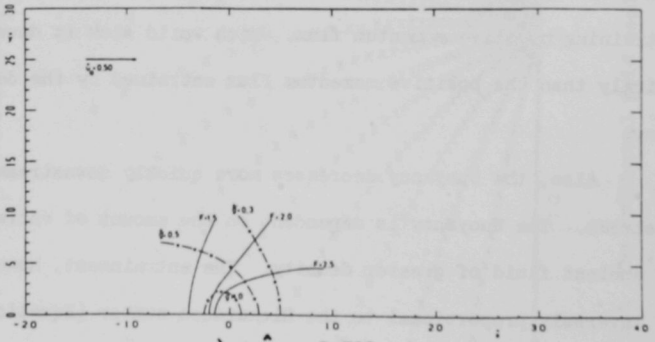

c) $\hat{u}_a = 0.500.$

Figure 4-5 Equi-Froude number and equi-buoyancy contours for a radial source discharging into an ambient flow. Near-field non-dimensionalization is used.

buoyancy results obtained. These effects grow more pronounced with increasing ambient velocity as seen by the variations in Figure 4-5 a through c. This effect can also be seen in Figure 4-6 which, for the case of $\hat{u}_a = 0.157$, shows the variations in the properties of the density current up- and downstream along the +x and -x axes.

Figure 4-7 a to c shows equi-height contours of value 0.30, 0.25, 0.20, 0.15 and 0.10, and equi-velocity contours 0.25, 0.5 and 1.0 again for the three ambient velocities considered. Also, Figure 4-6 summarizes the variations along the x-axis. The velocity shows distorted circles similar to the Froude numbers discussed previously. The height, however, distorts from an initially circular profile ($h = 0.1$), to non-circular profiles, this being seen in Figure 4-6 from the height values upstream slightly decreasing after an initial increase, whereas this decrease does not occur downstream.

4.4 A Simplified Model for Moving Ambient ($\hat{u}_a > 0$)

The results presented in Section 4.2 indicate that some of the density current properties, such as Froude number, velocity and buoyancy, vary such that their contours are approximately circular (albeit with displaced centers). This circular behavior was also obtained for the stagnant case (Section 4.2), although in this case the circles were centered on the origin.

This similarity suggests a simpler (though not accurate) model, obtained by simply shifting downstream, in a Galilean

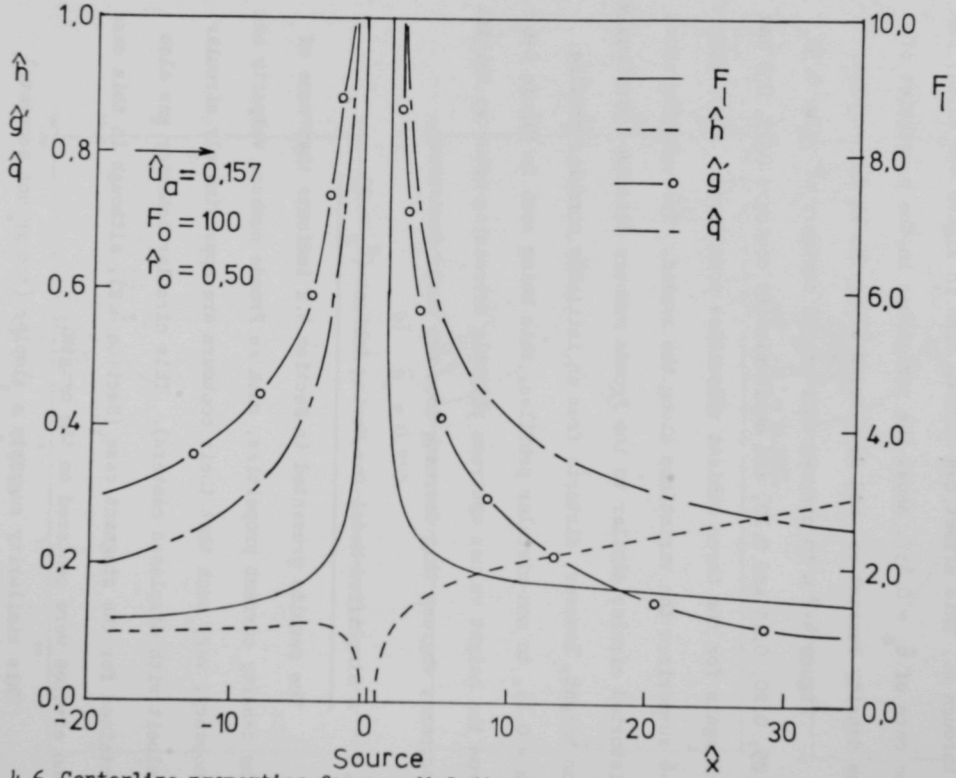

Figure 4-6 Centerline properties for a radial discharge into a moving ambient, $\hat{u}_a$ = 0.157, using the entrainment function of Jirka (1982). Near-field nondimensionalization is used

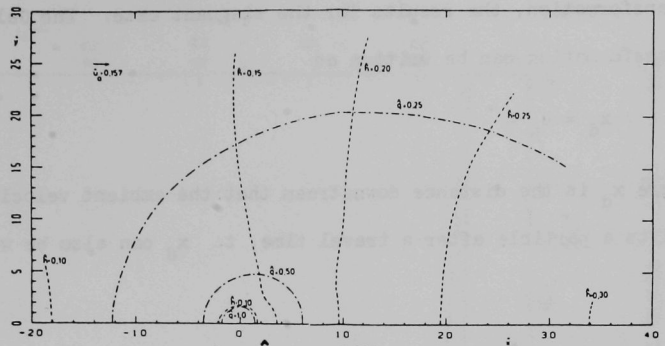

a) $\hat{u}_a = 0.157.$

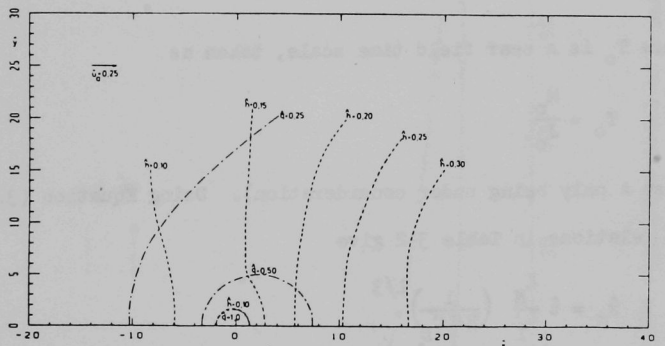

b) $\hat{u}_a = 0.250.$

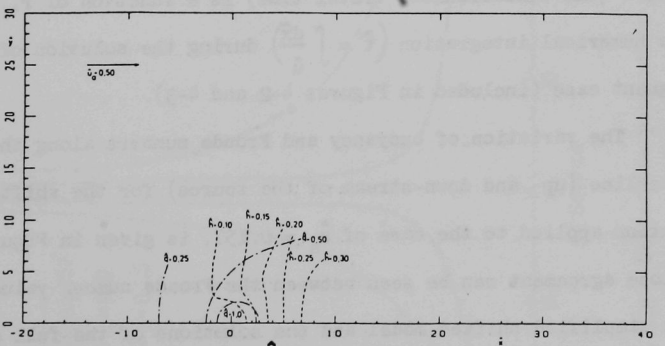

c) $\hat{u}_a = 0.500.$

Figure 4-7 Equi-velocity and equi-height contours for a radial source discharging into an ambient flow. Near-field nondimensionalization is used.

transformation, the results for the stagnant case. The Galilean transformation can be written as

$$x_d = u_a \, t \tag{4.23}$$

where x_d is the distance downstream that the ambient velocity, u_a, shifts a particle after a travel time, t. x_d can also be written as

$$x_d = u_a \, \hat{t} \, T_o \tag{4.24}$$

where T_o is a near field time scale, taken as

$$T_o = \frac{M_o}{J_o} \tag{4.25}$$

(Case A only being under consideration). Using Equation (3.77) and the relations in Table 3-2 give

$$\hat{x}_d = \hat{t} \, \frac{\ell_N}{\ell_I} \left(\frac{1}{2\pi C_D}\right)^{1/3} \tag{4.26}$$

where $\hat{t}$ (the dimensionless travel time) is a function of $\hat{r}$, obtained by a numerical integration $\left(\hat{t} = \int \frac{d\hat{x}}{\hat{u}}\right)$ during the solution of the stagnant case (included in Figures 4-2 and 4-3).

The variation of buoyancy and Froude numbers along the centerline (up- and down-stream of the source) for the shifted solution applied to the case of $\hat{u}_a = 0.157$, is given in Figure 4-8. A close agreement can be seen between the Froude number values in this simplified shifted model and the solutions of the full equations (Figure 4-6). The buoyancy values are not as close, as might be

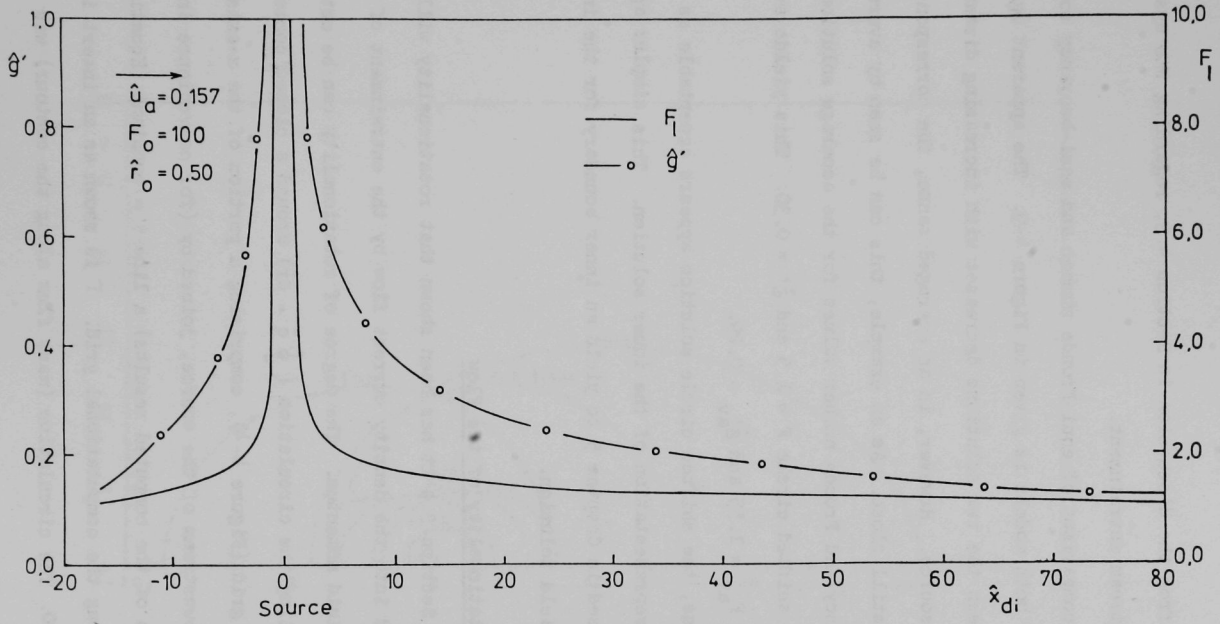

Figure 4-8 Centerline properties from the simplified model of a radial discharge into a moving ambient, $\hat{u}_a = 0.157$.

expected from the discussion in Section 4.3, regarding the upstream and downstream entrainment.

A comparison of equi-Froude number and equi-buoyancy contours for both models is given in Figure 4-9. The apparent agreement between the two solutions decreases with increasing distance from the source. However, in an averaged sense, the correspondence is still close. As an example, this can be seen by averaging the buoyancy and Froude number values for the accurage solution along the shifted circle $F = 1.5$ and $\hat{g}' = 0.30$. This yields average values of $F_{av} = 1.55$ and $\hat{g}'_{av} = 0.29$.

Thus, the shifted circle solution appears acceptable as an averaged representation of the inner solution. This simpler approach will be used in Chapter 5 to yield an inner boundary for the intermediate field solution.

4.4.1 Rotationality of the Flow

In Section 3.4 it has been shown that rotationality will be introduced into the density current flow by the entrainment of ambient fluid momentum. The degree of rotationality can be estimated by evaluating the circulation ($\oint \bar{q} \cdot d\bar{r}$) around a closed contour, Γ, of the grid (Figure 4-4), comprising a portion of the x-axis both up- and downstream of the source, joined by (for convenience in evaluation of the computed results) a line ψ = constant (Equation 4.22), along the computational grid. Γ is shown as an insert in Figure 4.10. The circulation (mass flux along the contour) was

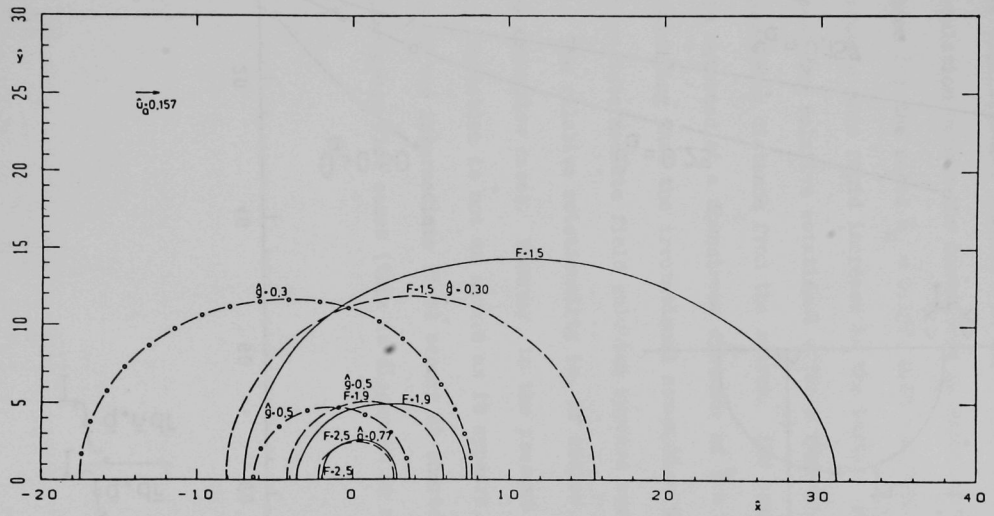

Figure 4-9 A comparison of the buoyancy and Froude numbers from the simplified and accurate models for a radial discharge into a moving ambient, $\hat{u}_a = 0.157$.

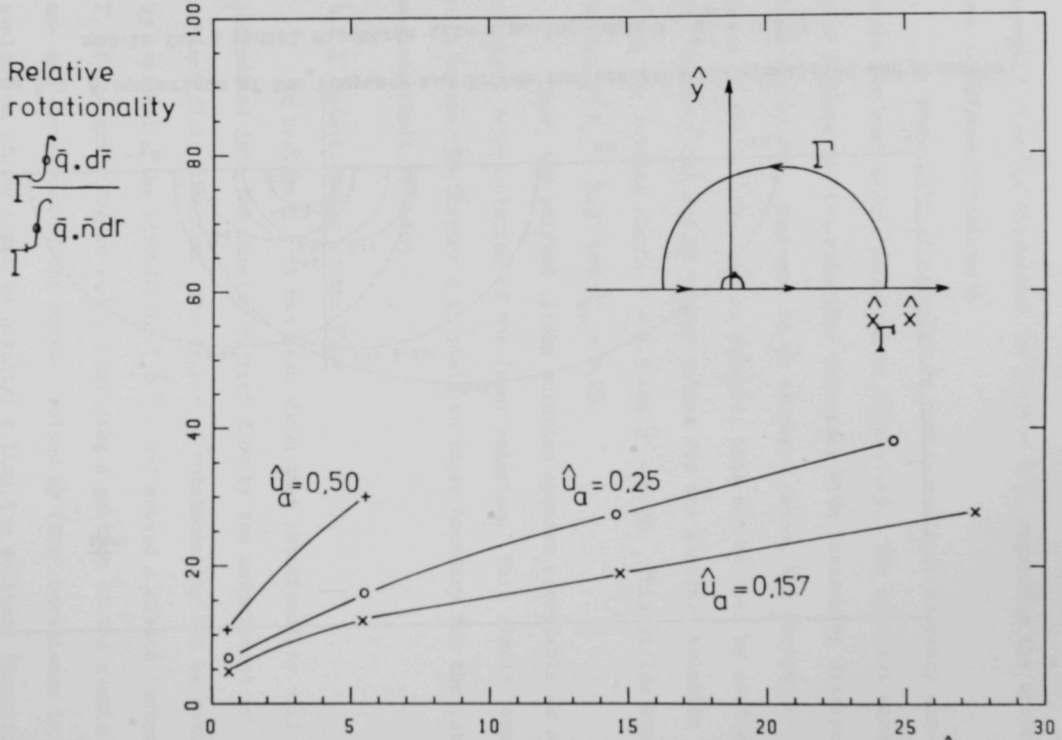

Figure 4-10 Variation of circulation around a contour, Γ, (as a percentage of the local normal mass flux) with $\hat{x}_\Gamma$, the downstream point of intersection of Γ with the $\hat{x}$ axis. Circulation values for $\hat{u}_a$ values of 0.157, 0.250 and 0.500 are considered.

normalized by the total mass flux normal to the contour ($\oint \bar{q} \cdot \bar{n} dr$, where $\bar{n}$ is a unit vector normal to $\bar{r}$) in order to obtain an estimate of its relative significance. Figure 4-10 shows the variation of this normalized circulation versus the downstream x_Γ value of the contour intersection for the cases $\hat{u}_a$ = 0.157, 0.25 and 0.50. It can be seen that after a more rapid increase in the initial strong entrainment zone, the relative rotational effects increase rather slowly with increasing distance from the source. For example, a value of 18% is obtained at a downstream distance of $\hat{r}$ = 15.0 for $\hat{u}_a$ = 0.157, indicating that the irrotational assumption that is made in the subsequent intermediate field solution appears acceptable to a first order. The relative rotationality is, of course, stronger for the higher crossflow cases. However, in the present modeling framework this limitation is not as severe as it appears, since the transition to the intermediate field occurs at shorter distances for these higher cross flow cases (this is discussed in more detail in Section 5.5).

CHAPTER 5

THE INTERMEDIATE FIELD (TRANSCRITICAL FLOW REGION) SOLUTION

The basic problem definition and choice of solution technique are dealt with in Section 5.1 and 5.2, respectively. The details of the numerical scheme are discussed in Section 5.3.

In Section 5.4, several aspects of the solution scheme, such as accuracy, stability and specification of boundary conditions, are examined in a simple numerical experiment, namely transcritical flow in a radially expanding channel.

Section 5.5 discusses the actual application to the problem under consideration, namely the intermediate field region for a buoyant source in an ambient crossflow.

Section 5.6 demonstrates the iterative technique involved in the selection of different grids until one is found which has the correct outer boundary shape (determined by comparing the 'outer' and 'inner' boundary height values).

Section 5.7 shows fully grid-iterated results for various flow conditions, thus giving a basis for prediction of the boundary shape for various relative intermediate to near field strengths.

5.1 Problem Definition

The equations governing the intermediate field transcritical region are given in non-dimensional form in Equations (3.65) to (3.67), together with the nonlinear potential Equation (2.35), which can be

written in a nondimensional form as

$$(\tilde{h} - \tilde{\phi}_{\tilde{x}}^{2})\tilde{\phi}_{\tilde{x}\tilde{x}} - 2\tilde{\phi}_{\tilde{x}}\tilde{\phi}_{\tilde{y}}\tilde{\phi}_{\tilde{x}\tilde{y}} + (\tilde{h} - \tilde{\phi}_{\tilde{y}}^{2})\tilde{\phi}_{\tilde{y}\tilde{y}} \tag{5.1}$$

where $\tilde{\phi} = \dfrac{\phi}{\ell_I\sqrt{\sigma h_s^{s+1}}}$. The problem can either be described using the mass and momentum conservation Equations (3.65) and (3.66), or, equivalently, the energy and mass conservation Equations (3.67) and (3.65). The potential Equation (5.1) is applicable whichever equation set is used, provided the solutions are smooth.

The boundary conditions have been described as:

1) An inner boundary (of circular shape, using the simplified near field model, Section 4.4).

   The exact location and flow conditions along this boundary will be known, using the arguments presented in Section 3.6.

2) An outer curved boundary, the "front", forming the horizontal interface between the density current and the ambient flow.

   The height, h_B, along this boundary, can be determined as a function of the boundary angle, θ, using Equation (3.45), which can be written in nondimensional form as

$$\tilde{h}_B = (\sin\theta)^{\frac{1}{s+1}} \tag{5.2}$$

   However, the boundary shape, θ, is not known a priori, and must be obtained by iteration. Each iteration consists of taking an initial boundary estimate (which will

be improved with each iteration), and solving for the flow field within this boundary. Thus a value for the height along the boundary is obtained, which can be compared with $\tilde{h}_B(\theta)$ from Equation (5.2). Based on this comparison, an alternative boundary shape is assumed, its flow field solved for, and again the heights compared. When agreement is reached, the converged boundary will have been found.

3) Symmetry conditions along the centerline of the flow.

4) A downstream boundary condition.

The flow will be supercritical on reaching this boundary, and hence no boundary conditions need be defined along it.

5.2 Choice of Solution Technique

The equations and boundary conditions defining the flow field have been discussed in Section 5.1. The solution method chosen can be seen to require the ability to:

1) Model nonlinear supercritical and subcritical flows.

2) Model unknown possible shock positions.

3) Obtain accurate solutions along unknown, curved boundaries.

Various methods of solution are possible, as discussed in general in Section 2.6. They are:

a) The hodograph method.

b) Numerical approaches, using finite difference or finite element schemes.

Method (a), the hodograph method, as discussed in Section 2.6, applies the hodograph transformation to the nonlinear equation set in the physical plane, to obtain a linear equation set in the hodograph plane. This method appears to offer many advantages, in particular as the linearity in the hodograph plane allows the use of superposition. However, difficulties arise when the Jacobian, J (Equation 2.93), of the transformation takes on zero or infinite values, resulting in multivalued solutions. In practice, this is a considerable obstacle, particularly as the case J = 0 occurs near the shock lines which form an important part of the problem under consideration.

Another severe difficulty with this method would be accounting for the curved boundaries in the hodograph plane.

Method (b) comprises the many possible numerical approaches, including shock patching and shock capturing methods, and finite difference and finite element schemes, (Section 2.6).

Within the domain of finite difference methods, the papers of Jameson (1971, 1974) and Caughey and Jameson (1977a, 1977b, 1979), develop (as discussed in Section 2.6) a method of shock capturing by adding an artificial viscosity to the equations describing the flow, which also takes care of accurate type-differencing of the equations. This results in a shock representation which conserves energy -

described as "E-curves" in Section 2.2. In addition, they introduce a finite volume formulation, the use of which allows an accurate representation of such geometrical difficulties as the curved boundaries, without the difficulties involved with a global transformation.

Finite element methods would allow for flexibility in the shape of the domain, and also for irregularly shaped elements, allowing variable detail. However, any significant deviation in the external boundary would result in errors due to possible greatly enlarged sub-elements. The creation of extra elements to alleviate this problem would require significant program changes. As in finite difference methods, an artificial viscosity concept developed by Hafez *et al*. (1978) has been used (Tatum, 1982 and Bredif, 1983) which allows shock capturing and accounts for the appropriate equation type in super- and subcritical regions. The resulting shock is also energy conserving, as described above.

Choice of Solution Method

The hodograph method was determined unsuitable due to the disadvantages listed previously. Both finite element techniques and Caughey and Jameson's finite difference (finite volume) technique offered obvious possibilities, although both would have to be modified for the particular problem under consideration. In both methods, computational time and costs would likely be large.

Due to the immediate availability at the time this

investigation was begun (1980), the finite difference program of Caughey and Jameson, was the favoured alternative. This method is described in detail in the following, together with certain alterations that pertain to the present hydraulic problem.

5.3 Numerical Scheme

The equations used in this solution procedure are the conservation of mass and energy Equations (3.65) and (3.67). The potential Equation (5.1), will be referred to in this section as an aid to understanding the flow properties.

5.3.1 Upwinding Considerations

If a local Cartesian co-ordinate system (s,n) is introduced, such that the s-direction lies along the local flow direction, the the potential Equation (5.1) can be rewritten as

$$(c^2 - q^2)\phi_{ss} + c^2\,\phi_{nn} = 0, \tag{5.2}$$

where

$$\phi_{ss} = \frac{1}{q^2}\,(u^2\phi_{xx} + 2uv\phi_{xy} + v^2\phi_{yy}) \tag{5.3}$$

$$\phi_{nn} = \frac{1}{q^2}\,(v^2\phi_{xx} - 2uv\phi_{xy} + u^2\phi_{yy}). \tag{5.4}$$

Taking the potential equation in the form of Equation (5.2) clarifies the decision on which parts of the equation should be upwinded in a supercritical regime to obtain an appropriate directional bias. Thus, terms in ϕ_{ss} and ϕ_{nn} should be approximated using upwinded and central

differences, respectively. The stencil used for each part is as shown in Figure 5.1. The upwind difference formulae can be written as

$$\phi_{xx} = \frac{\phi_{i,j} - 2\phi_{i-1,j} + \phi_{i-2,j}}{\Delta x^2} \tag{5.5}$$

$$\phi_{xy} = \frac{\phi_{i,j} - \phi_{i-1,j} - \phi_{i,j-1} + \phi_{i-1,j-1}}{\Delta x \ \Delta y} \tag{5.6}$$

$$\phi_{yy} = \frac{\phi_{i,j} - 2\phi_{i,j} + \phi_{i,j-2}}{\Delta y^2} \tag{5.7}$$

if u, v are positive. Thus these upwind formulae for ϕ_{xx}, ϕ_{xy} and ϕ_{yy} can be though of as approximating the expressions $\phi_{xx} - \Delta x \phi_{xxx}$, $\phi_{xy} - (\frac{\Delta x}{2} \phi_{xxy} + \frac{\Delta y}{2} \phi_{xyy})$ and $\phi_{yy} - \Delta y \phi_{yyy}$, respectively. Thus, the effect of using upwind differences for the ϕ_{ss} term is to introduce, due to the truncation errors, a term of the form

$$(1 - \frac{c^2}{q^2})\Big(\Delta x (u^2 u_{xx} + uvv_{xx}) + \Delta y (uvu_{yy} + v^2 v_{yy})\Big) \tag{5.8}$$

Because of the second order diffusion terms, this can be interpreted as the addition of an artificial viscosity term, which will be referred to later in this section.

5.3.2 Finite Volume Scheme and Associated Lumping Error

The finite volume scheme has been discussed in Section 4.1. Applying this local transformation to the mass conservation Equations (3.65), yields

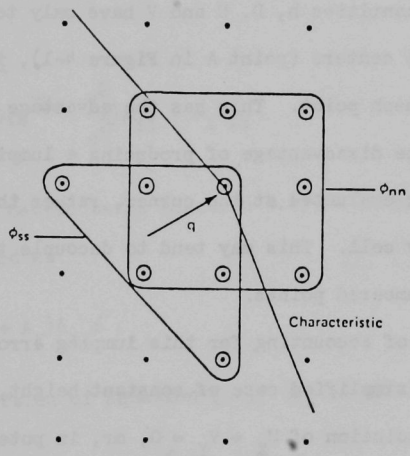

Figure 5-1 The rotated difference stencil. Showing the points contributing to the upwinded (ϕ_{ss}) and central differenced (ϕ_{nn}) parts of the potential Equation (5.2) when applied to a supercritical region, (after Jameson, 1978) .

$$\frac{\partial}{\partial X}(hDU) + \frac{\partial}{\partial Y}(hDV) = 0 \tag{5.9}$$

where D is the determinant of the Jacobian of the transformation, given in Equation (4.4) and X and Y are the contravariant coordinates (Section 4.1). It should be noted that this treatment has the advantage that the quantities h, D, U and V have only to be evaluated at the primary cell centers (point A in Figure 4-1), i.e., only at one point for each mesh point. This has the advantage of reducing computing time, but the disadvantage of producing a lumping error due to the fluxes being evaluated at the corner, rather than the face-center of the auxiliary cell. This may tend to decouple the solution at odd- and even-numbered points.

A method of accounting for this lumping error is indicated by considering the simplified case of constant height, which reduces the problem to the solution of $U_X + V_Y = 0$, or, in potential form,

$$\mu_{YY}\delta_{XX}\phi + \mu_{XX}\delta_{YY}\phi = 0, \tag{5.10}$$

where the μ, δ notation is as defined in Section 4.1. Expansion of Equation (5.10) yields the relation

$$\phi_{i,j} = \frac{1}{4}(\phi_{i+1,j+1} + \phi_{i+1,j-1} + \phi_{i-1,j+1} + \phi_{i-1,j-1})$$

in which the decoupling is apparent. Adding a term of the form $-\epsilon\,\Delta Y\,\delta_{XY}\phi$ effects a movement of the evaluation point from A to B as ϵ changes from 0 to 1/2. Accounting similarly for each face necessitates adding a term $-\epsilon\,\delta_{XXYY}\phi$ to Equation (5.10) (assuming $\Delta Y = 1$).

The lumping error in the general case is treated analogously to that above. The coefficient of the $\delta_{XY}\phi$ term is taken as the sum of the coefficients of the ϕ_{XX} and ϕ_{YY} terms, respectively. So that, as

$$(\rho DU)_X \approx \rho D(g^{11} - \frac{U^2}{c^2})\phi_{XX} = A_X\phi_{XX} \tag{5.11}$$

and

$$(\rho DV)_Y \approx \rho D(g^{22} - \frac{V^2}{c^2})\phi_{YY} = A_Y\phi_{YY} \tag{5.12}$$

where g^{ij} are the metric terms (Section 4.1), a lumping correction term can be defined as

$$Q_{XY} = (A_X + A_Y)\delta_{XY}\phi \ . \tag{5.13}$$

Thus the final version of Equation (5.9) can be written as

$$\mu_Y\delta_X(hDU) + \mu_X\delta_Y(hDV) - \frac{\epsilon}{2}\,\delta_{XY}Q_{XY} = 0.$$

5.3.3 <u>Addition of Artificial Viscosity</u>

As discussed in Section 5.2, the method chosen achieves stability in the supercritical regions by explicitly adding an artificial viscosity in conservation form, such that the mass conservation equation, Equation (5.9), can be written as

$$\frac{\partial}{\partial X}(hDU + P) + \frac{\partial}{\partial Y}(hDV + Q) = 0. \tag{5.15}$$

P and Q could also be interpreted as artificial mass fluxes, P is defined as

$$P \approx \mu D|U|\delta_X \rho \tag{5.16a}$$

or, in finite difference form

$$P_{i+1/2,j} = \hat{P}_{i,j} \qquad \text{if } U > 0$$

$$= \hat{P}_{i+1,j} \qquad \text{if } U < 0$$

where

$$\hat{P} = \frac{\mu\rho D}{c^2}(U^2\delta_{XX} + UV\delta_{XY})\phi \tag{5.16b}$$

i.e., while the expression for P is defined using central differences, the term $\delta_X P$ is effectively upwinded. A similar treatment is used for Q, which is defined as

$$Q \approx -\mu D|V|\delta_Y \rho \tag{5.17a}$$

and

$$\hat{Q} = \frac{\mu\rho D}{c^2}(UV\delta_{XY} + V^2\delta_{YY})\phi \tag{5.17b}$$

In the above, μ is a switching function of the form

$$\mu = \max\left(0,\ 1 - \frac{c^2}{q^2}\right) \tag{5.18}$$

to ensure that artificial viscosities are only added if the Froude number, $F = \frac{q}{c}$ is greater than one. Two issues regarding the switching

function are explored in Section 5.4.

- how F should be represented (averaged) when used to determine the shock position.
- whether an alternative value, F^2_{alt}, having a value slightly different from unity, would aid stability if used as an alternative cut-off value to unity itself.

It can be seen that the combined effects of $\delta_X P$ and $\delta_Y Q$, give, in the supercritical region,

$$\delta_X P + \delta_Y Q = \frac{\rho D}{c^2}\left(1 - \frac{c^2}{q^2}\right)(\Delta x U(U\phi_{XXX} + V\phi_{YYY})$$

$$+ \Delta Y V(U\phi_{XYY} + V\phi_{YYY})). \qquad (5.19)$$

This is consistent with the contravariant form of Equation (5.8), which was the term formed from summing the truncation errors introduced by taking upwinded differences for the ϕ_{ss} term.

This shows that a central differencing scheme can be used throughout, with just the addition of the term in Equation (5.19) in the supercritical regions in order to introduce the correct directional bias.

5.3.4 Solution of the Difference Equations

For a given geometry and boundary conditions, iterative methods are required to solve the finite difference approximations to the highly implicit equations describing the problem under consideration. In Jameson and Caughey's work, quasi-time dependent iterations were used,

since successive iterative approximations to a solution of the potential Equation (5.1), could be thought of as solutions of an unsteady flow problem described by

$$(h - u^2)\phi_{xx} - 2uv\phi_{xy} + (h - v^2)\phi_{yy} - 2\bar{\alpha}\phi_{xt}$$

$$- 2\bar{\beta}\phi_{yt} - \bar{\gamma}\phi_t = 0 \qquad (5.20)$$

where the coefficients $\bar{\alpha}$, $\bar{\beta}$ and $\bar{\gamma}$ should be chosen to ensure fastest convergence to the final (steady-state) solution. An analysis of the values required for these coefficients was made by Caughey (1978). Applying the transformation

$$T = t - \frac{\alpha}{F^2 - 1} s + \beta n \qquad (5.21)$$

to Equation (5.20), converts it to the diagonal form

$$(1 - F^2)\phi_{ss} + \phi_{nn} + \left(\frac{\alpha^2}{F^2 - 1} - \beta^2\right)\phi_{TT} - \gamma\phi_T = 0 \qquad (5.22)$$

which can be seen to be a damped wave equation. The analysis of Jameson (1974), indicated that for critical cases ($F < 1$), the damping term, $\gamma\phi_T$, is required to remove dependence upon the arbitrary initial conditions. In the supercritical case, damping is not required, due to the orientation of the characteristic cone (Caughey, 1978). However, the relation

$$\alpha^2 > (F^2 - 1)\beta^2 \qquad (5.23)$$

must be obeyed in order to ensure that the streamwise direction remains timelike in the unsteady problem.

The iterative approach adopted is a Successive Line Over Relaxation (SLOR) scheme, which solves for a provisional potential value, $\phi'_{i,j}$ over constant 'i' lines. In order to calculate this provisional solution within a subcritical regime, the central differenced equations can be written in a form

$$\frac{(h - u^2)}{\Delta x^2}\left(\phi^{n+1}_{i-1,j} - 2\phi'_{i,j} + \phi^{n}_{i+1,j}\right)$$

$$\frac{- 2uv}{4\Delta x\Delta y}\left(\phi^{n}_{i+1,j+1} - \phi^{n}_{i+1,j-1} - \phi^{n}_{i-1,j+1} + \phi^{n}_{i-1,j-1}\right)$$

$$\frac{+ (h-v^2)}{\Delta y^2}\left(\phi^{n}_{i,j+1} - 2\phi^{n+1}_{i,j} + \phi^{n+1}_{i,j-1}\right) = 0 \qquad (5.21)$$

where the superscript n is such that $t = n\Delta t$. The distribution of updated (n+1) terms is determined to ensure diagonal dominance (that the maximum contribution to, say, $\phi'_{i,j}$ comes from $\phi_{i,j}$ rather than the total contribution from the neighbouring points, this being a sufficient but not necessary condition for linear stability). The new value, $\phi^{n+1}_{i,j}$ is obtained from the provisional value via the relation

$$\phi^{n+1}_{i,j} = \phi^{n}_{i,j} + \omega(\phi'_{i,j} - \phi^{n}_{i,j}) \qquad (5.22)$$

where ω is the over-relaxation factor. If the correction at each point is written as

$$C^n_{i,j} = \phi^{n+1}_{i,j} - \phi^n_{i,j} \tag{5.23}$$

then Equation (5.21) can be rearranged to the form

$$\left(\frac{h - u^2}{\Delta x^2}\right)(C_{i,j} - C_{i-1,j}) + \left(\frac{h - v^2}{\Delta y^2}\right)(-C_{i,j+1} + 2C_{i,j} - C_{i,j-1})$$

$$+ \left(\frac{2}{\omega} - 1\right)\left(\frac{h - u^2}{\Delta x^2}\right) C_{i,j} = R_{i,j} \tag{5.24}$$

where $R_{i,j}$'s is the residual, composed of a central difference form of Equation (5.1) evaluated at the nth iteration. Noting that $C_{i,j}$ is a discrete approximation to $\Delta t \phi_t$, enables an evaluation of $\bar{\gamma}$ by comparing Equations (5.20) and (5.24), as

$$\bar{\gamma} = \left(\frac{2}{\omega} - 1\right)(h - u^2)\frac{\Delta t}{\Delta x^2} . \tag{5.25}$$

This shows that ω must be less than 2 for positive damping. A von Neumann convergence test (Roache, 1976) can be applied for the case of a rectangular domain and periodic boundary conditions. This involves making a 'separation of variables' assumption, such that ϕ^n can be written as

$$\phi^n = G^n e^{ipx} e^{iqy} \tag{5.26}$$

where i in just this case represents the complex number $\sqrt{-1}$, p and q denote general x and y positions, and the growth factor,

$G = \phi^{n+1}/\phi^{n}$, the scheme being convergent if $|G| < 1$. It was shown by Caughey that a sufficient condition for this to occur, is, if the damping term is sufficiently large to counteract the destabilizing effects of the ϕ_{xy} term. Specific optimal values of ω are difficult to obtain for other than simple linear problems. However, by experience, Caughey (1978) cites values of 1.5 to 1.8 as reasonable for nonlinear problems.

A similar analysis can be carried out for the supercritical case. Additional consideration when determining the updated terms must be that Equation (5.23) is satisfied, together with the condition that $\gamma = 0$, as indicated by a von Neumann analysis. Caughey (1978) used upwinded formulae having the form

$$\phi_{xx} = \frac{2\phi^{n+1}_{i,j} - \phi^{n}_{i,j} - 2\phi^{n+1}_{i-1,j} + \phi^{n}_{i-2,j}}{\Delta x^2} \tag{5.27}$$

$$\phi_{xy} = \frac{2\phi^{n+1}_{i,j} - \phi^{n}_{i,j} - \phi^{n+1}_{i,j-1} - \phi^{n+1}_{i-1,j} + \phi^{n}_{i-1,j-1}}{\Delta x\ \Delta y} \tag{5.28}$$

These produce an approximation to Equation (5.23) as

$$\alpha = (F^2 - 1)\left(\frac{u}{q}\frac{\Delta t}{\Delta x} + \frac{v}{q}\frac{\Delta t}{\Delta y}\right) . \tag{5.29}$$

An additional ϕ_{st} term, $\omega_s \Delta t \phi_{st}$, is generally also added in the form $(u,\ v > 0)$

$$\omega_s \left(\frac{u}{\Delta x}(C_{i,j} - C_{i-1,j}) + \frac{v}{\Delta y}(C_{i,j} - C_{i,j-1})\right) \tag{5.30}$$

where ω_s is a parameter used to determine the amount of ϕ_{st} to be added, and is chosen as $\omega_s \geq 0$, taking the smallest value required to ensure Equation (5.23) is satisfied.

Thus the final equation for describing subcritical and supercritical flows ($\gamma = 0$, i.e., $\omega = 2$) can be written as

$$\alpha_1(C_{i,j} - C_{i,j-1}) + \alpha_2(C_{i,j} - C_{i,j+1})$$

$$+ \alpha_3(C_{i,j} - C_{i-1,j}) + \alpha_4 C_{i,j} = R_{i,j} \quad (5.31)$$

where

$$\alpha_1 = (h - v^2 + 3\mu v^2 + \omega_s v \Delta y) \frac{1}{\Delta y^2}$$

$$\alpha_2 = (h - v^2 + \mu v^2) \frac{1}{\Delta y^2}$$

$$\alpha_3 = (h - u^2 + 3\mu u^2 + \omega_s u \Delta x) \frac{1}{\Delta x^2}$$

$$\alpha_4 = \left(\frac{2}{\omega} - 1\right) (h - u^2) \frac{1}{\Delta x^2} \quad (5.32)$$

and $R_{i,j}$, the residual, is now made up of centered differences for the ϕ_{nn} terms and upwinded differences for the ϕ_{ss} terms (in supercritical regions, or centered differences in subcritical regions).

It can be seen that Equation (5.31) can be arranged to

$$(\alpha_1 + \alpha_2 + \alpha_3 + \alpha_4) C_{i,j} - \alpha_1 C_{i,j-1} - \alpha_2 C_{i,j+1}$$
$$= \alpha_3 C_{i-1,j} + R_{i,j} \quad (5.33)$$

where the right hand side is known. Equation (5.33) forms a tridiagonal matrix system which can be solved directly. The same approach as that described above for a finite difference approximation can be applied to the finite volume formulations of the governing Equation (5.31), with only the α coefficients assuming different values. This was the approach adopted by Caughey (1978) for aerodynamic problems having similar nonlinear governing equations (gas analogy, Section 2.3). However, the present hydraulic application contains much stronger shocks (jumps), due to the flow being much more supercritical than supersonic in the aerodynamic application. Thus, a pentadiagonal matrix system was introduced, which added some extra stability to the scheme. This pentadiagonal scheme allows the inclusion of contributions from the viscosity terms over additional points, such that the equation relating the correction terms (analogous to Equation (5.31) in the tridiagonal system) can be written as

$$\alpha_1 (C_{i,j} - C_{i,j-1}) + \alpha_2 (C_{i,j} - C_{i,j+1}) + \alpha_3 (C_{i,j} - C_{i-1,j})$$

$$+ \alpha_4 C_{i,j} + \alpha_5 (C_{i,j} - C_{i,j-2})$$

$$+ \alpha_6 (C_{i,j} - C_{i-2,j}) = R_{i,j} \qquad (5.34)$$

where, for U, V > 0,

$$\alpha_1 = hD\left(g^{22} + \frac{3\mu V - V^2 + \omega_s V_{max}(|U|, |V|)}{h}\right)$$

$$\alpha_2 = hD\left(g^{22} + \frac{\mu V - V^2}{h}\right)$$

$$\alpha_3 = hD\left(g^{11} + \frac{4\mu U^2 - U^2 + \omega_s U_{max}(|U|, |V|)}{h}\right)$$

$$\alpha_4 = \left(\frac{2}{\omega} - 1\right) hD\left(g^{11} - \frac{U^2}{h}\right)$$

$$\alpha_5 = -\mu DV^2$$

$$\alpha_6 = -\mu DU^2 \qquad (5.35)$$

and $R_{i,j}$ is the residual of Equation (5.15).

The pentadiagonal solution can be solved as for the tridiagonal system.

It should be noted at this point that the residual, $R_{i,j}$, gives a numerical evaluation of the left-hand side of Equation (5.15), which, in the converged case, should equal zero, the right-hand side of Equation (5.15). Thus the size of $R_{i,j}$ gives an estimate of how close or far from convergence the solution is at any point, and the increase or decrease of say the maximum residual $R_{i,j}$ shows whether the solution procedure is diverging or converging, respectively.

5.4 Numerical Experiment: Flow in a Radially Expanding Channel

This section discusses the application of the transcritical program to the flow of water in a radially expanding channel. This simple application is used to investigate the stability, shock treatment, and general accuracy of the program representation of the flow, as for this radial case, a theoretical solution is available for comparison. The latter is obtained from the continuity equation,

$$Q = qhr \tag{5.36}$$

where r is the radial distance from the source, together with the Beroulli Equation (3.66). These combine to give a cubic equation in q,

$$\frac{q^3}{2} - q + \frac{Q}{r} = 0 \tag{5.37}$$

solution of which gives the speeds at any point r. It should be noted that, Equation (5.37) being cubic, three roots are available for a given radial distance. Of these, one will be in the supercritical range, one subcritical, and one negative. The latter is physically unrealistic, as speeds, having no directional properties, must be positive.

For the case considered, theiinner boundary condition was taken as Q = 0.50 at r = 1.0. If the initial velocity is supercritical (q = 1.00), the theoretical solution can progress along the supercritical arm of the solution, as shown in Figure 5-2,

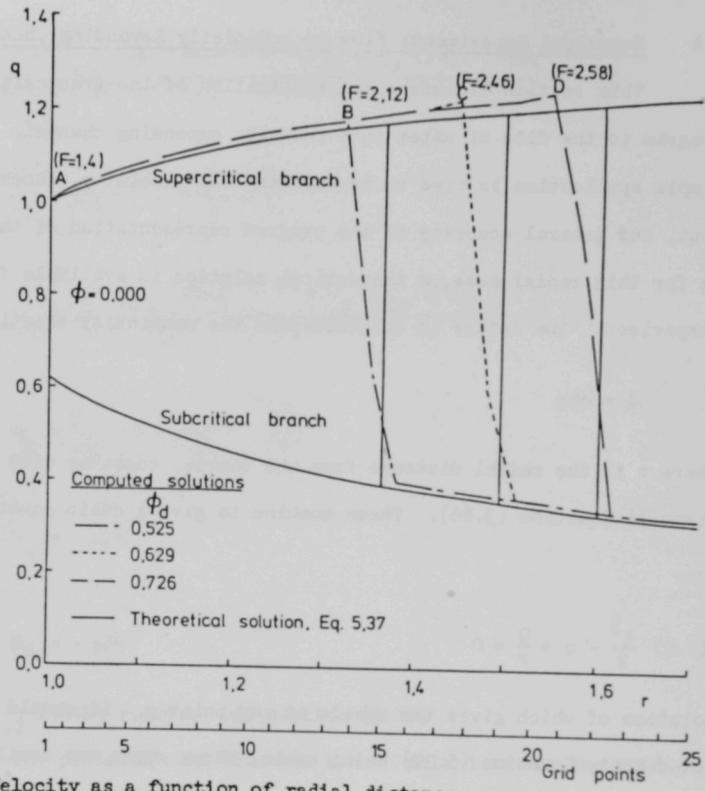

a) Velocity as a function of radial distance.

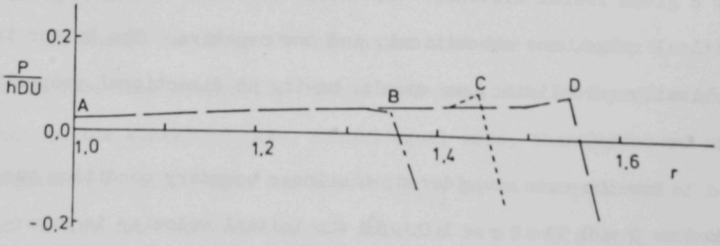

b) Ratio of artificial mass flux, P, to contravariant mass flux, hDU .

Figure 5-2 Velocity and artificial mass flux as a function of distance for a radial channel, using the transcritical program .

whereas an initially subcritical inflow ($q = 0.62$) will proceed subcritically. At any point, the supercritical solution can undergo a jump and become subcritical. Typical energy conserving jumps 'E' curves are shown in Figure 5-2. Energy conserving rather than momentum conserving jumps are shown, this being the type implicit in the numerical model formulation.

The numerical results are obtained by using a radial grid starting at $r = 1$, where a velocity, $q = 1.00$, is imposed as a boundary condition, the grid increment, Δr, being ≈ 0.025, as shown in Figure 5-2. If the flow is to undergo a jump, i.e., the downstream flow is subcritical, a downstream boundary condition is required - a given potential value, ϕ_d. (If the flow downstream is supercritical, no boundary condition is required as the downstream flow properties should be determined by the upstream conditions.) The various computational solutions shown in Figure 5-2 are obtained by imposing the various values of ϕ_d given in the diagram.

The computational solution can be seen to predict higher velocities than the theoretical solution for both the supercritical and subcritical regimes. This can be explained as follows. Both the theoretical and computational solutions start with a given physical mass flux ($Q = 0.50$). However, the computational scheme has an additional artificial mass flux, (viscosity related) as discussed in Section 5.3.1, and it is this total of physical and artificial mass flux which is conserved. As the supercritical solution progresses, the increased velocity values lead to increased artificial

fluxes and hence reduced physical mass fluxes. A reduced physical mass flux, from Figure 2-7, results in a larger superciritical velocity prediction, as is found in the supercritical region of Figure 5-2.

However, Figure 5-2 shows that the computationally predicted velocity is also larger than the theoretical value in the subcritical region after the jump. This can be explained by realizing that the mass flux, now entering the subcritical region, is the sum of the initial physical mass flux, Q, defined, plus the initial artificial mass flux defined within the program. Thus a mass flux is present, which is slightly greater than that on which the theoretical solution is based, leading to slightly larger calculated velocities from the numerical scheme.

If the solution were to consist of the subcritical branch only (i.e., $q = 0.62$) then no such error would have been introduced.

5.4.1 Shock Determination - Switching Function

Figure 5-2 shows that the scheme serves to average the shock over about 3 grid spacings. Whether the flow at any point is treated as supercritical or subcritical which, to some extent influences the jump width is dependent on the switching function, μ (Equation 5.18), i.e., on whether F is greater or less than one. In order to obtain better stability, i.e., slightly more averaging across a jump, values of F dependent on several neighbouring points rather than just the point (i,j) in question, can be used. In particular, if no F

averaging is used, a feedback can sometimes occur between the artificial and physical mass fluxes, leading to a velocity overshoot, (Points C and D in Figure 5-2), which can sometimes be large enough to cause the program iterations to diverge. Various averaging methods were tested for the radial case, such as

$$F^2_{i,j} = \frac{F^2_{i-1,j} + F^2_{i,j}}{2} \tag{5.38}$$

and

$$F^2_{i,j} = \sqrt{F^2_{i-1,j}\, F^2_{i,j}} \tag{5.39}$$

It was found that Equation (5.38) gave most stability so that this was adopted, and used to generate Figure 5-2.

An additional method of increasing stability, used for the early iterations, when the overshoot is more likely to occur, due to possibly poor initial conditions, can be used. This is to introduce an artificial Froude number cut-off, F^2_{art}, which is taken as less than 1.0, generally 0.9 or 0.8, or even as low as 0.5 if a very strong jump is expected. Once the quasi-time-dependent solution approaches convergence, this can gradually be increased back towards 1.0. Lower values of F_{art} cause the solution to be treated as supercritical (i.e., artificial viscosities added over more grid elements). This appears to discourage the formation of overshoots, and hence enables a better approximation to the solution to be obtained before the strong jumps are allowed to occur.

5.4.2 Values of the Coefficients ω and ω_s

In Section 5.3.3 mention was made of Caughey's (1978) original recommendation, which, for his aerodynamic applications, was for over-relaxation factor values, ω, of 1.5 to 1.8, as mentioned in Section 5.3.3. Similar values were found useful for the present hydraulic application, although values of 1.4 were sometimes used for initial iterations, and values of 1.8 would only be used very close to convergence. Values of 2.0 were automatically set in subcritical regions.

Section 5.3.3 pointed out that the coefficient, ω_s, should be greater than or equal to zero, but as small as possible. Values of 0.40 were generally used initially, decreasing to 0.35 in later stages of convergence.

5.5 Application of the Transcritical Model to a Radial Discharge Into a Moving Ambient: General Procedures

The following general steps need to be undertaken in constructing an intermediate field transcritical solution:

For a given value of the ratio of intermediate to near field strength, ℓ_I/ℓ_N:

1) Define the inner boundary conditions according to the transition conditions obtained from the near-field solution (Sections 3.6 and 5.7).

2) Assume an intermediate field solution domain and generate an orthogonal grid.

3) Carry out a transcritical solution for the domain.

4) Evaluate the frontal boundary conditions (height matching) and adjust the solution demain. Iterate to step two.

5.5.1 Near-Intermediate Field Transition Conditions

In Section 5.5, solutions for the transcritical intermediate field are presented for a full range of relative near-intermediate field strength values, ℓ_I/ℓ_N. The determination of the boundary conditions appropriate for these ℓ_I/ℓ_N values will be discussed herein.

A simplified near field model for a moving ambient, involving a Galilean transformation of the stagnant case solution (shifted circles), was presented in Section 4.4. The latter model provides a method of obtaining the type of boundary discussed in Section 3.6. This assumes radial flow properties across it, together with an "equi-energy transition", obtained by equating the Bernoulli equations for the near and intermediate flows as given in Equation (3.78).

In practice the boundary position (transition radius), $\hat{r}_T$, can be evaluated from ℓ_I/ℓ_N using the numerical near field model; this result is plotted in Figure 5-3. The flow properties at this transition, $\hat{h}(\hat{r}_T)$, $\hat{q}_T(\hat{r}_T)$ and $F_{\ell T}(\hat{r}_T)$, can also be evaluated from the numerical results given in Figure 4-1. The radius $\hat{r}_T$, in the intermediate field non-dimensionalization, is, by simple manipulation,

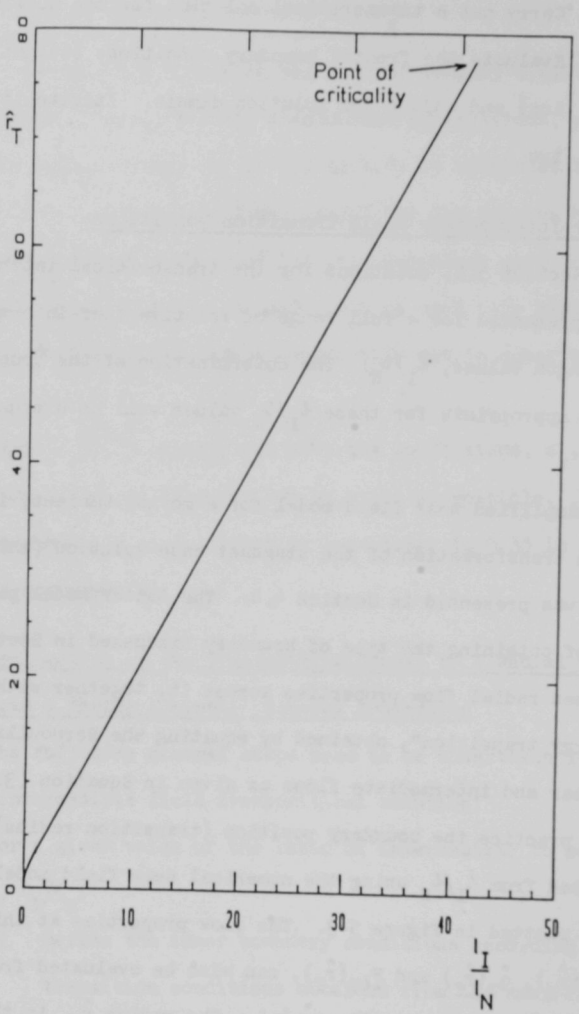

Figure 5-3 The variation of the transition radius, $\hat{r}_T$, with the relative intermediate to near-field strengths, ℓ_I/ℓ_N .

$$\hat{r}_T = \frac{\hat{r}_T}{\ell_N} \frac{\ell_N}{\ell_I} = \hat{r}_T \frac{\ell_N}{\ell_I} \quad . \tag{5.40}$$

Similarily the location of the center of the circle, obtained from $\hat{x}_d$, given by Equation (4.26), can be written in the intermediate field non-dimensionalization as

$$\tilde{x}_d = \hat{x}_d \frac{\ell_N}{\ell_I} \tag{5.41}$$

Thus a complete definition of the location and flow properties of the equi-energy transition between the near and intermediate fields is obtained as the upstream boundary condition for the transcritical flow domain.

5.5.2 Generation of an Orthogonal Grid (Using a Boundary Integral Equation Method)

A typical orthogonal grid used for this application is as shown in Figure 5-4. (An orthogonal grid is used due to it's relative ease of generation.) The location of the inner displaced circle C1C2 is determined by the relative near- and intermediate field strengths as represented by the transition conditions, discussed in Sections 3.6 and 5.7. The downstream boundary, D1D2, is located, from experience, far enough downstream to ensure that the flow has become everywhere supercritical, having passed through a shock and critical line. The stagnation point, S, and the shape of the boundary SD1 is determined by iteration, as described in Section 5.6.

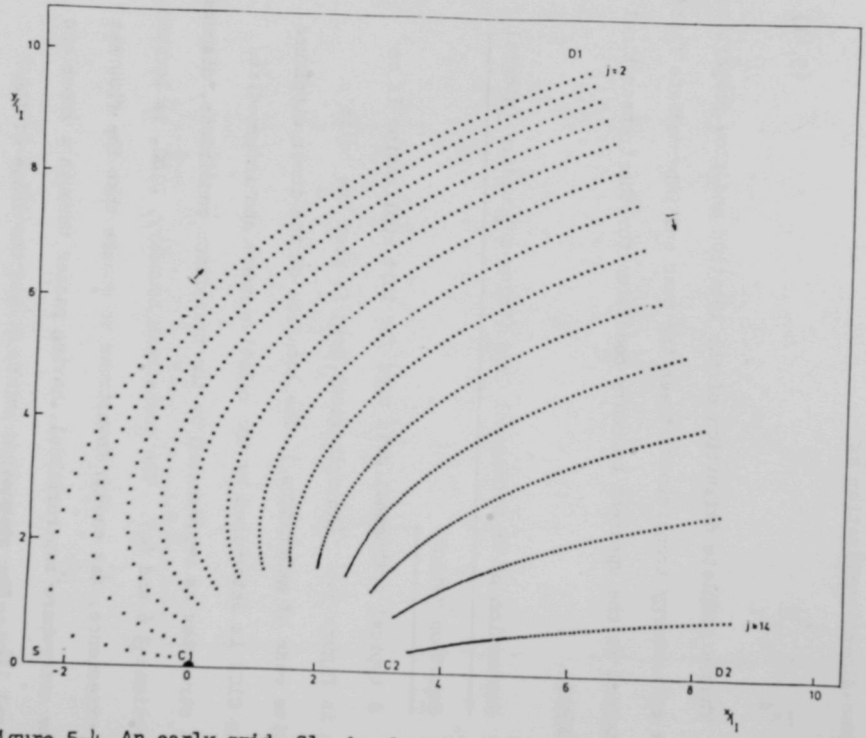

Figure 5-4 An early grid, G1, developed using the BIEM method, and used for the transcritical program

The basic shape SD1, may initially be sketched by hand, and is then specified by the quintic polynomial most closely matching their shape, selected in order to obtain a more regular boundary.

Once the boundary has been specified in this manner (at any stage of the iterative process), the internal orthogonal grid system is generated as outlined in Figure 5-5. The first step (Figure 5-5a) consists of solving the Laplace equation for ϕ

$$\phi_{xx} + \phi_{yy} = 0 \tag{5.42}$$

within the proposed boundary, with the Neumann and Dirichlet boundary conditions as shown in Figure 5-5a. This yields actual values of ϕ along the boundary between points C1 and D1 and C2 and D2. Step two solves the Laplace equation for ψ,

$$\psi_{xx} + \psi_{yy} = 0 \tag{5.43}$$

with the boundary conditions of Figure 5-5b, to give values of ψ along C1 to C2 and D1 to D2. It should be noted that the boundary along C1D1 is taken as $\psi = K\pi$, where K should be estimated from equating the mass flux along C1C2, (calculated from the solution of part a), with that through C1C2 in part b ($K\pi$). In general, for these grids, K was ≈ 1. Thus, x, y, ϕ and ψ values are known all around the proposed boundary. The object of this procedure is to determine the x, y co-ordinates of the intersection of the "potential lines" and "streamlines" which can now be defined. This will yield

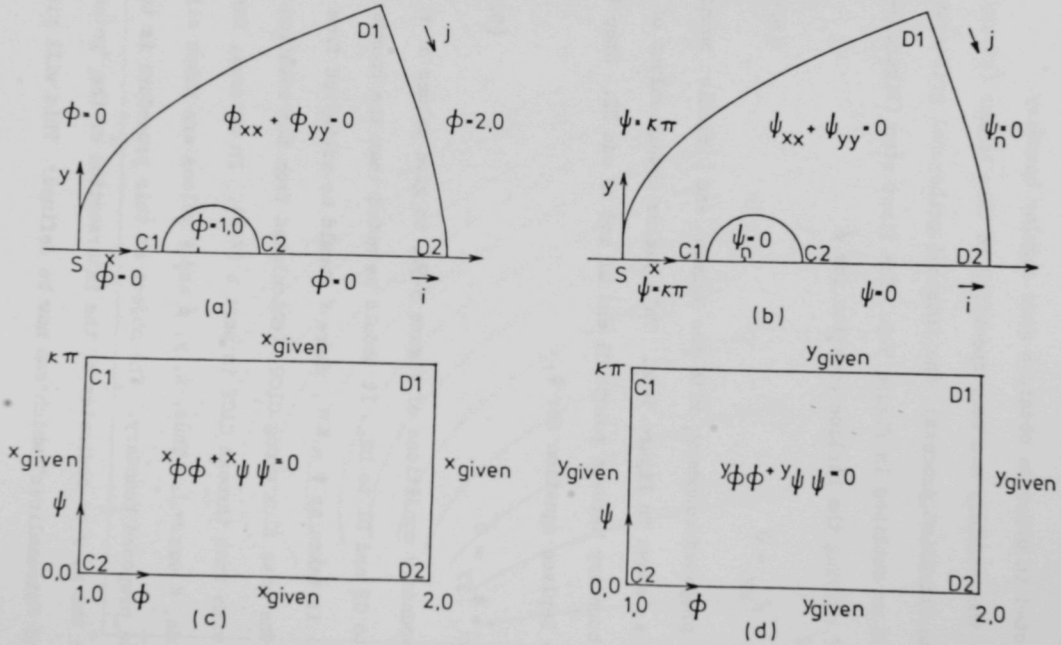

Figure 5-5 Definition sketches of the BIEM applications required for the grid generation.

an orthogonal grid with the point clustering being determined by the values of "potential" and "streamlines" selected.

The method used to determine the intersection points (where eliminates the need for interpolation) is to invert the problem, and solve a Laplace equation for x,

$$x_{\phi\phi} + x_{\psi\psi} = 0 \tag{5.44}$$

and y,

$$y_{\phi\phi} + y_{\psi\psi} = 0 \tag{5.45}$$

with the Dirichlet boundary conditions obtained from the first two steps. The ϕ-ψ domain of solution is as shown in Figures 5-5c and d, respectively. Thus the complete set of grid points shown in the example of Figure 5-4 can be obtained.

There remains the problem of actually solving the Laplace equation. A computationally efficient Boundary Integral Element Method (BIEM) is used, the program, with minor modifications, being given in Liggett and Liu (1983), in which it is denoted as GM8. The BIEM method is based on an expression for Green's second identity, simplified by assuming the two functions U and V obey Laplace's equation as

$$\int_{\Gamma} \left(U \frac{\partial V}{\partial n} - V \frac{\partial U}{\partial n} \right) dA = 0 \tag{5.46}$$

where Γ is the boundary of a domain, D, having an area A, and a

local normal direction $\bar{n}$. U is chosen as a velocity potential and V, as a "free space Green function", which, for two-dimensional problems, is taken as

$$V = \ln r \tag{5.47}$$

where r is the distance between a singular point P (r=0) and a point Q on the boundary. The potential at any point, P, can be expressed in terms of a boundary integral as

$$2\pi\phi(P) = \oint_{\Gamma} \left(\phi(Q)\frac{\partial}{\partial n}(\ln r) - \ln r \frac{\partial}{\partial n}\phi(Q)\right) ds \tag{5.48}$$

where the variables are defined in Figure 5-6.

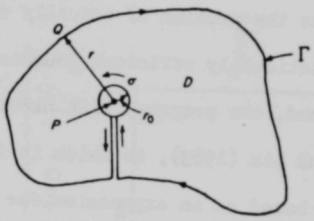

Figure 5-6. Definition diagram for boundary integration used in B.I.E.M. method. The arrows indicate the direction of integration around the boundary curve, Γ, of the domain D. P is a singularity separated from D by the circle σ, radius r_o. (after Liggett and Liu, 1983).

However, only one of ϕ and $\frac{\partial\phi}{\partial n}$ will be defined at any boundary point, for a well posed problem. The unknown values can be obtained from taking P as a boundary point, when Equation (5.48) can be written as

$$\alpha\phi(P) = \oint_{\Gamma} \left(\frac{\phi}{r} \frac{\partial r}{\partial n} - \ln r \frac{\partial\phi}{\partial n} \right) ds \qquad (5.49)$$

where α is the angle between the boundary segments at P. The integral on the right-hand side can be discretized, with ϕ and $\frac{\partial\phi}{\partial n}$ evaluated at each boundary node, a linear variation being assumed between nodes. If P is taken as each of N boundary points, a system of N equations in N unknowns will be obtained, allowing evaluation of the unknown ϕ or $\frac{\partial\phi}{\partial n}$ values, and hence allowing evaluation of any internal point P within the domain.

It was found that the transcritical program was sensitive to slight nonuniformities in the grid. Thus the grid generation was carried out using double precision arithmetic on a 32-bit computer. In addition, a large number of points was used along each boundary, in particular, along C2 to D2 in an attempt to eliminate irregularities due to insufficient points. The grid generation procedure can thus be summarized as:

1) Decide on the required domain shape either initially, or from previous iterations. In particular, the distribution of points along C2 to D2 has to be chosen with care in order to minimize later interpolations: sufficient density near C2 to ensure a reasonable distribution between O and

S, and sufficient density near D2 to avoid overly large artificial viscosities while keeping the overall number as small as possible, generally about 130. The boundary SD1 is approximated by a quintic polynomial to eliminate irregularities.

2) The first BIEM application is made to obtain $\phi(x,y)$, for that portion of the boundary for which $\phi_n = 0$ had been specified.

3) The second BIEM application is made to obtain $\psi(x,y)$ for that position of the boundary for which $\psi_n = 0$ had been specified.

4) Values of ϕ corresponding to points along C2D2 are selected, and the locations of these ϕ values interpolated for along C1D1.

5) Similarly, values of ψ corresponding to points along C1C2 are selected and interpolated for along D1D2.

The boundaries are now specified completely in terms of ϕ and ψ. The problem is inverted to calculate all internal points.

6) The third BIEM application is made to calculate the x coordinates corresponding to the required ϕ and ψ intersections.

7) The fourth BIEM application is made to calculate the y coordinates.

Thus the final grid is obtained. An example of an early grid, G1, is given in Figure 5-4, while Figure 5-7 shows one, G5, at the

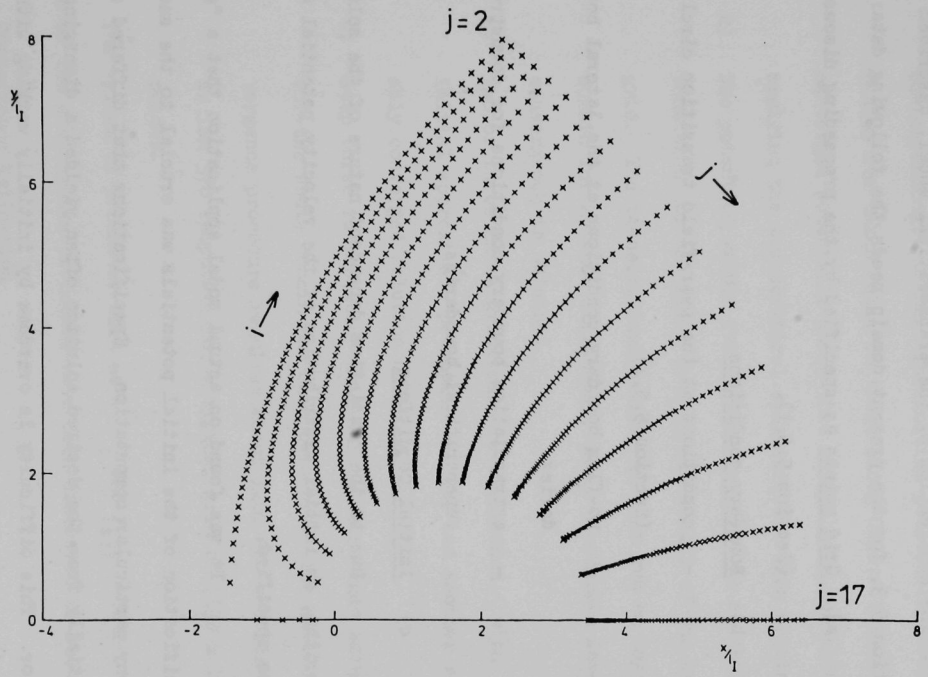

Figure 5-7 A typical grid, G5, developed using the BIEM method, and used for the transcritical program .

end of the boundary height matching process, i.e., a fully iterated grid for a given value of ℓ_I/ℓ_N (= 41.2).

5.5.3 Obtaining a Transcritical Flow Solution for a Given Grid

The application of the transcritical model, described in Section 5.3, for the present domain needs the following data:

a) Grid points as specified by the preceeding discussion, (Section 5.5.1).

b) Boundary conditions

- conditions at the near-field transition circle (Section 5.5.1).
- no-flux boundary conditions at the lateral boundaries.
- extrapolation boundary conditions for downstream supercritical boundaries.

c) Initial Conditions

Due to the quasi-time dependent nature of the solution algorithm, an initial distribution of the velocity potential needs to be specified.

It was found on actual model application that a "good" specification of the initial potentials was crucial to the success of any particular computation. Specifications that differed substantially from the desired solution often yielded a diverging behavior. This difficulty is overcome by initially working with a limited domain (only a few gridlines (j = constant)), and then gradually enlarging the domain by adding a few additional gridlines

at a time. This is carried out as follows:

1) A ficticious radial grid is constructed, having four grid lines with points along the positive x axis having values corresponding to C2D2. The initial potentials along each radius are taken equal to those along C2D2. Values of converged potentials along this radial grid, obtained by applying the transcritical solution, are then obtained.

2) The potential values from Step 1 are used as an initial condition for the first four (j= 14 to 17) of the actual grid. The transcritical program is then run on this sub-domain for 200-300 iterations, until a moderate level of convergence is obtained.

3) Two or three extra gridlines are then added - with initial approximate potential values, and another reasonably converged solution obtained.

4) Step three is repeated until a fully converged solution for the whole domain has been obtained. The entire convergence procedure requires about 1200 CPU seconds on an IBM 370 computer, for a typical grid of (130 x 16) points.

The values of parameter such as ω, ω_s and F_{art} used at various stages of the convergence procedure have been discussed in Section 5.4.

Convergence Estimation

One method of estimating convergence has been discussed in

Section 5.3.4, i.e., the rate of decrease of the maximum residual within the solution domain. In addition, a more globally averaged estimate can be obtained from comparing values of the total physical and artificial mass flux input into the domain through C1C2 and output through D1D2. In general, when these values differed by less than $\approx 0.1\%$ of the input mass flow, the solution obtained was regarded as being well converged. Another method of applying this mass flow continuity consideration as an estimate of convergence is to split the entire domain into, say, 9 sub-regions (using increments in both the i and j directions), and examine the flux differences across their boundaries, which should again be zero for a converged solution. Values of 0.5% of the input mass flow were the largest obtained in a solution considered as converged.

5.5.4 Successive Grid Modification Until Full Matching at Frontal Boundary

The solution obtained using the grid, G1, shown in Figure 5-4 (corresponding to $\ell_I/\ell_N = 41.2$) is shown in terms of height (thickness) contours in Figure 5-8. The upstream boundary conditions, determined by the transition conditions between the near and intermediate fields (Section 5.5.1), for $\ell_I/\ell_N = 41.2$, are a normal flow (Froude number of 1.05, i.e., just slightly supercritical) out of a circular boundary, radius 1.84, with a center displaced from the origin to $\alpha = 1.54$ (due to developments in the early stages of this work the inner boundary of G1 does not exactly conform to the circular shape). The

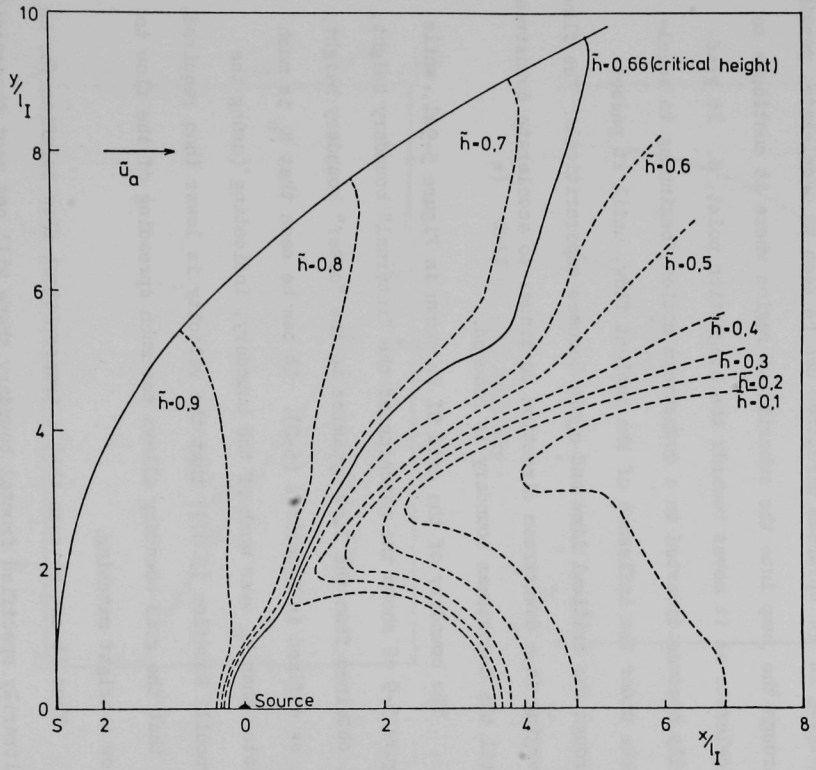

Figure 5-8 Height contours for the non-matched solution for ℓ_I/ℓ_n = 41.2. Calculated using grid G1, Figure 5-4.

height contour marked by a dotted line represents the jump location and/or critical line, depending on whether the flow across it moves from supercritical to subcritical or subcritical to supercritical, respectively, as discussed in Section 2.2. The supercritical flow emerging in an upstream direction can be seen to decelerate, passing through the jump into the subcritical region where it continues to decelerate as it moves towards the stagnation point, S. It gradually becomes diverted to a downstream motion, beginning to accelerate under the influence of the ambient flow, until it passes through the critical line and again becomes supercritical. The flow emerging in a downstream direction continues to accelerate downstream until the downstream boundary is reached.

The boundary of the grid G1 is shown in Figure 5-9a1, while Figure 5-9 a2 shows the matching of the "internal" boundary height, h_b, obtained from the flow dynamics to the "outer" boundary height, h_B, as defined in Equations (5-2). It can be seen that h_b is much greater than h_B over much of the boundary, indicating (using the Bernoulli Equation (3.67)) that the velocity is lower than required, or, that the grid boundary allows too much spreading of the flow to allow a height matching.

Thus it can be seen that a transcritical flow solution for an arbitrarily specified frontal boundary shape will not meet the specific frontal boundary height matching condition that governs the interplay between the ambient flow and the density current intermediate field

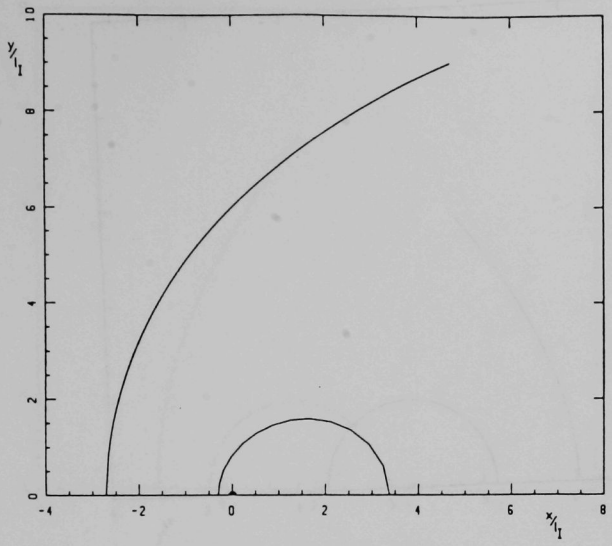

a) Grid G1, (1) boundary

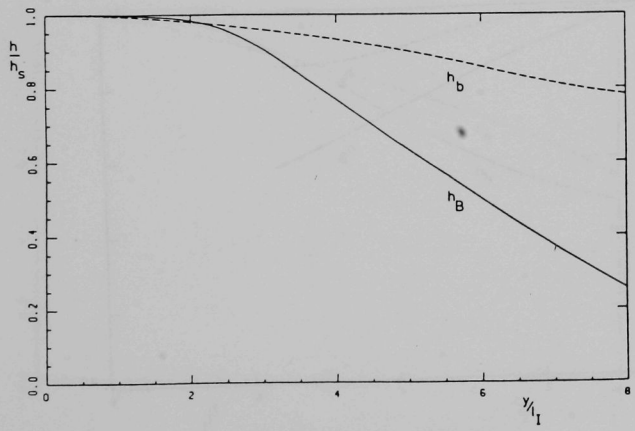

(2) height variation.

Figure 5-9 The stages involved in obtaining a fully matched frontal boundary shape.

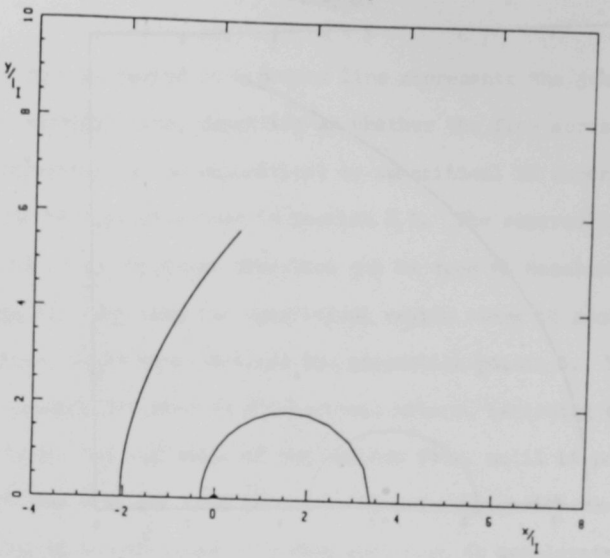

b) Grid G2, (1) boundary

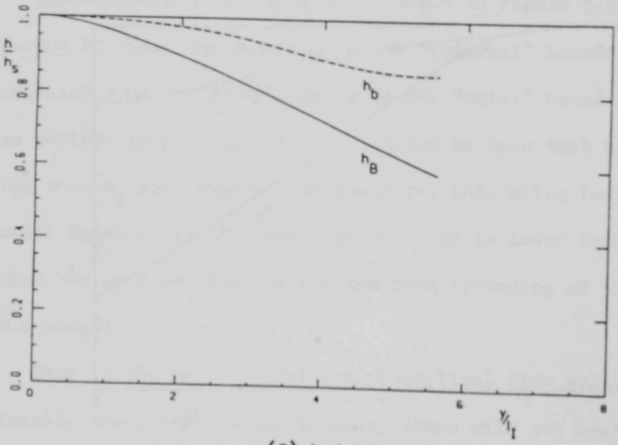

(2) height variation.

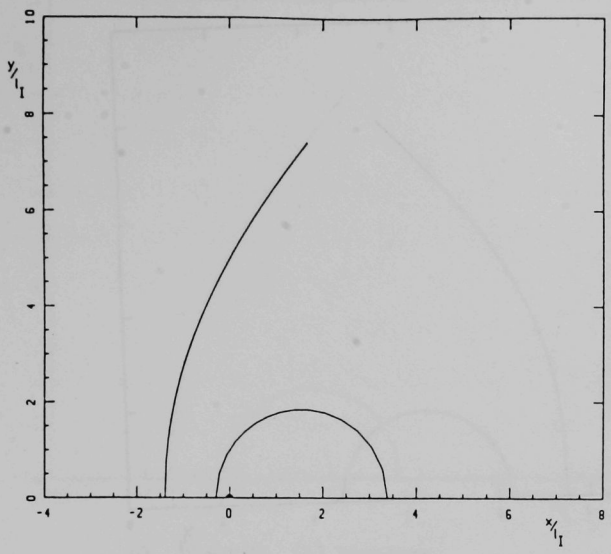

c) Grid G3, (1) boundary

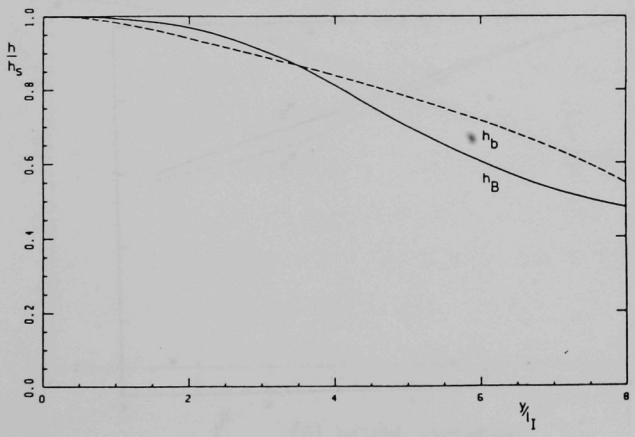

(2) height variation.

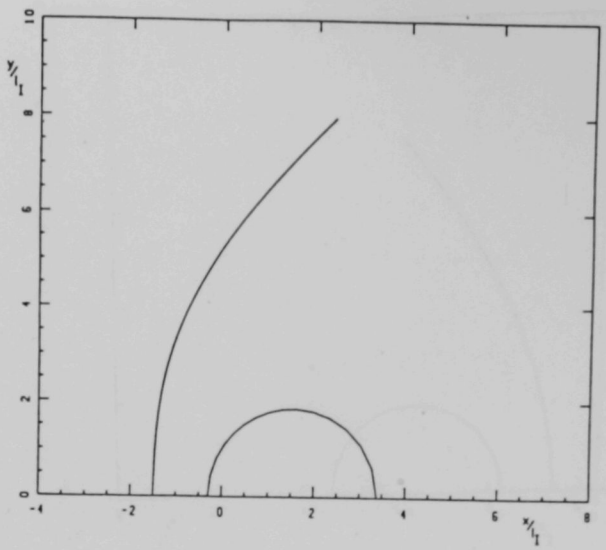

d) Grid G4, (1) boundary

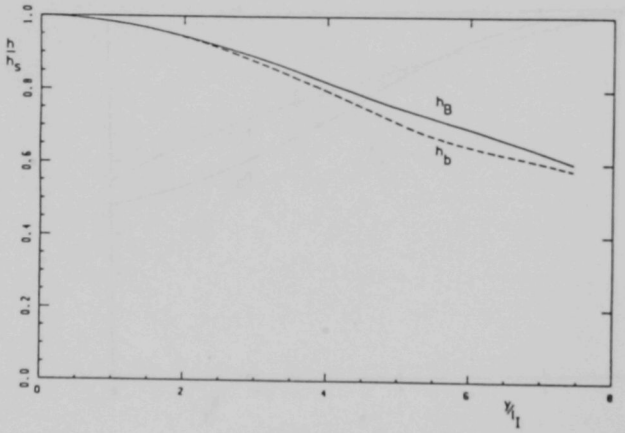

(2) height variation.

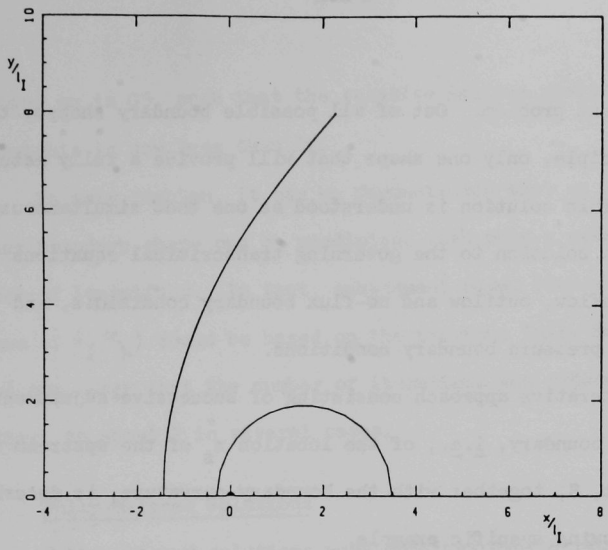

e) Grid G5, (1) boundary

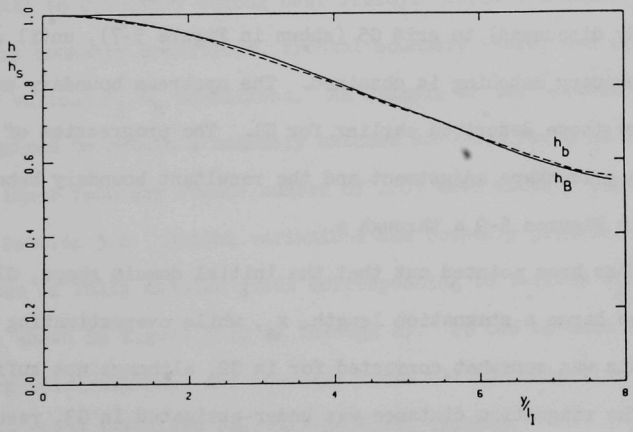

(2) height variation.

in the present problem. Out of all possible boundary shapes, there is, in principle, only one shape that will provide a fully matched solution. This solution is understood as one that simultaneously represents a solution to the governing transcritical equations with specified inflow, outflow and no-flux boundary conditions, and to the frontal pressure boundary conditions.

An iterative approach consisting of successive adjustments of the frontal boundary, i.e., of the location x_s of the upstream stagnation point, S, together with the boundary curvature, is described in the following specific example.

This example related to five successive grid changes G1 (Figure 5-4, with a flow field shown in Figures 5-8 and 5-9 a1 and a2, and already discussed) to grid G5 (shown in Figure 5-7), until a frontal boundary matching is obtained. The upstream boundary conditions are those described earlier for G1. The progression of the successive grid shape adjustment and the resultant boundary behaviour is shown in Figures 5-9 a through e.

It has been pointed out that the initial domain shape, G1, assumed too large a stagnation length, x_s, while overestimating the width. This was somewhat corrected for in G2, although not sufficiently. The stagnation distance was under-estimated in G3, resulting in internal heights which were too large in this region. In G4, the stagnation length has been decreased while the downstream spreading has been increased, resulting in a much better fit which is again

improved on in G5, such that the relative maximum deviation between the heights is now less than 2%.

In this fashion, it can be demonstrated that an accurate, unique boundary shape can be predicted, with only a relatively small number of iterations. In fact, subsequent cases (for alternative values of ℓ_I/ℓ_N) could be based on the previous fully matched solutions, such that the number of iterations was reduced even further, to about 2 in several cases.

5.6 Fully-matched Solutions

Fully matched solutions were obtained over a range of relative field strengths, with ℓ_I/ℓ_N values varying from 4.1 (very weak near field) to 0.9 (very strong near field). Table 5-1 summarizes the inner boundary conditions, frontal boundary shape, and results shown for various ℓ_I/ℓ_N conditions. An example of the various iterations required to obtain a boundary matched solution for grid G5, applying an inner boundary Froude number of 1.05 have already been discussed in Section 5.6. Height variations and boundary profiles for further cases of fully matched grids corresponding to various ℓ_I/ℓ_N values, are shown in Figure 5-10 (a through e). It can be seen that the stagnation distance and boundary width all increase with increasing near field influence (decreasing ℓ_I/ℓ_N values).

The internal flow dynamics for solutions having selected ℓ_I/ℓ_N values are shown in Figure 5-11, (ℓ_I/ℓ_N = 41.2, grid G5), Figure 5-12, (ℓ_I/ℓ_N = 14.1, grid G6) and Figure 5-13 (ℓ_I/ℓ_N = 3.0,

Table 5-1

Summary Table of the Results Presented for the Intermediate Field Transcritical Region.

Grid	G5	G6	G11	G8	G12	G10
$\frac{\ell_I}{\ell_N}$	41.2	14.1	7.0	3.0	1.5	0.88
$\tilde{x}_d$ (displacement of circle center)	1.54	1.40	1.33	1.32	1.34	1.45
$\tilde{r}_T$ (radius of circle)	1.84	1.90	2.03	2.25	2.67	3.05
F_{ℓ_T}	1.05	1.25	1.43	1.70	2.01	2.32
$\tilde{q}$	0.82	0.94	1.01	1.09	1.16	1.21
$\lvert\tilde{x}_s\rvert$	1.43	1.66	1.94	2.28	2.84	3.45
$\tilde{b}(o)$	5.18	5.44	6.12	6.38	7.76	9.0
$\hat{Q}(\hat{r}_T)$	10.80	5.65	3.84	2.55	1.85	1.42
Figures						
boundary height	5-9 (e1)	5-10(a1)	5-10(b1)	5-10(c1)	5-10(d1)	5-10(e1)
boundary shape	5-9 (e2) and 5-15	5-10(a2) and 5-15	5-10(b2) and 5-15	5-10(c2) and 5-15	5-10(d) and 5-15	5-10(e2) and 5-15
internal height	5-11(a)	5-12(a)	-	5-13(a)	-	-
internal velocity	5-11(b and c)	5-12(b)	-	5-13(b)	-	-

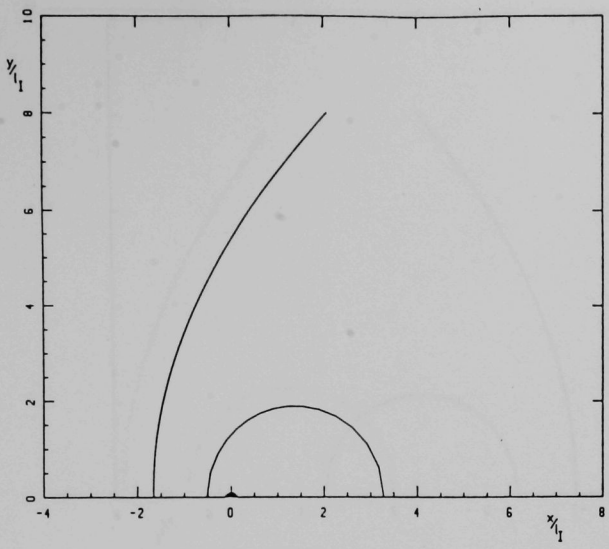

a) Grid G6, $\ell_I/\ell_N = 14.1$ (1) boundary shape

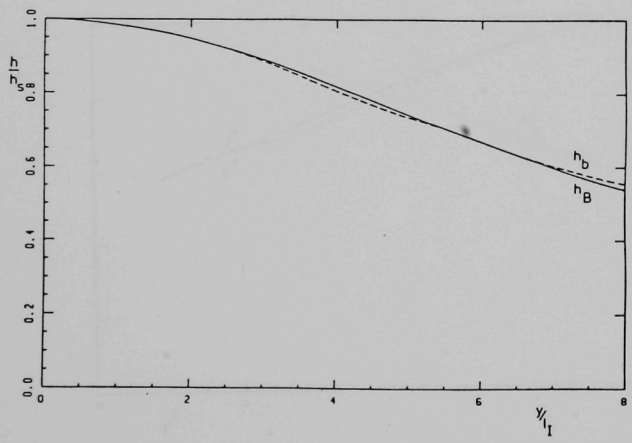

(2) height variation.

Figure 5-10 Internal and boundary heights and the boundary profile for matched grids corresponding to various ℓ_I/ℓ_N values.

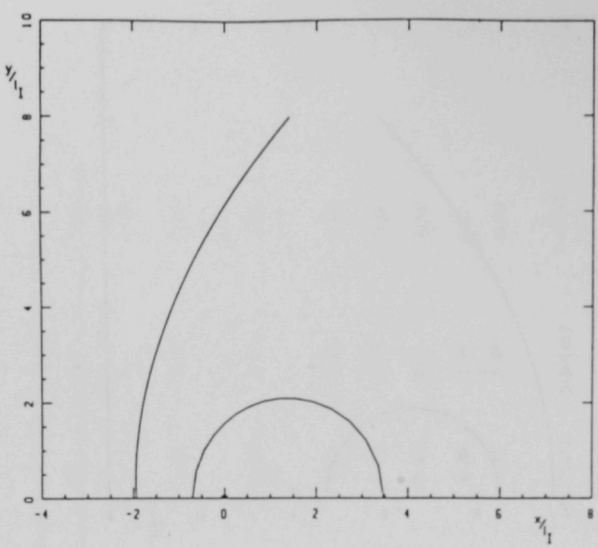

b) Grid G11, $\ell_I/\ell_N = 7.0$ (1) boundary shape

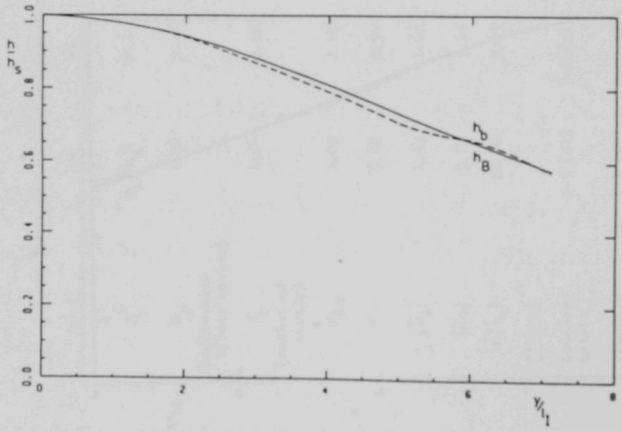

(2) height variation.

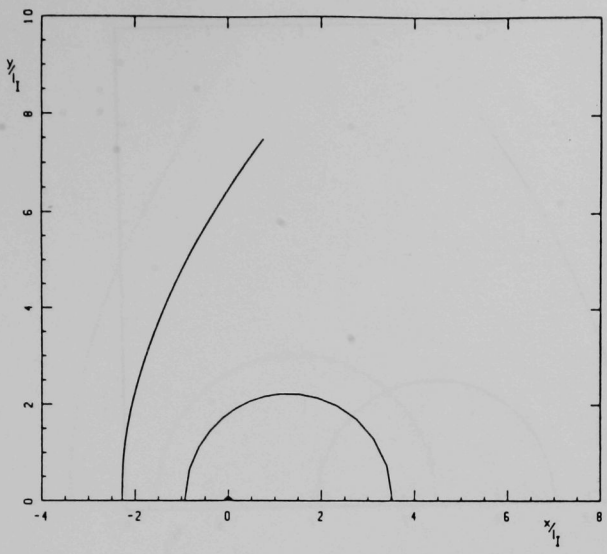

c) Grid G8, $\ell_I/\ell_N = 3.0$ (1) boundary shape

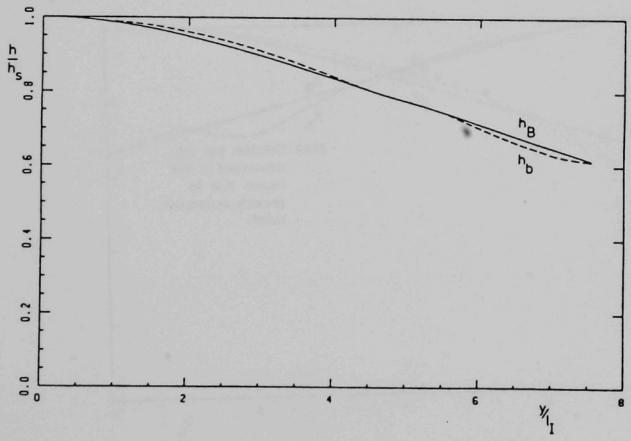

(2) height variation.

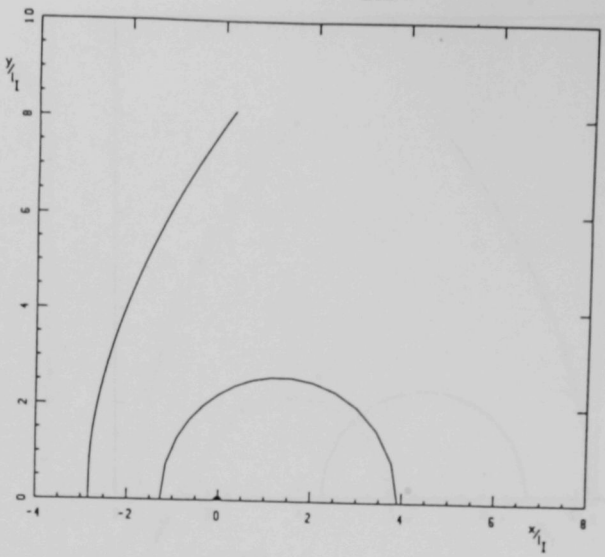

d) Grid G12, $\ell_I/\ell_N = 1.5$ (1) boundary shape

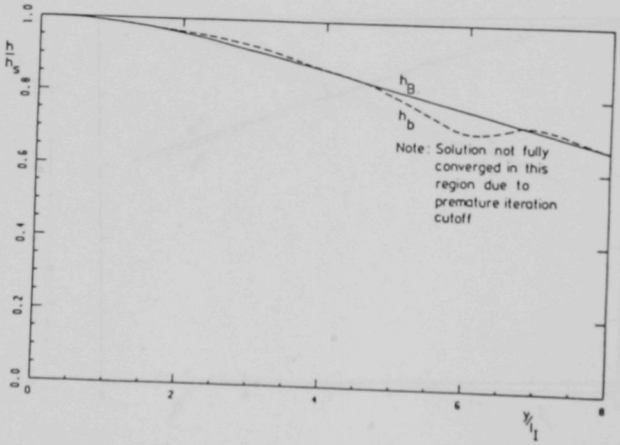

(2) height variation.

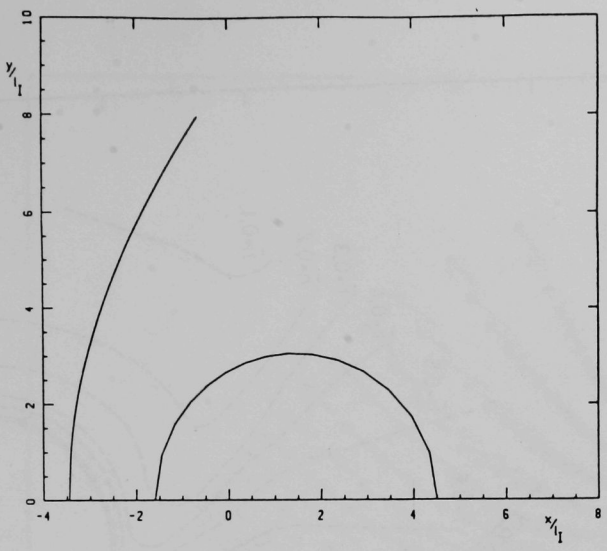

(e) Grid G10, $\ell_I/\ell_N = 0.88$ (1) boundary shape

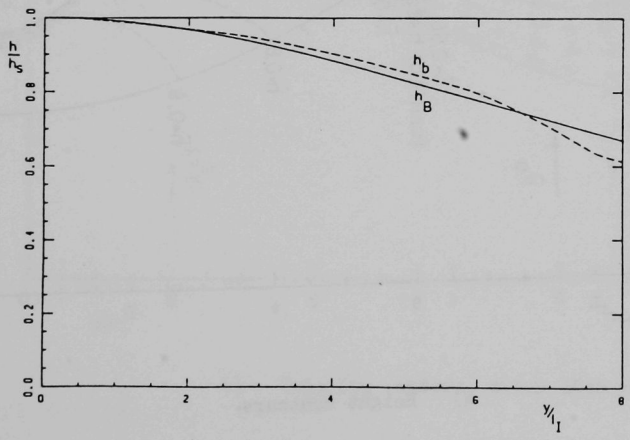

(2) height variation.

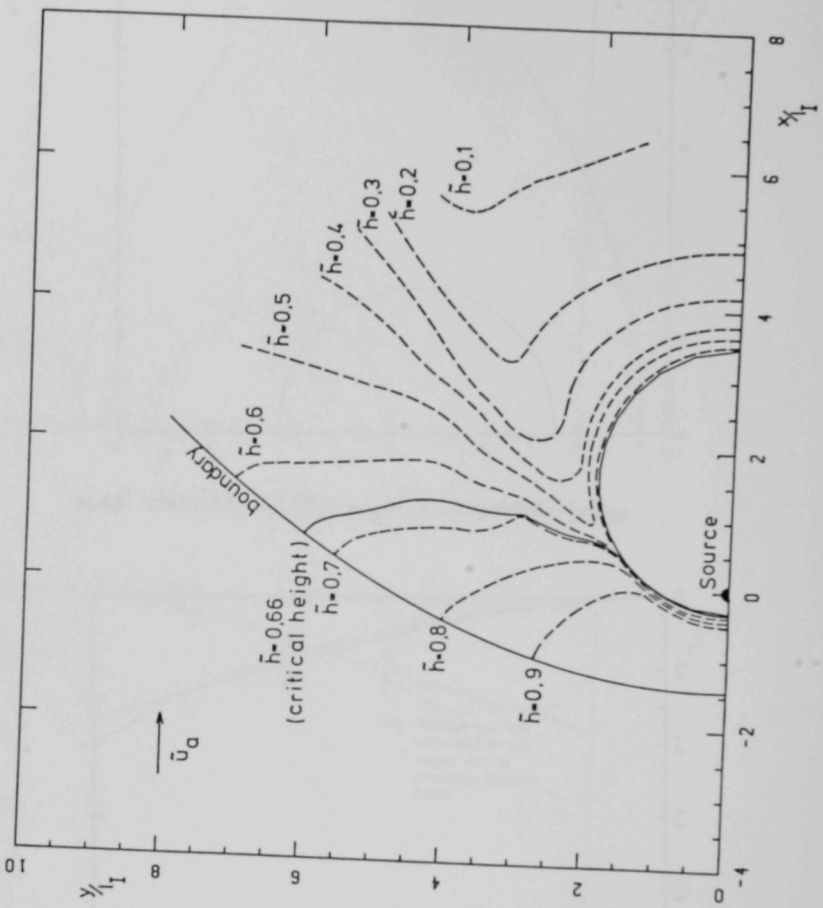

a) Height contours.

Figure 5-11 Results for the transcritical region of the intermediate field, for ℓ_I/ℓ_N = 41.2 (Grid G5).

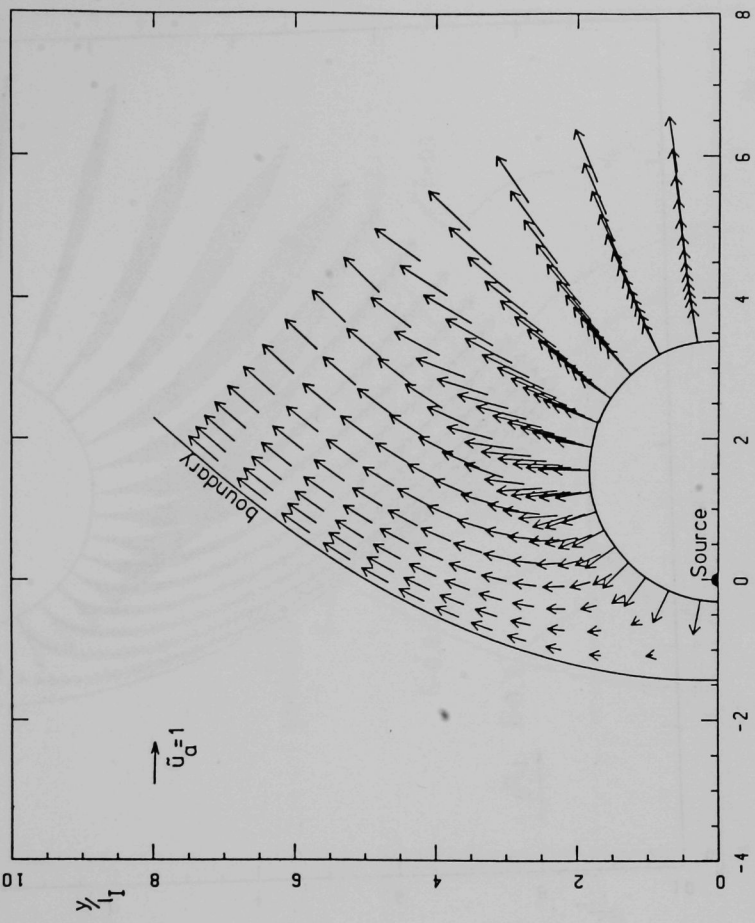

b) Velocity vectors, every 10th point plotted

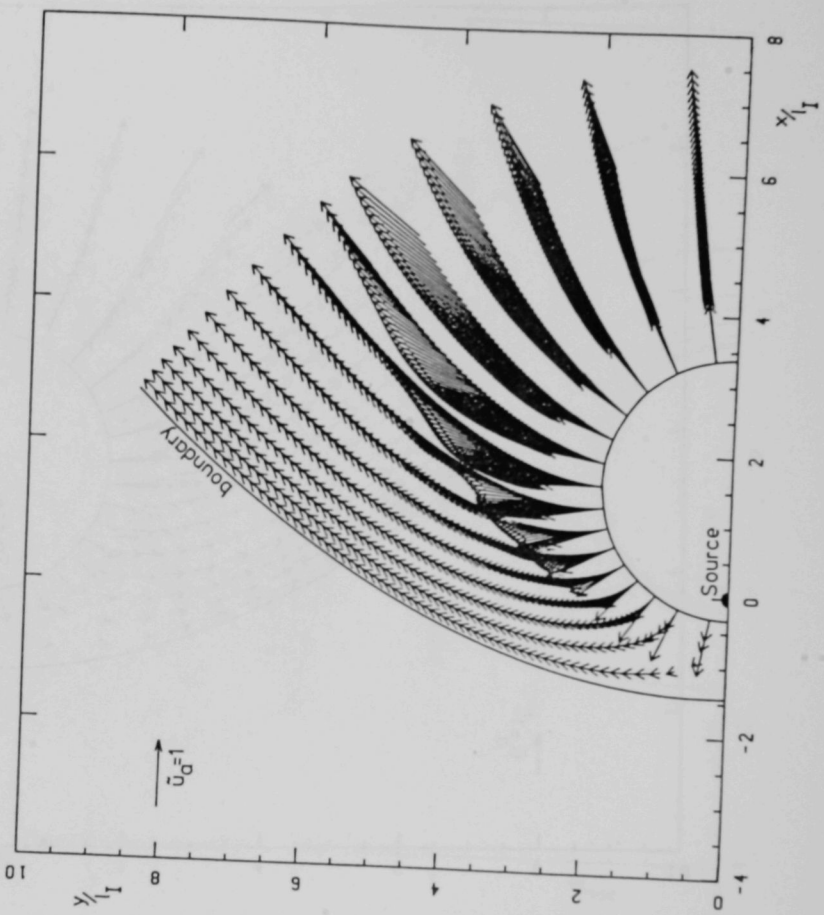

c) Velocity vectors, every 2nd point plotted.

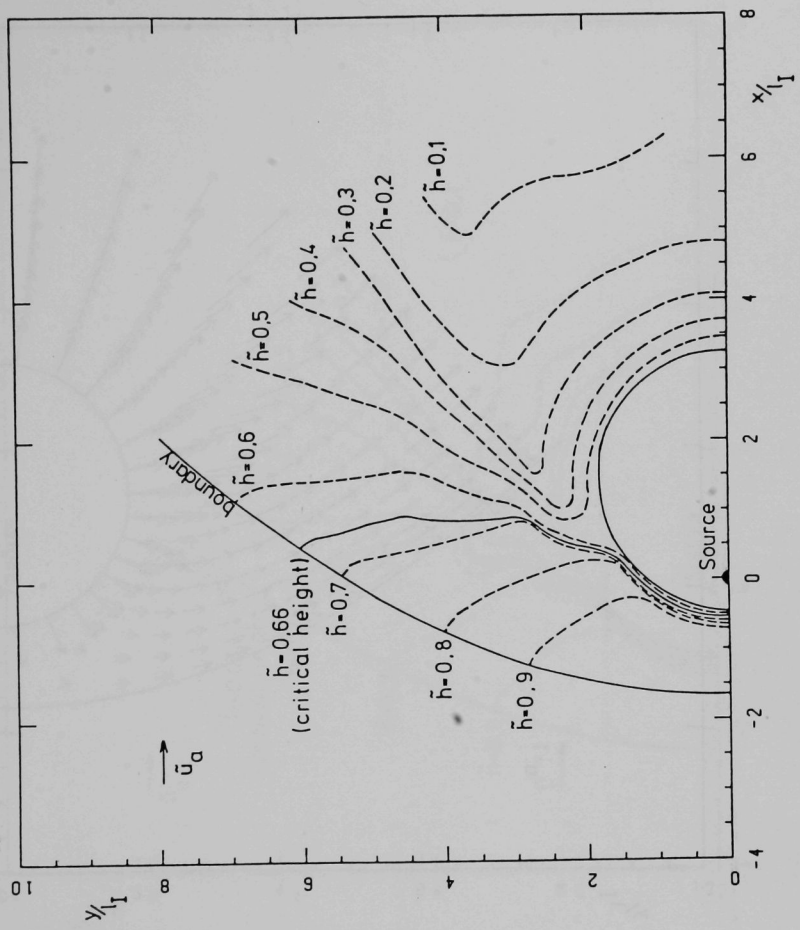

a) Height contours

Figure 5-12 Results for the transcritical region of the intermediate field, for ℓ_I/ℓ_N = 14.1 (Grid G6).

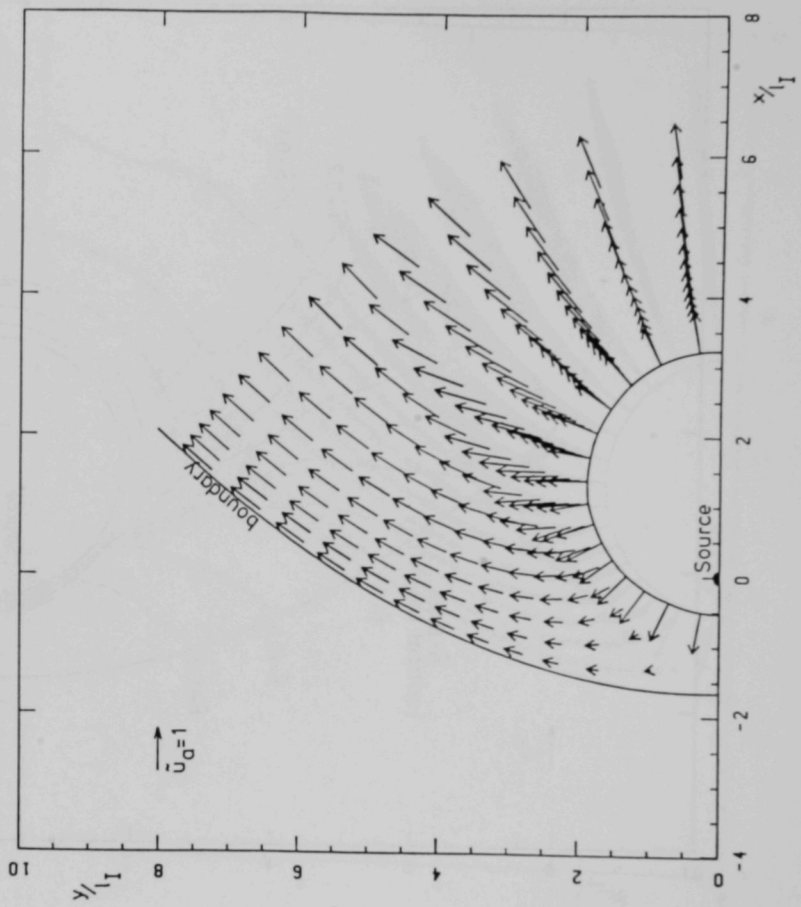

b) Velocity vectors, every 10th point

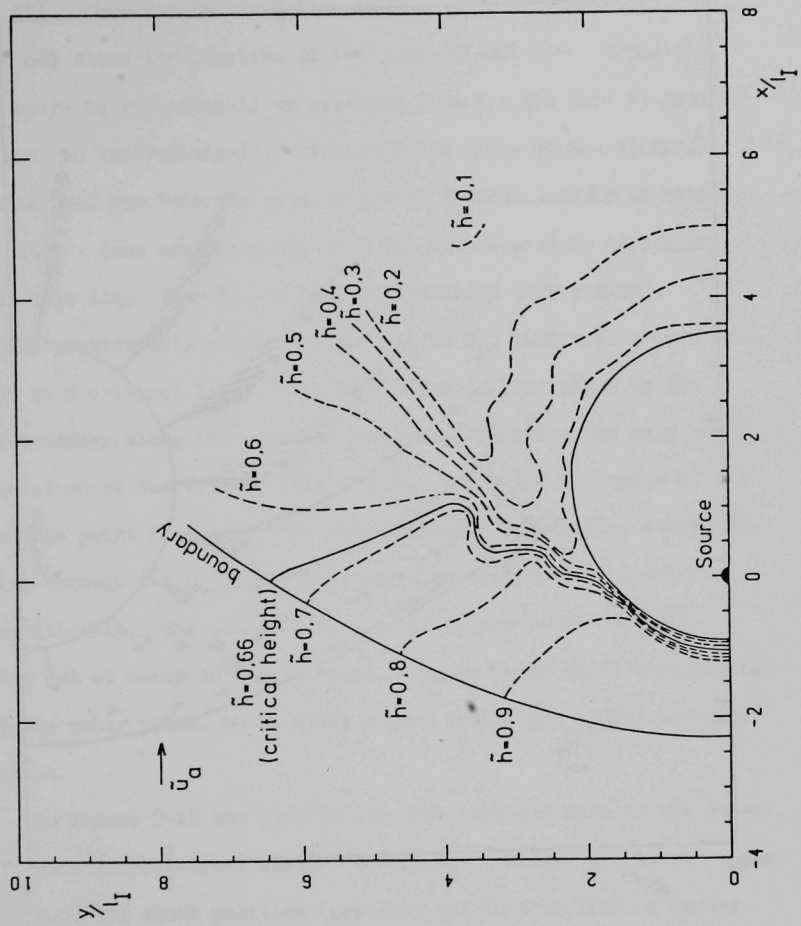

a) Height contours

Figure 5-13 Results for the transcritical region of the intermediate field, for ℓ_I/ℓ_N = 3.0 (Grid G8).

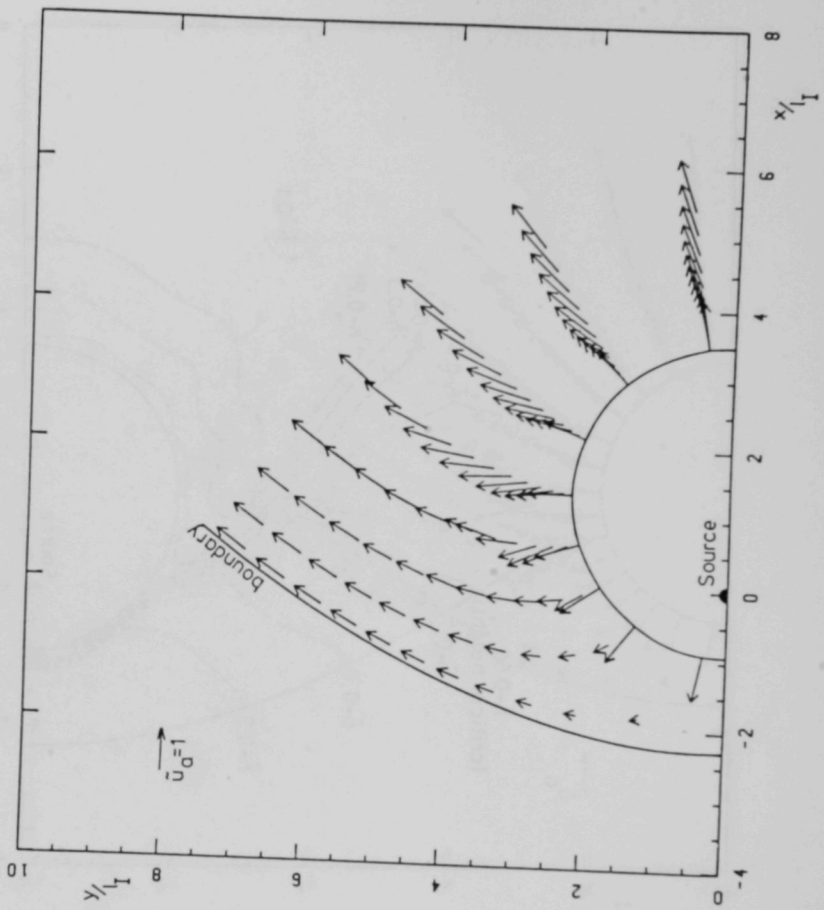

b) Velocity vectors, every 10th point.

grid, G8). Consider Figure 5-11: In Figure 5-11a, the line ($\tilde{h}$ = 0.66) shows the location of the jump (if the flow is passing from super- to subcritical) or critical line (if the flow is passing from sub- to supercritical). Figures 5-11a and b viewed together, indicate that the velocity vectors change discontinuously in magnitude, and, - less conspicuously from the plot - also in direction, across this line, from Sh_1 to Sh_2 (indicating a jump region), but pass continuously across it from Sh_2 to C_1, (indicating that this region is a critical line). The shock line is very close to the inner boundary along its upstream portion, indicating the very rapid deceleration of the flow in this region. After the influence of the stagnation point is passed, the flow starts to accelerate, eventually passing through the critical line, and then continues to accelerate supercritically. The velocity vectors in Figure 5-10b are only plotted out at every 10th grid point. Figure 5-10c shows them plotted for every other point, which gives a good indication of the velocity variation.

In Figure 5-13 the jump is somewhat stronger than in the others, due to more supercritical initial conditions. Slight oscillations are seen around the shock position (probably due to some lack of convergence). In addition, slight oscillations emerge in the supercritical region, radiating from the shock. These appear to be due to instabilities introduced by the shock, and are very constant in form, being only slowly damped out with increasing iteration. These

oscillations do not appear in the subcritical region. Experience with the model for even higher velocity cases (i.e., decreasing values of ℓ_I/ℓ_N) showed that these oscillations tended to become stronger. Ultimately, for even lower values of ℓ_I/ℓ_N (≤ 1.0), this tendency for oscillation and instabilities proved to be an apparent limit of the model applicability.

5.7 Summary of (Fully Matched) Intermediate Field Solutions

The preceding results, in graphical form, show clearly the influence of the near-field dynamics on the overall shape and internal flow dynamics of the intermediate field transcritical domain. Probably the single most meaningful measure of this influence is the upstream stagnation length, $|\tilde{x}_s| = |x_s|/\ell_I$, plotted as a function of ℓ_I/ℓ_N (see Figure 5-14). The data show a significant dependence upon ℓ_I/ℓ_N for the range ℓ_I/ℓ_N between 1 and 40. However, outside this range, i.e., $\ell_I/\ell_N \to 0$ and $\ell_I/\ell_N \to \infty$, asymptotic regions are reached. This can be understood from the following considerations: The ratio ℓ_I/ℓ_N can be expanded in terms of the initial momentum and buoyant fluxes, M_o and J_o, respectively, and ambient velocity, as

$$\frac{\ell_I}{\ell_N} = \frac{J_o^{3/2}}{2\pi C_D u_a^3 M_o^{3/4}} \tag{5.50}$$

Thus, when the initial momentum flux is very large compared with the buoyancy flux, the ratio ℓ_I/ℓ_N tends to 0, and, inversely a relatively large buoyancy flux results in ℓ_I/ℓ_N tending to ∞. In general, the

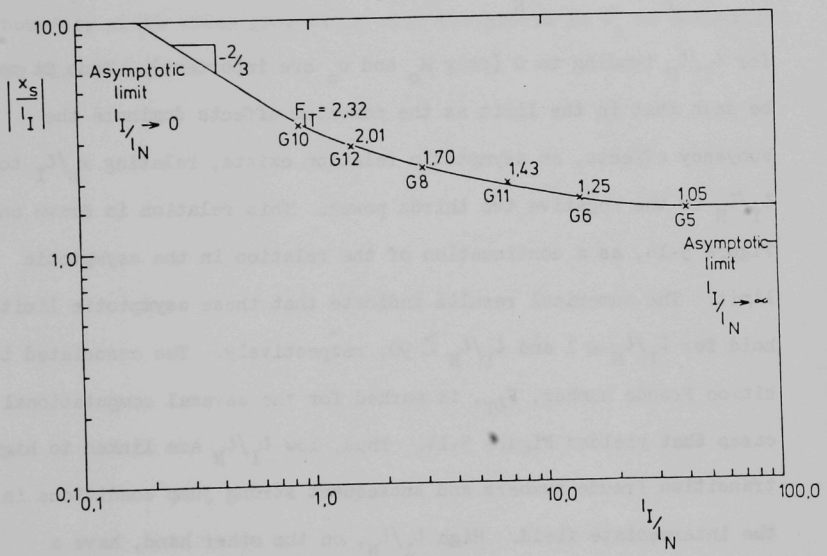

Figure 5-14 The stagnation length as a function of the relative intermediate to near-field length scales.

stagnation length, x_s, is a function of J_o, M_o and u_a, or, if non-dimensionalized by ℓ_I , $x/\ell_I = f(\ell_I/\ell_N)$. However, for the two limiting cases, the relationship simplifies to x/ℓ_I = constant, for ℓ_I/ℓ_N tending to ∞ (only J_o, and u_a are important), and to

$$\frac{x}{\ell_I} = \text{const.} \left(\frac{\ell_I}{\ell_N}\right)^{-2/3} \tag{5.51}$$

for ℓ_I/ℓ_N tending to 0 (only M_o and u_a are important). Thus it can be seen that in the limit as the momentum effects dominate the buoyancy effects, an asymptotic relation exists, relating x_s/ℓ_I to ℓ_I/ℓ_N to the negative two thirds power. This relation is drawn on Figure 5-14, as a continuation of the relation in the asymptotic limit. The numerical results indicate that these asymptotic limits hold for $\ell_I/\ell_N \leq 1$ and $\ell_I/\ell_N \gtrsim 90$, respectively. The associated transition Froude number, $F_{\ell T}$, is marked for the several computational cases that yielded Figure 5-14. Thus, low ℓ_I/ℓ_N are linked to high transition Froude numbers and subsequent strong jump conditions in the intermediate field. High ℓ_I/ℓ_N, on the other hand, have a transition Froude number that asymptotically approaches unity, the critical value. The minimum $F_{\ell T}$ value for the present computation was 1.05 (ℓ_I/ℓ_N = 41.2, grid G5), and is very close to theoretical criticality (see also the discussion on the volatility of the near-critical flow behavior in Sections 2.3 and 4.2). The next lower case modeled (ℓ_I/ℓ_N = 14.1, grid G6) is associated with only a

slightly higher Froude number, $F_{\ell T} = 1.25$, giving an indication that an asymptotic regime in the ℓ_I/ℓ_N range is indeed approached.

The various boundary shapes corresponding to the ℓ_I/ℓ_N values solved for and summarized in Figure 5-14, have been shown in Figure 5-8 and Figure 5-10 (see Table 5-1 for details). These are now brought together in Figure 5-15 to emphasize the growth in boundary width which goes along with the growth in $\tilde{x}_s$ as summarized in Figure 5-14.

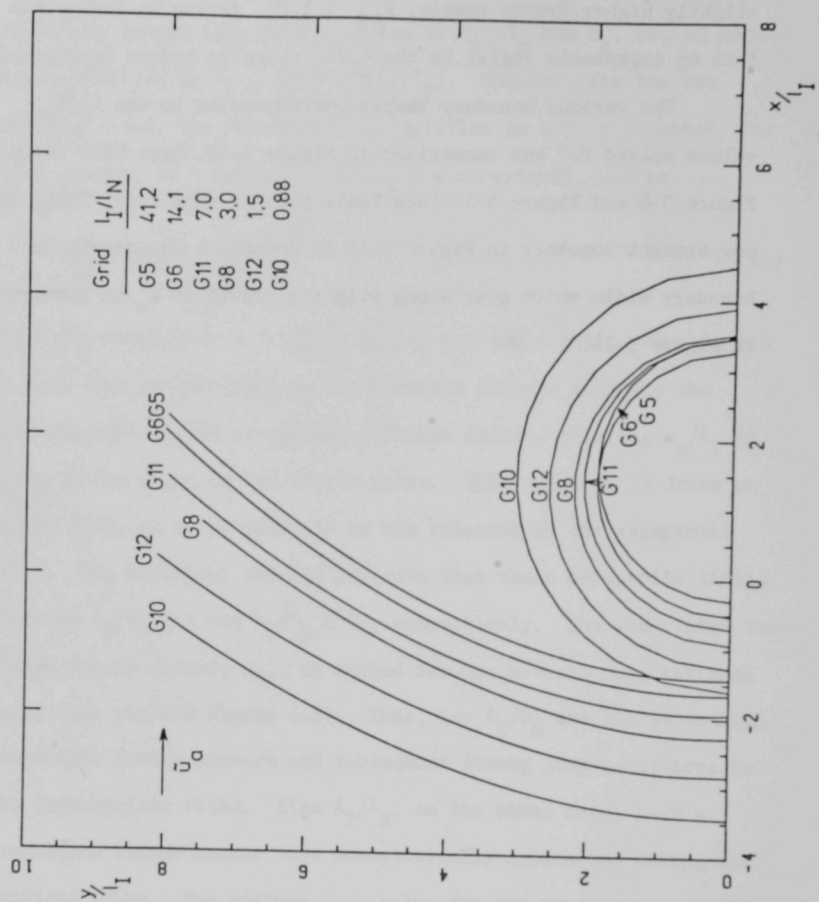

Figure 5-15 Variation of transcritical region boundary shape with ℓ_I/ℓ_N.

CHAPTER 6

THE INTERMEDIATE FIELD (SUPERCRITICAL FLOW REGION) SOLUTION

The intermediate field supercritical region occurs downstream of the transcritical flow region and extends to the far field region, as discussed in Section 3.1. A numerical model is formulated that solves the governing Equations (3.72) and (3.73) (in nondimensionalized form, assuming a Case A stratification type). These equations include interfacial friction, which plays an increasingly important role within this region - depending on the governing non-dimensional parameters (see Section 3.5.2). The limiting case of zero friction is of fundamental interest for comparison to elementary theories (Section 2.1.3).

6.1 Numerical Computations - MacCormack's Method

The flow in this region is supercritical (*i.e.*, it is of hyperbolic type, all information passing downstream) and non-entraining. Various numerical solution methods applicable to hyperbolic equations were discussed in Section 2.6. These were further summarized in Section 4.1, where the MacCormack scheme (an explicit stepping technique) was chosen as the most suitable method for modeling of the entraining supercritical flow in the near field. The same method can be applied in this case, with the entrainment set to zero, and, instead, a frictional term appearing in the equations. Thus, the non-dimensional controlling Equations (3.72) and (3.73)

are written in vector form as

$$\frac{\partial F}{\partial x} + \frac{\partial G}{\partial y} = H \tag{6.1}$$

where

$$F = \begin{Bmatrix} hu \\ u^2h + \frac{1}{2}h^2 \\ uvh \end{Bmatrix} \; ; \; G = \begin{Bmatrix} hv \\ uvh \\ v^2h + \frac{1}{2}h^2 \end{Bmatrix} \; ; \; H = \begin{Bmatrix} 0 \\ \lambda_i V'(u_a - u)|u_a - u| \\ \lambda_i V'(-v)|-v|) \end{Bmatrix}$$

where V' is the volume flux parameter defined in Equation (3.62). The MacCormack scheme can then be applied in the form summarized in Equation (4.3).

The finite volume scheme (Section 4.1.1) is applied, for consistency with the near and transcritical intermediate field approaches, particularly to simplify its boundary condition with the latter) and also to facilitate the application of the boundary conditions along the curved outer boundary. The non-dimensionalized equations (Equation 6.1) in contravariant form can be written as

$$\frac{\partial F}{\partial X} + \frac{\partial G}{\partial Y} = H \tag{6.2}$$

where

$$F = \begin{Bmatrix} hDU \\ hDUu + \frac{1}{2} y_Y h^2 \\ hDUv + \frac{1}{2} x_Y h^2 \end{Bmatrix} ; \; G = \begin{Bmatrix} hDV \\ hDVu - \frac{1}{2} y_X h^2 \\ hDVv - \frac{1}{2} x_X g' h^2 \end{Bmatrix} ; \; H = \begin{Bmatrix} 0 \\ \lambda_i V' D(u_a - u) | u_a - u| \\ \lambda_i V' D(-v) | -v| \end{Bmatrix}$$

6.1.1 Solution Details

The solution procedure is as listed in Section 4.1.2, apart from the calculation of the dependent variables, u, v, h. This difference is due to the lack of entrainment in this supercritical region, which eliminates the need for a buoyancy equation, as g' will be constant, and thus no longer one of the dependent variables. The modified relations are written as

$$v = \frac{x_Y}{y_Y} \frac{FB(2)}{FB(1)} + \frac{FB(3)}{FB(1)} - u \frac{x_Y}{y_Y} \tag{6.3}$$

$$u = \left(y_Y \frac{FB(1)}{h} + x_Y^2 \frac{FB(2)}{FB(1)} + y_Y x_Y \frac{FB(3)}{FB(1)} \right) (y_Y^2 + x_Y^2) \tag{6.4}$$

$$0.5 h^3 + \left(\frac{x_Y FB(3) - y_Y FB(2)}{x_Y^2 + y_Y^2} \right) h + \frac{FB(1)^2}{(x_Y^2 + y_Y^2)} = 0 \tag{6.5}$$

where FB(i), i = 1,2,3 are the intermediate predictions of the F flux values.

6.1.2 Initial and Boundary Conditions

Initial conditions are required at the upstream boundary only, as this is a marching scheme. This upstream boundary is taken

directly from the transcritical solution. The converged potential and grid values from all points in the transcritical solution are retained, so that once the point 'i' at which the supercritical solution is required to start has been decided upon, the appropriate potential and grid values can be obtained.

The treatment of the "no-flux" centerline and the outer (frontal) boundary is similar to that used in the near field model, apart from small modifications due to the constant buoyancy and presence of a frictional rather than entrainment terms. As for the transcritical regime, no downstream boundary is required, as this will be self-determined by the marching scheme.

6.1.3 Automatic Grid Generation and Matching of the Frontal Boundary

A significant feature of the model formulation is the automatic step-wise generation of the computational grid during the downstream march. This is carried out such that the frontal boundary shape simultaneously meets the inner and outer pressure matching.

The location of the first two lines (i = 1 and 2) of grid points are determined as part of the upstream boundary, as discussed in Section 6.1.2. Thereafter the grid must be generated so as to effect a height matching, as discussed for the transcritical region (*i.e.*, the "inner" boundary height, h_b, obtained from the flow dynamics matched to the "outer" boundary height, h_B, as defined by Equation 5.2). This matching could be obtained by iteration on possible boundary positions, a method used for the transcritical

region (Chapter 5). However, due to the marching nature of the solution procedure in the totally supercritical region, a more direct method of boundary determination is available. This involves, if the flow has been calculated up to a point 'i', choosing a boundary angle, θ_{i+1} as

$$\theta_{i+1} = \sin^{-1}\left(h_{b,i}\right) \tag{6.6}$$

where it should be remembered that h_b is the internal boundary height. This effectively sets

$$h_{B,\ i+1} = h_{b,i} \tag{6.7}$$

i.e., the external boundary height at the new point is equal to the internal boundary height already calculated at the previous point. This involves an "explicit" approximation. The accuracy of this formulation (Equation 6.7) was checked by using an alternative specification,

$$h_{B,\ i+1} = \frac{h_{b,i} + h_{b,i-1}}{2} . \tag{6.8}$$

This gave very little change in the final boundary shape, which indicates that either expression is sufficiently accurate. It should be noted that at the upstream boundary, h_b and h_B must be equal, as this is obtained from the converged transcritical solution.

Once the boundary angle has been defined, and hence the boundary point (i,j=2), the remaining grid points (i,j=3...16) are

determined by keeping the ratios of the angles of the 'j = constant' lines to the local boundary angle as the same as in the grid line forming the upstream boundary (i=1).

Figure 6-1 shows a typical grid generated using this method - in fact this figures shows the "cell-averaged" grid values, i.e., each point drawn represents the center of each actual grid cell. This shows the points of evaluation of the flow variables using the finite volume scheme.

6.2 Numerical Experiment: Application of the MacCormack Supercritical Scheme to an Initially Uniform Grid

The purpose of this experiment was to model the lateral plume spread from an initially uniform buoyant inflow from a source of finite width, into an ambient stream. Solutions for this case can be compared to those from the "one-dimensional theories" discussed in Section 2.1.

The initial conditions taken were those of an uniform horizontal supercritical velocity, q = 1.03 (F = 1.51) applied on a grid defined as:

$$x(1; \Psi_j) = 1.0; \; x(2,\Psi_j) = 1.04 \; ;$$

$$y(1; j) = 1.0 - (j-1)\, 0.2, \; j = 1,6 \; ;$$

$$y(2;j) = 1.02 - (j-1)\, 0.204, \; j = 1,6;$$

The variation of the calculated width, b, with downstream distance, x, is shown in Figure 6-2, for values of the parameter $\lambda_i V'$ of 0.0

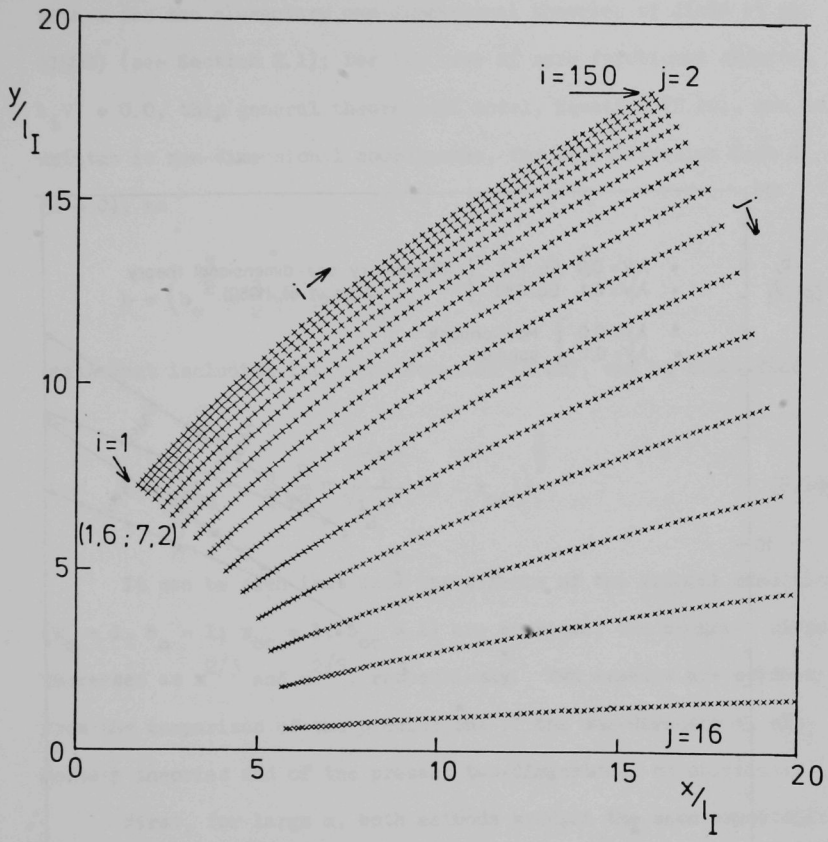

Figure 6-1 A typical grid used for the supercritical region of the intermediate field (every other point in the 'i' direction shown).

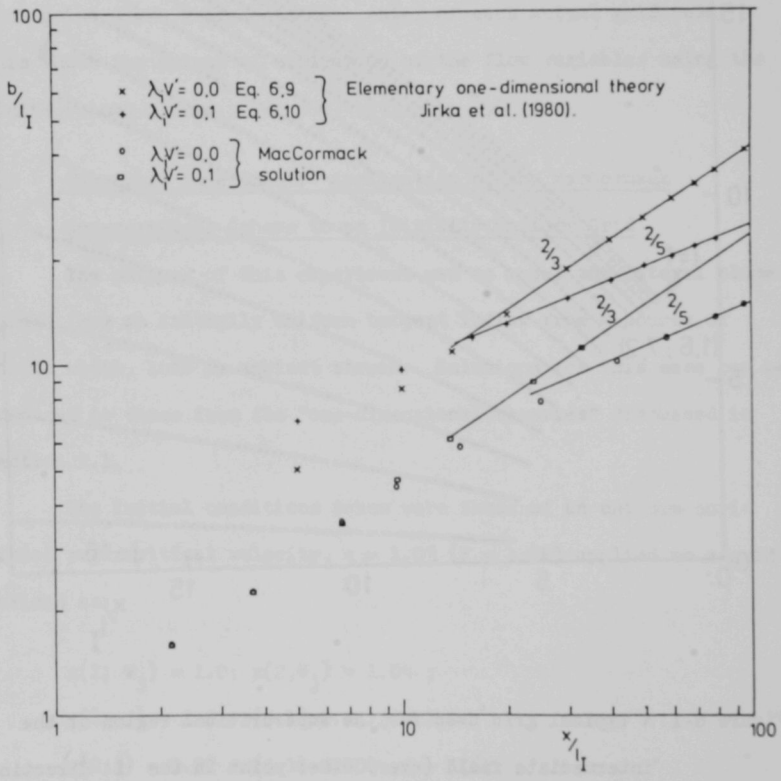

Figure 6-2 Boundary variation with downstream distance for the one-dimensional model of Jirka et al., 1980, and the numerical simulation for 'uniform' initial conditions

and 0.1. Also shown in Figure 6.2 is the boundary width variation with x for the elementary one-dimensional theories of Jirka et al. (1980) (see Section 2.1); for the case of zero frictional effects, $\lambda_i V' = 0.0$, this general theoretical model, Equation (2.20), can be written in non-dimensional coordinates, for stratification Case A (s = 0), as

$$b = \left(b_o^{\frac{3}{2}} + \frac{3}{2}\sqrt{\pi}\,(x - x_o)\right)^{2/3} \tag{6.9}$$

while that including friction, Equation (2.28), can be simplified to

$$b = \left(b_{oc}^{\frac{5}{2}} + \frac{5}{2}\sqrt{\frac{3}{2}}\,\pi\sqrt{\frac{C_D}{\lambda_i V'}}\,(x - x_{oc})\right)^{\frac{2}{5}} \tag{6.10}$$

It can be seen that once the effects of the initial conditions ($x_o = 1$, $b_o = 1$; $x_{oc} = 1$, $b_{oc} = 1$) are overcome, the boundary width increases as $x^{2/3}$ and $x^{2/5}$, respectively. Two aspects are evident from the comparison of the predictions of the one-dimensional elementary theories and of the present two-dimensional calculations:

First, for large x, both methods predict the same asymptotic behavior, namely an $x^{2/3}$ spreading for the inviscid case and an $x^{2/5}$ spreading for the frictional case. This validates the treatment of the frontal boundary condition in the two-dimensional formulation.

Second, the degree of spreading in the two-dimensional calculation is significantly lower (factor of about 2). The main reason

for this mismatch appears to lie in the omission of the lateral (y) acceleration terms from the simple one-dimensional theories. In reality, these reaction terms seem to play an important role in the spreading process. The error, thus introduced, is carried over in the entire downstream domain!

6.3 Application to the Intermediate Field Supercritical Domain

6.3.1 Typical Values of the Frictional Parameter, $\lambda_i V'$

Using the expression for V', Equation (3.62), for stratification Case A (s = 0), evaluated for the "typical" oceanic conditions given in Section 3.1.1, yields a value of $V' \approx 40$. For the laboratory experiments carried out by Jirka et al. (1980), a range of V' values typically between 1 and 20 was obtained. Adams et al. (1981) indicate values of λ_i for fully turbulent oceanic conditions as 10^{-3}, whereas for the less turbulent laboratory conditions ($R_e \approx 5 \times 10^{-3}$), a λ_i value of 5×10^{-3} is more applicable. These values give $\lambda_i V'$ values for oceanic conditions (V' between 10 and 50), of between 0.01 and 0.05, and $\lambda_i V'$ laboratory values of between 0.05 and 0.10. Therefore, $\lambda_i V'$ values of 0.1, 0.05 and 0.01 were investigated, together with the frictionless case ($\lambda_i V' = 0.0$), which is of interest from a fundamental viewpoint.

6.3.2 Results

The MacCormack scheme was applied as a downstream continuation of several of the transcritical flow computations that have been

Table 6-1

A Summary of the Results Presented for the Intermediate Field Supercritical Region.

$\lambda_i V'$ \ ℓ_I / ℓ_N	41.2 Fig.	14.1 Fig.	7.0 Fig.	3.0 Fig.
0.0	6-3a (i,ii)	6-7a (i,ii)	6-8 (i,ii)	6-9a(i,ii)
	6-5a (i,ii)			
	6-6 (iii)			
0.01	6-3b (i,ii)	-	-	-
	6-6 (iii)			
0.05	6-3c (i,ii)	-	-	-
	6-6 (iii)			
0.10	6-3d (i,ii)	6-7b (i,ii)	-	6-9b(i,ii)
	6-6 (iii)			

(i) denotes a graph of velocity vectors

(ii) denotes a graph of height contours

(iii) denotes a plot of frontal boundary shape

summarized in Table 5-1 and associated figures. Results of the Mac Cormack computations for various ℓ_I/ℓ_N and $\lambda_i V'$ values, as summarized in Table 6-1, are given.

In some of these cases the upstream boundary for the MacCormack scheme was equal to the curved downstream boundary of the trans-critical calculation and corresponding flux boundary conditions were applied. In other cases, a certain degree of overlapping between the two computational domains was adopted.

First the complete results for $\ell_I/\ell_N = 41$, i.e., the asymptotic case of negligible near field effect (see Figure 5-14) are discussed, the respective velocity vectors and height contours being shown in Figure 6-3a to d. It can be seen that the increasing frictional effects cause the (self-determined) outer (frontal) boundary to increase in width much more slowly [as would be expected from the theoretical formulae predictions, Equations (6.9) and (6.10)]. In addition, this effect is felt throughout the flow (as can be seen from a comparison of the velocity vectors), as might be expected from the interfacial friction acting over the whole of the horizontal interface (bottom) of the density current. The frictional effects can also be seen to decrease the velocity magnitude in general. This however, does not neccessarily increase the heights in the entire flow domain, as the simple Bernoulli Equation (3.67), no longer holds, due to the frictional effects. For the most part the heights do, in fact, increase apart from a small region near the outer boundary (see

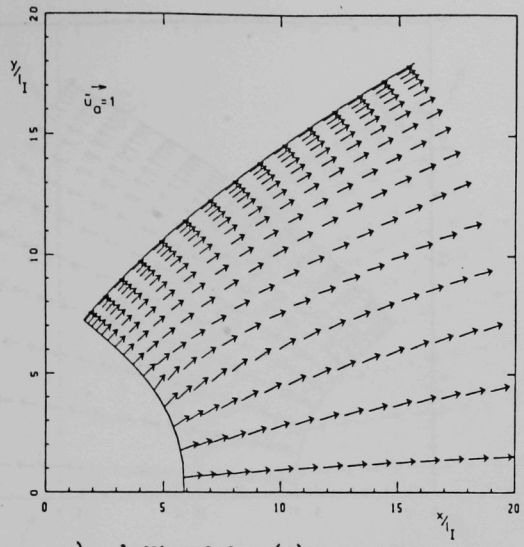

a) $\lambda_i V' = 0.0$ (1) velocity vectors

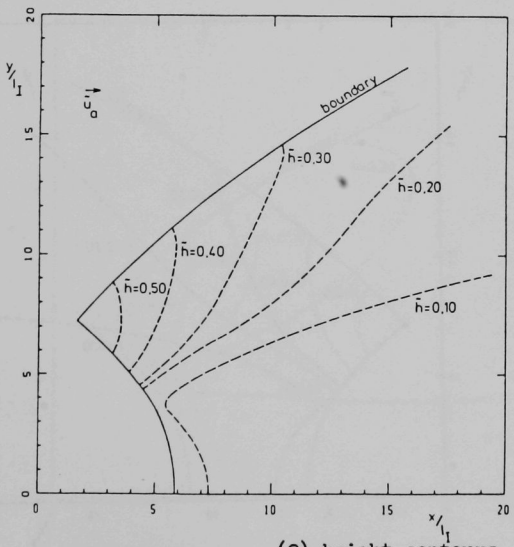

(2) height contours.

Figure 6-3 Results for the supercritical region of the intermediate field, for $\ell_I/\ell_N = 41.2$.

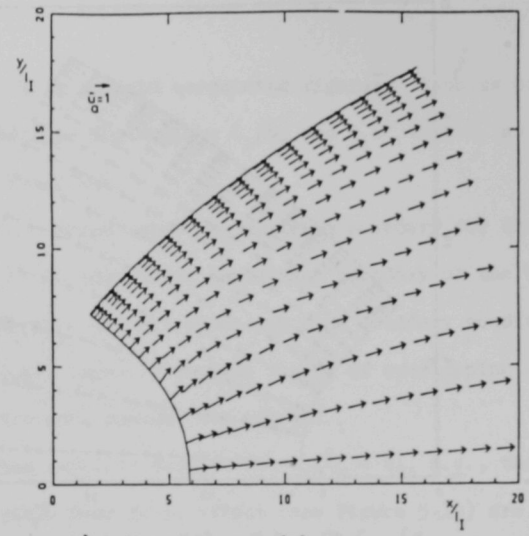

b) $\lambda_i V' = 0.01$ (1) velocity vectors

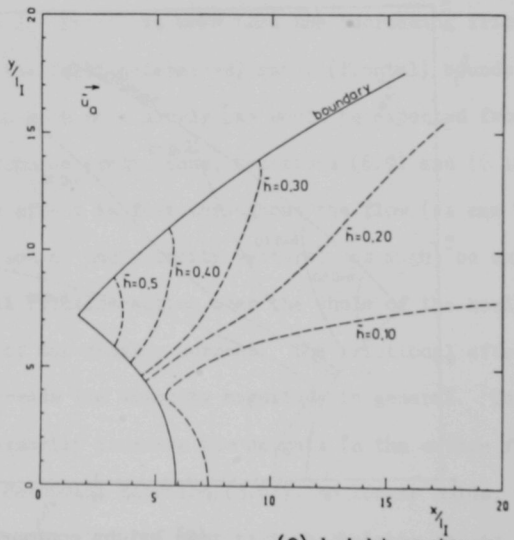

(2) height contours.

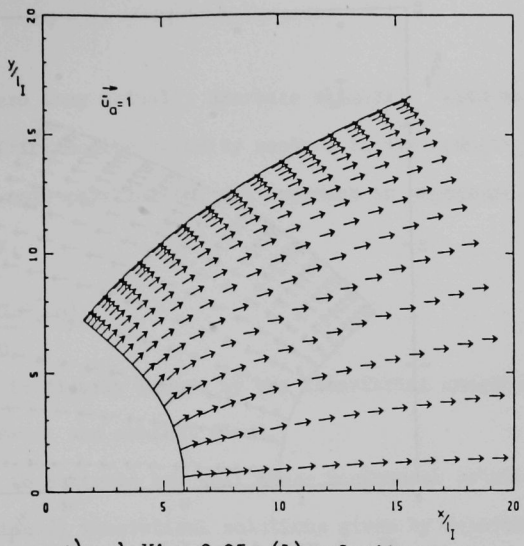

c) $\lambda_i V' = 0.05$ (1) velocity vectors

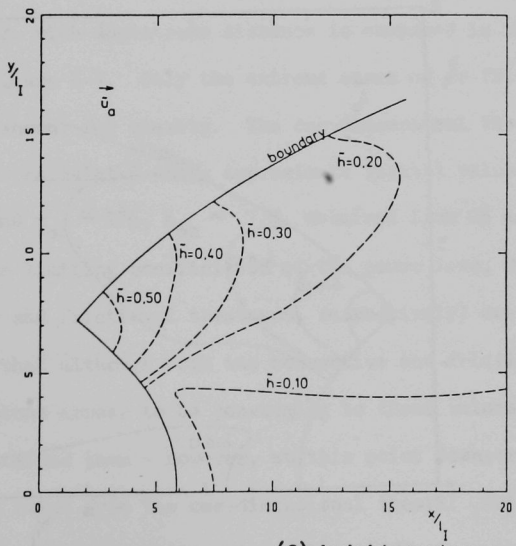

(2) height contours.

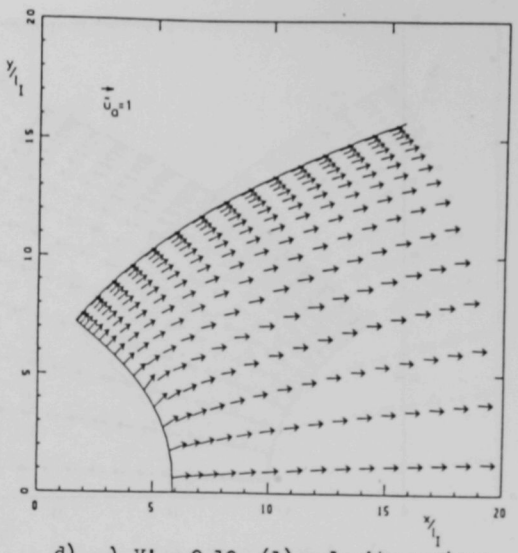

d) $\lambda_i V' = 0.10$ (1) velocity vectors

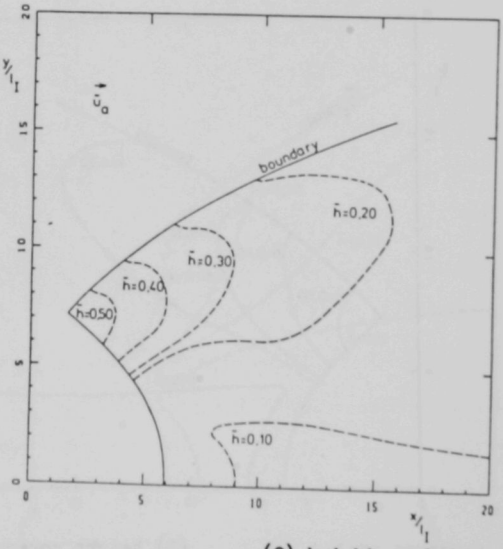

(2) height contours.

Figure 6-3d) where they actually decrease slightly. Also note that for increasing friction the velocity vectors in the downstream section become more and more parallel to, and approach in magnitude, the ambient velocity,

$$\tilde{u}_a = \left(\frac{1}{\sqrt{C_D}}, 0\right) .$$

This phenomenon is clearly caused by the interfacial momentum transfer between the internal and ambient flows.

In order to estimate how well these MacCormack solutions match the (one-dimensional) theoretical solutions given by Equations (6.9) and (6.10) for no friction and frictional effects, respectively, the boundary increase with downstream distance is compared in the log-log plot given in Figure 6-4. Only the extreme cases of no friction and $\lambda_i V' = 0.1$ are shown, for clarity. The one-dimensional theoretical values shown are calculated using approximate initial values of $x_o \approx 1.6$, $b_o \approx 7.2$ and $x_{oc} \approx 1.6$, $b_{oc} \approx 7.2$, obtained from G5 as shown in Figure 6.1. The limiting coefficients of the power laws, 2/3 and 2/5 (for convective and frictional treatment, respectively) are also drawn. It can be seen that although both the convective and frictional numerical solutions appear to be converging to these values, they have not yet obtained them - however, at this point downstream, neither has the value from the one-dimensional theory! This is due to the initial conditions still having a large effect on the solution. The fact that in Section 6.2 the density current, which has small

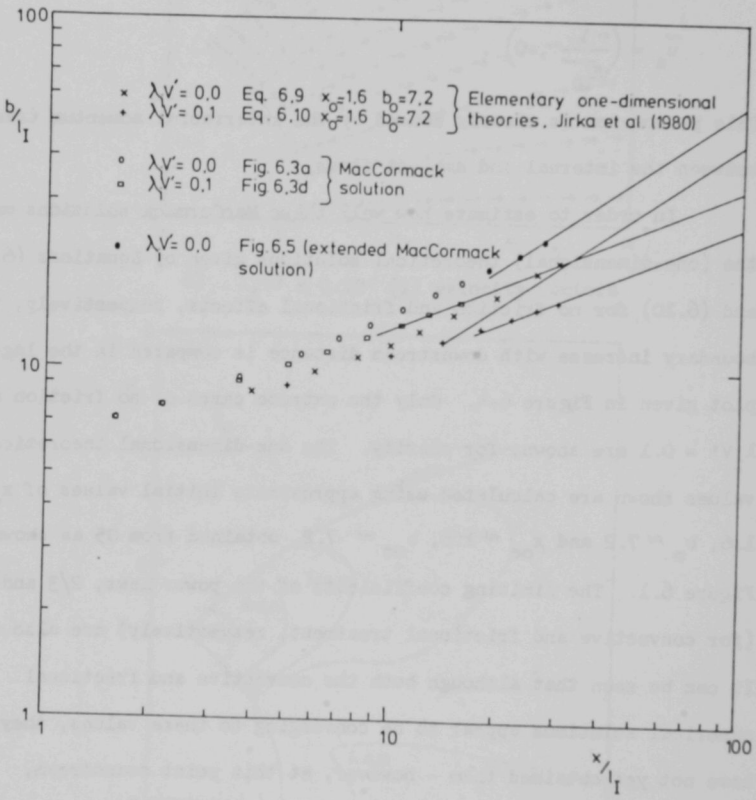

Figure 6-4 Boundary variation with downstream distance for one-dimensional model of Jirka et al., 1980, together with numerical simulation for the supercritical region of the intermediate field corresponding to $\ell_I/\ell_N = 41.2$.

initial dimensions has easily obtained these values, indicates that they would be attained eventually. In order to check this, Figure 6-5 shows the supercritical region extended to larger distances downstream, and in this additional region the current spreading approaches the behavior predicted from the one-dimensional theory as predicted.

Figure 6-6 forms a summary plot showing the frontal boundary shape for the various friction cases (including zero friction), corresponding to $\ell_I/\ell_N = 41$. This emphasizes the decrease in boundary spreading brought about by frictional effects.

6.3.3 Additional Comments

Mention should be made at this point of various limits of applicability of the MacCormack solution.

High velocities: These occur particularily for downstream extensions for the frictionless cases of low ℓ_I/ℓ_N solutions, and are the reason that the solution for $\ell_I/\ell_N = 3$ (Figure 6-9) was terminated earlier than the other supercritical regions. These extremely high speeds cause the solution to become unrealistic (i.e., exceeding the maximum possible velocity for frictionless cases) - a phenomenon also encountered by Garvine (1982), who used a different numerical scheme on a similar problem. This will be discussed further in Chapter 7.

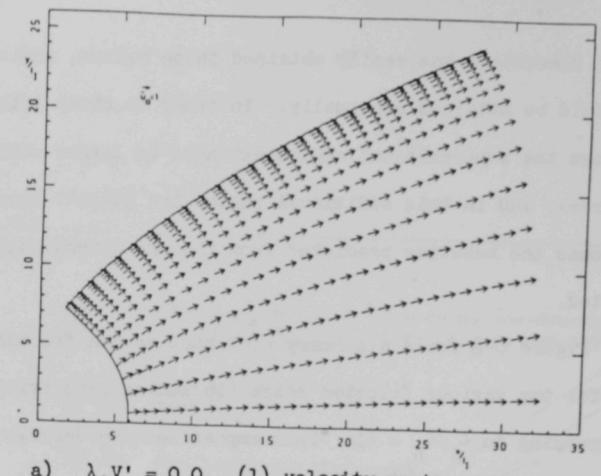

a) $\lambda_i V' = 0.0$ (1) velocity vectors

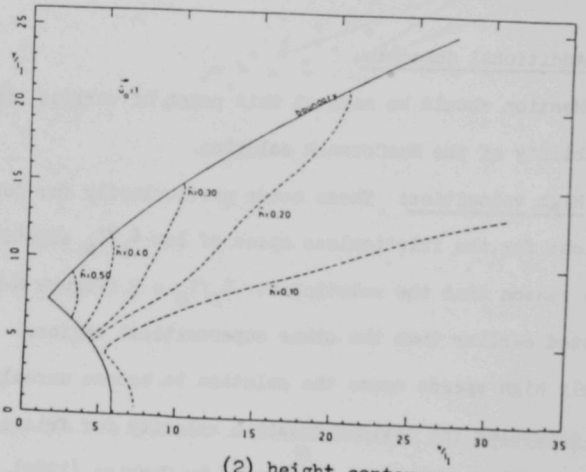

(2) height contours.

Figure 6-5 Results for the supercritical region of the intermediate field for $\ell_I/\ell_N = 41.2$ - downstream extension.

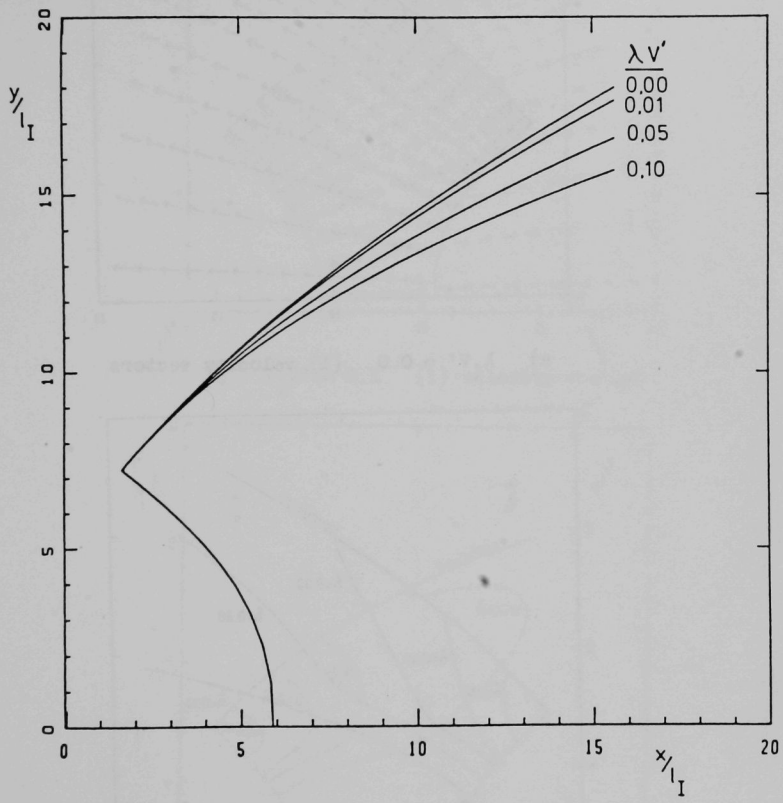

Figure 6-6 Variation of matched boundary curves with friction coefficient for the case of $\ell_I/\ell_N = 41.2$.

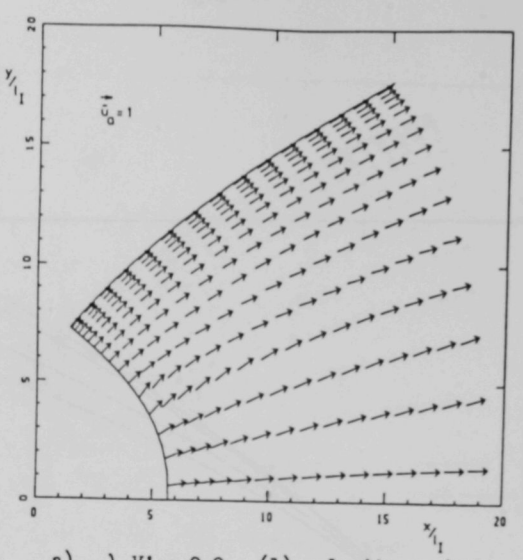

a) $\lambda_i V' = 0.0$ (1) velocity vectors

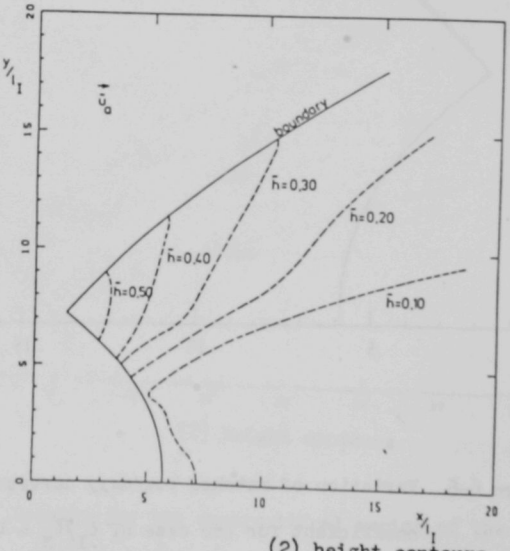

(2) height contours.

Figure 6-7 Results for the supercritical region of the intermediate field for $\ell_I/\ell_N = 14.1$.

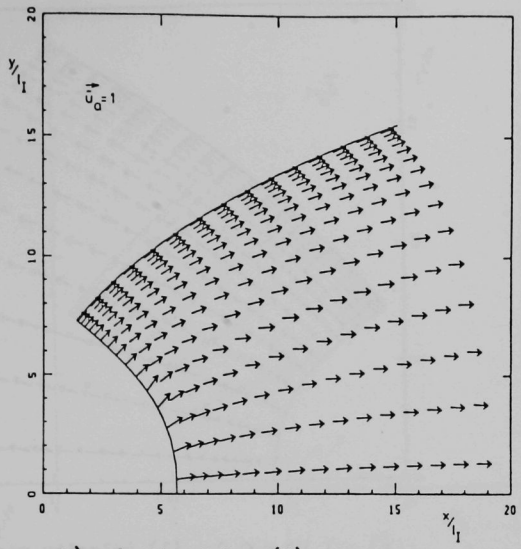

b) $\lambda_i V' = 0.1$ (1) velocity vectors

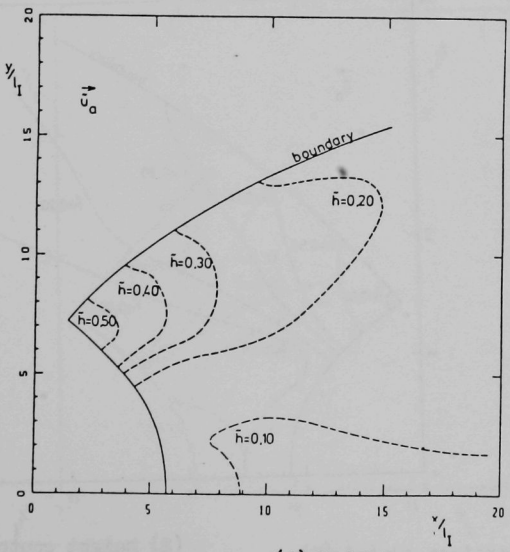

(2) height contours.

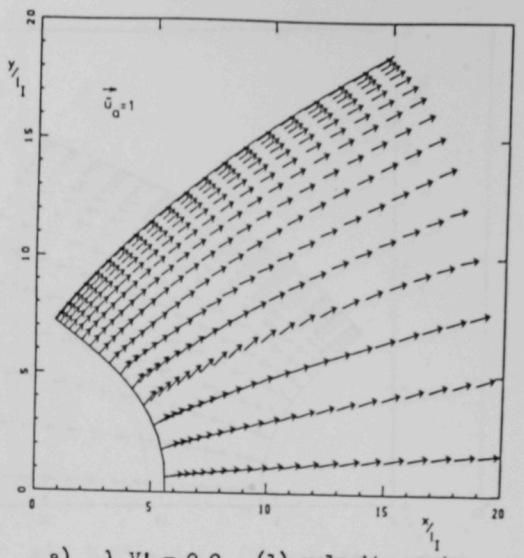

a) $\lambda_i V' = 0.0$ (1) velocity vectors

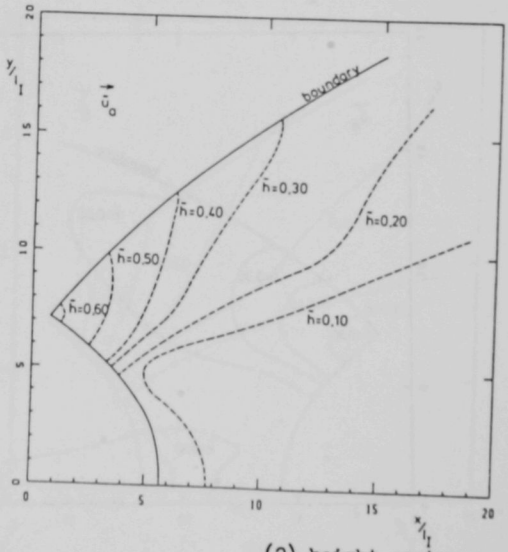

(2) height contours.

Figure 6-8 Results for the supercritical region of the intermediate field for $\ell_I/\ell_N = 7.0$.

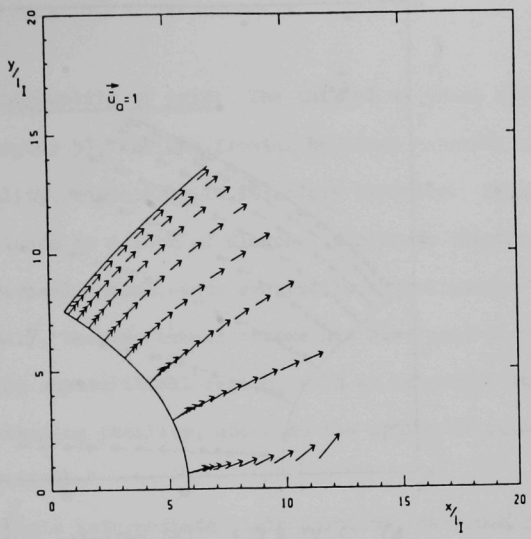

a) $\lambda_i V' = 0.0$ (1) velocity vectors

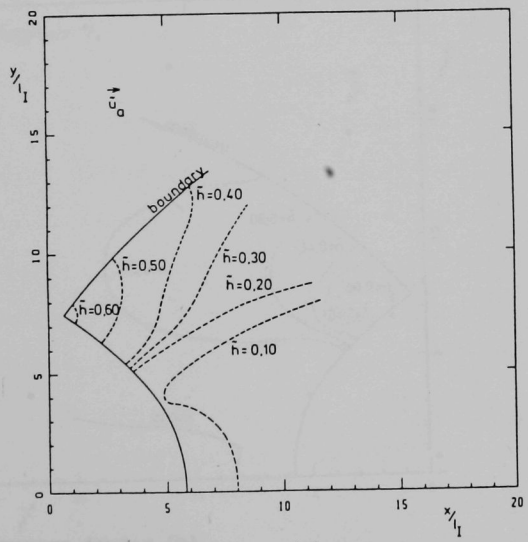

(2) height contours.

Figure 6-9 Results for the supercritical region of the intermediate field for $\ell_I/\ell_N = 3.0$.

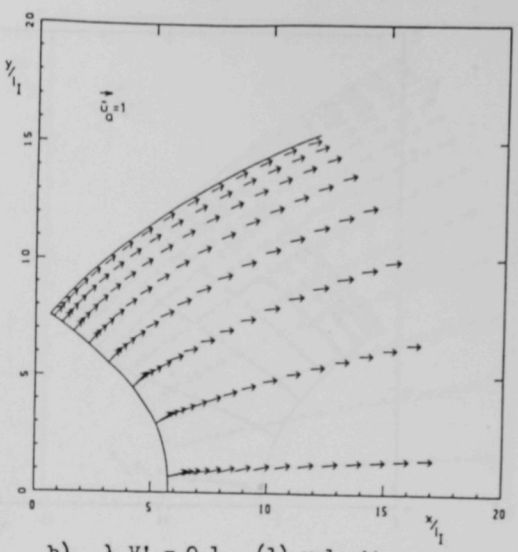

b) $\lambda_i V' = 0.1$ (1) velocity vectors

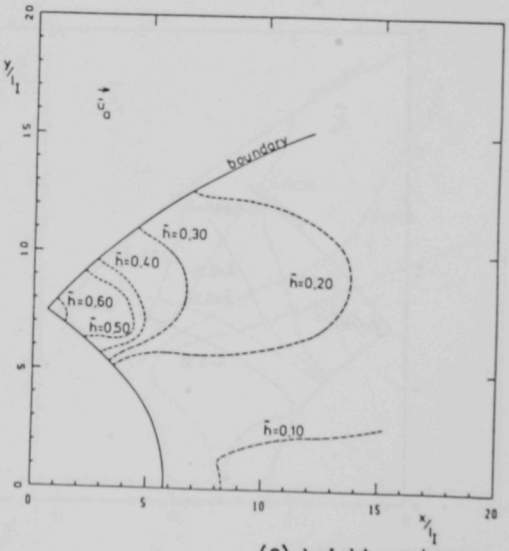

(2) height contours.

Non-orthogonality of grid: The initial upstream grid is orthogonal (Chapter 5), but the frontal boundary generation destroys this orthogonality, especially in its close vicinity. This lack of orthogonality leads to a lack of diagonal dominance (Section 5.3) within the numerical scheme, and, eventually a divergence.

In summary, the MacCormack scheme has been used to obtain solutions to the supercritical region, with an automatic boundary (and grid) generating facility, and also the option of including the effects of friction.

The complete intermediate field solution, obtained by combining the solutions for the transcritical and supercritical regions will be discussed in Chapter 7.

CHAPTER 7

SUMMARY OF PREDICTIONS, COMPARISON WITH EXPERIMENTAL DATA AND ENVIRONMENTAL APPLICATIONS

7.1 Complete Predictions

7.1.1 Summary of Intermediate Field Results

The results for the intermediate field transcritical region (with inner boundary determined by the relative near-intermediate field strengths, ℓ_I/ℓ_N , Section 5.5.1) and its downstream supercritical extension have been discussed in Chapters 5 and 6, respectively. These are now combined, to obtain a complete description of the intermediate field, in the figures summarized in Table 7.1.

Figures 7-1, 7-2 and 7-3 show the full intermediate field solutions, (both velocity field (i) and current thickness (ii)), for their various ℓ_I/ℓ_N values. The delineation between the transcritical and supercritical regions is indicated as a solid line. These figures serve to illustrate the small changes which occur between ℓ_I/ℓ_N values of 41.2, 14.1 and 3.0, respectively. The first serves to illustrate the behavior of a discharge within the asymptotic region, while the second and third are relatively equally spaced on a logarithmic scale, to indicate the behavioural changes with ℓ_I/ℓ_N values.

The effect of interfacial friction on the intermediate field behaviour is illustrated by presenting the internal flow fields for

Table 7-1

Summary Table of the Results Presented for the Full Intermediate Field

$\frac{\ell_I}{\ell_N}$	41.2	14.1	7.0	3.0
grid	G5	G6	G11	G8
$\lambda_i V'$	Fig.	Fig.	Fig.	Fig.
0.0	7-1a(i,ii)	7-2a(i,ii)		7-3a(i,ii)
	7-4 (iii)	7-5 (iii)		7-6 (iii)
	7-7 (iii)	7-7 (iii)	7-7(iii)	7-7 (iii)
0.01	7-4 (iii)	-	-	-
0.05	7-4 (iii)	-	-	-
0.10	7-1b(i,ii)	7-2b(i,ii)		7-3b(i,ii)
	7-4 (iii)	7-5 (iii)	-	7-6 (iii)

(i) Denotes a plot of velocity vectors.

(ii) Denotes a plot of height contours.

(iii) Denotes a plot of frontal boundary shape.

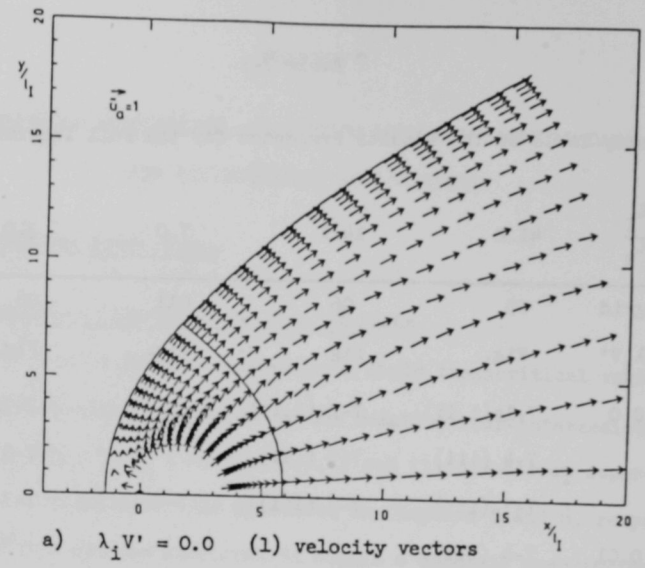

a) $\lambda_i V' = 0.0$ (1) velocity vectors

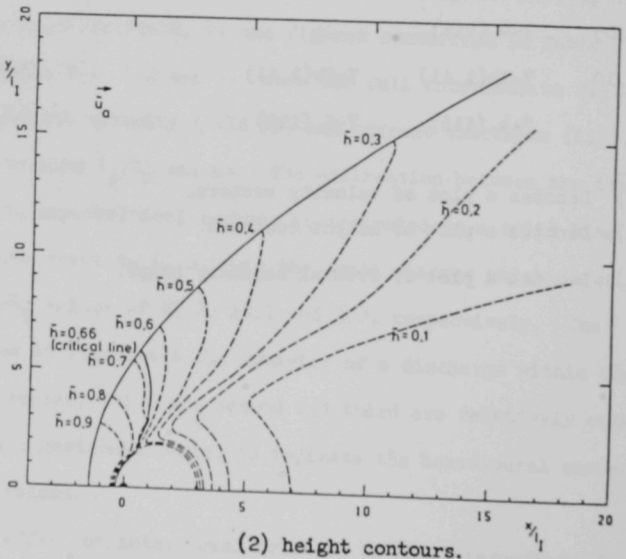

(2) height contours.

Figure 7-1 Results for the full intermediate field for $\ell_I/\ell_N = 41.2$.

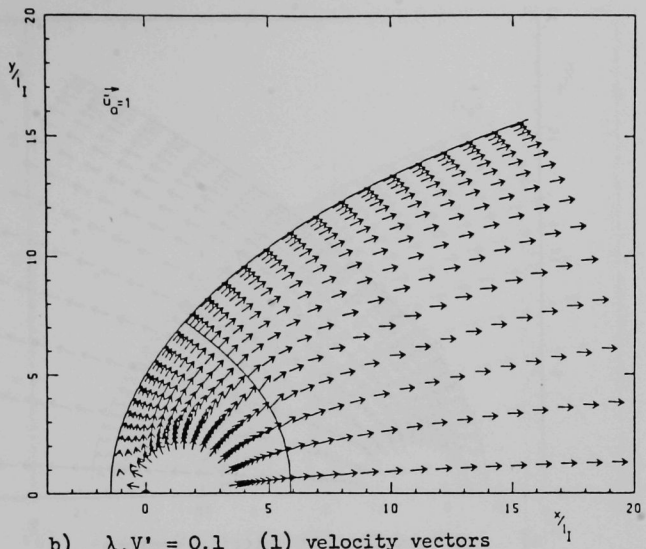

b) $\lambda_i V' = 0.1$ (1) velocity vectors

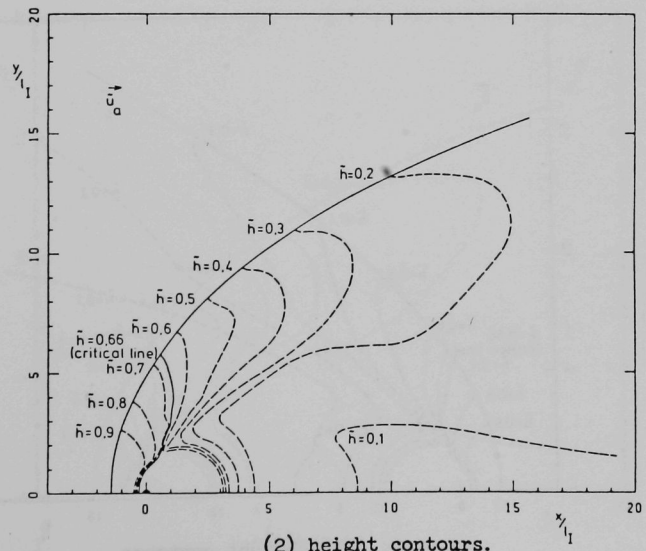

(2) height contours.

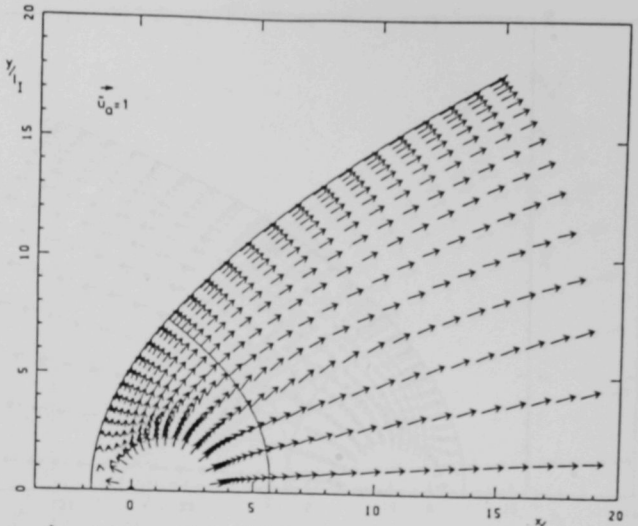

a) $\lambda_i V' = 0.0$ (1) velocity vectors

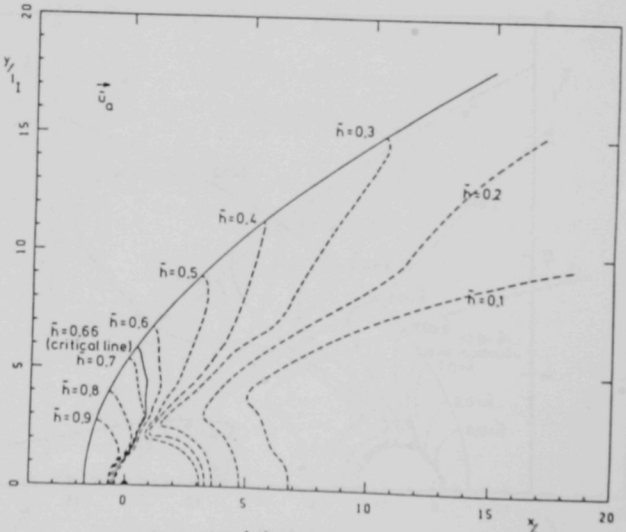

(2) height contours.

Figure 7-2 Results for the full intermediate field for $\ell_I/\ell_N = 14.1$.

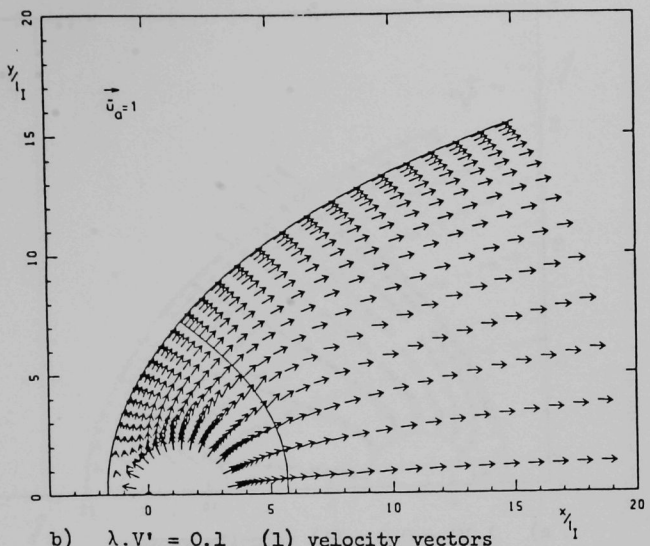

b) $\lambda_i V' = 0.1$ (1) velocity vectors

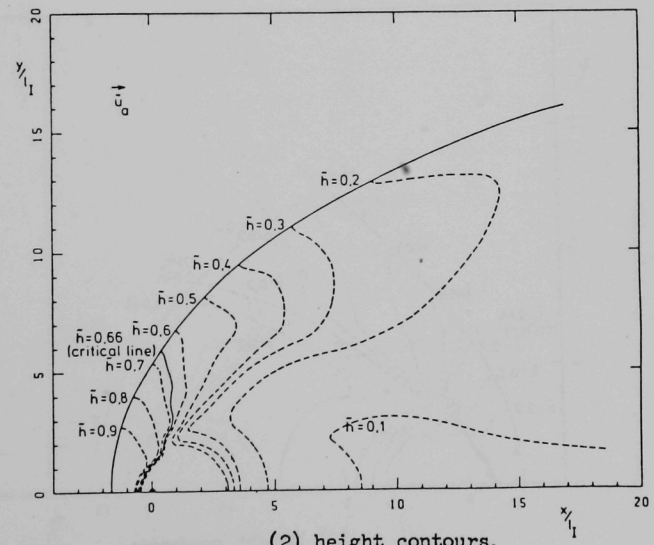

(2) height contours.

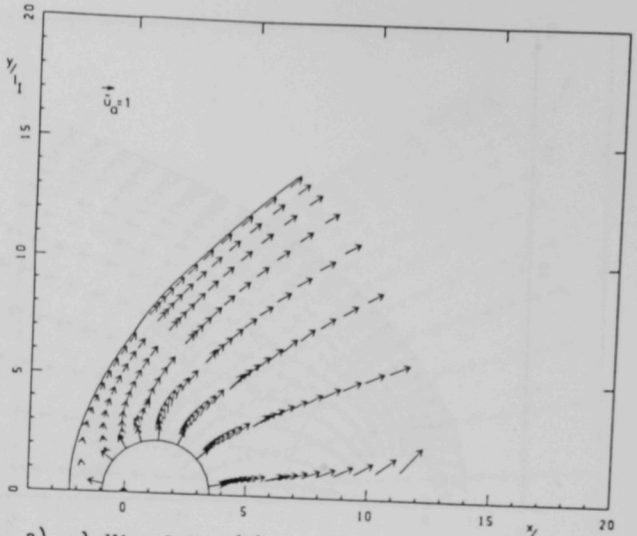

a) $\lambda_i V' = 0.0$ (1) velocity vectors

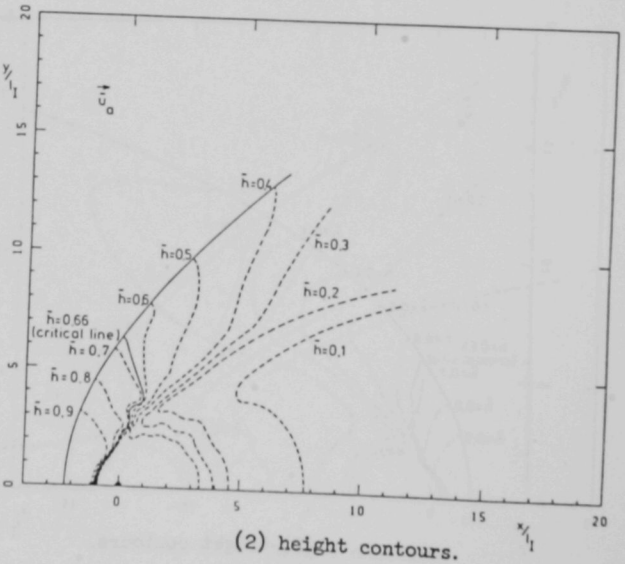

(2) height contours.

Figure 7-3 Results for the full intermediate field for $\ell_I/\ell_N = 3.0$.

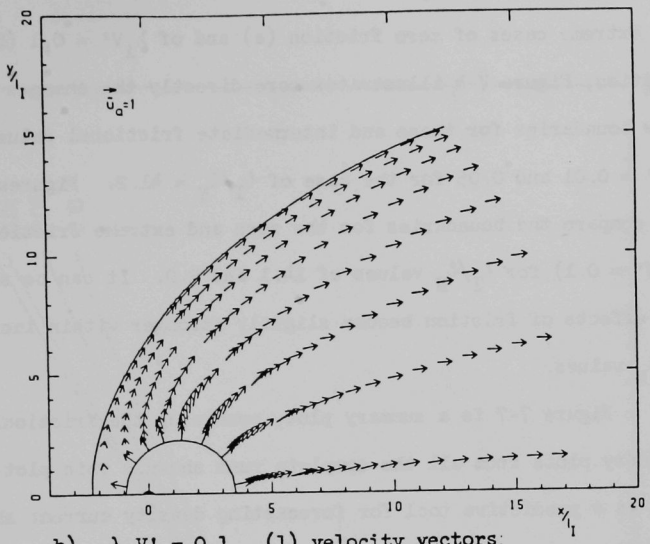

b) $\lambda_i V' = 0.1$ (1) velocity vectors

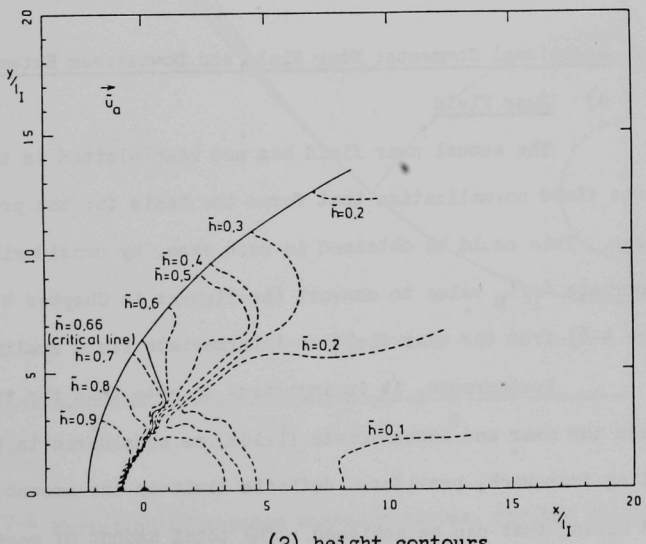

(2) height contours.

the extreme cases of zero friction (a) and of $\lambda_i V' = 0.1$ (b). In addition, Figure 7-4 illustrates more directly the changes in the flow boundaries for these and intermediate frictional values of $\lambda_i V' = 0.01$ and 0.05 for the case of $\ell_I/\ell_N = 41.2$. Figures 7-5 and 7-6 compare the boundaries for the zero and extreme frictional case ($\lambda_i V' = 0.1$) for ℓ_I/ℓ_N values of 14.1 and 3.0. It can be seen that the effects of friction become slightly stronger within increasing ℓ_I/ℓ_N values.

Figure 7-7 is a summary plot, combining the frictionless boundary plots from all the complete runs shown. This plot can be used as a predictive tool for forecasting density current shapes for various relative near to intermediate field strengths.

7.1.2 Additional Comments: Near Field and Downstream Extensions

a) Near Field

The actual near field has not been plotted in the intermediate field normalization that forms the basis for the preceding figures. This could be obtained in each case, by considering the appropriate ℓ_I/ℓ_N value to convert the figures in Chapter 4 (e.g., Figure 4-6) from the near field to intermediate field scaling.

Furthermore, it is important to note that the transition between the near and intermediate fields, as considered in the modeling framework, provides a definite limit on the amount of near-field mixing that can be achieved. The total amount of near-field flow (at the transition point), $Q/(M_o^{5/4}/J_o^{1/2})$ is given as a

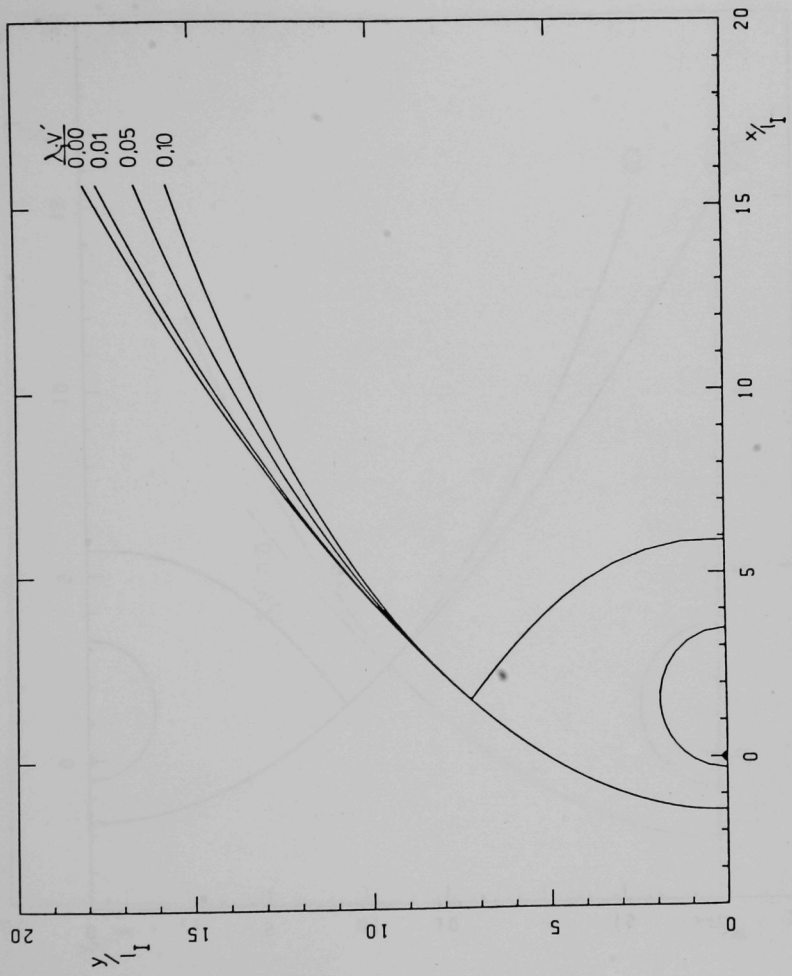

Figure 7-4 Variation of matched boundary curves, for the full inter mediate field, with friction coefficient for $\ell_I/\ell_N = 41.2$.

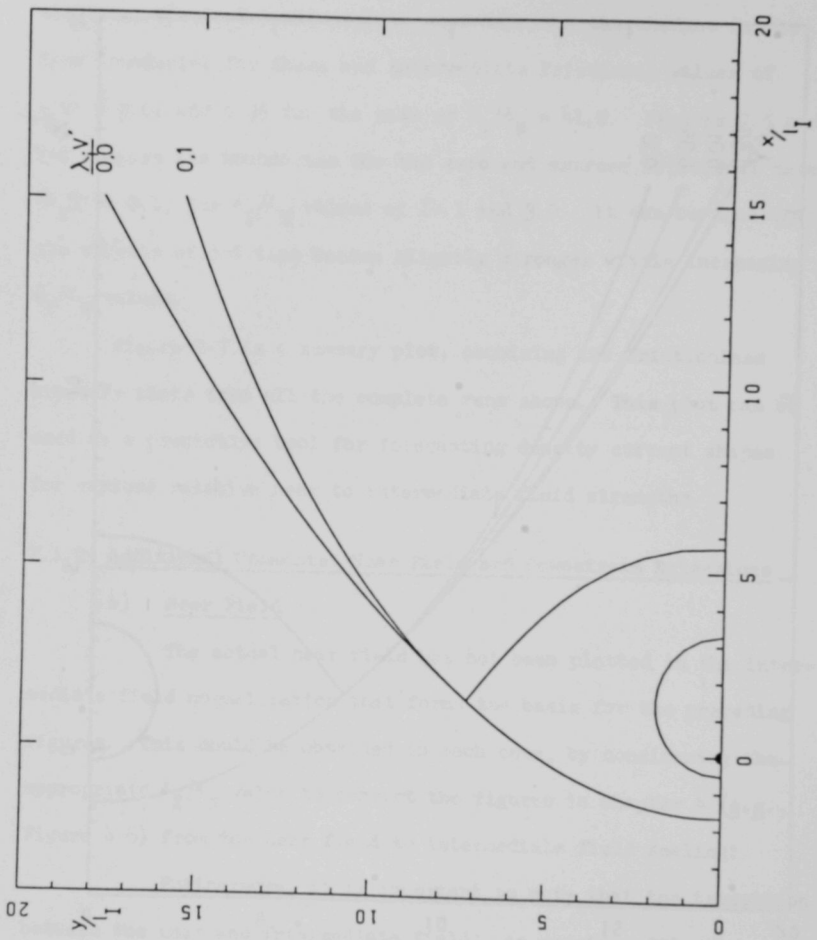

Figure 7-5 Variation of matched boundary curves, for the full intermediate field, with friction coefficient for $\ell_I/\ell_N = 14.1$.

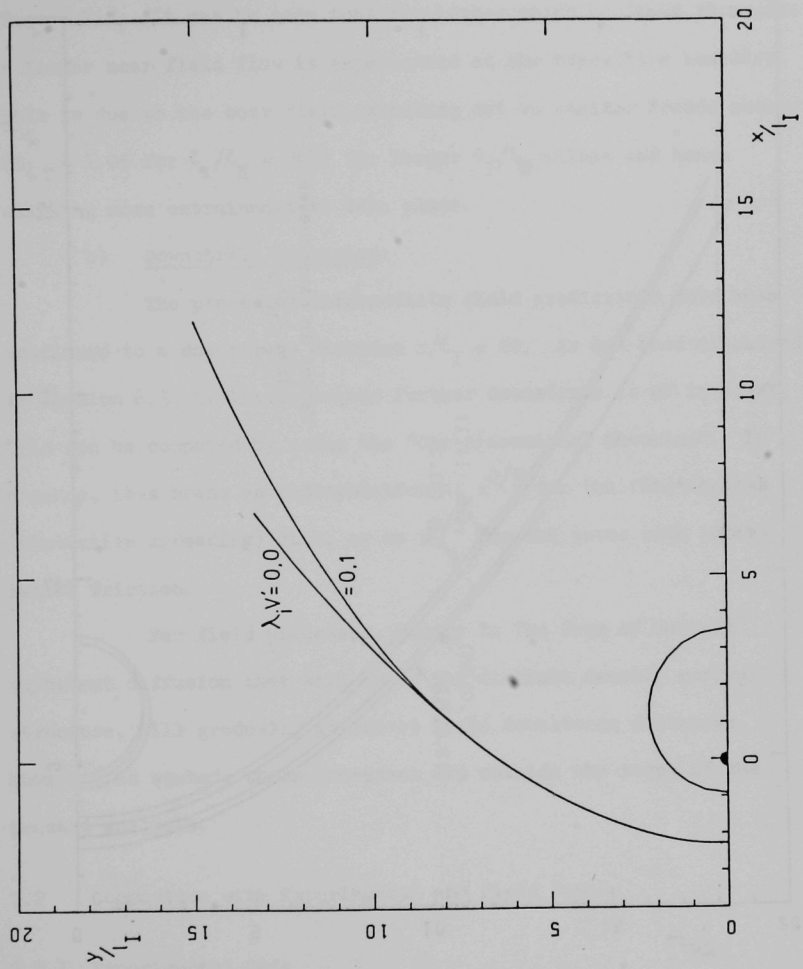

Figure 7-6 Variation of matched boundary curves, for the full inter mediate field, with friction coefficient, for $\ell_I/\ell_N = 3.0$.

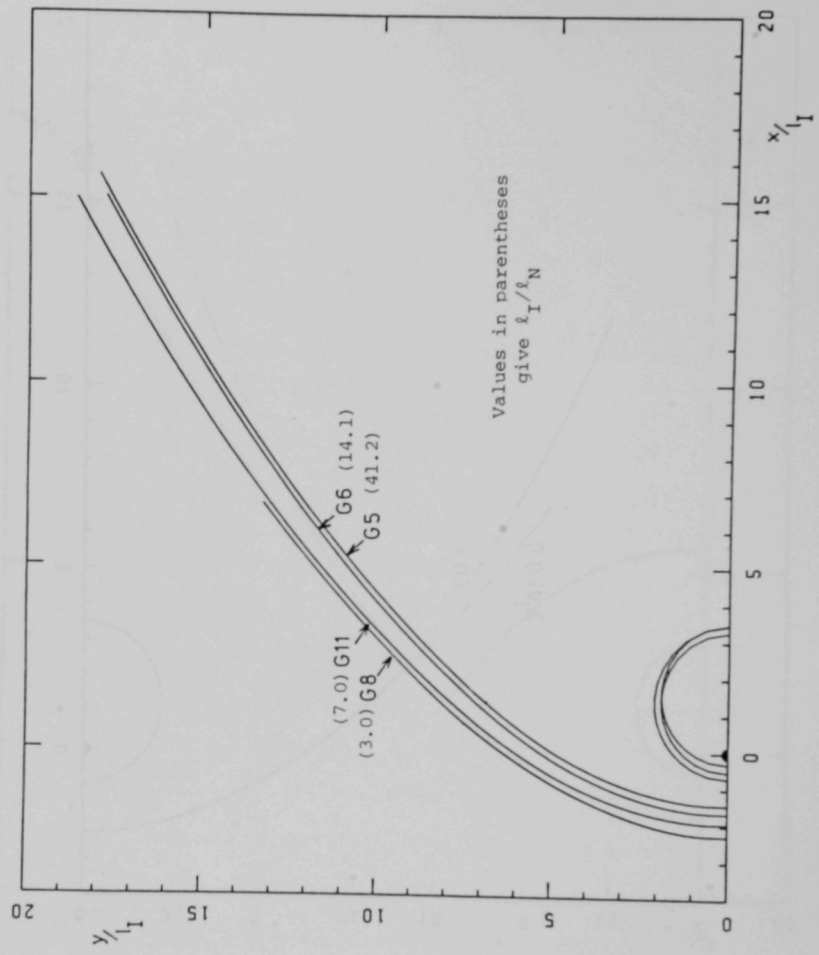

Figure 7-7 Comparison of intermediate field boundary shapes for various ℓ_I/ℓ_N values, (for zero interfacial friction, $\lambda_i V' = 0.0$).

function of the relative intermediate to near-field strengths in Figure 7-8. It can be seen that for larger relative field strengths a larger near field flow is experienced at the transition boundary. This is due to the near field extending out to smaller Froude numbers ($F_{\ell T} = 1.05$ for $\ell_I/\ell_N = 41$) for larger ℓ_I/ℓ_N values and hence allowing more entrainment to take place.

b) Downstream Extension:

The preceding intermediate field predictions have been continued to a downstream distance $x/\ell_I = 20$. As has been discussed in Section 6.3, if the behaviour further downstream is of interest, this can be computed by using the "one-dimensional theories". In essence, this means an extrapolation as $x^{2/3}$ for the frictionless (convective spreading) case, or as $x^{2/5}$ for the cases with interfacial friction.

Far field processes, mostly in the form of ambient turbulent diffusion that will erode the distinct density current structure, will gradually govern at large downstream distances. However, as stated, these processes are outside the scope of the present analysis.

7.2 Comparison with Experimental and Field Data

7.2.1 Experimental Data

Jirka *et al.* (1980) and Chen (1980) investigated the density current formed by heated water discharged from a stationary source into a moving ambient. Huq (1983) studied density currents formed by

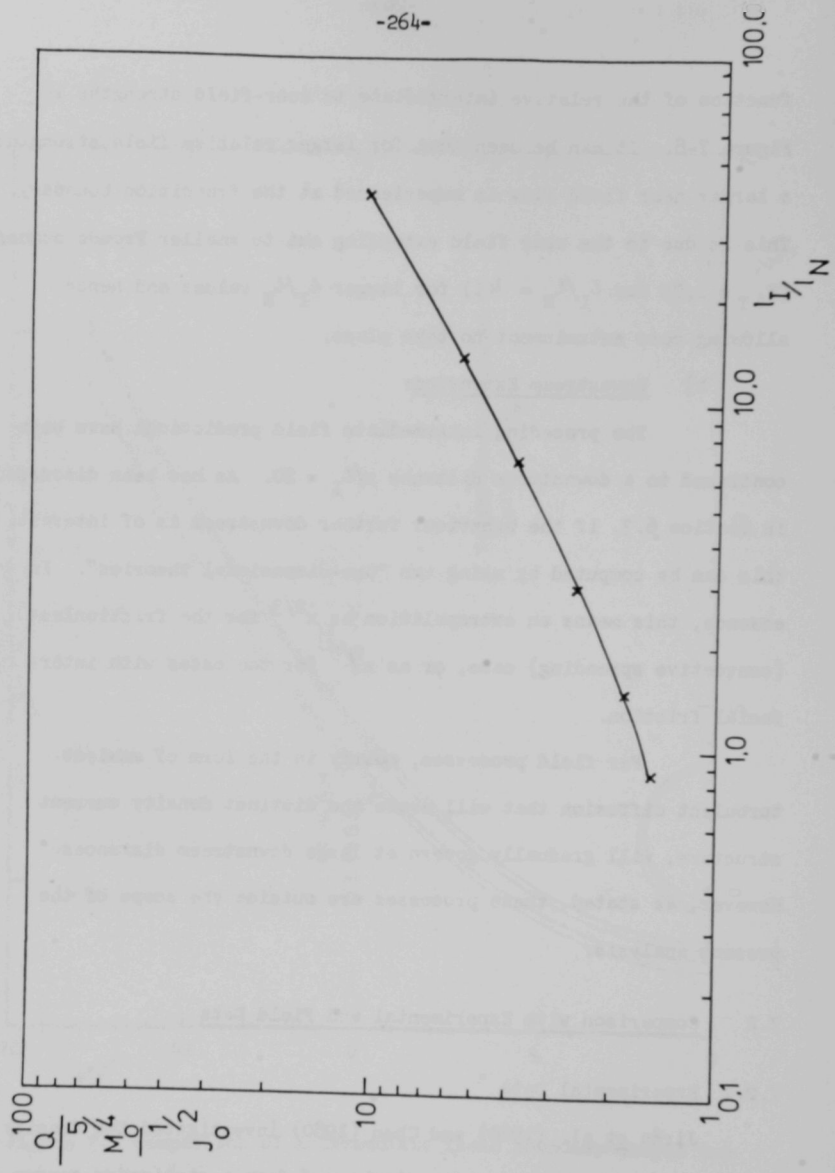

Figure 7-8 Variation of total near-field dilution, $\hat{Q}$, with relative intermediate to near-field strengths, ℓ_I/ℓ_N.

either temperature or/and salinity differences. In both cases the discharge was from a moving source into a stationary ambient. Except for possible minor differences due to turbulence in the moving ambient flow (stationary source), both methods should produce similar results.

The upstream intrusion length, x_s, normalized by the intermediate field length, ℓ_I (Table 3-4) is drawn as a function of the relative field strengths, ℓ_I/ℓ_N, in Figure 7-9. In addition, in order to investigate the width of the density current, Figure 7-10 gives the relationship between the width at the source, b(o), with ℓ_I/ℓ_N.

The results of Huq (1983) and Jirka et al. (1980) were carried out for, in general, similar initial flow properties. Typical values in both studies are: momentum flux ≈ 2000 cm^4/s^2, buoyancy flux ≈ 4000 cm^4/s^3, and ambient velocity ≈ 3 cm/s. These combine to give typical length scales of $\ell_N \approx 5$ cm and $\ell_I \approx 24$ cm. In particular, the ranges of values used in these studies are summarized in Table 7-2. The radial discharge device shape was similar in both studies, having a radius $r_o = 7.5$ cm, with a slot height, h_o, of between 2 and 6 cm (Jirka et al., 1980) and between 2 and 4 cm (Huq, 1983).

As shown in Figures 7-9 and 7-10, both of the above data sources, which were obtained using different techniques (moving versus stationary source) appear to be consistent with each other. Over their common range, the different data showed excellent agreement.

In the range ℓ_I/ℓ_N less than 30, the experimental data all

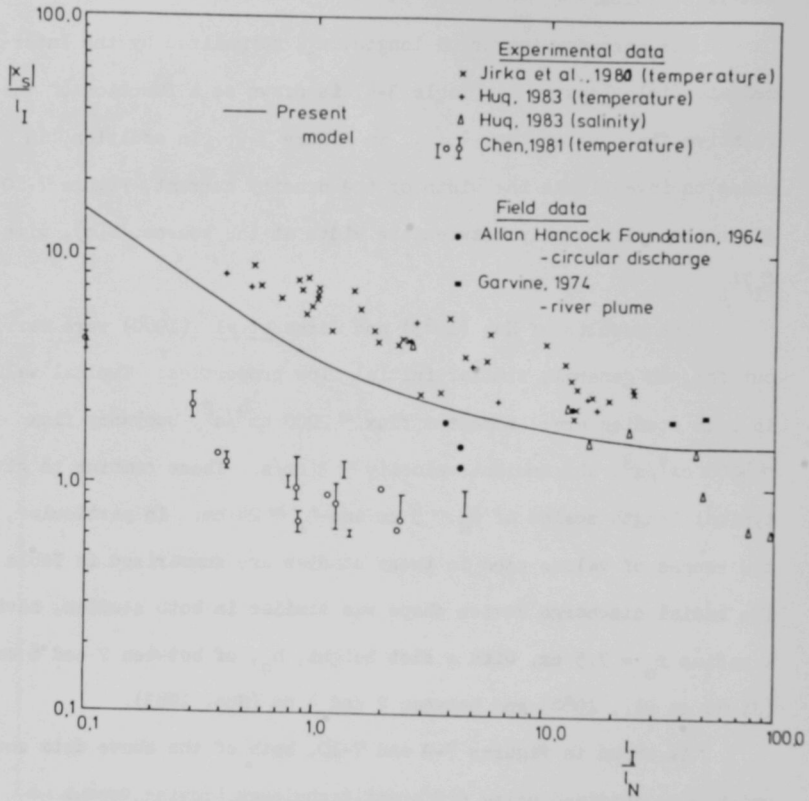

Figure 7-9 Comparison of experimental and field data with the numerical estimation of the normalized stagnation length, $|x_s|/\ell_I$.

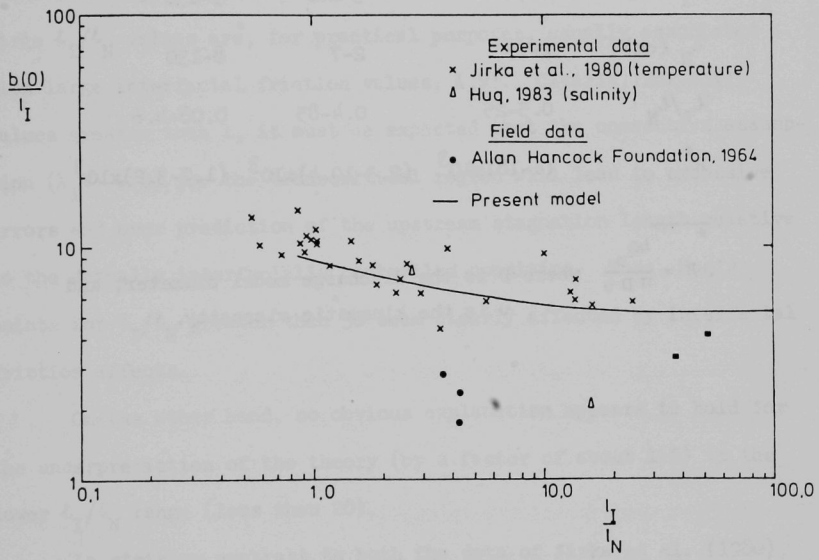

Figure 7-10 Comparison of experimental and field data with the numerical estimation of the normalized current width at the source, $\frac{b(x=0)}{\ell_I}$, as a function of the ratio of intermediate to near-field strengths, ℓ_I/ℓ_N.

Table 7-2

Range of Flow Parameters Used in Various Experimental Data Sources.

	Jirka et al. (1980)	Huq (1983)	Chen (1980)
ℓ_I (cm)	7-70	3-100	5-130
ℓ_N (cm)	2-15	2-7	8-130
ℓ_I/ℓ_N	0.5-25	0.4-85	0.08-4.6
R^*	$(1\text{-}18)\times10^3$	$(2.3\text{-}10.4)\times10^3$	$(1.7\text{-}3.2)\times10^3$

* $R = \frac{4Q_o}{\pi D \nu}$ where D is the discharge model diameter, and ν is the kinematic viscosity.

have somewhat higher stagnation lengths, x_s/ℓ_I, than predicted by the present theory. On the other hand, Huq's data points for ℓ_I/ℓ_N values greater than 30 fall considerably below the theory.

The reason for the latter mismatch can be seen by considering the range of $\lambda_i V'$ values in both studies: $\lambda_i V' = 0.003$ to 0.3 in Jirka et al. (1980) and $\lambda_i V' = 0.06$ to 11 in Huq (1983). Thus some of Huq's data experience considerable frictional effects. Furthermore, large ℓ_I/ℓ_N values are, for practical purposes, usually associated with large interfacial friction values, $\lambda_i V'$. Clearly, for $\lambda_i V'$ values greater than 1, it must be expected that the convective assumption ($\lambda_i V' = 0$) for the transcritical region will lead to excessive errors and over prediction of the upstream stagnation length relative to the actually interfacially controlled condition. Thus, Huq's points for ℓ_I/ℓ_N greater than 30 seem clearly affected by interfacial friction effects.

On the other hand, no obvious explanation appears to hold for the underprediction of the theory (by a factor of about 1.5) in the lower ℓ_I/ℓ_N range (less than 20).

In striking contrast to both the data of Jirka et al. (1980), and Huq (1983), the study by Chen (1980) indicates considerably lower stagnation lengths (no width information being given). These stagnation length values are plotted on Figure 7-9. It can be seen that relative to the previous two studies, the mismatch is of the order of 10.

Various possibilities exist, which might explain this discrepancy: 1) differences in the ℓ_I/ℓ_N range, 2) differences in Reynolds number, and 3) possible difficulties with the radial discharge device in Chen's experiment. In order to investigate these possibilities, the initial conditions and range of flow parameters used for Chen's experiments should be noted. Typical initial conditions are: momentum flux values of $\approx 7000\ cm^4/sec^2$, buoyancy flux $\approx 200\ cm^4/sec^3$ and an ambient velocity of ≈ 1.0 cm/sec, which give typical length scales of $\ell_N \approx 54$ cm and $\ell_I \approx 31$ cm. The ranges of values used are again given in Table 7-2. The radial discharge device shape used had a radius $r_o \approx 7.6$ cm and a height, $h_o \approx 0.3$ cm.

Thus, considerable overlap exists in the ℓ_I/ℓ_N values considered in all three experimental studies. Also, the Reynolds number values for all experiments are well above a critical value of 1,000 to 3,000, required for turbulent flow conditions to result. Thus the first two possible explanations for the discrepancies can be discounted.

However, the third possibility should be considered further, as it is, in fact, difficult to generate a truly uniform flow through a radial slot discharge device. This has to do with the fact that the flow is decelerating as it travels from an inner chamber through a radial slot of finite length to the outside. Difficulties in generating such flows have been noted earlier by Jirka _et al_. (1977).

The problem can be understood by the differentiation of the

Bernoulli equation (neglecting friction within the slot) which gives

$$\frac{d}{dr}\left(\frac{q^2}{2}\right) + \frac{d}{dr}\left(\frac{p}{\rho}\right) = 0 \qquad (7.1)$$

where p is the pressure. For a radial slot with constant height, h_o, the velocity will decrease by virtue of continuity, thus $\frac{d}{dr}\left(\frac{q^2}{2}\right) > 0$, leading to an adverse pressure gradient. Thus the flow is liable to finite internal separation effects, which may be triggered by any geometry or frictional imperfection within the model and, much more importantly, by an uneven pressure field in the ambient fluid surrounding the device. In case of an ambient crossflow, there is, of course, a highly uneven pressure distribution (with maximum stagnation values on the upstream side). Also, the problem will be most severe if large ratios, r_o/r_i exist (r_o = outer radius of slot, r_i = inner radius of slot = chamber radius).

To overcome this problem, Jirka et al. (1980), used a model with several features: a short slot length, $r_o/r_i \leq 1$ and internal baffles and dissipation devices (wire screens) to minimize the effect of imperfection in the slot geometry. The shortness of the slot discourages the development of the adverse pressure gradients and resulting instabilities. Another method of overcoming this problem was used by Jirka et al. (1977). They designed the upper surface of the radial slot so as to decrease the slot height with increasing distance from the inner radius, such that the flow area was constant, and hence no deceleration took place in the flow. Furthermore, they split the

inner chamber into several sections, each with a separate supply line. Despite these measures, some imperfections in the radial flow distribution persisted, albeit tolerable.

Chen's model, however, had an extreme ratio, $r_o/r_i \approx 2$, with a constant slot height, h_o, and thus strong adverse pressure gradients under any magnitude of discharge flow. This, together with the higher upstream outside pressure field, may well have significantly reduce the discharge flux (and momentum flux) into the upstream direction, and therefore correspondingly reduced the stagnation lengths. Chen does not discuss this potential problem, but does not offer conflicting evidence either, in the form of, say, stagnant reference experiments with documented radial uniformity.

7.2.2 Field Data

Two types of field data are included in Figures 7-9 and 7-10.

- Buoyant discharge from a submerged single port on the ocean bottom, (photographs from the Allan Hancock Foundation, 1964).
- Riverine plume discharge into a saline estuary, (Garvine, 1974) (discussed in Section 7.3.1).

The initial discharge data for the first (submerged discharge) requires some manipulation to take account of the effects of ambient velocity and ambient mixing during its ascent to the surface. These considerations will now be discussed in more detail. The flow is discharged from a submerged single port at a rate, $Q = 5.26\ m^3/s$ and at a depth, $H = 16.8$ m and buoyancy $g'_o = 0.245\ m/s^2$ into an ambient

flow, u_a = 0.175 and 0.160 m/s, respectively. If, during its ascent from the ocean bottom to surface, the discharge is assumed to be a perfect plume, the following computations can be made: The mixing with the ambient takes place such that the mass flux at any height, z, is given by Rouse et al.'s (1952) equation

$$Q = 0.15\ (Q_o g_o')^{1/3}\ z^{5/3} \tag{7.2}$$

after Fischer et al. (1979). Also, an averaged speed within the plume is given by

$$q_u = \frac{4.7}{2}\ (Q_o g_o')^{1/3}\ z^{-1/3}\ , \tag{7.3}$$

Upon reaching the surface, the plume begins to spread horizontally such that the initial horizontal speed is approximately equal to the vertical velocity prior to the horizontal motion (Lee and Jirka, 1981). Using the above data, an estimate for the final dilution after the ascent is, $S = \frac{Q}{Q_o} = 3.4$, and the initial spreading velocity, q_u = 1.0 m/s. In addition, the plume will acquire horizontal velocity in the downstream direction due to bending brought about by the ambient flow momentum. An estimate of this bending can be obtained from Wright's (1977) trajectory law, which can be stated as

$$\left(\frac{z}{\ell_m}\right) = 2.0\ \left(\frac{x}{\ell_m}\right)^{1/2} \tag{7.4}$$

where ℓ_m is defined as

$$\ell m = \frac{M_o^{1/2}}{u_a} \tag{7.5}$$

and M_o is the initial source momentum flux. Equation (7.4) allows estimation of the angle, θ, of the plume to the horizontal, as

$$\theta = \tan^{-1} \left(\frac{dz}{dx}\right) \tag{7.6}$$

At a height, H, this is evaluated as the impingement angle, $\theta \approx 65^o$, in this case. Once the angle of the plume to the horizontal is known, a simple one-dimensional momentum analysis of the impingement process yields the relative discharge in the upstream (-x) direction,

$$Q_u = SQ_o \left(\frac{1 - \cos \theta_i}{2}\right) \tag{7.7}$$

and in the downstream (+ x) direction,

$$Q_d = SQ_o \left(\frac{1 + \cos \theta_i}{2}\right) \tag{7.8}$$

For $\theta_i \approx 65^o$, Equation (7.8) yields $Q_u \approx 0.3\ SQ_o$ as opposed to $Q_u = 0.5\ SQ_o$, which would hold for zero plume bending (or initial radial discharge).

In principle, the actual non-uniform flow distribution calculated in this manner could be specified as a boundary condition for the present modeling framework (as opposed to the radial uniformity assumed in the present study). However, an approximate procedure, for comparison purposes - especially as far as the prediction of upstream stagnation is concerned - may be to simply multiply the entire flux quantities by the factor $(1 - \cos \theta_i)$ (i.e., 0.6 in the present

case) to account for the reduced upstream fluxes.

If the data is treated in this manner, then it can be seem from Figures 7-9 and 7-10 that one data points fall very close to the numerical predictions for the stagnation length. It is slightly below the experimental data of Jirka et al. (1981) and Huq (1983). The frictional effects alone could not account for this discrepancy, as low $\lambda_i V'$ values of ≈ 0.3 obtained. However, it should be noted that slight discrepancies in the ambient velocity, flow rate, etc. could easily account for the slight differences observed.

The riverine data from Garvine (1974) also shows very good agreement with the numerical predictions. Again frictional effects are minor ($\lambda_i V' \approx 0.2$), and the slight discrepancies could easily be explained by difficulties in estimating the field parameters, such as estimating an uniform ambient velocity along the banks of an estuary having a sloping bottom. The exact method of treating the river plume data (which are generated by a side channel inflow rather than a radial discharge!) is explained in the subsequent section.

In summary, the predictions and the framework of the present numerical modeling study appear to be well confirmed by both different laboratory experimental data (largely discounting Chen's results, however) and field data.

7.3 Predictions

The purpose of this section is two-fold: first to demonstrate

how the tabulated and graphed results of the present study can be applied to different environmental discharge problems, without necessitating actual numerical model implementation. Second, to show both the magnitude and features of large scale environmental density currents and their strong sensitivity to ambient conditions.

7.3.1 Application to a River Discharge

The numerical solution presented in this thesis was solved for a radial source discharging into an ambient flow. However, a river discharge into an ambient flow, i.e., a line source along the x-axis rather than a radial (or point) source, can be thought of as approximately similar.

The principal assumptions of the riverine application are, as shown in Figure 7-11, that the upstream edge of the river inflow is approximately the origin of the co-ordinate system and that near-field effects play a rather minor role. The latter assumption should hold if the inflow is critical at the river mouth (with stagnant saline wedge intrusions) or only mildly supercritical, since the further mixing is then strongly suppressed, also, in view of the unusually large source dimension, W (see also Jirka et al., 1981). The first assumption appears readily acceptable if the near-field configuration of Figure 7-2 is considered: instead of the radial circle, whose upstream edge is always close to x = 0 in the intermediate field normalization, a laterally distributed inflow can be assumed.

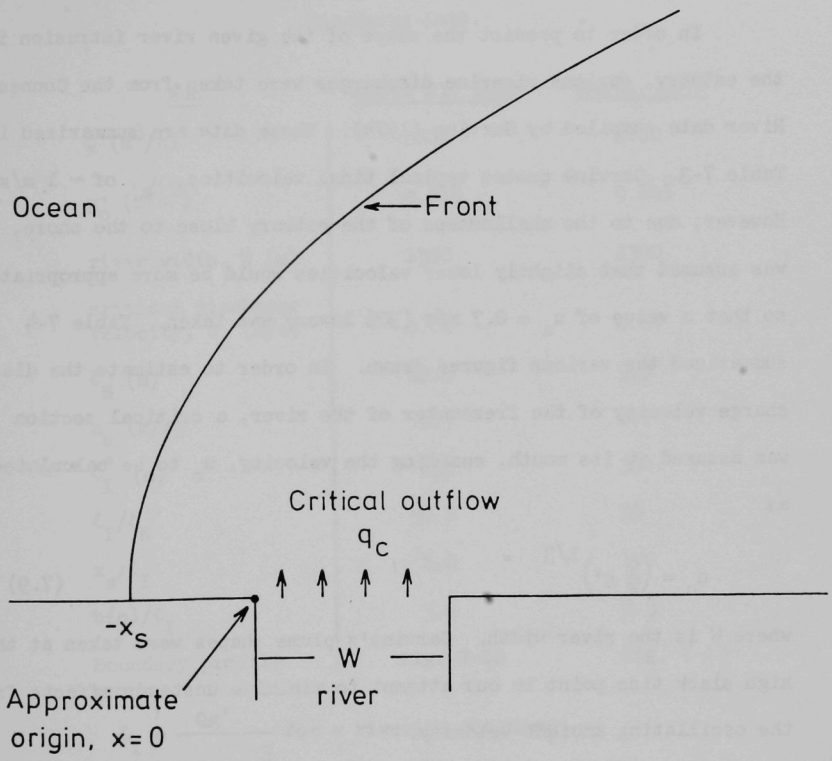

Figure 7-11 Schematic diagram of Riverine plume.

It should be noted that an obvious later application of the present numerical model would be to run them using a grid and inner boundary conditions equivalent to a river discharge.

In order to predict the shape of the given river intrusion into the estuary, various riverine discharges were taken from the Connecticut River data compiled by Garvine (1974). These data are summarized in Table 7-3. Garvine quotes typical tidal velocities, u_a, of ~ 1 m/s. However, due to the shallowness of the estuary close to the shore, it was assumed that slightly lower velocities would be more appropriate, so that a value of $u_a = 0.7$ m/s (30% lower) was taken. Table 7-4 summarized the various figures drawn. In order to estimate the discharge velocity of the freshwater of the river, a critical section was assumed at its mouth, enabling the velocity, u_c to be calculated as

$$u_c = \left(\frac{Q}{W} g'\right)^{1/3} \tag{7.9}$$

where W is the river width. Garvine's plume shapes were taken at the high slack tide point in our attempt to minimize unsteady effects from the oscillating ambient velocity.

Figures 7-12 and 7-13 show predictions of the riverine plume for various flow conditions corresponding to two cases of the Connecticut river plume for which data are available. Figure 7-12 shows a boundary mismatch of a factor of ≈ 1.5, while Figure 7-13 shows even better agreement. The greater divergence in Figure 7-12 might in part be due to the larger frictional effect ($\lambda_i V' \approx 0.3$),

Table 7-3

Summary of Some of Garvine's (1974) Connecticut River Discharge Data.

Run	April 21, 1972	May 1, 1972
Q (m^3/s)	2800	1600
g_o' (m/s^2)	0.245	0.245
river width, W (m)	1300	1300
critical discharge velocity, u_c (m/s)	0.81	0.67
ℓ_N (m)	12.5	9.5
u_a (m/s)	0.7	0.7
ℓ_I^* (m)	635	364
ℓ_I/ℓ_N	50.8	38
x_s/ℓ_I	2.0	1.9
$b(o)/\ell_I$	3.6	3.3
Boundary profile	Fig. 7-12	Fig. 7-13

* $\ell_I = \dfrac{Qg'}{\pi C_D u_a^3}$ for a riverine discharge.

Table 7-4

Riverine Discharge Predictions.

Case	Q (m^3/s)	g_o' (m/s^2)	W (m)	u_c (m/s)	u_a (m/s)	ℓ_N (m/s)	ℓ_I (m)	ℓ_I/ℓ_N
1	1500	0.245	1300	0.66	0.5	9.20	936	102
2	2500	0.245	1300	0.78	0.5	10.5	1560	149
3	1500	0.245	1300	0.66	1.0	9.20	117	12.7
4	2500	0.245	1300	0.78	1.0	11.9	194	16.4

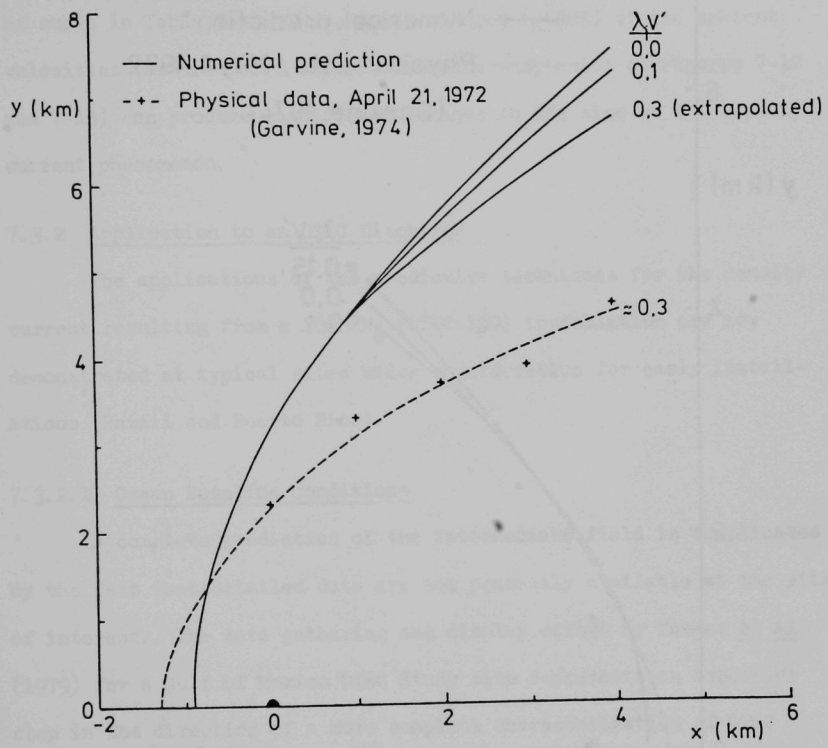

Figure 7-12 Comparison of predicted with actual boundary shapes for the Connecticut River plume, April 21, 1972, (field data from Garvine, 1974).

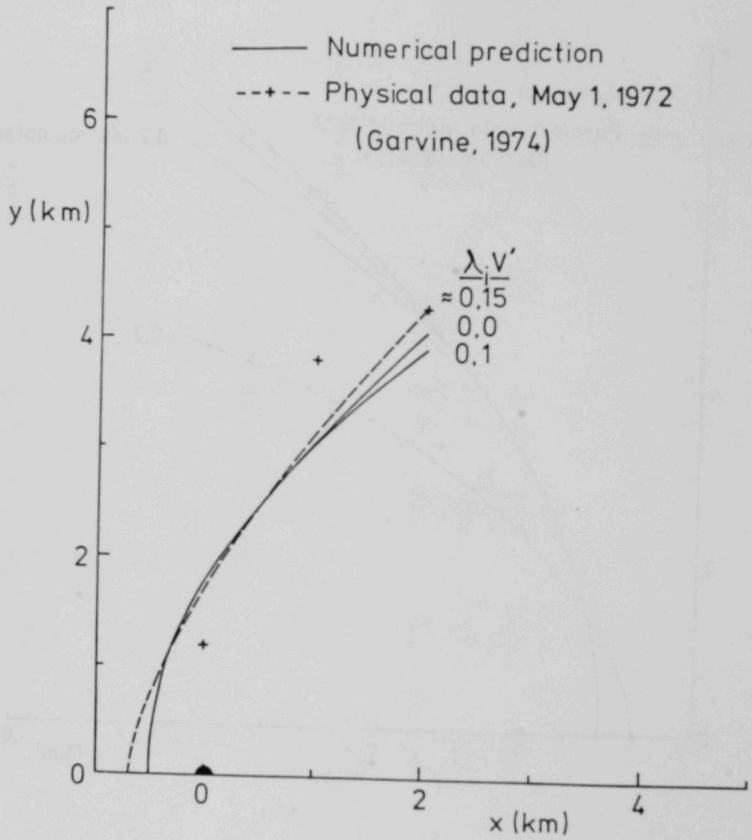

Figure 7-13 Comparison of predicted with actual boundary shapes for the Connecticut River plume, May 1, 1972, (field data from Garvine, 1974) .

but is probably due, as discussed previously, to the difficulties in estimating the ambient parameters.

The prediction in Figure 7-14 illustrates the strong sensitivity of the boundary shape to various changes in environmental parameters as shown in Table 7-4. Thus, small changes (± 30%) of the ambient velocities (assumed 0.70 cm/s in the data suspension of Figures 7-12 and 7-13) can produce significant changes in the size of the density current phenomenon.

7.3.2 Application to an OTEC Discharge

The applications of the predictive techniques for the density current resulting from a 100 MW_e (OTEC-100) installation are now demonstrated at typical sites under consideration for early installations (Hawaii and Puerto Rico).

7.3.2.1 Ocean Baseline Conditions

A complete prediction of the intermediate field is complicated by the fact that detailed data are not presently available at the sites of interest. The data gathering and display effort by Thomas *et al.* (1979) for a Gulf of Mexico OTEC Study site represents an important step in the direction of a more complete characterization of OTEC sites. From this study, vertical temperature and velocity distributions and a long term record (17 days) of the temperature and density variations within the the thermocline have been shown in Figures 3-2 and 3-4, respectively. Figure 3-3 summarized typical density profiles from the Gulf of Mexico, Hawaii and Puerto Rico. However, velocity

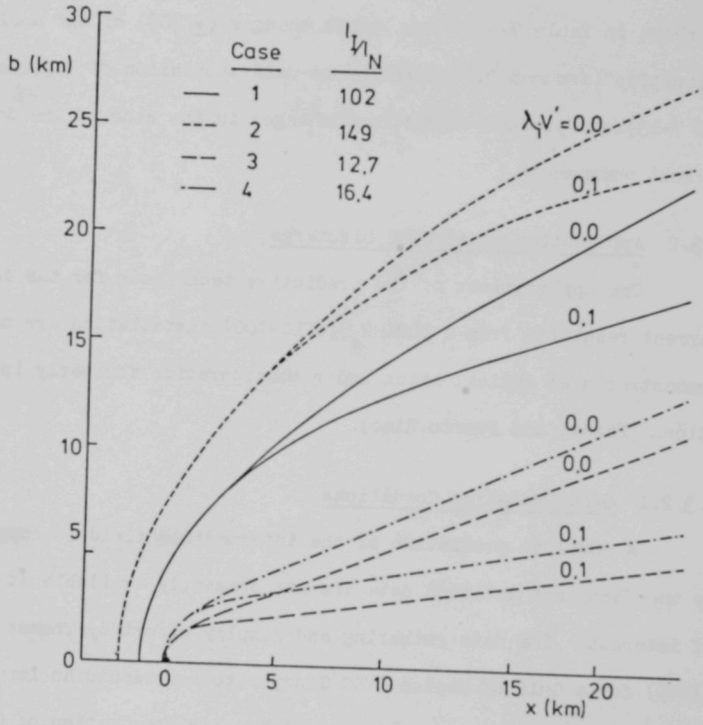

Figure 7-14 Sensitivity runs for Riverine discharges

measurements below the surface and in the region of the thermocline are very limited. The following estimates are available:

Gulf of Mexico	Typical = 15 to 20 cm/s	
	Extreme = 0 to 50 cm/s	
Puerto Rico	Typical = 10 cm/s	Based on geostrophic calculations, Atwood *et al.*, (1976)
	Extreme = 0 to 20 cm/s	
Hawaii	Typical = 10 to 15 cm/s	Near shore measurements Bathen (1977)
	Extreme = 0 to 30 cm/s	

Based on these background data, values of Brunt Vaisala frequencies of N = 0.010, 0.015 and 0.020 s^{-1}, and of ambient velocities of u_a = 0.10, 0.15 and 0.20 m/s were selected, as shown in Table 7-5.

7.3.2.2 Plant Design

Various OTEC intake and discharge configurations are under study, no candidate design having evolved at this stage. Of fundamental importance for the subsequent flow field is whether a mixed or separate mode (see Section 1.2) is adopted for the condenser and evaporator effluents (Jirka *et al.*, 1977; Adams *et al.*, 1979). This choice determines the amount of mixing and the terminal level of the effluent, it having moved vertically within the ambient ocean until this equilibrium level (if a linear stratification) or interface is reached. For simplicity, a mixed discharge design is assumed, but with a variable mixing ratio, S. Various studies

(op. cit.) have related the dilution to the plant design parameters, these suggesting the adoption of three dilution levels.

Mean	Low	High
$S = 5$	$S = 2$	$S = 10$

Alternatively, the computed results following can be applied to separate discharge modes. In that case, the dilution factor would be twice as large.

The 100 MW_e OTEC plant flowrate is given by $Q_o = 1000\ m^3/s$, a typical discharge velocity being taken as $U_o = 2\ m/s$.

7.3.2.3 Applicability of the Present Model to OTEC Discharges

It should be noted at this point that the modeling effort contained in this study, while devised for all three stratification cases described in Section 3.1, is only carried out for Case A, i.e., a surface discharge on a homogeneous ocean. The differences between this model and that for Cases B and C (interfacial spreading and equilibrium level spreading in a linear stratification, respectively) lies in the mixing characteristics in the near-field. For Case A stratification, the entrainment of ambient fluid reduces the effective buoyancy while increasing the flows, whereas for Cases B and C, flow augmentation only occurs due to the entrainment consisting of approximately equal amounts of more and less dense fluid. (This can be seen from the governing equations in 3.2). The intermediate field, however, which does not experience entrainment, could be used for both Cases A and B. Thus, in order to apply this model to oceanic

conditions, several assumptions have to be made:

i) The intermediate flow field is assumed diluted by the values of S, given in Section 7.3.2.2. This is equivalent to saying that this is the dilution which occurs during both its vertical rise and the horizontal near-field motion. This assumption is borne out by the experiments of Huq (1983), who measured total dilutions for a radial discharge into a linearly stratified ambient as ≈ 3.5.

ii) The values of density differences felt by the density current are estimated by the following process: The effective gravity, g'_o is obtained from the linear stratification by a function of the local vertical height of the density current, h. An averaged value for this can be obtained by assuming a value equal to one half of the stagnation height, h_s. Thus the effective gravity obtained from

$$g'_o = N^2 h_s. \tag{7.10}$$

A value for the stagnation height is obtained, using the relation $h_s = C_D \frac{u_a^2}{g'}$ (Table 3-4). Equating these two expressions, yields

$$g'_o = \sqrt{C_D}\, N\, u_a, \tag{7.11}$$

Table 7-5

OTEC-100 Intermediate Field Predictions.

Case	N (s^{-1})	u_a (m/s)	h_s (m)	g'_o (m/s^2)	Q_o (m^3/s)	S	Q (m^3/s)	$g' = \frac{g_o}{S}$ (m/s^2)	ℓ_N (m)	ℓ_I (m)	ℓ_I/ℓ_N	$\lambda_i V'$
1	0.015	0.10	6.7	0.0015	500	5	2500	0.00030	205	597	2.91	0.09
2	0.010	0.10	10	0.0010	500	5	2500	0.00020	251	398	1.59	0.04
3	0.020	0.10	5	0.0020	500	5	2500	0.00040	178	796	4.47	0.16
* 4	0.015	0.15	10	0.0022	500	5	2500	0.00044	170	259	1.53	0.02
5	0.015	0.20	13.3	0.0030	500	5	2500	0.00060	145	149	1.03	0.01
6	0.015	0.10	6.7	0.0015	500	10	5000	0.00015	205	1194	5.82	0.18
7	0.015	0.10	6.7	0.0015	500	2	1000	0.00075	205	239	1.16	0.04

which is the relation used to calculate g_o' in Table 7-4. The value of effective gravity would, for the surface case (A) be divided by the dilution value S. However, in an attempt to more accurately represent Case B, the dilution effect on the effective gravity is ignored, the value g_o' being assumed to apply throughout.

7.3.2.4 Density Current Sensitivity

The various runs summarized in Table 7-5 and plotted in Figures 7-15 (boundary shapes) and 7-16 (boundary heights) were designed to test the density current sensitivity over the possible ranges of ambient conditions. The effects of variations in the ambient velocity are investigated in Cases 1, 4 and 5. It can be seen that the current experiences a great sensitivity to this flow parameter, with large boundary changes for small velocity variations.

Stratification changes are investigated in Cases 1, 2 and 3, while volume changes are investigated in Cases 1, 6 and 7. It can be seen that the density current is very sensitive to any changes in ambient conditions, but rather more sensitive to changes in stratification, and, in particular to ambient velocity, than to discharge volume.

In all cases it can be seen that the current has horizontal dimensions of the order of kilometers, while vertical dimensions are only of the order of meters, that is, a wide, thin density current is produced. Due to its great sensitivity to the ambient conditions,

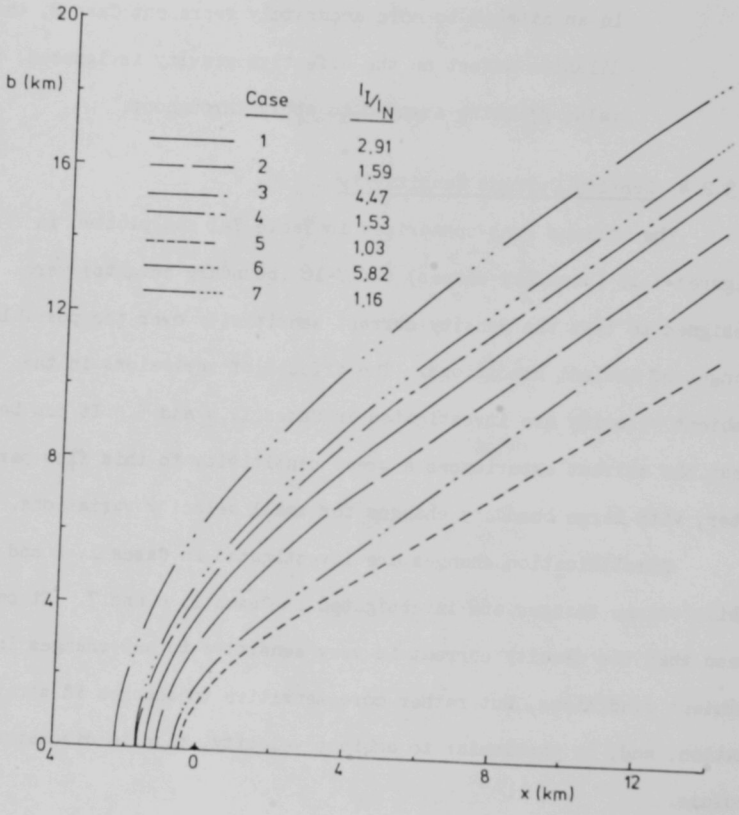

Figure 7-15 OTEC-100 sensitivity runs: plan view

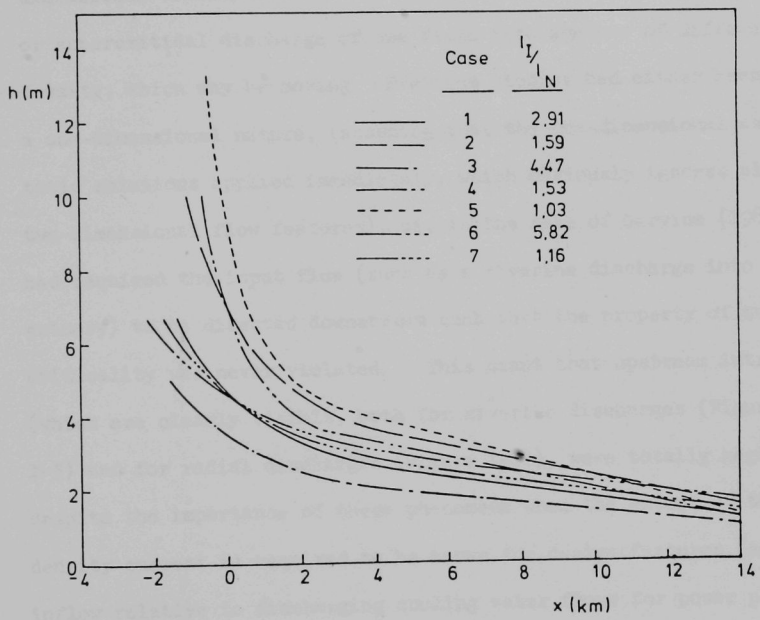

Figure 7-16 OTEC-100 sensitivity runs: side view

where reasonably small changes cause current boundary variations of the order of kilometers, an understanding of the basic sensitivity processes (and ambient conditions) is environmentally important.

CHAPTER 8

SUMMARY, CONCLUSIONS AND SUGGESTIONS FOR FUTURE WORK

A numerical study has been carried out of the highly two-dimensional density current flow field resulting from the critical or supercritical discharge of one fluid into another of different density, which may be moving. Previous studies had either been of a one-dimensional nature, (assuming that the one-dimensional asymptotic solutions applied immediately, which obviously ignores all two-dimensional flow features), or, in the case of Garvine (1982), had required the input flow (such as a riverine discharge into an estuary) to be directed downstream such that the property of supercriticality was never violated. This meant that upstream intrusions (which are clearly visible, both for riverine discharges (Figure 1-3) and for radial discharges (Figure 1-1)), were totally neglected, despite the importance of these phenomena when the extent of the density current is required to be known for design features (such as inflow relative to discharging cooling water flows for power plants, or relative OTEC plant sitings within energy parks to eliminate inter-plant recirculation possibilities, to give but two examples).

The analytical treatment and numerical model formulation for the entire density current was carried out by dividing the density current into two regions: A near-field region and an intermediate field region. Different relative strengths of these fields (as measured by the ratio of their respective length scales) ultimately

control the total flow dynamics. The conclusions drawn from each of these models will be discussed separately in the following sections.

8.1 The Near-Field

The near-field is the region of supercritical entraining flow occurring after the fluid is released from the source. The theoretical framework for this region was developed for three differerent stratification conditions, (Case A: Surface source with homogeneous ambient, Case B: Interface source with homogeneous ambient, and Case C: Equilibrium source with linear ambient stratification). However, the final numerical model application was limited to the Case A stratification. This stratification case has rather different flow dynamics from the others. This is due to entrainment only occurring on the lower interface for a surface jet, resulting in a reduction of buoyancy while preserving the total buoyancy flux, whereas symmetric entrainment keeps a constant buoyancy for the other cases.

The numerical scheme adopted to model the depth integrated equations is the explicit, marching, finite difference scheme of MacCormack (1971). This was applied for a radial surface discharge into both a stagnant and moving ambient. On the basis of a comparison of these results, a simplified model for the case of discharge into a crossflow was developed, involving shifting the circulating symmetric results from the stagnant case downstream, using a Galilean

transformation, to account for the ambient flow.

Ultimately, in combination with the subsequent intermediate field model, it is demonstrated that there is a significant interaction between the two regions. The dynamics of the near-field, such as mixing, point of flow criticality, etc., have been shown to be intimately related to the properties of the intermediate field, and vice versa, as illustrated by the transition conditions for the near-intermediate field boundary. In particular, the total near-field dilution is controlled by the cut-off imposed by the intermediate field boundary condition. Thus a strong near-field will affect the intermediate field flow dynamics, by causing the transition boundary to be much enlarged with supercritical velocities existing along it, which thus cause an enlarged intermediate field, and density current, in general. Alternately, a relatively larger intermediate field allows the near-field to continue its entraining, expanding flow for longer before the transition point occurs, but when it does, the flow is critical (for the asymptotic case of very large intermediate field), leading to lower transition velocities and a smaller density current in general.

8.2 Intermediate Field

The intermediate field is the region of transcritical non-entraining flow, occurring after the flow has passed through the near-field. The intermediate field can be subdivided into two regions, the transcritical region, which includes both super- and

subcritical regions, (the latter of which mainly occur in the upstream intrusion region), and the totally supercritical region, which includes increasing important frictional effects, and occurs after the flow has passed through the transcritical region. As no entrainment is assumed to occur in the intermediate field region, both stratification cases A and B can be described by an identical model.

The transcritical part of the intermediate field, especially for large near-field strengths, is composed of strong internal hydraulic jumps and two-dimensional behaviour, including, in particular, the upstream intrusion region. The depth-averaged equations, which are solved for, have been shown to form a hydraulic analogy for the compressible gas flow equations, which suggested the modification of the transonic gas flow program of Jameson and Caughey (1979) to solve the inviscid transcritical flow equations.

The depth-averaged equations for the supercritical flow region including the interfacial friction effects, are solved by, again, an application of the MacCormack scheme.

The inner boundary conditions for the transcritical flow region are, as already discussed, transmitted by the conditions at the transition boundary. A circular, equi-energy boundary condition is assumed.

The intermediate field is solved for various relative intermediate to near-field strengths. It was shown that two asymptotic limits exist, for $\ell_I/\ell_N \to \infty$ (or in practice, $\gtrsim 40$), and for large

near-field effects, $\ell_I/\ell_N \to 0$ (or in practice, $\lesssim 1$).

The frictional effects entering the solution in the supercritical region are found to affect the whole of the flow field, rather than just the boundaries, causing the velocity vectors to become aligned with the ambient flow, and hence conform with the elementary one-dimensional theories. In the absence of frictional effects, the convective flow would tend to "slide" over the surface of the ambient, leading to unrealistically large velocities - a problem also encountered by Garvine (1982). The frictional effects also have a significant influence on the boundary shape of the density current.

An important feature brought out by these models is the "memory" of the flow, in that, differences in initial conditions, such as initial widths as flow distributions, will be 'remembered' downstream. The flow, once its asymptotic spreading rate is reached, will retain this information as a constant width difference throughout the whole of the downstream region.

8.5 Suggestions for Future Work

Obvious extensions of this study present themselves:

1. Linear ambient stratification (Case C), should be accounted for within both the transcritical and supercritical numerical model. This might be preferable where the results are being used for predictions in an ambient ocean. In particular, the discussion in Section 2.2 indicates that for given upstream flow conditions the

internal jumps will be less strong, and hence move easily modeled by the constant energy assumption.

2. Frictional effects should, eventually, be included both in the transcritical and MacCormack models. This is not possible in the former, potential solution, but has already been incorporated into the supercritical MacCormack scheme.

3. The MacCormack scheme, in general, proved to be of use for a great variety of supercritical flows. In the present study it was applied to entraining and frictional flows. Also, it was applied on both specified and self-generated domains, indicating that it could easily be applied to flows through particularly shaped regions - curved boundary conditions being easily accounted for by the finite volume scheme which it contains.

4. Both of the fundamental models, i.e., the MacCormack scheme for the supercritical region, and the transcritical model offer considerable flexibility towards the modeling of other types of stratified and free surface flow conditions.

In particular, the flow of initially supercritical flows down spillways with possible transitions to subcritical flows, could be predicted using this combination of methods.

5. In the case of jets that are not discharged at their equilibrium level (i.e., with a rising or falling near-field trajectory), the development and matching of a move appropriate near-field model to estimate the initial mixing should be developed.

6. Another extension which might be incorporated into the

model might be a method of accounting for bottom topography within, say, a river or estuary, where the relative density current to total depth ratios are significant, and hence would be likely to affect the boundary shape, as discussed with regard to the drag coefficient in Section 2.1.

7. Unsteadiness in ambient conditions, such as velocity, should be accounted for. This has already been done in an approximate way (using dimensional arguments by Jirka et al. (1980)), but due to the constantly fluctuating environmental parameters, a more accurate method would be appropriate. This should involve incorporating an actual time dependence into the models used.

8.4 Comparison with Observations

The numerical results from this modeling procedure have been compared with several sets of experimental data. The experimental results of Jirka et al. (1980) and Huq (1983), were considered. Both involved discharging a bouyant fluid onto the surface of an ambient which had a relative motion compared with the source. A good agreement was obtained with both these data sets. No agreement was obtained, however, with the data of Chen (1980), who carried out similar experiments. This mismatch, however, may be attributed to possible problems in his discharge flow generation.

Thus good agreement was obtained, with the data of Jirka et al. (1980), and Huq (1983), especially as a certain variability is expected for the turbulent phenomenon considered.

8.5 Environmental Applications

The data were applied to environmental problems of two different types.

- Riverine plumes formed by fresh river water discharge into coastal water.
- OTEC discharges.

Both of these applications indicate that the resulting density current should have a large horizontal extent, ($\approx$ km) but shallow vertical extent ($\approx$ m).

Considerable sensitivity was found to ambient environmental conditions such as u_a and g' (N).

REFERENCES

Adams, E. E., Harleman, D. R. F., Jirka, G. H., and Stolzenbach, K. D. (1981) "Heat disposal in the water environment," Ralph M. Parsons Laboratory for Water Resources and Hydrodynamics, M. I. T., Cambridge, Mass.

Albertson, M. L., Dai, Y.B., Jensen, R. A., and Rouse, H. (1950) "Diffusion of submerged jets," Trans., ASCE, Vol. 115, Paper No. 2409.

Allan Hancock Foundation, University of Southern California. (1964) "Final Report on an investigation on the fate of organic and inorganic wastes discharged into the marine environment and their effects on biological productivity," September 15.

Ames, W. F. (1965) "Nonlinear partial differential equations in engineering," Mathematics in Science and Engineering, Vol. 18, Academic Press, New York.

d'Arsonval, Arsene. (1881) "Utilisation des forces naturelles. avenir de l'electricite," La Revue Scientifique, 370-72.

Atwood, D. K., Duncan, M. C., Stalcup, M. C. and Barcelona, M. I. (1976) "Ocean thermal energy conversion: Resource assessment and environmental impact for proposed Puerto Rico site," Dept. of Marine Sciences, University of Puerto Rico, Mayaguez.

Bache, D. H. (1976) "Density current surges, parts I and II," J. Hyd. Res., Vol. 14, No. 1.

Bathen, K. H. (1977) "An evaluation of oceanographic and socio-economic aspects of a near-shore OTEC pilot plant in sub-tropical Hawaiian waters," National Science Foundation, Energy Resource and Development Administration, Washington, DC.

Beam, R. W. and Warming, R. F. (1976) "An implicit finite difference algorithm for hyperbolic systems in conservation form," J. Comp. Phys., Vol. 23.

Benjamin, T. B. (1968) "Gravity currents and related phenomena," J. Fluid. Mech., Vol. 31, pt. 2.

Benjamin, T. B., and Lighthill, M. J. (1954) "On cnoidal waves and bores," Proc. Roy. Soc. (London) A, Vol. 224.

Blanvillain, C., and Thirifays, M. (1970) "Visualisation des interactions entre les sillages d'un rotor et les aubes d'un diffuseur sur un montage hydraulique," Rech. Aerosp., No. 1970-2.

Boucherot, P. (1928) "L' utilisation rationnelle de l'eau glacee du fond des oceans", Conf. 11th Feb., Sorbonne, Paris.

Bradley, J. N. and Peterka, A. J. (1957) "The hydraulic design of stilling basins," Proc. ASCE, J. Hyd. Div., Vol. 83, No. HY5.

Bredif, M. (1983) "A fast finite element method for transonic potential flow calculations," AIAA Paper No. 83-0507.

Briley, W. R., and McDonald, H. (1975) "Solution of the three-dimensional compressible Navier-Stokes equations by an implicit technique," Proc. Fourth Int'l. Conf. on Numerical Methods in Fluid Dynamics, Boulder, Colorado, June 1974, in Lecture Notes in Physics, Vol. 35, Springer, New York.

Britter, R. E. and Simpson, J. E. (1978) "Experiments on the dynamics of a gravity current head," J. Fluid. Mech., Vol. 88, pt. 2.

Caughey, D. A. (1978) "Numerical calculation of transonic potential flows," Lectures presented at a Short Course on Advances in Computational Fluid Dynamics at the University of Tennessee Space Institute, Tullahoma, Tennessee, December 4-8.

Caughey, D. A. (1980) "A limited perspective on computational aerodynamics," AIAA 13th Fluid and Plasma Dynamics Conf., Snowmass, Colorado.

Caughey, D. A. (1982) "The computation of transonic potential flows," Ann. Rev. Fluid Mech., Vol. 14.

Caughey, D. A., and Jameson, A. (1977a) "Calculation of transonic potential flow fields about complex, three-dimensional configurations," Transonic Flow Problems in Turbomachinery, ed. T. C. Adamson, M. Platzer, Hemisphere Publ. Corp., Washington.

Caughey, D. A., and Jameson, A. (1977b) "Accelerated iterative calculation of transonic nacelle flowfields," AIAA J., Vol. 15.

Caughey, D. A., and Jameson, A. (1979) "Numerical calculation of transonic potential flow about wing-body combinations," AIAA J., Vol. 17.

Chan, S. T. K., Brashears, M. R., and Young, V. Y. C. (1975) "Finite element analysis of transonic flow by the method of weighted residuals," AIAA Paper 75-79.

Chen, H. C. (1976) "Applications of the finite element method to compressible flow problems," Ph.D. thesis, Cornell University, Ithaca, NY.

Chen, J.-C. (1980) "Studies on gravitational spreading currents," W. M. Keck Laboratory of Hydraulics and Water Resources, Report No. KH-R-40, Cal. Inst. Tech.

Chow, V. T. (1959) Open-Channel Hydraulics, McGraw-Hill, Kogakusha, Ltd.

Chung, T. J. (1978a) Finite Element Analysis in Fluid Dynamics, McGraw-Hill Book Co., New York.

Chung, T. J. (1978 b) "Recent advances in transonics with finite elements," U.S.-Japan Seminar on Interdisciplinary Finite Element Analysis, Cornell University, Ithaca, NY.

Chung, T. J., and Hooks, C.G. (1976) "Discontinuous functions in transonic flows," AIAA Paper No. 76-329.

Chung, T. J., and Hooks, C. G. (1977) "Discontinuous trial and test functions for the full potential equations," Proc. Int. Symp. on Innovative Numerical Analysis in Engineering and Applied Sciences, Versailles, France, May 23-27.

Claude, G. (1928) "L'Energie thermique des mers," Conf. 11th Feb., Sorbonne, Paris.

Claude, G., and Boucherot, P. (1928) "Sur l'utilisation de l'energie thermique de mer," Proc. Academie des Sciences (CRAS), 4th June.

Cohen, R. (1979/1980) "Energy from ocean thermal gradients," Ocean Energy, Oceanus, Vol. 22, No. 4, Winter.

Courant, R., and Friedrichs, K. O. (1948) Supersonic Flows and Shock Waves, Interscience Publishers, Inc., New York.

Courant, R., Isaacson, E., and Reis, M. (1952) "On the solution of nonlinear hyperbolic differential equations by finite differences," Comm. Pure and Appl. Maths., Vol. V.

Crossley, H. E., and Harleman, D. R. F. (1952) "Studies on the validity of the hydraulic analogy to supersonic flow, Part 5. Towed model investigations of transonic flow," A. F. Tech. Rep. No. 5983, M. I. T., Wright Air Development Center.

Daily, J. W., and Harleman, D. R. F. (1966) Fluid Dynamics, Addison-Wesley Publishing Company, Inc., Reading, Mass., USA.

Dronkers, J. J. (1969) "Tidal computations for rivers, coastal areas and seas," Proc. ASCE, J. Hydr. Div., HY1.

Ellison, T. H., and Turner, J. S. (1959) "Turbulent entrainment in stratified flows," J. Fluid. Mech., Vol. 6, Part 3.

Fay, J. A. (1980) "Gravitational spread and dilution of heavy vapor clouds," 2nd. IAHR Symp., Trondheim, June.

Fischer, H. B., List, E. J., Koh, R. C. Y., Imberger, J., and Brooks, N.H. (1979) Mixing in Inland and Coastal Waters, Academic Press, NY.

Friedman, Linda, and Reitzel, J. (1979) "Environmental Impact Assessment for OTEC-1," Proc. 6th OTEC Conf., Washington, DC.

Friedrichs, K. O. (1958) "Symmetric positive linear differential equations," Comm. Pure and Appl. Math., Vol. 11.

Garvine, R. W. (1974) "Physical features of the Connecticut River outflow during high discharge," J. Geophys. Res., Vol. 79, No. 6.

Garvine, R. W. (1977) "Observations of the motion field of the Connecticut River plume," J. Geophys. Res., Vol. 82.

Garvine, R. W. (1982) "A steady-state model for buoyant surface plume hydrodynamics in coastal waters," Tellus, Vol. 34, No. 3, June.

Gourlay, A. R., and Mitchell, A. R. (1966a) "Alternating direction methods for hyperbolic systems," Numerische Mathematik, Vol. 8.

Gourlay, A. R., and Mitchell, A. R. (1966b) "A stable implicit difference method for hyperbolic systems in two space variables," Numerische Mathematik, Vol. 8.

Grubert, J. P. (1980) "Experiments on arrested saline wedges," J. Hyd. Div., ASCE, Vol. 106, No. HY6.

Hafez, M. M., Murman, E. M., and South, J. C. (1978) "Artificial compressibility methods for numerical solutions of transonic full potential equation," AIAA Paper No. 78-1148.

Henderson, F. M. (1966) Open Channel Flow, The Macmillan Company, NY.

Heskestad, G. (1965) "Hot-wire measurements in a plane turbulent jet," J. Appl. Mech., Vol. 32, No. 1.

Homma, T., Kamogawa, H., Nagasaki, S., Uehara, H., Teramoto, T., and Kajikawa, T. (1979) "Design considerations of 100-MW_e commercial scale OTEC power plant and a 1-MW_e class engineering test plant," Proc. 6th OTEC Conf., Washington, DC.

Howarth, L. (1953) Modern Developments in Fluid Dynamics: High Speed Flow, Vol. 1, Oxford University Press, London.

Hoyt, J. W. (1962) "The hydraulic analogy for compressible gas flow," Appl. Mech. Rev., Vol. 15, No. 6.

Huq, P. (1983) "Experimental investigations of three-dimensional density currents in stratified environments," Master's thesis, Cornell University, Ithaca, NY.

Ippen, A. T., and Harleman, D. R. F. (1952) "Certain quantitative results of the hydraulic analogy to supersonic flow," Ohio State Univ. Eng. Expt. Stn. Bulletin 148-150.

Isaachsen, I. (1911) "Innere vorgange in stromenden flussigkeiten und gasen," z VDI, Vol. 55.

Jameson, A. (1971) "Transonic flow calculations for aerofoils and bodies of revolution," Aerodynamics Rep. 391-71-1, Gruman Aerospace Corp., Bethpage, NY.

Jameson, A. (1974) "Iterative solution of transonic flows over aerofoils and wings including flows at Mach 1," Comm. Pure and Appl. Math., Vol. 27.

Jameson, A. (1975) "Transonic potential flow calculations in conservation form," Proc. 2nd, AIAA Computl. Fluid Dyn. Conf., Hartford.

Jameson, A. (1978) "Transonic Flow Calculations," from Numerical Methods in Fluid Dynamics, Ed. H. J. Wirz and J. J. Smolderen, Hemisphere Publ. Corp., Washington.

Jameson, A., and Caughey, D. A. (1977) "A finite volume method for transonic potential flow calculations", Proc. AIAA 3rd Computl. Fluid Dyn. Conf., Albuquerque, NM.

Jirka, G. H. (1978) "Preliminary guidelines for the siting of multiple ocean thermal energy conversion plants," report to Div. of Solar Energy, Dept. of Energy, Cornell University, Ithaca, NY.

Jirka, G. H. (1979) Fluid Mechanical Aspects of Ocean Thermal Energy Conversion, Proc. SIMS Conf. Alta, Utah, ed. John David Buckmaster.

Jirka, G. H. (1982) "Turbulent Buoyant Jets in Shallow Fluid Layers," in Turbulent Jets and Plumes, ed. W. Rodi, Pergammon Press, Oxford, UK.

Jirka, G. H., Johnson, R. P., Fry, D. J., and Harleman, D. R. F. (1977) "Ocean thermal energy conversion plants: Experimental and analytical study of mixing and recirculation," Ralph M. Parsons Lab. for Water Resources and Hydrodynamics, Dept. of Civil Engineering, M. I. T., Technical Report No. 135.

Jirka, G. H., Johnson, R. P., and Sargent, F. E. (1981) "Radial source-sink flow in stratified ocean," J. Hyd. Div., ASCE, Vol. 107, No. HY12.

Jirka, G. H., and Jones, J. M. (1978) "Analysis of the intermediate field of OTEC induced density currents," (Interim Report), School of Civil and Environmental Engineering, Cornell University, Ithaca, NY.

Jirka, G. H., Jones, J. M., and Sargent, F. E. (1980) "Theoretical and experimental study of the intermediate field dynamics of ocean thermal energy conversion plants," School of Civil and Environmental Engineering, Cornell University, Ithaca, NY. Report submitted to U. S. Dept. of Energy.

Jouget, E. (1920) "Quelques problemes d'hydrodynamique generale," J. Math. Pures Appl., Vol. 8, No. 3.

Kantorovich, L. V., and Krylov, V. I. (1958) Approximate Methods of Higher Analysis, Interscience Publishers, NY.

Kao, T. W. (1977) "Density currents and their applications," J. Hyd. Div., Proc. ASCE, Vol. 103, No. HY5.

Keulegan, G. H. (1957) "Thirteenth Progress Report on Model Laws for Density Currents: An Experimental Study of the Motion of Saline Water from Locks into Fresh Water Channels," NBS Report 5831, U.S. Dept. of Commerce.

Keulegan, G. H. (1958) "Twelfth Progress Report on Model Laws for Density Currents: The Motion of Saline Fronts in Still Water," NBS Report 5831, U. S. Dept. of Commerce.

Keulegan, G. H. (1966) "The mechanism of an arrested saline wedge," Estuary and Coastline Hydrodynamics, ed. by Ippen, A. T., McGraw-Hill Book Co., New York, NY.

Klein, E. J. (1966) "The hydraulic analogy to compressible gas flow-theory and limitations," ASME-EIC Fluids Engineering Conference, Denver, Colorado.

Koh, R. C. Y., and Fan, L-N. (1970) "Mathematical Models for the Predictions of Temperature Distributions Resulting from the Discharge of Heated Water into Large Bodies of Water," USEPA Report, Water Pollution Control Research Series 16130, DWO 10/70.

Kutler, P. (1969) "Application of selected finite-difference techniques to the solution of conical flow problems," Ph.D. thesis, Iowa State University, Iowa City, Iowa.

Kutler, P. and Lomax, H. (1971) "Shock-capturing, finite-difference approach to supersonic flow," J. Spacecraft, Vol. 8, No. 12.

Kutler, P., Warming, R. F., and Lomax, H. (1973) "Computation of space shuttle flowfields using noncentered finite-difference schemes," AIAA J., Vol. 11, No. 2.

Laitone, E. V. (1947) "Exact and approximate solutions of two-dimensional oblique shock flow," J. Aero. Sci., Vol. 14, Part 1.

Lamb, Sir H. (1945) Hydrodynamics, Dover Publications, New York.

Larsen, J., and Sorensen, T. (1968) "Buoyancy spread of wastewater in coastal regions," Eleventh Conference on Coastal Engrg., London, Vol. 2.

Lavi, A., and Zener, C. (1975) "Solar sea power plants: Electric power from the ocean thermal difference," Naval Engineers Journal, April.

LeBot, Y., and Bernard, P. (1972) "Analyse par analogie hydraulique du decollement tournant dans les compresseurs," Rech. Aerosp. No. 1972-4.

Lee, J. H. W., and Jirka, G. H. (1981) "Vertical round buoyant jet in shallow water," J. Hyd. Div., ASCE, Vol. 107, No. 12.

Liggett, J. A., and Liu, P. L-F. (1983) The Boundary Integral Equation Method for Porous Media Flow, George Allen and Unwin, London.

Lomax, H., Kutler, P., and Fuller, F. B. (1970) "The numerical solution of partial differential equations governing convection," AGARD-A9-146-70, Advisory Group for Aerospace Research and Development, Paris, France.

Mach, E. (1887) "Photography of projectile phenomena in air," Akademie der Wissenschaften, Vienna, Math. Naturwiss. Kl. Sitzungsber, Vol. 95, No. 2.

MacCormack, R. W. (1969) "The effect of viscosity in hypervelocity impact cratering," AIAA Paper No. 69-354.

MacCormack, R. W. (1971) "Numerical solution of the interaction of a shock wave with a laminar boundary layer," from Holt, M., ed. (1971), "Proceedings of the 2nd International Conf. on Numerical Methods in Third Dynamics," Letcture Notes in Physics, Vol. 8, Springer-Verlag, New York.

Mahmood, K. and Yevjevich, V. (ed.) (1975) Unsteady Flow in Open Channels, Vol. 1, Lithocrafters, Ann Arbor, Michigan.

Manins, P. C. (1976) "Mixed region collapse in a stratified fluid," J. Fluid Mech., Vol. 77.

Marchand, P. (1979) "The French OTEC Program," 6th OTEC Conf., Washington.

Middleton, G. V. (1966a) "Experiments on density and turbidity currents: I. Motion of the head," Canadian Journal of Earth Sciences, Vol. 3.

Middleton, G. V. (1966b) "Experiments on density and turbidity currents: II Uniform flow of density currents," Canadian Journal of Earth Sciences, Vol. 3.

Morton, B. R., Taylor, Sir Geoffrey, and Turner, J. S. (1956) "Turbulent gravitational convection from maintained and instantaneous sources," Proc. Roy. Soc., Vol. 234.

Murman, E. M., and Cole, J. D. (1971) "Calculation of plane, steady transonic flows," AIAA J., Vol. 9.

Owczarek, J. A. (1964) Fundamentals of Gas Dynamics, International Textbook Co., Scranton, Pa.

Preiswerk, E. (1938) "Application of the methods of gas dynamics to water flows with free surface," Part 1. Flows with no energy dissipation, Part 2. Flows with momentum discontinuities (hydraulic jumps), Tech. Mem. Nos. 934 and 935, NACA.

Richards, W. E. (1979) "The U.S. ocean energy systems program," Proc. 6th OTEC Conf., Washington, DC.

Richtmyer, R. D. (1963) "A survey of difference methods for non-steady fluid dynamics," NCAR Tech. Note 63-2, Boulder, Colo.

Riddell, J. F. (1970) "Densimetric exchange flow in rectangular channels: IV. The arrested saline wedge," la Houille Blanche, No. 4.

Roache, P. J. (1976) Computational Fluid Dynamics, Hermosa Publishers, Albuquerque, NM.

Roberts, P. J. W. (1977) "Dispersion of buoyant wastewater discharged from outfall diffusers of finite length," Report No. KH-R-35, W. M. Keck Laboratory of Hydraulics and Water Resources, Div. of Engrg. and Appl. Sci., Cal. Inst. of Tech., Pasadena, Cal.

Rodi, W. (1975) "A Review of Experimental Data of Uniform Density Free Turbulent Boundary Layers," in Studies in Convection, B. E. Launder, ed., Academic Press, London.

Rouse, H., Yih, C-S., and Humphreys, H. W. (1952) "Gravitational convection from a buoyant source," Tellus, Vol. 4.

Sargent, F. E. (1983) "A comparative study of density currents and density wedges," Master's thesis, Cornell University, Ithaca, NY.

Shapiro, A. H. (1953) The Dynamics and Thermodynamics of Compressible Fluid Flow, Vols. 1 and 2, John Wiley & Sons, NY.

Shen, S-F. (1977) "Finite-element method in fluid mechanics," Ann. Rev. Fluid Mech., Vol. 9.

Shirazi, M. A., and Davis, L. R. (1974) "Workbook of thermal plume predictions, Vol. 2, surface discharges," Report No. EPA-R2-72-0056, U.S. Environmental Protection Agency, Corvallis, Oreg.

Simpson, J. E. (1969) "A comparison between laboratory and atmospheric density currents," Quarterly Journal of the Royal Meteorological Society, Vol. 95.

Simpson, J. E. (1972) "Effects of the lower boundary on the head of a gravity current," J. Fluid. Mech., Vol. 53, pt. 4.

Simpson, J. E. (1982) "Gravity currents in the laboratory, atmosphere and ocean," Ann. Rev. Fluid Mech., Vol. 14.

Stolzenbach, K. D., and Harleman, D. R. F. (1971) "An analytical and experimental investigation of surface discharges of heated water," Tech. Rep. No. 135, R. M. Parsons Lab. for Water Resources and Hydrodynamics, Div. of Civ. Engrg., M. I. T., Cambridge, Mass.

Svensen, R. A. (1979) "An overview of the OTEC-1 design," Proc. 6th OTEC Conf., Washington, DC.

Tatum, K. E. (1982) "Finite element methods for transonic flow analysis," AIAA Paper No. 82-0930.

Taylor, G. I. (1954) "The dispersion of matter in turbulent flow through a pipe," Proc. Roy. Soc. A, Vol. 223.

Tepper, M. (1950) "A proposed mechanism of squall lines: The pressure jump line," J. Meteo., Vol. 7, No. 1.

Tepper, M. (1952) "The application of the hydraulic analogy to certain atmospheric flow problems," U. S. Dept. of Commerce, Research Paper No. 35.

Thomas, G. G., Minton, S. M., and Molinari, R. L. (1979) "Data from the Atlantic Oceanographic and Meterological Laboratories OTEC Plant Study Site in the Gulf of Mexico," NOAA-AOML, Miami, Fla.

Trimble, L. C., Potash, R. L. (1979) "OTEC goes to sea (a review of mini-OTEC)," Proc. 6th OTEC Conf., Washington, DC.

Turner, J. S. (1973) Buoyancy Effects in Fluids, Cambridge University Press, Cambridge, UK.

U. S. Bureau of Reclamation (1955) "Research Studies on Stilling Basins, Energy Dissipators and Associated Appurtenances," Hydraulic Laboratory Report No. Hyd-399, June 1.

Vadus, J. R., and Giannotti, J. G. (1980) "Ocean Thermal Energy Conversion: Ocean Engineering," Joint Panamerican Congress on Ocean Engineering/International Workshop on Coastal Engineering, Mexico City, Mexico.

von Karman, T. (1940) "The engineer grapples with nonlinear problems," Bull. Am. Math. Soc., Vol. 46.

von Mises, R. (1958) Mathematical Theory of Compressible Fluid Flow, Academic Press, Inc., New York.

Wilkinson, D. L., and Wood, I. R. (1972) "Some observations on the motion of the head of a density current," J. Hydr. Res., Vol. 10, No. 3.

Williams, J. M. (1973) "The spread of warm water from an outfall in a tidal flow," Math. and Hydr. Modeling of Estuarine Pollution, London, HMSO.

Wright, S. J. (1977) "Mean behaviour of buoyant jets in a crossflow," J. Hyd. Div., ASCE, Vol. 103, No. HY5, Proc. Paper 12944, May.

Wu, J. (1969) "Laboratory results of salt water intrusion," J. Hyd. Div., Proc. ASCE, Vol. 95, No. HY6.

APPENDIX I

OCEAN THERMAL ENERGY CONVERSION (OTEC): PAST, PRESENT AND FUTURE

I-1 Historical Development

The principle behind OTEC was first proposed by the French physicist Arsene d'Arsonval (1881) who suggested utilizing the temperature difference between a warm spring in Paris and the colder waters of the Seine to drive a heat engine which would generate electricity. The heat engine he proposed was a closed cycle system as shown in Figure I-1 using sulphur dioxide as a secondary or internal working fluid. This would be alternately evaporated by the warm water flow, made to drive a turbine, and condensed by the cold water flow.

Later, his friend and student Georges Claude (Claude, 1928; Boucherot, 1928; Claude and Boucherot, 1928), suggested an open cycle system using sea-water as the working fluid. He built a 60 kW plant and succeeded in generating electricity both along the River Meuse in France, and during 1930, in the ocean off the coast of Cuba. In 1933, Claude transformed the 10,000 ton cargo ship Tunisie into the first floating potential OTEC plant. However, due to difficulties in laying the 650 m long and 2.50 m wide cold water pipe required, the project was abandoned.

A 40 MW project, Abidjan, was proposed by Claude in 1940. However, it was soon transformed into a 10 MW open-cycle, shore based

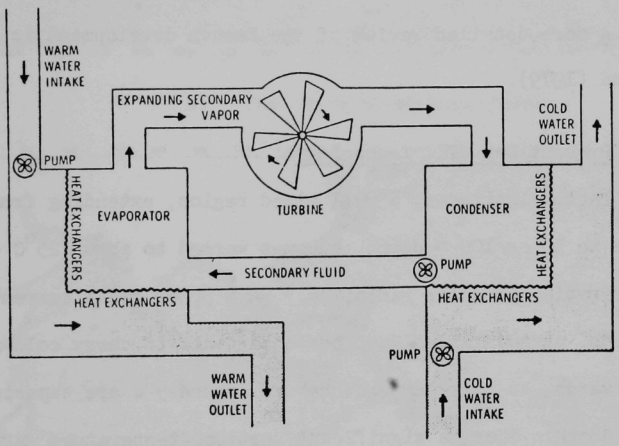

Figure I-1 A closed-cycle OTEC heat engine (after Cohen, 1979/80)

plant, with two units of 3.5 MWe net power and a 4 km cold water pipe, being taken charge of by the government company 'Energie des Mers'. During the period until 1955 various investigations were made of the heat engine system, and pipe laying methods, such that it became clear that the Abidjan project was technically feasible. However, political reasons, coupled with the very low cost of oil during this time led to the plant never being constructed.

A more detailed review of the French development is given in Marchand (1979).

I-2 Present Day OTEC Technology

In low latitudes, a well mixed region, extending from the sea surface to 50 or 100 m depth, becomes warmed to about 25°C due to the absorption of solar radiation. Warm upper ocean currents move polewards, necessitating deep ocean currents to carry cold water equatorwards, so that temperatures of around 5°C are experienced at 1000 m depth. Thus, a significant vertical temperature variation is maintained in the ocean, even though its form and magnitude may change with latitude, local weather variations, season, etc. Typical tropical or subtropical vertical density profiles are given in Figure 3-2, while Figure I-2 gives annual average monthly temperature differences (ΔT) between the ocean surface and the 1000 m depth, showing that large areas have average monthly ΔT values greater than 20°C. Thus, although the thermal gradient is a low grade energy resource, it is at least plentiful, free and renewable.

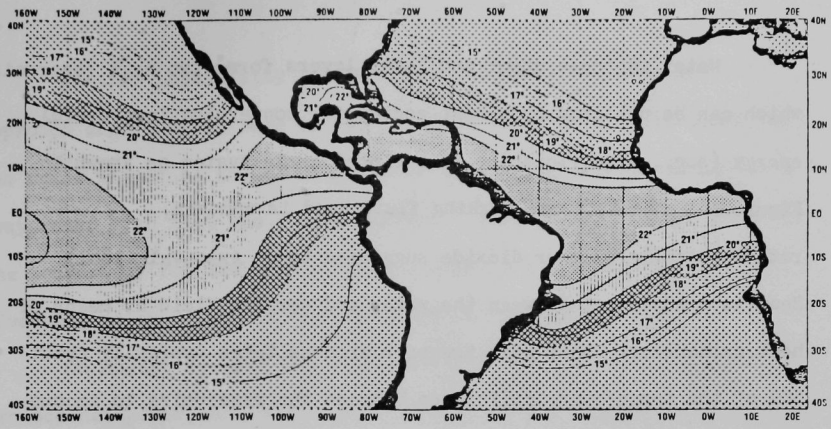

a) for the Western hemisphere

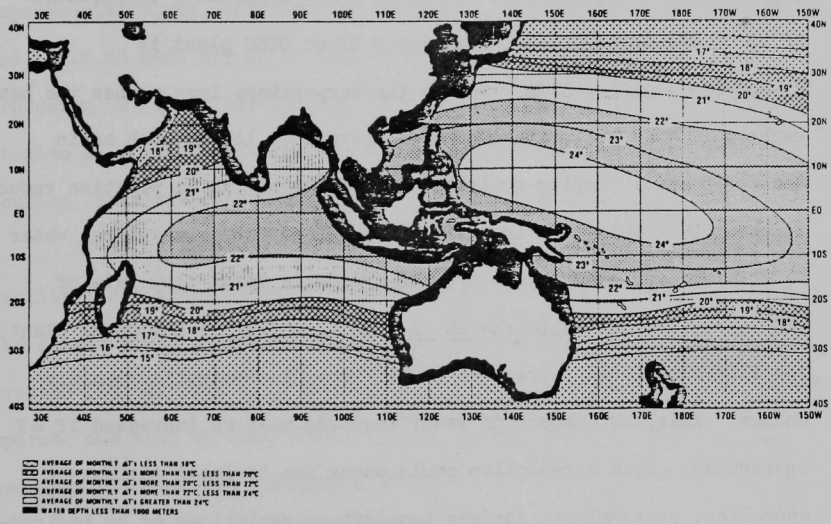

b) for the Eastern hemisphere

Figure I-2 The annual average monthly temperature differences between the ocean surface and 1,000 m depth, shown in degrees Celsius, (after Cohen, 1979/80).

Water in these upper and lower layers forms two heat reservoirs which can be utilized by a heat engine for conversion into useful energy (e.g., electricity). In a closed cycle system as shown in Figure I-1, the internal working fluid used is ammonia, rather than the sulphur dioxide suggested by d' Arsonval (1881). Heat is transferred between the water and working fluid by means of heat exchangers. This heat transfer process takes typically about 50% of the temperature difference between the reservoirs to accomplish (Lavi and Zener, 1975). Assuming a temperature difference (ΔT) between the reservoirs of $20^{o}C$, and a warm water temperature of $25^{o}C$, the ideal thermal efficiency of an OTEC plant is $\eta = 20/(25 + 273) = 6.7\%$. Due to the temperature loss across the heat exchangers, together with additional parasitic losses such as in the ocean water pumping systems, this efficiency is in practice reduced to about 2%. This very low efficiency necessitates very large water flow rates: for example, to produce 100 MW, a total flow rate of 1000 m^3/s is required (Jirka et al., 1981) while for a 1000 MW plant, the flow rate would correspond to half the Mississippi's mean discharge! This vast amount of water required must be increased if ΔT is reduced. Such a reduction could occur due to local weather anomalies, seasonal sea surface temperature variations or by recirculation of the discharged water into the warm water inlet. However, it can be reduced if the exchanger becomes more efficient. Thus, it can be seen that a key part of OTEC development must be the design of the heat exchangers.

Another possibility for the heat engine is the open cycle approach described in some detail by Cohen (1979-1980) which uses the sea water itself as the working fluid, this being deaerated and flash evaporated such that the steam produced drives the turbines. However, the technology for the closed cycle system is at present further advanced, so that this is the major option currently pursued.

On August 2, 1979 the first floating, at sea OTEC plant to produce net power, MINI-OTEC, went into operation off Ke-Ahole Point, Hawaii, and continued until December 1979. This barge-mounted experimental plant, discussed in detail in Trimble and Potash (1979) was built to test key power system components, and succeeded in producing 50 KWe of electricity (gross) or about 10 KWe of net power; it also gave valuable information on the pressing problems of biofouling, corrosion and their countermeasures.

In April 1981, OTEC-1, a T2 tanker converted into a 1 MWe test facility, commenced operation which was planned to continue for three and a half years. An overview of the OTEC-1 design is given in Svensen (1979). The primary purpose of this plant is again to operate and test an OTEC module at sea, assess developing heat exchanger technology, evaluate biofouling and corrosion and to determine potential environmental impacts.

The Japanese have also been investigating their own OTEC possibilities, as described in Homma _et al_. (1979). In 1974 they established an OTEC committee to overview their research, and they are

now planning their own 1 MWe tanker based test plant to facilitate the design of a 100 MWe plant.

I-3 Potential Future OTEC Uses and Applications

The temperature gradient which forms the ocean thermal resource has the great advantage of being renewable. It is also steady, day and night, enabling OTEC plants to be used as baseload plants, i.e., producing electricity continuously, and hence comparable with other baseload sources such as coal and nuclear power plants. The OTEC electricity must either be transported to shore via submarine cables or be used in situ. The latter option entails the manufacture of energy intensive products such as aluminum, ammonia, hydrogen, chlorine and magnesium. This would enable plants to operate in a 'grazing' mode, moving to a region of maximum thermal resource as required, whereas electricity transmission to shore, requires them to be stationary. However, plants in the Gulf of Mexico could provide valuable baseload contributions to the Southern States, a region having the lowest electricity reserve margin and fastest electrical growth in the U.S. (Cohen, 1979-1980): also it would supply the U.S. Islands such as Puerto Rico and Hawaii as discussed in Richards (1979). This 'island strategy' is also particularly interesting as frequently very deep water is found relatively close to the islands enabling reduction of transmission costs and energy independence for the islands which frequently are dependent on oil generated electricity.

Typical sizes of commercial plants would be from 10 MWe to

500 MWe, the limiting size probably being determined by the ability to construct the platforms cost effectively and also due to recirculation possibilities between the plant outflow and inflow, reducing the thermal resource, and environmental considerations (Cohen, 1979-1980). These plants may operate individually or in energy 'parks' composed of several plants. This would reduce transmission costs, but careful consideration of water recirculation between plants reducing the thermal resource would have to be made, as in Jirka (1978).

A more detailed summary of general technical developments, remaining problems, and future plans is given in Vadus and Giannotti (1980), while other general overviews are given by Jirka (1979) and Cohen (1979-1980).

APPENDIX II

HISTORICAL OVERVIEW OF THE HYDRAULIC ANALOGY TO COMPRESSIBLE GAS FLOW

The mathematics of this analogy is discussed in Section 2-2. This appendix will confine itself to the historical usage of the analogy.

The similarity between compressive shock waves in gases and the surface water waves found around obstacles in rivers was noticed as early as 1887 by the Austrian physicist E. Mach (1887). Later, in 1911, Isaachsen showed one of the first experimental demonstrations of the analogy, applying it to, among other things the study of nozzle flow (Isaachsen, 1911). It was not until 1920 that Jouget (Jouget, 1920) established the basic mathematical relationships comprising "the hydraulic analogy", i.e., the analogy between free surface water flow and compressible gas flow. He realized that, due to the nature of the equations, the analogy only applied to a gas having a ratio of specific heats, $\gamma = 2$ and not 1.4 as is the case with air.

Thus, the basic analogy occurs between the two-dimensional flow of an inviscid, homogeneous isentropic gas, having a constant ratio of specific heat capacities, γ, and the two-dimensional flow of an inviscid, homogeneous, shallow fluid experiencing no surface tension effects, and confined to a channel with a horizontal bottom and with vertical walls. The analogy states that, provided γ for

the gas equals 2 then,

$$\frac{h}{h_o} = \frac{\rho}{\rho_o} = \left[\frac{T}{T_o}\right]^{\frac{1}{(\gamma-1)}} = \left[\frac{p}{p_o}\right]^{\frac{1}{\gamma}}$$

$$\underbrace{\sqrt{gh} = c}_{\text{water}} = \underbrace{a = \sqrt{\gamma gRT} = \sqrt{\frac{\gamma p}{\rho}}}_{\text{gas}}$$

where h and h_o are water depths, ρ , T, p being density, temperature and pressure, respectively of the gas, a the speed of sound in a gas and c the velocity of a surface wave propagation in a fluid. Thus measurement of the water heights gives information about the various gas dynamic parameters. It should be noted, however, that other effects such as capillary waves, have no part in the analogy.

The main use made of the analogy in these and following cases were the investigation of air flows, supersonic and subsonic, around various obstructions, by means of experimental work on shallow, free-surface water flows. These hydraulic experiments at the time were easier to carry out than the gas experiments, the latter being much more difficult and expensive.

One of the best known studies of the hydraulic analogy was made by Ernst Preiswerk, as part of his doctoral thesis now translated (Preiswerk, 1938, Parts 1 and 2). He completed a mathematical investigation of both subsonic and supersonic analogy methods (Preiswerk, 1938, Part 1) together with a consideration of the

applicability of the analogy in the presence of a discontinuity such as a jump or shock. He concluded that, in principle, a shock in a compressible gas with $\gamma = 2$, is not fully analogous to a hydraulic jump in water flow over a horizontal bottom (see Table 2-3). However, provided that weak discontinuities only are admitted, the analogy between the two flows is still satisfied to a first approximation.

During the 1940's and 1950's the usage of the hydraulic analogy gained in popularity, a detailed summary of its development and applications being given by Hoyt (1962). Some particular advances during this time, however, will be listed herein:

The hydraulic analogy proved particularly useful, experimentally, in the field of transonic flow. This is due to transonic wind-tunnel facilities encountering difficulties due to the shock waves generated being almost perpendicular to the bodies under investigation. This can be seen to occur for transonic cases (Mach number $M \sim 1$), due to the Mach angle, α, where $\alpha = \sin^{-1}\left(\frac{1}{M}\right)$ (Shapiro, 1953) being near 90 degrees, where this is the angle the shock would make relative to the direction of the flow. Reflections of the shock from the wind tunnel walls would thus arrive back close enough to the body to distort the flow field. In a hydraulic channel the hydraulic jumps analogous to these shock waves can be trapped easily (Hoyt, 1962), thus eliminating the problem.

Laitone (1952), pointed out that the expression for the wave

velocity, $c = \sqrt{gh}$, which forms the basis of the analogy, as discussed in Section 2-3, only holds for negligible vertical accelerations (Lamb, 1945). He found, experimentally, that c tends to $\sqrt{gh}$, independent of the wavelength λ only for small water depths, of the order of 1/4 inch.

Crossley and Harleman (1952) extended the analogy to encompass unsteady rotational flow, making it applicable to accelerated transonic flows between curved shocks. They used a "towed model" type of apparatus to investigate transonic flow over wedge profiles. Ippen and Harleman (1952), pointed out that for both shock and expansion waves, calculated values of h_2/h_1 agreed well with calculated values of ρ_2/ρ_1 but not so well with other terms in the analogy, i.e., pressure and temperature ratios. Thus they suggested a useful strategy which they called a "modified analogy" would be to use experimental height ratios to calculate density ratios, thereafter calculating pressure and temperature from aerodynamic relations. They used this method to predict flow around various shapes using the water channel.

Various meteorological applications were suggested by Tepper (1950, 1952) who generalized the analogy to apply to not only one layer free surface flow, but to flow in two and three layers. He then used the method of characteristics to suggest an explanation for the erratic behavior of pre-frontal squall lines.

Klein (1966) made a critical evaluation of the theory and limitations of the hydraulic analogy. More recent usages of the

hydraulic analogy involve the investigation of flow through turbomachines. Blanvillain and Thirifays (1970) used free surface shallow water to visualize supersonic flow through turbine blades, while Le Bot and Bernard (1972) investigated the streamline pattern by using particles as tracers.